



TAMPEREEN TEKNILLINEN YLIOPISTO
TAMPERE UNIVERSITY OF TECHNOLOGY

Jonne Näkki

Properties of alloy 625 claddings made with laser and CMT methods



Julkaisu 1593 • Publication 1593

Tampere 2018

Tampereen teknillinen yliopisto. Julkaisu 1593
Tampere University of Technology. Publication 1593

Jonne Näkki

Properties of Alloy 625 Claddings made with Laser and CMT Methods

Thesis for the degree of Doctor of Science in Technology to be presented with due permission for public examination and criticism in Tietotalo Building, Auditorium TB109, at Tampere University of Technology, on the 23rd of November 2018, at 12 noon.

Tampereen teknillinen yliopisto - Tampere University of Technology
Tampere 2018

Doctoral candidate: Jonne Näkki
Materials Science
Engineering Sciences
Tampere University of Technology
Finland

Supervisor: Petri Vuoristo, Professor
Materials Science
Engineering Sciences
Tampere University of Technology
Finland

Pre-examiners: Antti Salminen, Professor
LUT School of Energy Systems
LUT Mechanical Engineering
Lappeenranta University of Technology
Lappeenranta, Finland

John Powell, Technical Director
Laser Expertise Ltd
Nottingham, UK

Opponents: Antti Salminen, Professor
LUT School of Energy Systems
LUT Mechanical Engineering
Lappeenranta University of Technology
Lappeenranta, Finland

Gerhard Posch, Vice President
Knowledge & Data Management / weldingACADEMY
Voestalpine Böhler Welding GmbH
Leoben, Austria

ISBN 978-952-15-4252-7 (printed)
ISBN 978-952-15-4279-4 (PDF)
ISSN 1459-2045

Abstract

Nickel-based alloy 625 is probably the most widely used nickel alloy. Alloy 625 is widely used as a coating or, cladding material, due to its superior corrosion resistance and good weldability.

Cladding, overlay welding, or weld overlay, is a method where some part of a metal component is coated with a layer of another metal, to obtain the better, more desirable properties of corrosion or wear resistance to this layer. By these means it is possible to get better properties to the section of the component that needs to withstand higher corrosion and/or wear load.

Two methods, were examined in this study, laser cladding with powder as a filler material and arc welding with CMT process using wire as a filler material. Laser cladding is a process whereby metal powder is injected into a laser beam through either coaxial or lateral nozzles. The laser beam melts the powder and a thin layer of the substrate surface. The melt solidifies very rapidly and forms a fine-grained microstructure with good mechanical and corrosion properties. CMT is an acronym for Cold Metal Transfer, a process developed and owned by the Austrian welding power source manufacturer, Fronius. The CMT process is an advanced, digitally controlled version of the traditional MIG/MAG arc welding process. The characteristic feature of the CMT process is cyclic retraction, a backward motion of the wire with a frequency of 70–80 Hz.

Laser cladding tests were performed with several alloy 625 powders as feedstock material. The tendency of these powders to produce hot cracks was studied with single bead tests. It turned out that there were variations in the content of the elemental impurities carbon, phosphor, sulphur and boron, as well as in the silicon, manganese, aluminium and titanium content of the powders. Powder that was free of aluminium and titanium, but contained a relatively large amount of boron turned out to be very crack sensitive. It was proved that the aluminium and titanium content of the alloy 625 feedstock powder affects the direction of the melt flow in the melt pool. Aluminium and titanium free powder produces an inward flow in the melt pool that leads to deeper penetration, steeper thermal gradients and a columnar dendritic structure, so that the last of the melt to solidify occurs at the weld centreline and hot cracks may form before that part of the melt which has a lower solidification temperature has totally solidified. In contrast, alloy 625 feedstock powder containing some aluminium and titanium leads to an outward melt flow in the melt pool, which in turn leads to shallower penetration, a lower temperature gradient and more equiaxed dendritic structure, so that the last of the melt to solidify melt is not at the weld centreline.

The applicability of using the CMT process in cladding was studied with single and adjacent beads with a stringer motion by using Ø1.2 mm alloy 625 wire as a feedstock material. Some tests were also conducted with the conventional MIG and pulsed MIG processes especially aimed at comparing the actual process power in all these three types of MIG processes: conventional MIG, pulsed MIG and CMT. The results of these tests showed that the actual arc power is lower with the CMT process than it is with conventional MIG and pulsed MIG

processes, although with the CMT process the actual arc power determined with AIP method was clearly higher than that determined with the common method where average the current is multiplied with the average voltage.

The CMT process allows the use of a relatively high travel speed of 1000 or 1200 mm/min. This is a relatively high travel speed for the arc welding process, but not for the laser cladding process. Higher travel speeds, in the range of 1400-1500 mm/min, led to instability in the melt pool, uneven beading and occasional underfill-type defects. However, it is also not possible to decrease the thickness of the cladding to below 2 mm by increasing the travel speed, or with any other method. With the CMT process, it was possible to use a relatively large transition, track displacement, of around 4 mm between the cladding passes, which increases the overall cover rate.

The results show that it is possible to produce flawless, low-dilution cladding with the CMT process, and the deposition rate can be up to 5 kg/h with a cover rate of over 0.2 m²/h. These values are about twice those achieved by the laser cladding equipment used in this study. In addition, when energy consumption values were multiplied with process efficiency values, the utilization of electrical energy in the CMT process was shown to be much more efficient than that of the laser cladding process. The calculations showed that the electrical energy needed to produce one square meter of alloy 625 cladding with the laser cladding process is 373 MJ, while it was only 66 MJ with the CMT process. In other words, the CMT process only consumes about one sixth (17%) of the energy needed for the laser cladding process.

Preface

The experimental studies for this thesis were conducted in Kokkola, starting with the studies in laser cladding, which were done at KETEK – Central Ostrobothnia Technology Centre in Kokkola Finland. The laser claddings for laser vs. CMT comparison were done at Kokkola LCC Oy. The CMT cladding studies were done at Centria University of Applied Sciences in Kokkola, Finland.

The laser cladding studies presented in this thesis were part of the research project “*Laser materials processing with high power*”, or Trilaser for short. They were part of the Finnish Metals and Engineering Competence Cluster’s (FIMECC Oy) Innovation & Network program. Studies with CMT arc welding process were made under the aegis of the EU funded Interreg project “*CMT – Nordic business opportunities from coating and additive manufacturing*”.

The work was supervised by Professor Petri Vuoristo at the Faculty of Engineering Sciences, Laboratory of Materials Science, Tampere University of Technology. Also Dr. Jari Tuominen from the same faculty also gave his guidance. I would also like to thank Mr. Juha Junkala, who operated both the laser and CMT equipment in cladding tests.

Tests with the CMT process were made using the welding robot cell of The Federation of Education in Central Ostrobothnia located in Kokkola next to Centria University of Applied Sciences.

I would also like to express my gratitude to Veli-Matti Korpisalo and Ilkka Piispanen of LCC Kokkola Oy, who made it possible to produce some test claddings using industrial laser cladding equipment.

Last but not least, I want to express my gratitude to my family Anu, Joel, Aaron, Joanna and Aada for their patience and support during the thesis work.

Kokkola, Finland, November 5th, 2018.

Author

Contents

Abstract	i
Preface	iii
Contents	iv
Acronyms and symbols	vi
1. Introduction	1
1.1. Background to the studies	1
1.2. Author's contribution and other publications	2
1.3. Objectives and contributions	3
1.4. Thesis outline	3
1.5. Alloy 625	4
1.5.1. History of alloy 625	4
1.5.2. Uses and applications of alloy 625	5
1.5.3. Alloy 625 as a cladding material	6
1.5.4. Alloying elements of nickel alloys	6
1.5.5. Alloying elements of alloy 625	8
1.5.6. Residual elements or impurities of alloy 625	10
1.5.7. Solidification of alloy 625	16
1.5.8. Laves phase	17
1.6. Hot cracking phenomenon	19
1.6.1. Solidification cracking	20
1.6.2. Factors affecting solidification cracking phenomenon	21
1.6.3. The evaluation of hot cracking sensibility	28
1.7. Melt pool surface tension and surfactants	29
1.8. Cladding processes	35
1.9. Powder vs. wire as a feedstock material	37
1.9.1. Powder characteristics	39
1.9.2. Powder vs. wire – surface area	41
1.10. Laser cladding	41
1.11. Cladding with wire and arc	43
1.11.1. Wire and arc cladding processes	43
1.11.2. Transfer modes in the MIG/MAG process	43
1.11.3. The CMT process	46
1.11.4. Shield gases in the welding of Ni-based alloys	54
1.11.5. Arc cleaning effect	56
1.12. Cladding defects	58
1.12.1. Cracks	58
1.12.2. Lack of fusion and lack of inter-run fusion	59
1.12.3. Humping	59
1.12.4. Underfill	60
1.12.5. Porosity	61
1.12.6. Undercutting	61
1.13. Mechanical parameters	62
1.13.1. Motion	62
1.13.2. Track displacement	63
1.13.3. Travel speed	64
1.13.4. Bead shape	64
2. Methods	67
2.1. The equipment in the cladding tests	67
2.1.1. Laser cladding equipment	67
2.1.2. CMT cladding equipment	68
2.2. Materials	69
2.2.1. Alloy 625 powders	69
2.2.2. Composition modification of alloy 625 powders	70
2.2.3. The alloy 625 wires	71
2.2.4. Alloy 625 plate	71
2.2.5. Cladding substrates	71
2.3. Laser cladding tests	72
2.3.1. Hot cracking tests with 11 alloy 625 powders	72
2.3.2. Hot cracking tests with modified alloy 625 powders	73

2.3.3.	High speed video imaging during single bead tests	74
2.4.	Cladding with arc process and wire	75
2.4.1.	Comparison of conventional MIG, pulsed MIG and CMT processes.....	75
2.4.2.	CMT tests with single beads.....	76
2.4.3.	CMT tests with adjacent beads.....	77
2.5.	Laser vs. CMT – comparison.....	78
2.6.	Measurements and examinations	79
2.6.1.	Analysis of the alloy 625 powders	79
2.6.2.	Hot crack measurement	80
2.6.3.	Metallography and microscopy.....	80
2.6.4.	Single bead dimension	81
2.6.5.	Hardness measurements	82
2.6.6.	Current and voltage measurements in arc welding tests	82
2.6.7.	Cladding substrate temperature	83
2.6.8.	Measurements of corrosion properties	84
3.	Results	87
3.1.	The results of the laser cladding studies.....	87
3.1.1.	Laser – composition and appearance of the alloy 625 powders	87
3.1.2.	Laser – preliminary hot cracking test results.....	90
3.1.3.	Laser – Hot cack results with 11 alloy 625 powders	92
3.1.4.	Laser – hot crack results after modification of the alloy 625 powders	99
3.1.5.	Laser – melt pool behaviour	103
3.1.6.	Laser – cladding with adjacent beads.....	106
3.2.	Results from cladding tests with arc and wire.....	106
3.2.1.	Conventional MIG, pulsed MIG and CMT processes – comparison.....	106
3.2.2.	CMT – wire feed speed	111
3.2.3.	CMT – the effects of shield gas and the auxiliary parameters.....	114
3.2.4.	CMT – results with single beads.....	120
3.2.5.	CMT – results with adjacent beads.....	130
3.3.	Results of comparison: laser vs. CMT cladding.....	136
3.3.1.	Laser vs. CMT – arc cleaning effect	136
3.3.2.	Laser vs. CMT – cladding appearance and cross sections.....	140
3.3.3.	Laser vs. CMT – process power and energy consumption	143
3.3.4.	Laser vs. CMT – microstructure.....	145
3.3.5.	Laser vs. CMT – corrosion resistance	152
4.	Discussion.....	155
4.1.	Cladding with laser and powder.....	155
4.1.1.	Laser cladding – powder morphology	155
4.1.2.	Laser cladding – parameters	155
4.1.3.	Laser cladding – hot cracks and powder impurities	155
4.1.4.	Laser cladding – the effect of aluminium and titanium in the powder.....	156
4.2.	Cladding with CMT process and wire	157
4.2.1.	CMT – arc power.....	157
4.2.2.	CMT – wire feed speed	158
4.2.3.	CMT – shield gas	159
4.2.4.	CMT – travel speed and track displacement.....	160
4.2.5.	CMT – hot cracks	161
4.2.6.	CMT – applicability of the process to cladding.....	161
4.3.	Laser cladding vs. CMT cladding.....	162
4.3.1.	Laser vs. CMT – surface cleaning	162
4.3.2.	Laser vs. CMT – coating thickness.....	163
4.3.3.	Laser vs. CMT – process energy and heat input	164
4.3.4.	Laser vs. CMT – microstructure.....	165
4.3.5.	Laser vs. CMT – cracks with powder No. 12.....	166
4.3.6.	Laser vs. CMT – corrosion resistance	166
5.	Final conclusions and recommendations.....	169
5.1.	Laser cladding	169
5.2.	CMT process	169
	References.....	173

Acronyms and symbols

CMT	Cold Metal Transfer	γ'	Gamma prime, Ni ₃ (Al, Ti) phase
MIG/MAG	Metal Inert/Active Gas Welding	γ''	Gamma double prime, Ni ₃ Nb phase
GMAW	Gas Metal Arc Welding	σ	Sigma phase
TIG	Tungsten Inert Gas welding	P	P phase
GTAW	Gas Tungsten Arc Welding	μ	μ phase
MMA	Manual Metal Arc Welding	Laves	Laves phase
SMAW	Shielded Metal Arc Welding	NbC	Nb Carbide
SAW	Submerged Arc Welding	TiN	Titanium Nitride
PTA	Plasma Transferred Arc welding	CPT	Critical Pitting corrosion Temperature
I	Current	Ni	Nickel
A	Ampere	Cr	Chromium
U	Voltage	Mo	Molybdenum
V	Volt	Nb	Niobium
AIP	Average Instantaneous Power	C	Carbon
k	Welding process efficiency factor	S	Sulphur
PR	Power Ratio	P	Phosphor
CTWD	Contact Tip to Work Distance	Al	Aluminium
WFS	Wire Feed Speed	Ti	Titanium
PFR	Powder Feed Rate	Si	Silicon
Ar	Argon gas	Mn	Manganese
He	Helium gas	Zr	Zirconium
CO ₂	Carbon dioxide gas	BTR	Brittle Temperature Range
H ₂	Hydrogen gas	CET	Columnar to Equiaxed Transition
N ₂	Nitrogen gas		
ALC	Arc Length Correction		
DC	Dynamic Control		
DC	Direct Current		
AC	Alternating Current		
TS	Travel Speed		
TD	Track Displacement		
OR	Overlapping Ratio		
OM	Optical Microscope		
SEM	Scanning Electron Microscope		
EDS	Energy Dispersive x-ray Spectrometer		
EDX	Energy Dispersive X-ray spectrometer		
Nv	Electron home number		
γ	Gamma phase		

1. Introduction

This study focuses on the properties of alloy 625 cladding and two, associated cladding processes: laser cladding and arc the welding process called CMT. Cladding is here defined as an outer layer of material covering another. Term cladding is used on variety of branches or sectors, but mostly on a field of construction and metalworking. And depending on a branch or sector, term cladding refers to slightly different issues. In a case of construction, cladding refers materials applied to the exterior of building. In a case of metalworking, cladding is a layer of metal connected to a layer of a different metal, or the process that connected them [1].

Nickel-based alloy 625 is probably the most widely used nickel alloy due to its versatile properties. Alloy 625 is often known by its most common brand name, Inconel 625. However, Inconel is in fact a registered trade mark owned by the Huntington Alloys Corporation, a subsidiary of the Special Metals Corporation [2]. Other well-known brand names for alloy 625 are Haynes 625, Nickelvac 625, Nicrofer 6020, Altemp 625 and Chronic 625 [3]. However, in this study, generic term 'alloy 625' is used.

Due to its good corrosion resistance, alloy 625 is used widely in overlay, or cladding, especially in waterwalls and tubings of boilers fuelled by waste materials [4]. There are various methods to make a cladding: thermal spraying, laser cladding with powder or wire as a feedstock material, and various methods of arc overlay welding, all of which will be discussed later.

1.1. Background to the studies

The initial motivation for the studies was that in the production of laser claddings, it was found that hot quality of alloy 625 feedstock powder varies from manufacturer to manufacturer, and even between different batches from the same manufacturer. This can make the cladding susceptible to hot cracking. During the time the studies were started, there was no any clear explanation for this, but what is clear is that crack are a particularly harmful type if welding defect because they often occur beneath the surface of the weld and hence can-not be detected with non-destructive (NDT) quality assurance methods such as the liquid penetrant test (PT) or ultrasonic testing (UT). The images below are taken with an optical microscope (OM, Fig. 1 a), and an electron microscope (SEM, Fig. 1 b). They show a cross section of alloy 625 cladding with some small hot cracks.

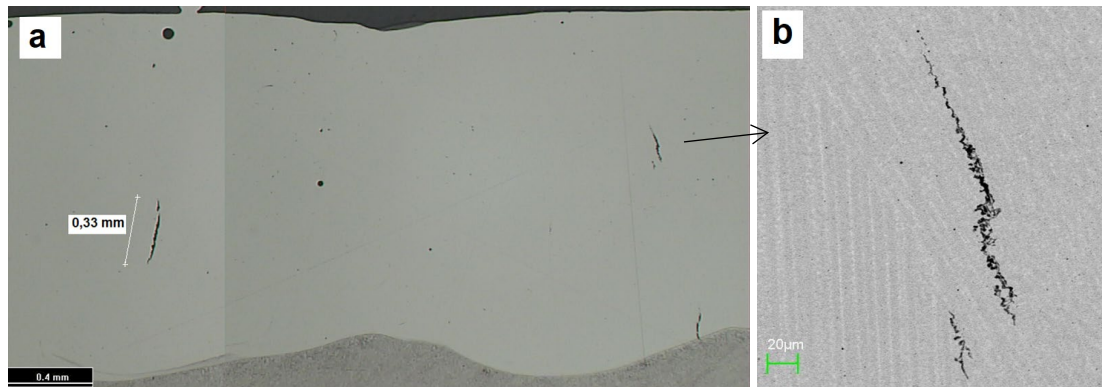


Fig. 1: Alloy 625 laser cladding with some hot cracking. Length of the largest cracks is around 0.3 mm. a) OM image, magnification: 30x. b) SEM BE image, magnification 200 [5].

Another issue for cladding with laser and alloy 625 powder is that there are often variations in the appearance of the cladding surface when the powder batch is changed. Again there is no clear explanation for this, but the variation in appearance is quite noticeable, as is shown in Fig. 2.

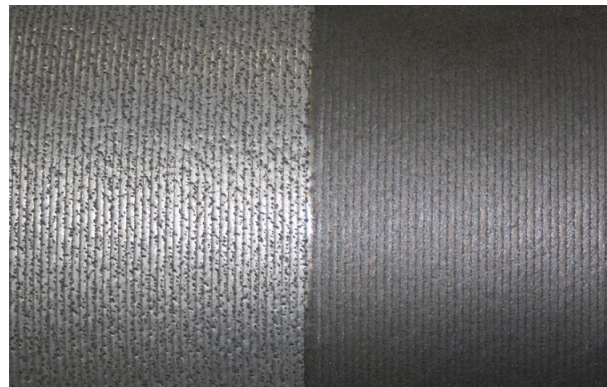


Fig. 2: Photograph of the surface of a laser-clad component using alloy 625 powder. The surface appearance changed when the alloy 625 powder batch was changed [5].

Cladding tests with the CMT process began at the beginning of 2016 and was mainly focused on studying the process' ability to produce claddings with low dilution and low heat input to the workpiece, the main advantages of the laser cladding process. The objective was to see whether these benefits could be reliably maintained in the on high-productivity cladding process. It was the properties and parameters of the CMT processes that were the main concern in the tests, rather than the occurrence of hot cracking.

1.2. Author's contribution and other publications

The author designed and performed all the measurements and calculations included in the experimental part of this work. The manuscript was written by the author and commented on by the supervisor Professor Petri Vuoristo and the co-researcher Dr. Jari Tuominen. Juha Junkala operated both the laser and CMT cladding test equipments.

Some of the laser cladding hot crack test results presented in this study had already been published at the ICALEO (The International Congress on Applications of Lasers & Electro-Optics) conferences held in 2012 in Anaheim, and in 2013 in Miami. The arc welding process

power measurement results with conventional MIG, pulsed MIG and CMT processes were published in the Finnish journal on welding technology “Hitsaustekniikka” in 2017.

1.3. Objectives and contributions

The following research questions (RQs) are addressed in this thesis:

- RQ.1: Determine the factors affecting the solidification cracking of alloy 625 in laser cladding using coaxially blown powder.
- RQ.2: Study the effect of some minor alloying elements of alloy 625, mainly aluminium and titanium, in the laser cladding process.
- RQ.3: Compare the actual arc power in conventional MIG, pulsed MIG and CMT processes.
- RQ.4: Understand the CMT process and the mutual interaction of two auxiliary CMT process parameters, Arc Length Correction (ALC) and Dynamic Correction (DC).
- RQ.5: Study the process parameters of CMT cladding with stringer motion.
- RQ.6: Compare the cladding properties of alloy 625 claddings made with laser and powder, and CMT and wire, as feedstock materials.

The contributions of the thesis are as follows:

- The factors that make laser cladding process with alloy 625 powder sensitive to hot cracking.
- Determination of the factors that have an effect in the fluid flow in the melt pool and the resulting penetration depth and dilution in laser cladding with alloy 625 powder.
- Determination of the differences in the arc power of the conventional MIG, pulsed MIG and CMT processes with the same wire feed speed (WFS) set value, as well as the differences between the arc powers determined both with traditional method using average current and voltage ($I_{aver} \times U_{aver}$) and Average Instantaneous Power (AIP) method.
- Understanding of the effect the auxiliary parameters ALC and DC have on the CMT process.
- Determination of the parameters: WFS, travel speed (TS), shield gas, track displacement (TD) etc., that produce good quality claddings with high productivity with the CMT process.
- Comparison of the main properties of the laser and CMT cladding processes and their resultant claddings.

1.4. Thesis outline

The thesis is divided into 4 main chapters. **Chapter 1, Introduction** contains a literature review of alloy 625, its history, uses, composition and properties. This chapter also discusses solidification cracking, melt pool surface tension, laser cladding with powder and cladding with gas-shielded arc welding (MIG/MAG). **Chapter 2, Methods**, presents a detailed description of the experimental procedures utilised for the different steps of this research study. This

chapter also describes the base materials, welding consumables, metallographic preparation and data acquisition methods used. The results of the tests are presented in **Chapter 3, Results** and discussed **Chapter 4, Discussion**. The final conclusions drawn from the experimental results are presented in **Chapter 5, Conclusions**.

While the emphasis in the studies on laser cladding with powder is on solidification cracking, the emphasis in the studies on MIG/MAG (CMT) welding and wire are on the CMT process itself, cladding parameters and deposition rate. The last part of the thesis contains a comparison of the process and properties of laser cladding and CMT cladding using powder and wire feedstocks respectively.

1.5. Alloy 625

Alloy 625 is a nickel (Ni)-based and alloyed with containing chromium (Cr), molybdenum (Mo) and niobium (Nb). Due to the solid solution strengthening provided by these elements, heat treatment is not usually needed to achieve the desired properties in the cladding. This combination of elements is also responsible for superior resistance to a wide range of corrosive environments of unusual severity, as well as to the effects of high-temperature, such as oxidation and carburization [6].

The following sections give some detailed information about alloy 625; its history, alloying elements and properties. The emphasis is on how the alloyed elements affect solidification and hot crack formation.

1.5.1. History of alloy 625

The development of alloy 625 (UNS N06625) begun in the 1950's to meet the then-perceived demand for a high-strength main steam-line piping material. The development started by determining how various amounts of the common major alloying elements: Cr, Mo, Nb, aluminium (Al) and titanium (Ti) affected on the strengthening in an alloy 600 base and a patent application was submitted in 1962 [7]. The development started with the need to have a new alloy for super critical steam power plants. One such power plant used 649 °C steam at 13.8 MPa. So, the goals for the development of the alloy were its weldability, high creep resistance, ease of fabrication into tubing and non-age hardening. Work had already been done in the 1950's on the strengthening effects of various amounts of the common major alloying elements, i.e., Cr, Mo, Nb, Al and Ti in an alloy 600 base. The strengthening effects of using these elements individually were not good enough, so it was decided to use Mo and Nb in combination with varying amounts of Ni. The alloy development lead first to the invention of an alloy with fairly similar composition to 625, namely 718, and a patent application for 718 was submitted in 1958.

One version of Ni-based alloy that preceded alloy 625 had a code name MS-2 and a composition of 60%Ni, 15%Cr, 3%Nb, 2%Mo, 0.5%Al, 0.5%Ti and the balance of Fe. It was discovered that this alloy could more readily compete with already available alloys in the markets if it had a higher room-temperature strength. Fortunately for the development of alloy 625, it was discovered that Cr and Mo, which were used to increase room-temperature strength, also increased the alloy's corrosion resistance. Consequently, the Cr and Mo

contents were increased to the current levels of 22%Cr and 9%Mo. This change in composition altered the course of development of the alloy and increased its marketing potential. The Al and Ti content were intentionally kept low to minimize the age-hardenability of the alloy. It was discovered that approximately 3.5–4% of Nb was needed to increase the creep strength of the alloy. Early in the alloy's history many heats were made with the Nb level in the 4.0–4.2% area, while most service or application data were from subsequent heats that had lower (3.6–3.8%) levels of Nb. While higher levels of Nb allow increased levels of strength after an aging cycle, the penalty of decreased room-temperature ductility levels after prolonged service exposure is not worth the small advantage that the capability of intentional aging provides [7]. The present specification of alloy 625 limits the Nb content to 3.15–4.15%, and the normal Nb content is around 3.6%.

1.5.2. Uses and applications of alloy 625

Alloy 625 welding products are widely used for the overlay of alloy steel tubes in coal-fired power boilers and municipal waste incineration waste-to-energy boilers. At high temperatures, halides are particularly aggressive corrodents for ferrous materials. According to one reference, alloy 625 had already established itself as the most widely used material for effective corrosion protection in waste boilers in 1997. This was due to the prevailing consensus that the corrosion rate of alloy 625 was less than 0.25 mm/y and that it outperformed typical steel tubing by a factor of at least 10 [8]. However, alloy 625 type cladding material in waste incineration plants is limited to service temperatures below 450 °C, since long service above this temperature, increased corrosion rates. For this reason, the even more highly alloyed (23%Cr, 16%Mo, 3.8%W) alloy 686 is more suitable and corrosion resistant in temperatures above 450 °C [9]. Alloy 625 is also often used in-situ, i.e. as repair overlay welding of boiler tubes. Furthermore, some procedures have been developed for the overlay of boiler tubes in a workshop prior to installation [10].

Alloy 625 welding wires are classified by the European standard ISO 18274 as Ni 6625 [11], and by the American standard AWS 5.14 as ERNiCrMo-3 [12]. Recent classification for alloy 625 powders to be used in additive manufacturing is also classified by the American ASTM F3056-14e1 standard as UNS N06625 [13]. All these standards state the same compositional limits for alloy 625, which are presented in Table 2 on p. 8.

Ni-Cr-Mo and Fe-Ni-Cr-Mo weldments, such as stainless steels, experience elemental segregation upon solidification. This results in some parts of the weld structure being enriched in the alloying elements, while others are depleted. As a result, some areas have reduced resistance to corrosion. For this reason, weldments deposited with matching composition welding products may not offer as good corrosion resistance as the wrought base metal. To counter this effect, these corrosion-resistant materials are normally joined with over-matching composition welding products. Due to this, alloy 625 welding products are particularly well suited for joining (welding) Mo bearing austenitic and super-austenitic stainless steels (e.g, types 316, 317, and 904L), and the 6% Mo and nitrogen-enhanced super-austenitic stainless steels.

1.5.3. Alloy 625 as a cladding material

Alloy 625 is very widely used as a corrosion-resistant weld overlay, i.e. as a cladding material. Alloy 625 cladding is typically between 2 and 5 mm thick. It can be applied using a variety of welding processes including manual metal arc welding (MMA), tungsten inert gas welding (TIG), metal inert/active gas welding (MIG/MAG), submerged arc welding (SAW), plasma transferred arc welding (PTA) and laser cladding with powder or wire as a feedstock material. Each process has its own pros and cons, in terms of the typical features of cladding such as the dilution level, deposition rate, or heat input to the base material. In the case of alloy 625 cladding, one very important consideration is the dilution of the clad layer by the substrate material, usually low-alloyed steel, as this dilution can have a dramatic effect on the corrosion resistance of the cladding.

Another consideration is the effect of heat input to the base material, since it has a direct effect on the formation and the size of the heat-affected zone (HAZ). The hardness of the HAZ of the steel base material is a significant issue in the case of base materials that generate hard martensite in the HAZ during the rapid heating and cooling of the process. A lack of toughness can generate cold cracking in the HAZ. The heat input to the base material can also cause distortion or changes in its dimensions, so it is advantageous if the heat input is low and so that these effects can be avoided or minimized. A good cladding process should be able to produce a defect-free clad layer with low dilution and small HAZ, and without any changes in the dilution or other properties for every production run, even when the feedstock material batch is changed during the same production run.

Another very important issue when deciding on a coating process is the efficiency of the process. It should have a high deposition rate in terms of input cladding mass per hour (kg/h), or even better, clad area per hour (m^2/h). Among the cladding methods mentioned above, SAW, or the very similar method, electroslag welding (ESW), are the most effective in terms of deposition rates and can achieve several dozen kilograms per hour. In contrast, a typical deposition rate of laser cladding with powder is only a few kilograms per hour. Other relevant concerns when selecting the best welding method for the cladding process include process flexibility, the rate at which it consumes feedstock material, the heat input to the base material, the energy efficiency and the cost of equipment, among others.

1.5.4. Alloying elements of nickel alloys

The usual alloying elements used in Ni-based superalloys, a category which includes alloy 625, are presented in Fig. 3. The term “superalloy” typically refers to the enhanced performance of the alloy, with Ni-based superalloys being high-temperature materials that also exhibit good resistance to corrosion. Fig. 3 and Table 1 show the atomic diameter difference of each alloying elements of Ni-alloys. There are some variation in these values between Fig. 3 and Table 1, since the values are from different sources. In addition, the electron home number N_v is shown in Fig. 3. In the past, this home number N_v , used to be used in a phase stability calculation routine called PHACOMP [14]. The primary objective of the PHACOMP routine is to predict the solid solubility of the γ -austenite matrix (gamma phase), i.e., the position of the phase boundary between the γ and $\gamma + \sigma$ (or P, μ , or Laves) phase fields [14].

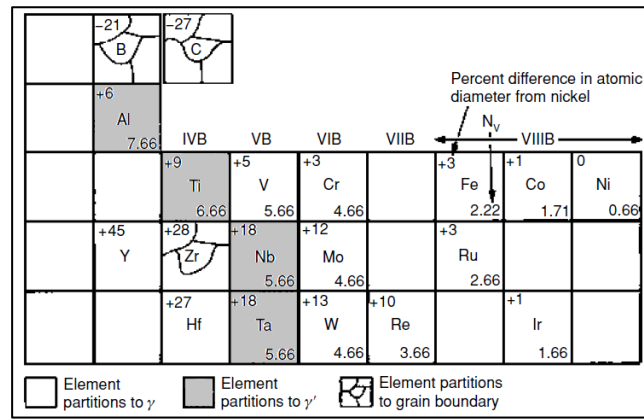


Fig. 3: Categories of elements important to the composition of Ni-based superalloys, and their relative positions in the periodic table [15].

Table 1: Summary of approximate atomic diameters and solubility data for various elements in Ni at 1000 °C [14].

Element	Approxim. atom size diff. to Ni, %	Approxim. solubility in Ni at 1000 °C, wt%
C	+43	0.2
Al	-15	7
Si	+6	8
Ti	-17	10
V	-6	20
Cr	-0.3	40
Mn	+10	20
Fe	+0.3	100
Co	-0.2	100
Cu	-3	100
Nb	-15	6
Mo	-9	34
Ta	-15	14
W	-10	38

The behaviour of each alloying element and its influence on the phase stability depends strongly upon its position within the periodic table (Fig. 3). The first class of elements includes Ni, cobalt (Co), iron (Fe), Cr, ruthenium (Ru), Mo, rhenium (Re) and tungsten (W); these tend to segregate to the austenitic γ and thereby stabilise it. The atomic radii of these elements are not very different from that of nickel. A second group of elements, Al, Ti, Nb and tantalum (Ta), have larger atomic radii and these promote the formation of ordered phases, such as the compound Ni_3 (Al, Ta, Ti), known as γ' (gamma prime). Boron (B), carbon (C) and zirconium (Zr) constitute a third class that tend to segregate to the grain boundaries of the γ phase, on account of their atomic sizes, which are very different from that of nickel [15].

The elements Co, Cr, Fe, Mo, Ta and Nb are generally used for solid solution strengthening. Elements that have a similar atomic size, electronic structure and crystal structure as nickel are likely to remain in the solid solution in the nickel matrix and the solubility of these elements is high. On the other hand, the ability of a dissolved solid solution strengthening

element to increase strength by solid solution hardening can be estimated by its atomic diameter difference compared to Ni [14]. The data in Table 1 shows that Al, Ti, Mn, Nb, Mo and W provide the best combination of atomic size difference and thus produce the relatively high solubility needed for solid solution strengthening.

1.5.5. Alloying elements of alloy 625

The main alloying elements of alloy 625 are Cr, Mo and Nb. There is usually some of the elements Al, Ti, Si, Mn and Fe, too. In addition to these, some residual, but detectable amounts of the harmful elements C, S, P, B and copper (Cu) are often present.

The compositional limits of alloy 625 are rather permissible according to standard ISO 18274 for welding consumables. Alloy 718, which has quite a similar composition to alloy 625, but higher concentrations of the alloying elements Nb, Al and Ti, has tighter compositional limits. The compositional limits of alloy 625 and 718 welding filler materials are presented in Table 2.

Table 2: Compositional limits (wt%) of Ni 6625 (alloy 625) and Ni 7718 (alloy 718) welding filler materials according to ISO 18274 [11].

	C%	P%	S%	B%	Mo%	Fe%	Mn%	Cr%	Ni%	Cu%	Si%	Al%	Ti%	Nb%
625	max 0.10	max 0.02	max 0.015	—	8.0– 10.0	max 5.0	max 0.50	20.0– 23.0	min 58.0	max 0.50	max 0.50	max 0.40	max 0.40	3.2– 4.1
718	max 0.08	max 0.015	max 0.015	max 0.006	2.8– 3.3	max 24	max 0.3	17.0– 21.0	50.0– 55.0	max 0.30	max 0.30	0.2– 0.8	0.7– 1.1	4.8– 5.5

As can be seen from Table 2, alloy 718 has tighter limits, especially for the impurity element B (0.006%), for which there is no prescribed limit for alloy 625. Alloy 718 also has a tighter range for Al and Ti, since there are both lower and upper limits, while for alloy 625 the content of these elements can be anywhere between 0 and 0.4%.

The compositional limits of alloy 625 powder for additive manufacturing (AM) are presented in the recently (2014) published standard ASTM F3056-14e1 [13] (*Standard Specification for Additive Manufacturing Nickel Alloy UNS N06625 with Powder Bed Fusion*), but these limits are the same as in the ISO 18274 (Table 2). However, the recent huge growth in the field of AM has had an effect in that some powder manufactures have introduced their own range of powders for AM purposes, which pay special attention to the particular quality requirements of AM. For example, H.C. Starck and Praxair have recently introduced (2016–2017) alloy 625 powder for AM with an upper limit of 0.010% for boron [16, 17], although the limits for other elements are the same as in the ISO 18274 and ASTM F3056-14e1 standards (Table 2).

1.5.5.1. Chromium

The main function of chromium (Cr) in alloy 625 is to enhance corrosion resistance, but it also enhances solid solution strengthening. Cr has a major effect on both wet corrosion and tolerance of high temperatures. The solubility of Cr in Ni matrix is 40%, but the atomic size difference compared to Ni is rather small: -0.3%, so Cr's capacity to increase solid solution strength is small. However, Cr readily generates carbides that increase the strength of the alloy if there is carbon present during solidification. Cr also has the ability to form stable oxides

and nitrides, which reduce the tendency for weld porosity compared to pure Ni or Ni-Co welds. Cr-bearing alloys are also more susceptible than other high-Ni alloys to hot cracking when other elements, notably Si, are present. For example, the hot cracking susceptibility of Ni-base weld metal containing 15% Cr is sharply increased as the Si increases from a few tenths of a percent to 1% [19].

1.5.5.2. Molybdenum

The function of molybdenum (Mo) is to provide (wet) corrosion resistance, especially resistance against localised corrosion pitting and crevice corrosion as well as stress-corrosion cracking in environments containing chlorine (Cl⁻) ions, like seawater. On the other hand, Mo reduces the high-temperature oxidation resistance of the alloy. The solubility of Mo in a Ni matrix is ~30% and the atomic size difference compared to Ni is large: -9%, so Mo is a good solid solution strengthener. Mo also creates the carbides MC, M₂₃C₆ and M₆C [19], and segregates to eutectic melt during solidification.

1.5.5.3. Niobium

Niobium (Nb) is added to the alloy mainly to give it strength, and it has little effect on corrosion resistance. Nb has the potential to strengthen Ni-based alloys with three mechanisms:

1. Solid solution strengthening – large atomic size difference, -15% compared to Ni.
2. Precipitation hardening by γ'' phase (gamma double prime, Ni₃Nb) formation.
3. Carbide (NbC) formation.

Nb does not dissolve extensively in Ni or Ni-20%Cr alloys. Its solubility is limited to about 7% in an Ni-20% Cr alloy at 1200 °C and this value falls with decreasing temperature. The atomic size mismatch of about -15% with respect to Ni is too large to allow greater solubility [20], but this large size difference does bring about a large solid solution strengthening effect. However, the limitation in solubility leads to segregation of Nb during the cooling and solidification of alloy 625. So, the segregation of Nb to the eutectic between dendrites is strong during weld pool solidification. According to factorial experiments the Nb solubility in the alloy appeared to be about 2.5% and increased as the Mo + Cr content decreased. Any higher content than this and the aging treatment starts to strengthen the alloy [7]. This increase in strength is presumably caused by the precipitation of γ'' phase (Ni₃Nb). During the development of alloy 625, it was found out that an Nb content of close to 4% is needed to yield the best high temperature creep properties if the Cr and Mo contents of the alloy are 22% and 9%, respectively [7]. Higher Nb contents would increase creep strength still further, but on the other hand Nb contents above 4% substantially decrease the room temperature strength after prolonged exposure in elevated temperature [7].

Nb increases the amount of γ' phase (Ni₃(Al, Ti)) both by contributing to its formation and also by decreasing the solubility of Al and Ti in the matrix, which in turn can further increase the amount of γ' [20]. The presence of Nb is also related to the formation of the Laves phase in Ni alloys which increases its brittleness and affects hot cracking during welding.

For historical reasons, the element Nb is also known by its older name of columbium (Cb) in the United States.

1.5.5.4. Aluminium and titanium

Usually the role of aluminium (Al) and titanium (Ti) in Ni alloys is to bring strength by the formation of the $\text{Ni}_3(\text{Al}, \text{Ti}) \gamma'$ (gamma prime) phase precipitates in the matrix. However, this γ' phase is not usually assumed to form in alloy 625 claddings since the percentage is rather low and this phase does not normally form unless prolonged annealing has been performed. The Al and Ti additions in alloy 625 are principally for refining purposes and are lower than in alloys such as 718 in order to enhance weldability [21]. Both of these elements, Al and Ti, also have some other functions, such as their effect on weldability. However, the effect of Al and Ti on the weldability of alloy 625 is contradictory. Floreen et al. [21] concluded (in 1994) that minimizing the amounts of the elements Nb, Fe, Mo, C and Si helps control the alloy's cracking tendency and hence improves its weldability, while minimizing the elements Al and Ti reduces its weldability. So, Floreen et al. stated that a certain amount of Al and Ti is helpful for weldability [21].

Although Ti partitions to the interdendritic regions, it does not appear to partition to the eutectic Laves. This seems counter-intuitive, since Ti forms a prototypical Laves phase with Fe as Fe_2Ti , although there is no Ni_2Ti phase in the Ni-Ti binary. Examination of the carbide compositions indicates that Ti plays a much larger role in the (Nb,Ti)C eutectic than it does in the γ /Laves eutectic [22]. In a study by Silva et al. [23] it was concluded that titanium together with nitrogen affected the solidification path of alloy 625 so that the TiN particles acted as nucleation agents for (NbTi)C precipitates. However, due to the high melting point of the Ti-nitrides (2927 °C), which is approximately twice the liquid temperature of the 625 alloy, it was assumed that there were TiN particles in the feedstock (wire) material and that these TiN particles were present in the liquid before solidification started. This issue is discussed more in section 1.5.7 on page 16.

Both Ti, and especially Al, have a great affinity to oxygen, meaning that Al in particular is a strong oxygen former and can form a slag on the melt pool surface in the cladding process. This feature is usually neglected in weldability studies of alloy 625 and other Ni based superalloys, but it can particularly affect the laser cladding process. This issue is discussed more in section 1.7 on page 29. It can be also assumed that Al and Ti can have an effect on porosity formation, since these elements will bind with oxygen and nitrogen gases from the melt pool.

1.5.6. Residual elements or impurities of alloy 625

Residual elements or impurities (C, P, S, B, Si, Cu, Pb, Zn, etc.) are defined as elements which are not added on purpose and which are difficult to remove using simple metallurgical processes. The presence of residual elements in Ni alloys can have some effect on the mechanical properties of wrought material, but their strongest effect is on weldability. Some residual elements have an effect due to their presence in the solid solution, but from the point of view of weldability, the largest effect comes from the elements that segregate at interfaces

(surface and grain boundaries), such as S, P and B. The solubility of these most detrimental impurity elements in Ni alloys is very limited. The solubility, partition coefficient and eutectic (melting, solidification) values for binary system with Ni and impurity elements are presented in Table 3.

Table 3: Summary of partition coefficients (k), maximum solid solubility and terminal eutectic temperature in Ni-P, Ni-S Ni-B and Ni-Si systems [14].

System	k	Maximum solubility (wt%)	Terminal eutectic Temperature
Ni-P	0.02	0.32 P	870 °C
Ni-S	~0	~0 S	637 °C
Ni-B	0.04	0.7 B	1093 °C
Ni-Si	0.70	8.2 Si	1143 °C

As the values in Table 3 show, S in particular has very low solubility and high segregation potential (low k), in addition to which the terminal eutectic temperature is low.

1.5.6.1. Silicon

Silicon (Si) is considered here as an impurity element since it does not have any advantageous effects on the properties of alloy 625. The Si content in alloy 625 is limited to less than 0.5%, and in the case of some other Ni alloys, Si is limited to much lower levels. Also in its wrought form, alloy 625 usually has a very low Si content.

Some studies have found that Si strongly promotes the formation of the Laves phase in Ni alloys [24]. The Laves phase is detrimental to low temperature mechanical and fatigue properties since it is hard and brittle. The Laves phase is an intermetallic compound with a hexagonal crystal structure and A_2B stoichiometry, where A represents the elements Ni, Fe, Cr and Co, while B represents the elements Nb, Ti, Si, and Mo. The solidification temperature range grows as the P and S contents in the alloy increase. On the other hand, it was found that with some S and P present in cast alloy 718, the addition of Si raised the γ /Laves eutectic reaction temperature while reducing its solidification temperature range [25].

Si has a significant effect on its processability since even rather small amounts of Si increase the fluidity of the melt. For example, it is easier to make a smooth weld overlay in SAW (Submerged Arc Welding) with a Si-rich flux than with a Si-free flux, since Si-free flux produces poor flow characteristics of the melt pool, and the surface of the resulting weld overlay is rough. On the other hand, alloy 625 SAW overlay welds made with a Si-rich flux contained plenty of hot cracks, while those made with a Si-free flux did not contain any [26]. However, welding fluxes for both SAW and ESW processes usually contain some Si, so a typical Si content in the weld overlay is around 0.3, even though the alloy 625 strip has a Si content of only 0.1% [27].

In contrast to wires, or other wrought forms of alloy 625, powders are usually alloyed with some amount of Si (0.3–0.5%) due to requirements of processing the powder. A certain amount of Si ensures the flowability of the melt through the small powder-atomizing nozzle. It

is possible that the Si is poor and hence a high-viscosity melt could get stuck in to the atomizing nozzle during the process [28].

1.5.6.2. Boron

Boron (B) forms several compounds with Ni, like Ni_3B , Ni_2B_3 , Ni_4B and NiB . The Ni-B equilibrium phase diagram is shown in Fig. 4 to illustrate the many intermetallic compounds that may exist between Ni and B. Solidification temperature of these compounds is rather low, between 1020–1095 °C.

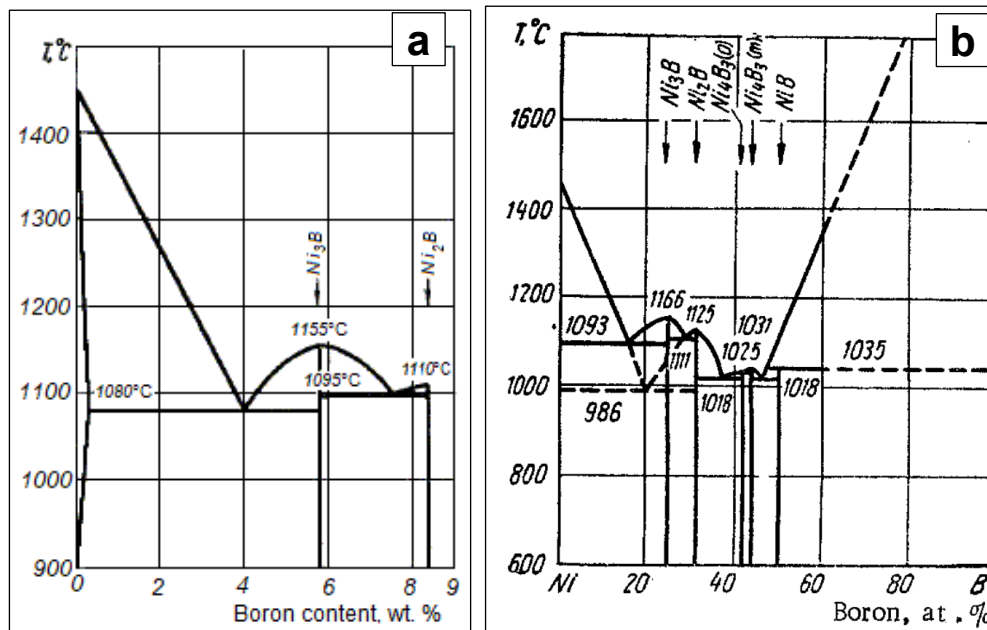


Fig. 4: Ni-B phase diagram. a) Part of the phase diagram of Ni-B. b) The whole phase diagram system of Ni-B [30].

Several studies have stated that B is the most detrimental element for the weldability of Ni alloys, since very small contents of B have been found to have a strong effect on the alloy's cracking tendency [31, 32, 33, 34, 48]. Most of the studies related to the effect of B in Ni alloys deal with precipitation-hardenable alloys like alloy 718, which can be regarded as a more alloyed version of alloy 625. There is a perception that B causes heat-affected-zone cracking sensitivity in alloy 718 welds if there is more than 0.003% of B [32]. Consequently, the B content in alloy 718 is limited to below 0.006%, while for alloy 625 there is no such limitation [11].

The detrimental influence of B on the alloy's weldability can be attributed to its strong segregation tendency and the formation of an M_3B_2 type phase that forms at a temperature of ~1200 °C. Boron also appears to lower the solid/liquid surface energy, which exacerbates cracking by promoting extensive wetting of the solidification grain boundaries and interdendritic regions by the terminal solute-rich liquid [14].

Chen et al. [33, 34] found out that electron beam welds in alloy 718 that contained 0.0043% of B had 7 to 20 times greater total cracking length compared to alloy (718) with its lower B level of 0.0011%. Other impurities (C, S, P) were very low level in these alloys. By lowering the C, S and P concentrations to a level as low as possible, the HAZ cracking was related

directly to the level of segregation of B at the grain boundaries, which occurred by non-equilibrium segregation during the pre-weld heat treatment.

On the other hand, B is added as an alloying element to some Ni alloys to enhance their high-temperature mechanical properties, particularly the creep resistance. B creates hard particles, borides, at the grain boundaries which inhibit the grain boundary slide, i.e. creep, at high temperatures. However, the B contents in some B-containing alloys are at a very low level. For example, Haynes 230, which can resist oxidation at extremely high temperatures (above 1000 °C) has an upper limit of only 0.015% for boron [35].

This ability of B to create borides at grain boundaries that prevent the grain boundary sliding at high temperatures can also decrease the ductility dip cracking of the HAZ of Ni alloys during the welding process. Lippold and Nissley [36, 37] found that grain boundary locking, promoted by the additions of Mo and B, seemed to improve the ductility dip cracking of Ni-base type Ni-30%Cr-8%Fe filler materials (52, 52M, etc.). Very small additions of B (0.003%) resulted in more precipitation of $M_{23}C_6$ along the weld metal grain boundaries, which enhanced grain boundary locking and ductility cracking resistance. Zirconium (Zr) also has some effect on the generation of these precipitates [37] and hence very small amounts of both B and Zr are added to 52M filler material to provide resistance to ductility dip cracking [38].

A small amount of B can also improve the fatigue properties of Ni alloys. Xiao et al. [39] found out that some amount of B increased the fatigue crack growth resistance of alloy 718 and improved the low cycle fatigue lifetime. In this study, B levels of 12, 29, 60 and 100 ppm were studied. Of these four alloys, a B content of 60 ppm (0.006%) displayed the best fatigue properties in a regime where the fatigue life was longer than about 300 cycles. However, the LCF lifetime decreased again as the B concentration increased from 60 to 100 ppm (0.010%). This was rationalized as being related to the mechanism of B atoms being able to form clusters which, along with boride precipitate particles, would act as obstacles to the dislocation movement, impede the dislocation slip, and thus enhance the fatigue crack growth resistance and the low cycle-fatigue life of alloy 718.

Tian et al. [41] have recently studied (2017) the microstructure of alloy 625 modified with 0.4% B. The purpose was to see whether a large B addition could decrease hot cracking sensitivity by increasing the amount of eutectic liquid, and hence heal the cracks through backfilling during the last solidification stage. Even higher B contents of 1–4%, together with a large Si content (1–4%), are used in so called self-fluxing Ni alloys to lower the melting temperature and to improve the wettability of the melt.

However, as was mentioned earlier, some powder manufactures have introduced their own range of alloy 625 powder especially for AM purposes, paying particular attention to the requirements for AM with an upper limit of 0.010% for B [16, 17]. This is probably related to the fact that it is essential to have a low content of impurity elements in AM in order to maintain high quality.

1.5.6.3. Sulphur and phosphor

Sulphur (S) is the most damaging of all the elements involved in the metallurgy of welding Ni alloys [19]. The presence of S in Ni-based superalloys also has a detrimental effect on the oxidation resistance and the stress-rupture life of the final product [42]. Some of the reasons for this can be deduced from the Ni-S binary phase diagram shown in Figure 5. The addition of S to Ni causes a large reduction in both the liquidus and solidus temperatures (Fig. 5). During solidification, a material with a low nominal S content may develop segregated areas which are high in S, and therefore have a correspondingly low melting point.

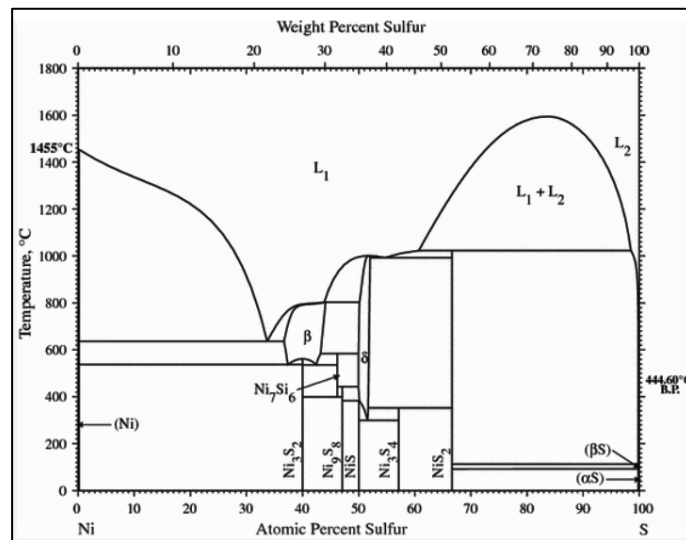


Fig. 5: Ni-S phase diagram [43].

Sulphur has a tendency for grain boundary segregation and is known to cause hot shortness in Ni alloys, since it forms a eutectic Ni₃S₂ phase with a melting (or solidification) point of 635 °C. This detrimental sulphide phase can already be found on grain boundaries with sulphur contents as low as 10 ppm [44]. Furthermore, S promotes the segregation of Nb to the interdendritic regions and Laves phase formation. On the one hand, the latter is directly detrimental for the mechanical properties of the weld and on the other hand, its formation leads to a depletion of Nb in the matrix and therefore reduces the solid solution strengthening potential of Nb, and reduces the maximal possible amount of the beneficial γ' phase in the alloy [25].

Both S and P, together with Si, also promote the formation of the Laves phase and the segregation of Nb in cast alloy 718 [25]. With increasing P and S contents, the solidification temperature range increases and complete solidification is delayed to lower temperatures. The effect of P on the hot cracking sensitivity of Ni alloys is quite similar to S. However, P is less detrimental since both the maximum solubility of P and the solidification temperature are higher (Table 3, 870 °C). However, unlike S, P cannot be bound with Mn.

One clear limitation for the detection of both S and P in alloy 625, is that Mo and Nb, which both certainly exist in the alloy and are segregated to the same eutectic, last-to-solidify liquid with S and P, have overlapping characteristic X-ray peaks with S and P. This means that the presence of Mo and Nb prevents the detection of small amounts of S and P in a microsection using the most versatile and common methods, i.e. electron microscope (SEM) and energy

dispersive X-ray spectrometry (EDS or EDX). Therefore, the detection of these elements from a cross-sectional examination of the microstructure needs to be made with the wave-length dispersive X-ray method (WDS), which can detect trace elements with better accuracy.

1.5.6.4. Carbon

With the presence of Nb, carbon (C) promotes the formation of a γ /NbC eutectic-type constituent instead of the γ /Laves eutectic [45]. This phenomenon, the connection between carbon content and the prevention of the Laves phase has been studied several times [22, 24, 45, 46, 47].

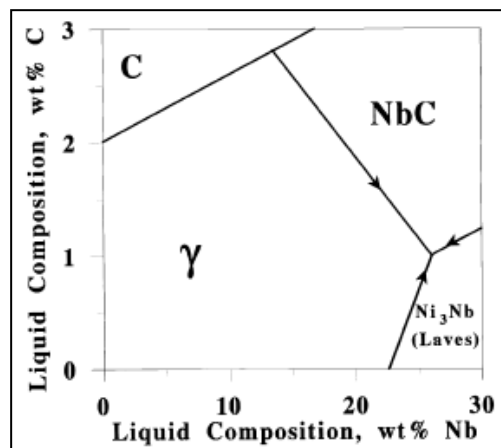


Fig. 6: Liquidus projection for the Ni-Nb-C system [47].

The effect of C on the formation of γ /NbC or γ /Laves is also dependent on the Si content. Cieslak et al. [45] studied the effect of elements Nb, C, and Si on the solidification of alloy 625 on a two-level scale. In an alloy with low C (0.009%) and no intentionally alloyed Si, a very small interdendritic constituent population was observed. The predominant phase was Laves. Some carbon (0.038%) promoted the formation of the γ /NbC constituent and eliminated the γ /Laves constituent when Si was not intentionally alloyed (Si content: 0.03%). Additional Si (0.38%) promoted the formation of the γ /Laves constituent and a γ /M₆C constituent when carbon was present in a low (0.008%) concentration. When both C and Si were alloyed at a higher level (C: 0.035%, Si: 0.46%), both a γ /NbC constituent and a γ /Laves constituent formed.

Benhadad, Richards and Chaturvedi [48] also studied the effect of minor elements C, B, and P on the weldability of alloy 718 alloy with a two level scale. The levels were C: 0.008% and 0.03%; B: <0.001% and 0.012%; P: <0.001% and 0.022%. It was shown that there was a connection between the amount of these elements and the weldability of the alloy although the effect of elements was not straightforward. The combination of both B and P showed the most detrimental effect on crack density, but the presence of some C (0.03%) in the alloy with some P and/or B seemed to decrease the length of the cracks in the HAZ. It was concluded that C mitigated the detrimental effects of B and P through the elimination of borides, and because some of the B was incorporated into the Nb rich carbides.

1.5.7. Solidification of alloy 625

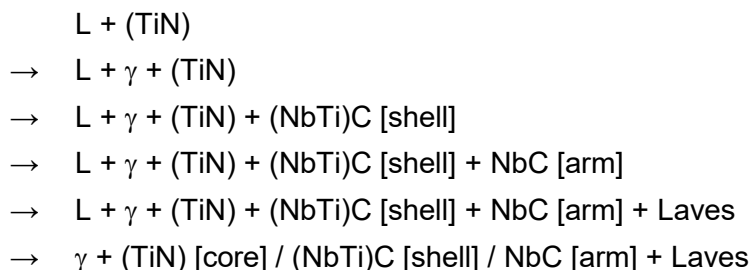
The solidification of alloy 625 and the resulting phases are dependent on the solidification rate. However, with normal solidification rates for the solidification of alloy 625, the dominant reaction is the enrichment of the residual interdendritic liquid with Nb and the consequent formation of an Nb-rich Laves phase and/or Nb carbide during the final stages of solidification [21]. However, the solidification of an alloy 625 weld results in a columnar dendritic microstructure that is compositionally segregated. The dendrite cores are slightly enriched with Fe, Ni, and Cr, whereas the interdendritic regions are enriched with Nb and Mo. In general, the extent of microsegregation depends on the characteristics of the solute(s) and the solidification parameters. In addition to solidification cracking, constituent segregation has both micro- and macro-scale effects on the corrosion properties of the deforming alloy. For example, studies have shown that corrosion fatigue took place on alloy 625 boiler tube claddings due to the microsegregation of Mo and Nb to the interdendritic region during weld solidification. Consequently, the alloy-depleted dendrite cores experienced preferential corrosion which acted as microscopic stress concentrators and crack initiation sites [49].

The solidification sequence of alloy 625 has usually been described by the reactions:

- $L \rightarrow \gamma + \text{NbC}$, or
- $L \rightarrow \gamma + \text{Laves}$, or
- $L \rightarrow \gamma + \text{NbC} + \text{Laves}$

and the resulting microstructure consists of a γ -dendritic phase with various amounts of Laves phase and/or Nb carbide between the dendrites. Fe and Si additions have been proven to increase the amount of Laves constituent and C additions increase the NbC content or prevent the formation of the Laves phase [24]. The Nb content of the Laves phase was measured to be above 20 (wt)%. From this it was concluded that as a consequence of the brittle Laves phase present in the welds, the measured hot cracking tendency was increased by the Si additions. On the other hand, these studies showed that cooling rates were substantially lower than for laser cladding.

A fairly recent study by Silva et al. [23] (2013) examined the solidification of alloy 625 cladding made with the TIG cold wire method. It was concluded that Ti together with nitrogen (N) affected the solidification path of alloy 625 so that the TiN particles acted as nucleating agents for (Nb,Ti)C precipitates. It was found out that the complete solidification path is:



In this study it was concluded that as TiN precipitates first from the melt, this makes them excellent nucleating agents for the formation of Nb and titanium carbide shells (NbTi)C around the TiN core. It was also found that the first-to-solidify nitride TiN core leads to structures called

NbC arms, and various precipitates were observed in the form of Nb-rich arms or needles, growing from a central core of TiN.

However, in this same study by Silva et al. [23], the solidification rate was clearly lower than it is in the laser or CMT process. The welding energy varied between 1000–1700 J/mm, the travel speed between 3–4 mm/s, the wire feed rate between 6–9 m/min, and the torch was oscillated. In CMT cladding with a wire feed-rate of 8 m/min, a stringer motion and a travel speed of 16.7 mm/s (1000 mm/min), the welding energy is usually around 150–200 J/mm. The lower welding energy, i.e. heat input, makes the solidification faster so that:

1. The solidification path is different when there less time for elements to segregate
2. Faster solidification means smaller dendrite structure and smaller phases precipitates that are more difficult to examine and analyse with normal methods like SEM EDS.

So rapid solidification in laser cladding with blown powder or CMT welding with wire affects the resulting microstructures and phases.

1.5.8. Laves phase

The Laves phase forms in the interdendritic region of a cast or weld structure during solidification. The existence of the Laves phase in the microstructure of Ni alloys has been associated with brittleness and hot cracking in Ni alloys. The interdendritic regions of the Laves phase create a favourable site for crack initiation and propagation, which affects the tensile and rupture properties, the ductility, the fracture toughness, and the fatigue life of the welded components. However, the formation and existence of the Laves phase in the microstructure is of concern mainly with more alloyed and age-hardenable alloys like 718. Less attention has been paid to the Laves phase in non-age-hardenable alloy 625. The segregation of some elements, mainly Nb, Si and Mo in this last-to-solidify interdendritic eutectic melt, has a strong effect on the formation of Laves. The more the Nb segregates in the interdendritic region, thus depleting the Nb in the matrix, the higher is the volume fraction of laves phase.

Laves is a hexagonal closely packed phase and is generally accepted to be in the form of A_2B , with Ni, Fe and Cr in the A position and Nb, Mo and Si in the B position. This unique chemical composition of the Laves phase, as mentioned above, distinguishes it from the other phases present in the Ni-Cr-Mo-Nb system (especially in terms of high Nb weight concentration). The formation of the Laves phase requires an Nb concentration ranging from 10–30% [51]. Consequently, the more the Nb segregates in the inter-dendritic region and thus depletes the Nb in the matrix, the higher is the volume fraction of laves phases. Laves phase depletes the matrix of significant amounts of useful strengthening alloying elements, making the matrix material softer.

Once it has been formed during the solidification of the weld metal, the Laves phase is difficult to remove by homogenization treatments. In order to dissolve the Laves phase, very high homogenisation temperatures are needed. However, the required homogenization temperature depends on the extent or degree of segregation produced in the weld. Slower

cooling and longer solidification time leads to more segregated phase structure than to rapid cooling and fast solidification.

Another effect of the Laves phase on alloy 718 is the precipitation of δ phase (delta) around the partially dissolved Laves particles during solution treatment. The δ phase requires about 6–8% Nb and precipitates in the range of 860–995 °C. The Delta phase cannot form during weld metal cooling because the time spent in the δ precipitation range is very brief. During postweld solution treatment in the δ precipitation range, as in the present case at 980 °C, δ precipitation occurs as in the form of δ needles in these regions of moderate Nb concentration around the Laves particles [81]. A large amount of Laves phase, and consequently δ needles, after heat treatment has been found to be connected to poor fatigue performance of alloy 718 welds.

Radhakrishna and Rao [52] studied TIG (Tungsten Inert Gas, or GTA – Gas Tungsten Arc) and EB (Electron Beam) welds of alloy 718. Weld solution treatment of a GTA weld at 980 °C did not homogenize and dissolve its Nb-enriched Laves phase in the TIG weld structure. However, this temperature turned out to be sufficient for EB (Electron beam) welds with a rapidly solidified structure. TIG welds required higher solution-treatment temperatures of in the order of 1100 °C. Additionally, the composition of the Laves phases differed substantially depending on the welding method and cooling rate. The Nb content of the Laves phase in EB welds was 12–15%, while in TIG welds the Nb content was around 22–26%. The base material contained an average of 5.1% Nb. It was concluded that the higher cooling rate of EB welds led to a lower level of segregation.

The formation of phases in rapid solidification has been recently been studied on in the laser additive manufacturing of alloy 625 [53, 54, 55, 56] where the solidification rate is far more rapid than with conventional welding methods. No Laves phase was detected from the structure of additively manufactured alloy 625 on in any of these studies. On a work of Ganesh et al. [53] studied the fatigue strength of laser rapidly manufactured alloy 625. In this study, no connection between the Laves phase and crack propagation was found and no Laves phase was not detected with X-ray diffraction (XRD). It was concluded that transgranular fatigue crack propagation in laser rapidly manufactured specimens was associated with slip on predominantly (111) planes.

According to measurements by Rombouts et al. [54], Ni-based γ phase and the carbides MC, $M_{23}C_6$, and M_6C were detected by x-ray diffraction from the microstructure of laser cladded alloy 625. Dinda et al. [55] reported similar results by finding only γ -Ni phase with x-ray diffraction (XRD) from the laser deposited alloy 625 samples. The authors assumed that the very small, submicron size of the some phases could have hindered the detection of other phases with XRD. The samples were solidified rapidly and, as a consequence, the primary dendrite arm spacing was $\sim 5 \mu\text{m}$ (Fig. 7). The following images show some SEM SE images from the microstructure of alloy 625. Fig. 1 shows a microstructure of rapidly solidified laser deposited alloy (stringer motion) [55]. Fig. 1 b shows a microstructure of slowly solidified alloy 625 cladding made with the pulse TIG method and a weaving motion [57]. The magnification is the same in both images and both microsections were examined in etched condition.

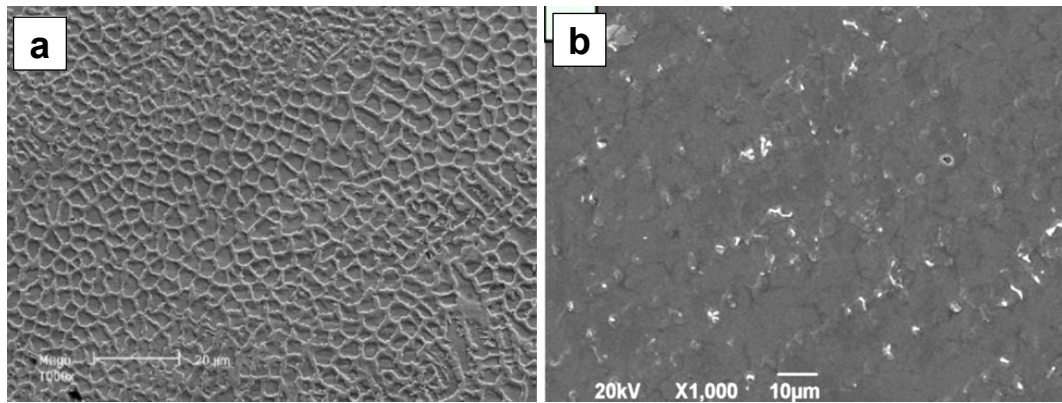


Fig. 7: Etched microstructure of deposited alloy 625. SEM images, original magnification 1000x. a) laser deposited, rapid solidification, perpendicular to the build direction, SE image [55]. b) Pulse TIG cladding, BE image [57].

Besides the differences in grain structure, the main difference between these two is that there are no other distinguishable phases in the laser deposited structure in Fig. 7 a. The phases that appear brighter in Fig. 7 b were stated to be Laves phase by the authors, Guo et al [57].

Antonsson and Fredriksson [58] studied solidification of alloy 718 (4.8% Nb) with varying cooling rates. With the most rapid cooling rate of 10 000 K/s interdendritic areas contained less Nb than those with cooling rates. In addition, no Laves phase could be found from the rapidly solidified samples. Rapid solidification decreases segregation of Nb to the eutectic and the authors assumed that the Nb content of approximately 16% in the eutectic was insufficient for the Laves phase to form. The primary dendrite arm spacing in the samples with rapid solidification was 3.5 to 4.5 μm.

1.6. Hot cracking phenomenon

Hot cracking is a general term which is quite often used to describe all types of cracking in metals which have originated in higher temperatures. A simple definition for hot cracking according to the standard EN ISO 17641-1 [59] is:

“Hot Cracks are material separations occurring at high temperatures along the grain boundaries (dendrite boundaries), when the level of strain and the strain rate exceed a certain level. Small cracks, which are visible only at magnifications of more than about 50x, are often described as micro fissures.”

The type of cracking is generally grouped by the temperature range over which they occur, but the classification is not unambiguous. However, one very good classification is made by one of the well-known expert in the field, J.C. Lippold [61] as follows: 1. *hot cracking*, 2. *warm cracking*, and 3. *cold cracking*. These are explained more in following paragraphs.

1. *Hot cracking* is associated with the presence of liquid films along grain boundaries or elsewhere in the structure. Hot cracking is further sub-divided into:

1.1 *Solidification cracking*, in which the cracks are formed during solidification from the liquid phase of weld metals. They can sometimes be visualized as dendrites that grow more slowly than the strains being imposed, so that they fail to fuse on

the weld centre line and leave a cavity or centreline crack. They usually extend up to the surface of the weld metal, but sometimes remain subsurface.

- 1.2 *Liquation cracking*, in which the cracks are formed in areas of liquation in the HAZ of the parent material or in multipass welds where the weld metal is reheated during the deposition of subsequent weld beads. They are often small (microfissures) and often subsurface in multi pass welds.

2. *Warm cracking* occurs in the solid state at temperatures between the solidus and approximately half the melting temperature of the material and may occur either during fabrication or subsequent postweld heat treatment. Types of warm cracking are:

- 2.1 *Ductility-dip cracking*
- 2.2 *Reheat cracking*
- 2.3 *Strain-age cracking*
- 2.4 *Lamellar cracking*

3. *Cold cracking* occurs at or near room temperature and is usually associated with the presence of hydrogen and hydrogen-assisted cracking mechanisms. This type of cracking is related more to steels with a ferritic (body-centered cubic) crystal structure, especially high-strength steels. Usually weld cold cracking is associated with the formation of martensite as the weld cools and the presence of hydrogen in the weld material or atmosphere.

In the standard EN ISO 17641-1 [59] the types of hot cracks are subdivided into three groups:

1. *solidification cracks*, 2. *liquation cracks* and 3. *ductility dip cracks*. So, the classification of the types of hot cracks is a bit ambiguous. However, in this study the emphasis is in solidification cracking, which occurs while the liquid weld metal cools down and solidifies.

1.6.1. Solidification cracking

Weld solidification cracking occurs during the final stages of solidification when the tensile shrinkage stress accumulates and liquid films still persist along the solidification grain boundaries in the structure. If the imposed shrinkage strain exceeds the inherent ductility of the solidifying weld metal, cracking will occur [61]. The lack of ductility can result from the presence of liquid metal, micro structural features, orientation (relative to the strain) and in some cases upon the presence of brittle impurities and low melting point (or liquated) films [66]. Furthermore, the amount of liquid metal that solidifies last can have a large effect on cracking tendency. This issue is dealt with in more detailed in its own section 1.6.2 on page 21. In this respect some alloy systems are particularly sensitive to the presence of impurity elements such as S, P and lead (Pb) etc. It is widely recognized that fully austenitic single-phase microstructures, particularly weld metals, are susceptible to hot cracking of one form or another. Impurity levels strongly influence the incidence of cracking in such microstructures [66].

Weld hot cracks, like any other type of crack-like features in a weld seam, are very detrimental, especially for the fatigue life of the weldment. A hot crack can act as an initiation site for a

fatigue crack to originate in a variable load. And as the variable load (fatigue) continues, the crack can grow so large that the remaining material is too thin to carry the load and fatigue failure occurs. Compared to fusion weldments, cracks are less severe in the case of overlay welding, since overlay welding is not designed to carry a load. However, long fatigue cracks that have originated from hot cracks in alloy 625 cladding, have been observed in some components [5].

Hot cracks are a harmful type of welding defect, since quite often they do not reach the surface of the weldment and hence cannot be detected with normal non-destructive (NDT) methods like the liquid penetrant test (PT), or with other methods. Some hot cracks in alloy 625 laser cladding were presented in Fig. 1 (page 2). Because of the detrimental and difficult-to-find nature of hot cracks, no type of cracks are allowed in fusion weld joints, regardless of size, according to standard ISO 5817 [62], the standard that defines the allowable size and amount of imperfections in fusion welds. In contrast, the standard does tolerate some other defects, like porosity, to a certain degree.

1.6.2. Factors affecting solidification cracking phenomenon

There are several factors affecting solidification cracking. The interaction of some of these factors, welding parameters, composition and restraint, are presented in Fig. 8.

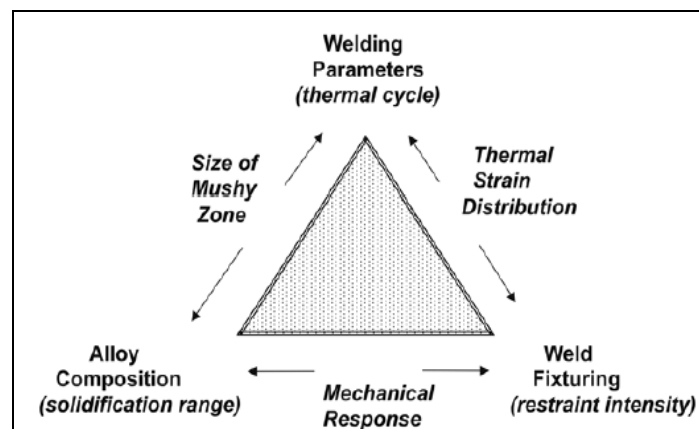


Fig. 8: Diagram indicating complex interaction between process parameters affecting weld solidification cracking [63].

However, there is rarely a simple interaction between the factors, but instead many complex interrelationships, making direct correlations between observation and theory difficult. There are several theories about the origin of solidification cracking. Some of these theories about the hot cracking phenomenon have been comprehensively summarized in a study by Cross [63], and other researchers and professionals [36] and are presented below.

1.6.2.1. Solidification range

In metallurgy the term *solidification range* means the temperature region that it takes for the liquid metal to solidify. Solidification starts at liquidus temperature as the first solid particles, i.e. the nucleus, start to nucleate in the melt. Solidification ends when the last remaining liquid solidifies at the solidus temperature. This whole range can extend over several hundred degrees and the *solidification range* is dependent on the composition of the melt, and indeed,

some elements can extend the range considerably. For example, sulphur can extend the solidus temperature in steel from around 1400 °C to 988 °C [63], while the liquidus temperature of steel is around 1500 °C.

It has long been appreciated that the solidification temperature range, often referred to as a brittle temperature range (BTR), plays an important role in a material's susceptibility to solidification cracking. An alloy with large solidification temperature range is often defined as being sensitive to hot cracking. However, the situation is more complicated than that, since some alloys with a large solidification range, such as Al-Mg alloys, which have exceptionally large solidification range, exhibit exceptionally good weldability. Other features, like the amount of last-to-solidify eutectic liquid, solidification rate and residual stress have a large effect on solidification sensitivity [63].

1.6.2.2. Back-filling

Back-filling refers to the drawing of liquid back through the dendritic network to feed solidification shrinkage. The concept of back-filling is reflected in foundry practices, where risers are strategically placed to feed hot spots to avoid hot tearing. In the case of welding, the molten weld pool serves as the reservoir of liquid, taking the place of a riser in a casting process. The backfilling effect is able to fill or "heal" solidification cracks during solidification and it is highly dependent on the amount of terminal last-to-solidify eutectic liquid in the melt. The crack healing effect is quite often cited as being responsible for the fact that alloy 625 is generally considered to have good resistance to weld solidification cracking [36].

1.6.2.3. The amount of last-to-solidify eutectic liquid

According to one well-accepted theory, the hot cracking tendency is related to the amount of terminal, last-to-solidify liquid during the final stage of solidification [14]. A small amount of terminal last-to-solidify liquid, generally less than approximately 1 (V)%, that exhibits high surface tension with the solid, will often promote solid/solid bridging, thereby reducing the cracking tendency. When the amount of terminal, last-to-solidify liquid is moderate, between approximately 1–10 (V)% and/or the surface tension is low, the liquid tends to wet the boundaries and form a continuous film. This type of morphology is most detrimental as it interferes with the formation of solid/solid boundaries, thus reducing the ability of the material to accommodate strain. When the amount of terminal liquid is high, greater than approximately 10 (V)%, it can often flow into the cracks and provide the "crack healing" effect. For a given alloy system, the solidification temperature range and the amount of terminal liquid are primarily controlled by composition. The processing parameters are also important under high cooling-rate conditions where dendrite tip undercooling can be significant [14]. However, according to some studies [70, 71], the amount of liquid needed for back filling has been reported to be in the range of 6–10 (V)%

1.6.2.4. Grain boundaries

Solidification cracking normally occurs along weld metal grain boundaries, although this is not necessarily always the case. The reason for this tendency is probably tied to the preferential segregation of the solute or impurity elements (e.g. sulphur in steel) to the grain boundaries,

even though it was originally partitioned between dendrites. A grain boundary provides a well-defined, high-energy planar interface upon which a liquid film can wet. Therefore, it follows that grain shape, structure and size should have a profound effect on cracking susceptibility [63].

1.6.2.5. The effect of welding speed and melt pool shape on solidification cracking

In welding processes that make continuous welds with a stringer motion, the molten metal pool is carried along the weld seam. In welding with a continuous power heat source and stringer motion, the molten metal pool moves forward, consuming fresh parent metal in front of it, while allowing molten metal to solidify behind. With a weaving motion the weld formation and shape is different, since wire and arc sweep across the large melt pool and cause mixing.

Under steady-state conditions, the molten metal pool stabilizes to a fixed shape. The leading (melting) end of the pool always has a circular shape but the trailing (solidifying) end is affected by the welding speed, which in turn can affect weld quality, for example in terms of its solidification cracking tendency.

The effect of the welding speed on the shape of the weld melt pool is presented in Fig. 9. As the speed increases, the pool becomes more elongated and appears tear-drop shaped, with its long axis along the weld seam [73].

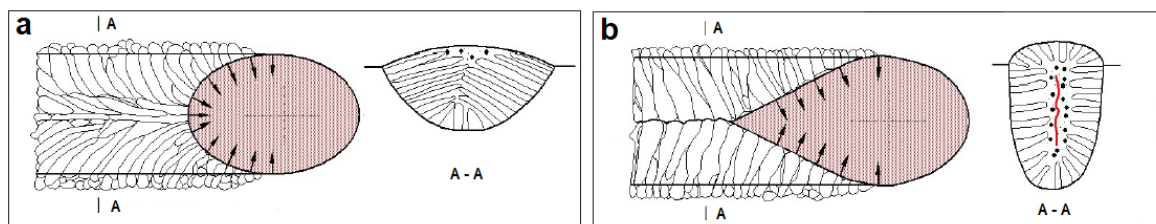


Fig. 9: The influence of welding speed on weld melt pool shape and solidification microstructure. a) Low welding speed – elliptical shaped melt pool. b) High welding speed – tear-drop shaped melt pool [73].

Welds made with a teardrop-shaped weld pool tend to be more susceptible to centreline solidification cracking than welds made with an elliptical-shaped weld pool. A steep angle seems to favour the head-on impingement of columnar grains growing from opposite sides of the weld pool and the formation of the continuous liquid film of low-melting-point segregates at the weld centreline [74]. In addition, at higher speeds, the weld pool becomes tear-drop shape and leaves V-shaped ripple marks on the weld surface. However, the outer appearance of the ripple marks is very deceptive as the grain structure inside can be quite different [73].

However, welding speed can only be regarded as one of the factors that affects the melt pool shape. If other parameters (base material and feedstock composition, heat input etc.) are kept constant, increasing the welding speed does change the shape of the melt pool from elliptical to tear-drop shaped. It can also be assumed that this change can happen if the welding speed is kept constant but other parameters are changed, for example the feedstock composition. Welding speed, melt pool shape, solidification and hot cracking density are also related to the temperature gradient, which is discussed in the following section.

1.6.2.6. The effect of the temperature gradient and solidification pattern on cracking

The cooling rate has a large impact on the resulting solidification structure and it is mainly dependent on the heat input and/or the welding speed. The higher the cooling rate, i.e., the shorter the solidification time, the finer the cellular or dendritic structure. A model of how to describe grain size and solidification mode can be achieved by using the temperature gradient and growth rate. The temperature gradient (R) is a physical quantity that describes the direction and rate of the temperature change. The solid/liquid interface growth rate (G) is a term to define growth during solidification. The effect of the temperature gradient G and the growth rate R on the solidification microstructure of alloys is summarized in Fig. 10. Together, G and R dominate the solidification microstructure. The ratio G/R determines the mode of solidification while the product of GR governs the size of the solidification structure [74]. The solidification mode changes from planar to cellular and dendritic as the ratio G/R decreases.

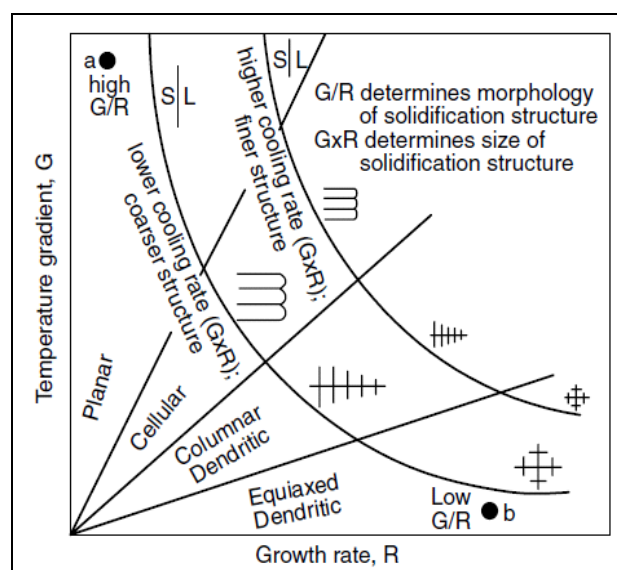


Fig. 10: The effect of temperature gradient G and growth rate R on the morphology and size of a solidification microstructure [74].

Generally, solidification leads to two types of solidification pattern, columnar and equiaxed dendritic. The term Columnar to Equiaxed Transition (CET) is used to describe this transition between these two. Of these two, equiaxed is usually the desired pattern in weld metal since it is less prone to solidification cracking than the columnar pattern. A fine equiaxed dendritic structure with abundant liquid between the grains can deform more easily under the stresses that occur in weld metal during solidification than a coarse columnar dendritic structure, and thus the equiaxed pattern has a lower susceptibility to cracking [74].

1.6.2.7. Backfilling hindered by Marangoni flows

One possible influence of surface tension involves temperature gradient-driven fluid flow, commonly known as the Marangoni effect. Holt et al. [89] proposed a theoretical standpoint that variations in sulphur content may influence interdendritic fluid flow and, hence, backfilling. For example, it was shown that at high concentrations of S (i.e. $dy/dT > 0$) the temperature gradient will drive flow out of the dendritic network, inhibiting the feeding of shrinkage. The Marangoni flow, surface tension and the effect of some constituents of Marangoni flow are discussed more in section 1.7 on page 29. In the proposition by Holt et al. [89] one of the

features of the growth of dendrites was the existence of temperature gradients along the dendrite axis. A dendrite tip surrounded by liquid has a higher temperature than the dendrite root. If the surface tension gradient ($d\gamma/dT$) is positive, meaning that surface tension increases with increasing temperature, the Marangoni flow causes the remaining fluid to flow from the root of the dendrite towards its tip. This increases the hot cracking tendency since the backfilling effect is weakened.

1.6.2.8. The effect of surface energy on backfilling

Savage and Dickinson [75] gave a similar explanation for the effect of S, Si and Mn on backfilling and hot cracking as did Holt et al. [89]. According to this theory, the deleterious effect of impurity elements, mainly sulphur, and the beneficial effects of Si and Mn, were explained by backfilling and the grain boundary energies. The theory states that the grain boundary energy σ_{SS} should be at least twice the liquid-solid interfacial energy, σ_{SL} .

$$\frac{\sigma_{SL}}{\sigma_{SS}} \leq \frac{1}{2}$$

According to Borland [60], if this ratio is lower than 1/2, continuous liquid films are formed along grain the boundaries and these generate hot cracking during solidification. On the other hand, ratios higher than 1/2 are beneficial since the liquid is then restricted to the grain edges and corners.

1.6.2.9. Change of compressive stress to tensile stress in the weld pool

Zacharia [69] studied the effect of dynamic stresses on hot cracking in type 316 stainless steel with sigma jig tests. The idea or theory presented in Fig. 11 can be extrapolated to the situation in laser cladding, where there is some fluctuation of the melt pool. An example of this fluctuation is illustrated later in this study in Fig. 67 on page 105.

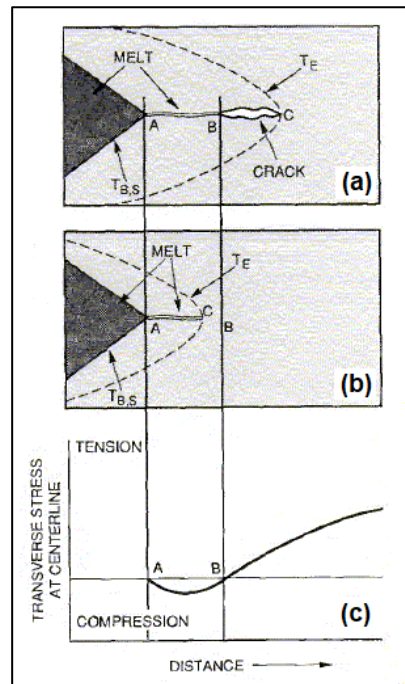


Fig. 11: Schematic presentation of conditions where the stress changes from compression to tensile in the weld pool [69].

Fluctuations on the melt pool surface, either caused by Marangoni flow or by powder feed fluctuations, can result in an occurrence where the hottest spot is occasionally shifted backwards. This shift could lead to the situation presented in Fig. 11 (a) where the area of the last-to-solidify liquid drifts from compression to tension and the weld centreline is torn open, so hot cracking occurs.

1.6.2.10. Stirring and oscillation

The CMT welding process differs from the normal pulsed MIG/MAG process since both the wire feed and the welding power are pulsed with a frequency of 70–80 Hz. Therefore, wire pulsing in the CMT process could be regarded as a type of oscillation or melt-pool stirring.

Different dynamic grain-refining techniques, including weld pool stirring, arc oscillation, and arc pulsation, have been studied and applied to fusion welding processes [74]. According to studies by Kou [74], transverse arc oscillation at low frequencies can produce alternating columnar grains. This type of grain structure can be effective in reducing solidification cracking. Columnar grains that reverse their orientation at regular intervals force the crack to change its direction periodically, thus making it more difficult for the crack to propagate. In addition to reducing solidification cracking, transverse oscillation can also decrease grain size and hence improve both the strength and ductility of the weld [74].

The oscillation amplitudes applied in studies on TIG welding of Al alloys [77, 78, 78, 79] were rather small and did not produce a wider bead than the stringer torch motion. For example, Kou and Le [77, 78] found that arc oscillations at much higher frequencies than 1 Hz, though ineffective for Al alloy 2014, are effective for alloy 5052. The amplitude in these studies was small, less than 2 mm. In a quite recent (2012) study by Biradar and Raman [79], it was concluded that autogenous TIG welds on Al alloy AA2014, with a mechanical oscillation amplitude of 0.9 mm and a frequency of 0.5 Hz, showed a significant reduction in the hot

cracking tendency. Magnetic arc oscillation has also been reported to reduce solidification cracking in magnesium and Al alloys, steel, and in tantalum and iridium alloys [74].

Some studies have been carried out on the effect that electron beam oscillation has on the mechanical properties of electron beam welding of stainless steel by Kar et al. [80], and alloy 718 by Reddy et al. [81]. Reddy et al.'s study concentrated on the effect of electron beam oscillation on Laves phase formation. Sivaprasad et al. [82] also studied the effect of arc oscillation and pulsing in TIG welding on the Laves phase and on the fatigue behaviour of TIG welds of alloy 718. Lim et al. [83, 84] studied the grain structure refinement of (Ni-based) alloy 690 welds made by magnetic arc oscillation in TIG welding. Grain refinement was supposed to assist in preventing solidification cracking. Optimum grain refinement was found to be produced by a 7 Hz oscillation frequency. Probable mechanisms for the grain structure refinement were thought to be constitutional supercooling and dendrite arm fragmentation.

In summary, although some studies have been published about oscillation and its effects on solidification cracking in arc welding, there are no studies particularly about the solidification cracking of Ni alloys and the effect of oscillation.

1.6.2.11. The effect of dilution on hot cracking

Based on the experience in laser cladding with alloy 625 powder, it has been discovered that some powder batches can generate hot cracks quite easily, while others do not, even though the compositions of the powders are within the compositional limits [86]. In addition, hot cracks don't usually occur when the dilution is low. The dilution in welding terms is defined as the amount of the base metal melted divided by the total amount of the weld metal (Eq. 9, p 81). The dilution in laser claddings is usually low, less than 10%, but due to real-life variations in the cladding process the dilution can be around 20%, especially if the component's surface is not flat but has curved sections.

Dilution increases the Fe content in the clad material. Increased Fe content in the clad material affects the solidification behaviour of alloy 625. Dilution can affect hot cracking susceptibility via different factors:

1. The presence of Fe in the Ni matrix can affect the segregation of other elements, mainly Nb, during solidification. This means that when there is a substantial amount of Fe in the liquid as it starts to solidify, Nb will segregate more strongly to the eutectic liquid that solidifies last. This phenomenon will be discussed more later.
2. Low-alloyed steel also contains some amounts of other elements, mainly C, Si and Mn, and the impurity elements S, P and B that can and probably will contribute to hot crack formation. The content of the impurity elements S and P in low-alloyed steels is usually limited to 0.035%, which would nevertheless be a high content for Ni alloy to bear without hot cracks. If S and/or P content of steel is 0.030%, a dilution of 10% from the steel substrate to the clad material brings an extra content of 0.003% of S and/or P to the cladding material.
3. Fe content favours the formation of the Laves phase, which in turn favours the formation of hot cracks.

4. High dilution is an indication of excessive laser power in relation to other parameters, mainly travel speed and powder feed rate. Excessive laser power and the resultant dilution indicates that the melt pool temperature during the cladding has been high. A high melt pool temperature leads to slower solidification and gives more time for impurities to segregate. However, the cooling rate, and thus the solidification rate, is much higher with laser cladding than it is with other cladding methods like PTA or MIG/MAG. The tendency of laser claddings to have hot cracks with high solidification rates is probably related to its faster solidification and the higher residual stresses of laser cladding, compared to arc welding methods [85].
5. The laser beam profile can also have its own effect on cracking. The beam profile, or the laser power distribution, is usually not even across the laser spot on the workpiece. The spot size with a circular beam in laser cladding is typically around ~5 mm. The highest energy density, and hence the hottest point, is at the centre of the spot. This is especially true with a Gaussian beam profile, but even occurs if the beam has a top-hat profile. With a larger, rectangular etc. beam shape the energy density and distribution would be more even throughout the beam.

1.6.3. The evaluation of hot cracking sensibility

The term “weldability” often refers to the “inherent” resistance of the (metal) material to cracking during welding. There are numerous methods to evaluate the hot cracking sensibility of materials, so-called hot cracking tests. A total of over 200 different techniques have been developed to study and quantify the cracking susceptibility of materials in welding [61]. Most test methods can be divided into three subcategories [66]:

1. Self-restrained tests
2. Externally loaded tests
3. Hot tensile tests

It should be emphasized that there is no “hot cracking” test which have been properly standardized and large variations in the actual setup of the testing are evident although the name of the test is the same.

1.6.3.1. Self-restrained tests

In these tests the tension is produced by stresses developed during solidification and cooling of a restrained weld. As the liquid metal on a weld cools down on a rigid substrate, the solidification and shrinkage that accumulate in the weld can cause high tension or residual stresses inside the weld metal. These tests are intended to assess the solidification cracking susceptibility of a weld metal in a single pass restrained weld.

Standard EN ISO 17641-2 [64] describes three types of self-restrained tests:

1. T-joint weld cracking test
2. Weld metal tensile test
3. Longitudinal bend test

The main advantage of self-restrained tests is that they are relatively simple to carry out and require no specialized testing equipment. The major disadvantage is that the results are qualitative, or possibly semi-quantitative in the case of the longitudinal bend test. A large number of tests would be required to assess the effect of all the welding variables and these can be both time-consuming and costly [66].

1.6.3.2. Externally loaded tests

These are tests that require the use of equipment, which is capable of imposing a strain on the test specimen whilst welding, or some other form of thermal cycle, is in progress. Probably the most widely used method in this category is the Varesstraint test. The name is a combination of the words **V**ariating **S**train. The test can be performed in both the transverse and longitudinal directions. The main disadvantage of externally loaded tests is the requirement for specialized equipment and procedures. Some studies have shown that reproducibility between laboratories is poor and that it is probably unreasonable to expect good agreement between a number of different types of test [66].

Interestingly, externally loaded tests like the Varesstraint tests have been found to give poorer than expected results, especially for alloy 625. It is assumed that these poor results are due to the ability of alloy 625 to “heal” from cracks at low restraint levels [65]. Alloy 625 forms considerable amounts of liquid of eutectic composition in the last stages of solidification and this tends to fill cavities between the dendrites that would otherwise be likely to cause cracks. When higher augmented strains are applied, such as during the Varesstraint test, this healing effect is ineffective and cracks may form [14].

1.6.3.3. Hot tensile test

In this test type, hot cracking susceptibility is determined by carrying out a tensile test while at the same time heating the specimen to simulate a welding thermal cycle. These tests require specialized equipment such as a Gleeble welding simulator [66]. The Gleeble testing method deals with the occurrence of the brittle temperature range (BTR) at high temperature during the solidification of the weld and the subsequent cooling. The BTR reflects the general appearance of the cracks occurring in the heat-affected zones of welds [67].

1.7. Melt pool surface tension and surfactants

The portion of metal that is in a molten state during the welding process, the so-called weld melt pool, consists of both melted filler material and melted base material. This molten metal flows before the melt solidifies, and the direction and quantity of this fluid flow has an intrinsic effect on the properties of the resulting weld, in terms of penetration and hot cracks.

There are several driving forces for this melt flow. In arc welding these forces include [74]:

1. The buoyancy force
2. The electromagnetic force or Lorentz force
3. The shear stress induced by the surface tension gradient at the weld pool surface (Marangoni flow)
4. The shear stress acting on the pool surface from the arc plasma

5. The arc pressure

Buoyancy force (1) comes from temperature and resulting density differences of liquid metal in the melt pool. Lorenz forces (2) mean forces induced by moving charged particles in the presence of magnetic and electric fields. The shear stress from arc plasma (4) is caused by the plasma moving outward at high speeds along a pool surface. This causes the liquid metal to flow from the centre of the melt pool surface towards the edges. The arc pressure (5) depresses the weld melt pool as can be seen in Fig. 28 on page 58.

In laser cladding, there is no electric arc, so there are no Lorenz forces (2), arc plasma (4), or arc pressure (5). So, it can be assumed that the buoyancy force (1) and surface-tension-driven convection (3) are the dominant convection mechanisms. Surface-tension-driven convection (3) is also called thermocapillary convection or Marangoni convection. Marangoni convection arises in response to the surface tension gradient and the flow is always in the direction of low to high surface tension [68]. The schematic presentation of the relation between the temperature dependency of the surface tension and the direction of the Marangoni flow is presented in Fig. 12. With the laser and a Gaussian beam profile used in this study, the most intense power is concentrated in the middle of the spot. This generates steep temperature gradients on the melt pool surface.

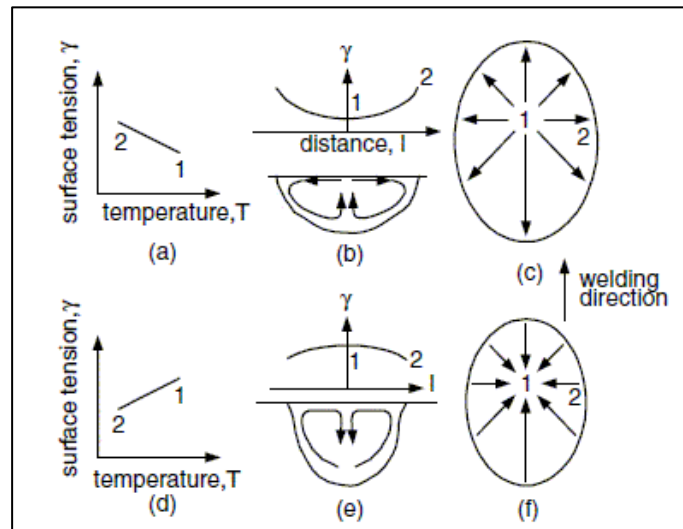


Fig. 12: Heiple's model for Marangoni convection in a weld pool: a, b, c) low sulphur steel. d, e, f) high-sulphur steel [74].

If the surface tension decreases as the temperature increases (Fig. 12, a–c), this causes an outward Marangoni flow. If the surface tension increases as the temperature increases, the direction of the flow is inward (Fig. 12, d–f). The surface tension of the melt depends strongly on its temperature and composition. Some elements have a significant effect on the viscosity of the melt pool, especially on its surface tension. Surfactants are compounds that lower the surface tension of a liquid, the interfacial tension between two liquids, or between a liquid and a solid.

Surfactants can be classified into three groups [87]:

1. Surface-active elements
2. Elements reacting strongly with surface-active elements
3. Elements that have little influence on the surface tension of the melt

Sulphur (S), in particular, has been found to be effective in creating a positive surface tension gradient and hence an inward flow in stainless steels [88]. Oxygen (O) has a similar effect on the surface tension, but its effect can be negated by the addition of deoxidants, such as Al, Mn and Ca. Al is not a surfactant, so it has no direct effect on the surface tension gradient, but it does have an indirect effect. Al can react with the oxygen in the alloy, and since O is not free to affect the surface tension gradient, the net effect of the Al is to decrease the surface tension gradient and hence the penetration depth [87].

It should here be noted that it is soluble \underline{O} which affects surface tension, not O in its combined form (e.g., oxides). Mills and Keene [88] pointed out that certain elements such as Ca, Al and Mg react strongly with O and form stable metallic oxides thus reducing the amount of soluble O (\underline{O}) in the melt to very low levels (e.g., a few ppm) [88]. Even very low concentrations of these reactive elements (Al, Ca) can have an effect on the process because of their effect on the surface active elements present. As can be seen from the results for the FeAlO system in Fig. 13, ca. 10^{-1} (0.1%) Al is enough to lower the soluble O to <5 ppm (0.0005%).

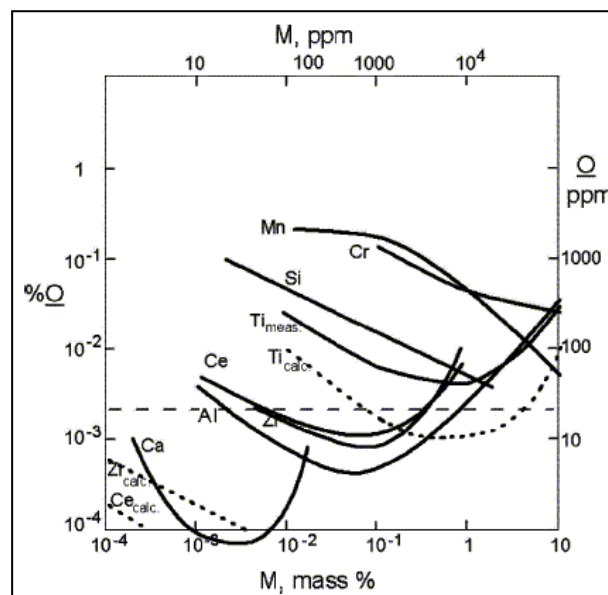


Fig. 13: The effect of different alloying additions (M) on the soluble O (\underline{O} %) content in the Fe-M-O system at 1873 K [88].

The graph in Fig. 13 show that Ca is the most effective element to bind soluble oxygen (\underline{O}) from liquid iron at 1600 °C (1873K) and to form oxides. The second most effective is Al, followed by Zr and cerium (Ce). Ti is clearly less effective, and is much like Si in this respect.

An Ellingham diagram (Fig. 14) is a graph showing the temperature dependence of stability for compounds. This analysis is usually used to evaluate how easy it would be to reduce the amount of metal oxides and sulphides. An Ellingham diagram is used to predict the equilibrium temperature between a metal, its oxide, and oxygen, and by extension, the reactions of a metal with sulphur, nitrogen, and other non-metals [90].

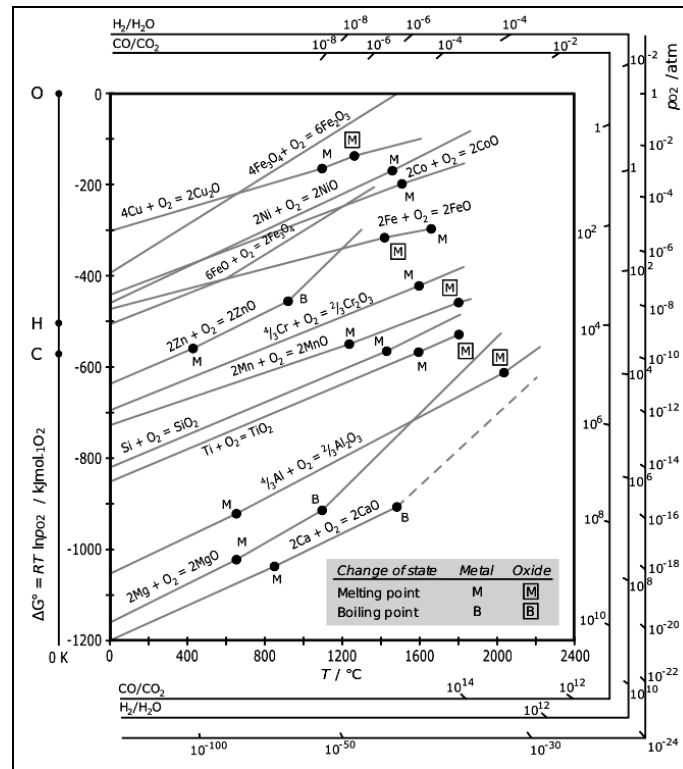


Fig. 14: Ellingham-diagram for the formation of oxides based on their standard free energy of formation over temperature [90].

An Ellingham diagram shows the order in which different oxides are formed. The location of the formation line for the first metal oxide in this diagram is very low, which shows that this oxide is formed before any of the metal oxides which are located higher up in the diagram. The diagram also shows that a metal which is located lower down on the diagram can reduce the amount of metal oxide formed from the metals located higher up. The diagram also shows Gibbs free energies for the formation of each metal in relation to the temperature. According to the diagram, the order for the formation of oxides is Ca, Mg, Al, Ti, Si, Mn, Cr, Zn, Fe etc. So, the order of elements in the Ellingham diagram above is much the same as in the Fe-M-O system presented in Fig. 13. In practice, the effect of the Ellingham diagram and the formation order of oxides is that if there is oxygen present at or above the melt pool in welding, and there is no, or not enough of any of the elements Ca, Mg, Al, Ti, Si or Mn, the next metal oxides, i.e. the Cr oxides, will be formed instead. Some Cr oxides were found from the microstructure of the laser cladding tests with powder No 12 (Fig. 119, p. 147).

The Gibbs free energies for the formation of some metal oxides together with the oxide densities are presented in Table 4.

Table 4: Gibbs free energies, densities and melting points of some metal oxides [90, 91]

Compound	Symbol	ΔG at 1200 °C kJ/mol	Density g/cm ³	Melting point °C
Iron oxide	FeO	-350	5.75	1377
Chromium oxide	Cr ₂ O ₃	-490	5.22	2435
Manganese oxide	MnO	-550	5.43	1945
Silicon oxide	SiO ₂	-615	2.65	1713
Titanium oxide	TiO ₂	-650	4.23	1843
Aluminium oxide	Al ₂ O ₃	-800	3.99	2072

The oxide density is another feature that has an effect on the oxide behaviour in the weld melt pool. The heavier oxides tend to remain in the melt pool, while the lighter ones rise to the melt pool's surface. Especially in the laser cladding process, with its high travel speed and rapid solidification, there is not enough time for oxides to rise to the surface of the melt pool.

The heat flow in the weld pool, the fluid flow, the composition of the weld metal and their effect on the weld shape in the fusion welding of stainless steel has been well documented in a number of studies, e.g. [68, 69, 70, 71, 72, 75, 87, 88]. However, fewer articles have been published about these same effects in the fusion welding of Ni alloys [50, 94, 95, 97, 98] and even fewer on overlay welding with Ni alloys [99]. There is one fairly recent study by Lee et al. [98] on laser cladding with alloy 718 powder which looked at the effect that the Marangoni flow and fluid convection had on the dendrite arm spacing. However, this study concentrated on modelling the fluid affected by Marangoni flow, rather than the compositional effects.

Of the few studies that have been conducted into the welding of Ni alloys and the melt pool, some were done in the early 1970's by Savage et al. [94, 95]. These studies looked at the effect of the elements S, P, Si, Al, Ti and Mn on the dimensions of the fusion zone, and the hot cracking tendencies of alloy 600 (Ni-15%Cr-12%Fe) were studied in TIG (GTA) welding. Modifications of alloys with low amounts of the minor alloying elements (S and P: ~0.002; Al, Ti, Si and Mn: ~0.05%) and with high amounts (S and P: 0.015; Al, Ti and Si: 0.5%; Mn: 1.0%) were prepared. The welding experiments were conducted in an argon atmosphere to prevent the effects of atmospheric contamination. A summary of the results from these experiments is presented in Fig. 15. The relative positive or negative effect of these minor alloying elements on the cross-sectional area and the penetration depth of the weld is neatly illustrated by the columns.

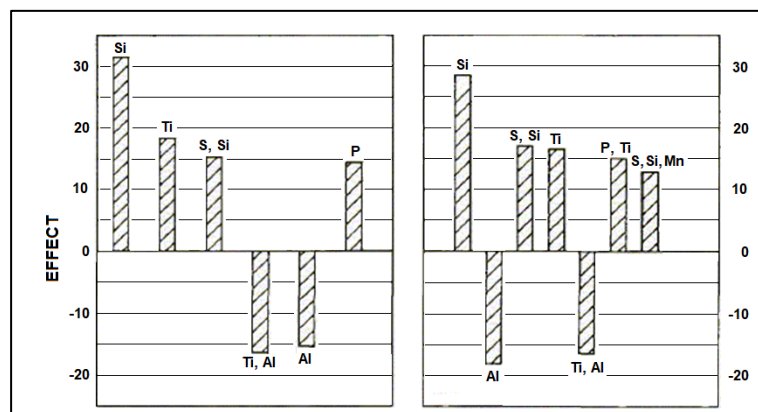


Fig. 15: Summary of the relative effects of minor alloying elements on cross-sectional area (left) and penetration depth (right) in TIG weld of alloy 600 [94].

The results show that Si had the largest positive effect on both the area and the penetration depth, meaning that the addition of Si clearly increased both of these features of the weld. Al, on the other hand, or a combination of both Al and Ti, had the largest negative effect, meaning that the addition of these elements decreased the area and penetration depth. The authors also concluded that these results showed that Ti inhibited the effect of Al because titanium alone, without Al, had a positive effect on both the cross-sectional area and the penetration depth.

A similar investigation into the effects of the elements S, P, Si, Al, Ti and Mn was conducted on the hot cracking tendencies of alloy 600 [95]. These results are presented in Table 5 as total crack lengths according to a Tigamajig test. According to Table 5, the elements S and P had a pronounced effect on the hot crack tendency of the alloy, while the effect of Si, Mn, Al and Ti was negative, indicating that these elements prevented the formation of hot cracks. The beneficial effects of both Mn and Si were reduced when both of these elements were present together, but Al and Ti clearly reduced the maximum crack length.

Table 5: Summary of the results of Tigamajig hot cracking tests on alloy 600 showing total crack lengths with minor element modifications [95].

	Treatment combination	Effect	Best value, mils
1% strain	S	45.4	132
	P	18.4	11
	S-Mn-Al	15.0	13
	S-P	14.7	191
	Si-Mn	14.2	46
	S-Si-Mn	12.8	45
	Si	-12.3	13
	P-Mn	-12.6	42
	S-P-Mn	-12.8	57
	Ti	-13.5	0
	Mn-Al	-15.8	8
	Al	-17.6	39
	S-Al	-17.9	98
	S-Si	-19.4	74
	Mn	-40.5	38
	S-Mn	-41.6	49
	Mean	-	44
2% strain	S	46	171
	S-Si-Mn	30	33
	Si-Mn	30	32
	Si	-24	27
	S-Si	-31	56
	Mn	-39	25
	S-Mn	-44	28
	Mean	-	49

Unfortunately, the effect of the element that has the greatest effect in the smallest quantities, namely B, was neglected in Savage et al.'s studies [94, 95]. In fact, the B content was not even mentioned, as it seems that at that time (1977) the effect of B on hot cracking was apparently not understood, or perhaps there were no available methods to measure it. However, it is plausible that the B content was the same in all of their experiments, so it should not affect the validity of the results.

In summary, the conclusions about melt pool surface tension are:

- Marangoni flow is the dominant convection mechanism in a laser cladding melt pool since there are no Lorenz forces, the forces induced on moving charged particles in the presence of magnetic and electric fields, and no arc plasma or arc pressure. In a laser with the Gaussian-type beam profile used in this study, power intensity is

concentrated on the middle of the spot. This generates steep temperature gradients in the melt pool surface. Arc welding is a different matter, and there are other forces affecting the melt pool.

- The surface tension of melt is dependent on the composition, particularly on the quantities of some minor impurity elements, mainly S and O in the case of stainless steel, but also Al and Ti in the case of Ni alloys. These elements are called surfactants.
- Normally the temperature dependence of surface tension is negative, meaning that surface tension decreases as the temperature increases. With certain amounts of surfactants, the temperature dependence of the surface tension ($d\gamma/dT$) changes to positive, meaning that the surface tension increases as the temperature does.
- It is the surface tension gradients on the surface of the melt pool surface which determine the fluid flow in the melt pool. These surface tension-driven flows are called Marangoni flows. There are also some other flow mechanisms, but it can be assumed that these do not have any effect if the heat source is a laser.
- The direction of the Marangoni flow is always from the lower surface tension towards higher surface tension.
- Ordinarily, with pure metals in an inert atmosphere, the temperature dependence of surface tension is negative. This means that the hottest site is at the middle of the weld pool and the edges are cooler.
- Therefore, surface tension is lower in the middle of the weld pool and higher at the edges, so this causes an outward Marangoni flow.
- When certain constituents, known as surfactants, are present in the weld pool, the temperature dependence of the surface tension changes to positive, i.e. the surface tension increases as the temperature increases. This causes an inward Marangoni flow which increases the penetration depth of the weld.

1.8. Cladding processes

According to the definition, cladding is the bonding together of dissimilar metals in order to produce a coating on top of a base material. In welding, the term cladding is one subcategory of the term weld overlay. The term weld overlay, or overlay welding, refers to the application of welding processes to deposit one or more layers of metal with specific characteristics onto a base metal in order to give the component desirable properties that the base metal lacks; or to restore the original dimension of the worn component. The procedure consists of the deposition of several weld beads arranged in a row, leading to the formation of a continuous surface layer [96].

In the case of metals, *cladding* usually involves adding a layer to improve corrosion resistance. If a layer is added to improve wear resistance, this is called *hardfacing*, especially if the layer is added using arc welding methods. A third sub-category of overlay welding, *buildup*, is a specific term to denote the deposition of weld metal on a base metal surface to restore the dimensional requirements of a component [96]. There is also a fourth term, *buffering* or *buttering*, in which an intermediate layer is deposited before applying the final coating. The *buffering* layer is used if the base metal and the top layer are not metallurgically compatible, though it also reduces residual stresses on the top layer which also helps to avoid cracking.

However, if a laser is used as the energy source, classification between *cladding* and *hardfacing* hardly ever occur, so all coatings produced with a laser are called laser claddings, regardless of whether the purpose of the layer is to protect the component from corrosion or from wear. The same applies to PTA cladding

Laser cladding is quite often considered to be a distinct coating process, separate from other overlay, or arc overlay welding processes. This distinction is made, for example, in the recently published (2013) *Encyclopedia of Tribology* [96]. This authoritative tome dedicates separate chapters to both weld overlay and laser cladding processes. Another recently published book, *Surface Engineering for Enhanced Performance against Wear* [103], distinguishes between torch processes, arc welding processes and high energy beam processes. The high-energy-beam processes category includes laser and electron beams.

Nevertheless, despite all the above distinctions and classifications, laser cladding is more or less an overlay welding process, as are arc processes. The important distinction is that the laser cladding process uses a laser beam as a heat source instead of an electric arc. The laser beam supplies the energy needed to melt both the feedstock and the base material. A laser cladding process using a coaxial powder feed (Fig. 20 a, p. 42) is very similar to a PTA cladding process, but the PTA process uses a concentrated electric arc (plasma) rather than a laser beam to melt the feedstock powder. However, a distinction should be made between weld overlay and thermal spraying processes, since in thermal spraying, the energy fed into the substrate material mainly comes from molten feedstock material, while the substrate itself is not melted directly by the energy source.

Whatever the method used to make the cladding, laser cladding with powder or wire feedstock, arc overlay welding including manual metal arc welding (MMA), metal inert/active gas welding (MIG/MAG), submerged arc welding (SAW), Tungsten Inert Gas welding (TIG) and Plasma Transferred Arc (PTA) welding [104], the choice usually comes down to which method gives the highest deposition rate and the best quality overlay for a particular application [105]. Other factors include the efficiency of the process, the cost of the cladding equipment and the type and cost of the feedstock material, all of which affect the manufacturing costs.

However, there are two shortcomings in the comparative values of different cladding processes:

1. The information and figures are often decades old and they do not represent the state-of-the-art situation.
2. The information and figures used in the comparison are often biased, indicating that some method was favoured when the figures were calculated.

For example, Table 6 is a fairly recent (2013) comparison between the efficiencies of different cladding methods [106].

Table 6: Key parameters of various cladding processes at high depositions rates [106].

Cladding process	Power (kW)	Deposition rate (kg/h)	Efficiency (kg/kW/hr)	Relative heat input/ distortion	Notes
High Power Diode Laser	7	9	1.29	1	Powder cladding rate. Expect greater efficiency & higher deposition with “dual hot wire”
Plasma Arc Welding (PTA)	7.5	5.4	0.72	3	250 A x 30 V + “hot wire” Heat input: 2 kJ/mm
Gas Tungsten Arc Welding (GTAW)	6	4.5	0.75	6	400 A x 15 V + “hot wire”
Gas Metal Arc Welding (GMAW)	12	7.6	0.63	10	400 A x 30 V, Ø2,8 mm wire Heat input: 1.5–1.7 kJ/mm
Submerged Arc Welding (SAW)	25	13.5	0.54	20	800 A x 32 V, Ø4 mm wire, DC Heat input: 2.2 kJ/mm
CMT (GMAW)*	4	5	1.25	?	175 A x 16,2 V, Ø1.2 mm wire Heat input: 0.2–0.3 kJ/mm

* Results from this study

Figures in the Table 6 seem to be biased. For example the values in for the GMAW (MIG/MAG) process with a thick Ø2.8 mm wire, a process power of 12 kW seems rather high. This deposition rate of 7.6 kg/h can be achieved with alloy 625 wire using normal wire thickness of Ø1.2 mm at a wire feed speed (WFS) of 13.4 m/min. With a pulsed MIG process, this WFS of 13.4 m/min would give arc power values of only around 8.3 kW with $I_{aver} \times U_{aver}$ method and around 9.4 kW with AIP method. However, these values are extrapolated from the arc power measurements that were taken with a WFS of up to 12 m/min (section 3.2.1, p. 106).

In addition, the values Table 6 are a bit misleading in the sense that only the effective power on the workpiece is included in the comparison. This comparison would be more neutral and less biased, if the total wall-plug power and the total electricity consumption were compared. Laser power sources, even direct diode lasers which are the most efficient ones, only have a wall plug efficiency of around 35–40% [18]. This efficiency is far less than that of arc welding power sources, which have wall plug efficiencies of around 90%.

Nevertheless, Table 6 does give some useful data on the achievable deposition rates of different cladding methods in terms of deposited feedstock mass per hour (kg/h), although all the methods presented in this table have relatively high productivity. Low-productivity processes are typically in the range of around 1 kg/h or less. Furthermore, the methods with the highest deposition rates are not included in Table 6. The ESW (Electro Slag Welding) method utilizes a metal strip as feedstock material, and can achieve deposition rates of over 20 kg/h with a single 60 mm strip [107].

1.9. Powder vs. wire as a feedstock material

The debate between powder or wire as a feedstock material has intensified recently because of the emergence of additive manufacturing [108, 109, 110, 111]. Most of the studies

comparing powder and wire as a feedstock material for cladding have concentrated on laser processes [112, 113, 117].

The quality of a powder is determined by its composition and by particle size and distribution, particle shape, surface morphology, and the amount of internal porosity (Fig. 16–19, p. 39). Variations in these features can result in considerable variations in the cladding process. In contrast, the properties and quality of wire as a feedstock material mainly arise from its composition, especially in the case of solid wire. This is because the other properties, such as surface quality, diameter and stiffness are easier to control so there is less variation between them. Wire feedstock is more consistent than powder because the technology for wire making is mature and the quality requirements for (arc) welding consumables are well established and stringent.

However, when it comes to laser cladding, any comparison between powder and wire as a feedstock material is rather academic, since wire feedstock is not really suitable for laser cladding. The surface area of wire is small, and it is reflective so it is difficult to melt wire with a laser beam. It can be done with a high-intensity laser beam, but it takes time, and the resulting cladding is highly diluted, in addition to which laser cladding with wire has a much narrower operating window [114]. Laser cladding using wire also suffers from low surface quality, low bonding strength, porosity, cracks and drop transfer. Drop transfer occurs when the melted liquid at the end of the wire does not flow smoothly and continuously onto the workpiece [116].

There is considerable scientific evidence that laser cladding with wire leads to poor productivity and/or large dilution. For example, in some recent (2015–2017) research by Abioye et al. [117, 118], laser cladding with Ø1.2 mm alloy 625 wire was studied. In one of these studies, laser power of 1.8 kW and a WFS of 0.8–1 m/min produced a poor deposition rate of only 0.5–0.6 kg/h. Furthermore, the dilution of one single bead was as high as 12%, although this was later reduced to a satisfactory 4.5% using multiple adjacent beads. Slightly higher wire feed rates still produced poor deposition rates and high dilution values. Another recent (2017) study by Xu et al. [119] with laser and Ø1.2 mm alloy 625 wire used laser power of 2.6 kW to produce a deposition rate of only 0.8–1.1 kg/h (WFS: 1.4–2 m/min). In addition, there was slow TS (0.36 m/min), small track displacement (~2.5 mm) and poor width-to-height ratio. The height of a single bead was relatively large, 2.7–2.9 mm, while the width was only 3.6 mm. This width-to-height ratio leads to large contact angle between the substrate and the bead, which hinders fusion between the beads when cladding with multiple beads.

Heigel et al. [112] have recently studied (2016) the differences between powder and wire feedstock in laser cladding with alloy 625. Although the deposition rates achieved in this study were generally low, the powder feedstock had a deposition rate of 0.8 kg/h while the wire feedstock was half of that, only 0.4 kg/h with 2.5 kW of laser power. Admittedly, the emphasis in this study was on residual stresses and deflection of alloy 625 substrate plate, rather than on possible cladding defects and the best utilization of the feedstock material.

However, the efficiency of the laser process can be increased substantially by using the Laser Hot Wire Cladding (LHWC) method, which involves running an electric current through the wire feedstock, rather than using an electric arc between the substrate and the tip of the wire

[120]. A recent (2016) study by Liu et al. [114], stated that a laser hot wire process with laser power of 8 kW was able to melt Ø1.2 mm alloy 625 wire at WFS of up to 19 m/min with a deposition rate of 10 kg/h. An example of a high-deposition-rate laser cladding process with alloy 625 powder is also presented in a study by Tuominen et al. [115]. In this study, laser cladding with an off-axis nozzle, laser power of 15 kW and a powder feed rate of 270 g/min (16 kg/h) had dilution of less than 5% with a cover rate of 0.6 m²/min.

1.9.1. Powder characteristics

The characteristics of powder that are usually stated on an analysis certificate include its chemical composition, particle size and the size distribution, its flowability (flow rate) and its apparent density. There are other features of a powder that can degrade the process performance and the cladding quality (Fig. 16–19). These undesirable features, cannot usually be deduced from the analysis certificate, but they can alter the melting response and resulting cladding properties. Some of these features are: fines (less than 45 µm in size) that degrade coating quality by causing fumes, porosity and surface oxides (Fig. 16), slag particle inclusions and oxidized particles that can produce porosity (Fig. 17), satellites (Fig. 16) and irregular shapes (Fig. 18) that can alter flow or melting characteristics [5].

The characteristics of powders that are usually stated in analyses certificate include chemical composition, particle size and the size distribution, flowability or flow rate and apparent density. Other features of powder that can degrade process performance and cladding quality (Fig. 16–19). These undesirable features presents on cannot usually be foreseen from the analyses certificate are satellites that can alter melting response to laser cladding (Fig. 16), fines (less than 45 µm in size) that degrade coating quality by causing fumes and surface oxides (Fig. 16), slag particle inclusions that can cause coating porosity (Fig. 17), irregular shapes that can alter flow or melting characteristics (Fig. 17), and oxidized particles (Fig. 18) [5].

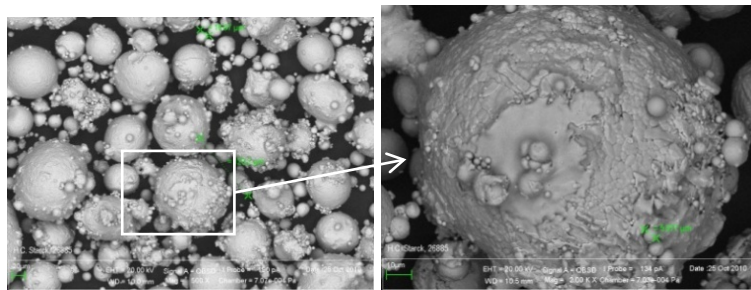


Fig. 16: Examples of undesirable powder features. SEM images with two magnifications. Fines and satellites [5].

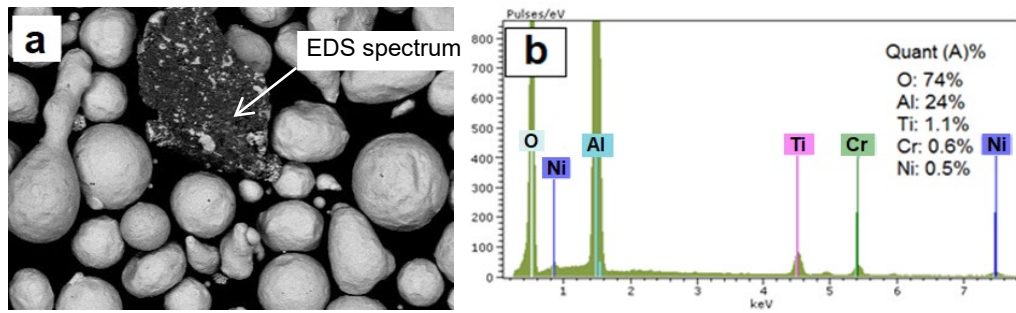


Fig. 17: Examples of undesirable powder features. a) SEM image: Slag particle inclusion and irregular shaped particles. b) EDS spectrum from the slag particle inclusion [5].

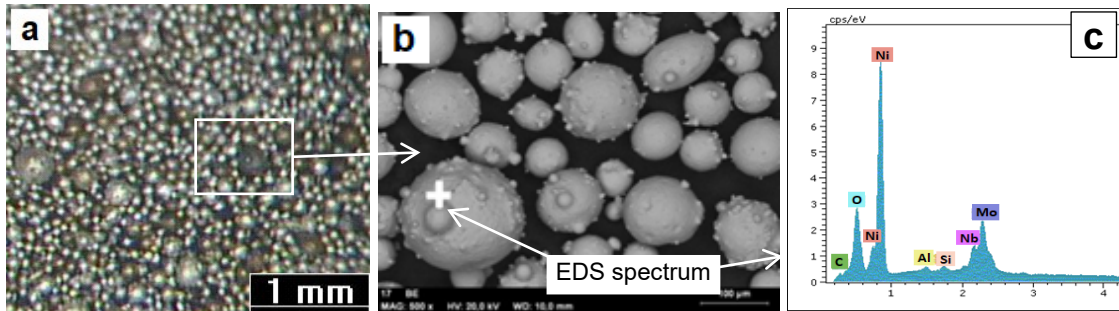


Fig. 18: Examples of undesirable powder features: oxidized particles. a) OM image, some clearly darker particles, b) SEM: image from darker particle, c) EDS point analyses spectra from the darker (oxidized) particle [5].

Hollow particles can also cause coating porosity (Fig. 19). Porosity in the powder feedstock is common in certain production techniques, like gas-atomisation (GA), because they entrap inert gas during production [108].

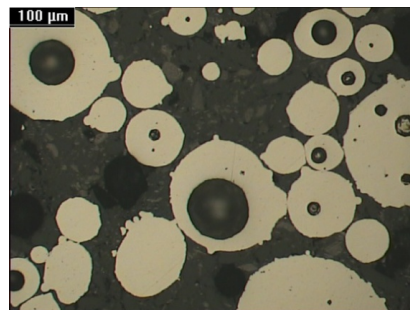


Fig. 19: Examples of undesirable powder features: Hollow particles. Microsection of alloy 625 powder. OM image [5].

Despite the fact that all the alloy 625 powders examined in this study contained some undesirable features, it seemed that quite often those features did not in themselves act as the origins of defects like porosity or hot cracks. For example, since some powders contained clearly visible dark oxidized particles, it was quite clear that the atomization gas applied in the atomizing processes contained some oxygen.

All the powders examined in this study were produced with the gas atomization process. Powder atomization has several parameters and determining which small changes control particle size distribution is a complex issue because there are so many variables which can influence the final atomisation. The requirements for the powder atomization process can, however, define some aspects of the composition of the alloy. For example, some manufacturers add Si to alloy 625 to ensure the flowability of the melt through the atomizing

nozzle during the whole process. It is possible that a Si-poor melt, and hence with a higher viscosity, can clog up the nozzle during the atomizing process [28].

1.9.2. Powder vs. wire – surface area

The surface of the feedstock material can easily be exposed to the atmosphere and this can contaminate the surface. In fact, the surface of the feedstock material can be contaminated or oxidized already during the powder atomisation process – and this is obviously what often happens – depending on the equipment and the gas shielding used in the process.

It can be assumed that the total amount of contamination is related to the total surface area of the feedstock material, which in turn is related to the form of the feedstock material. Powder has a substantially greater surface area than wire. The surface area of powder increases in inverse proportion to the particle size, raised to the second power.

The surface area of powder and wire can be calculated according to the following equations:

Powder particle (sphere, diameter = d):

$$A = 4 * \pi * \left(\frac{d}{2}\right)^2 \quad (1)$$

Wire (diameter: d, length: l):

$$A = \sim \pi * d * l \quad (2)$$

The difference between the total area of powder and wire, if the mass of alloy 625 feedstock material is 1 gram, is presented in Table 7.

Table 7: Number of particles and total surface area for alloy 625 powder with a mass of 1 g and wire length and total surface area for alloy 625 wire with a mass of 1 g.

Powder grain size	Number of powder particles (1 g)	Total surface area of powder (1 g)	Wire diameter	Wire length (1 g)	Total surface area of wire (1 g)
10 µm	230 000 000	71 000 mm ²	0.8 mm	250 mm	600 mm ²
50 µm	1 800 000	14 000 mm ²	1.0 mm	150 mm	480 mm ²
100 µm	227 000	7 100 mm ²	1.2 mm	120 mm	400 mm ²
150 µm	67 000	4 800 mm ²	1.6 mm	60 mm	300 mm ²

As can be seen from Table 7, the total surface area of wire feedstock is only a fraction of that of powder feedstock.

1.10. Laser cladding

In the laser cladding, the feedstock material is usually in a powder form and is fed either coaxially (from circumferentially around the laser beam, Fig. 20, a) or from the side of the beam (off-axis, Fig. 20, b). As mentioned earlier, wire is also sometimes used (Fig. 20, c), and there yet another method in which the material for the cladding is preplaced on the substrate with a binder (preplaced method).

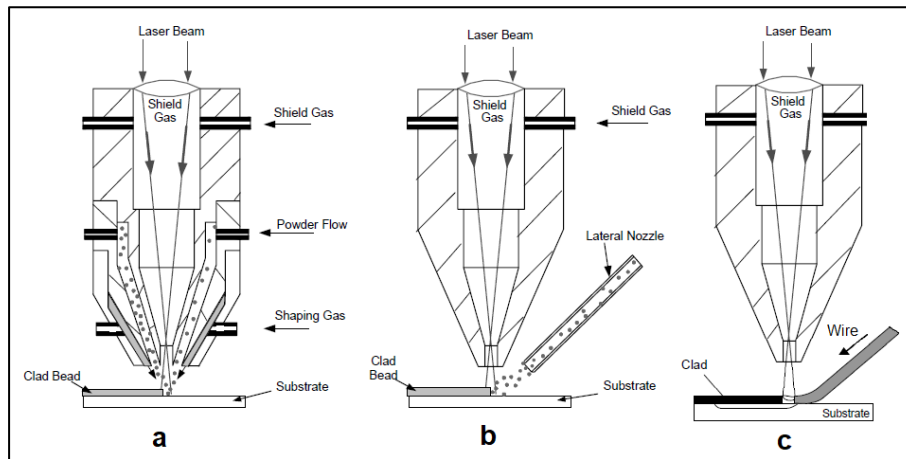


Fig. 20: Schematic presentation of different feedstock material systems in laser cladding [116].

The beneficial characteristics of laser cladding include [121]:

- The low heat input of laser cladding causes very little distortion to the component, which leads to a significant reduction in post-treatment operations.
- Low level of dilution from the substrate ensures the desired coating composition.
- The quality of the deposit is high – laser clads can be made with low porosity and few imperfections.
- High solidification and cooling rates result in fine-grained microstructures, which results in harder coatings with good wear and corrosion properties.

However, there are drawbacks. The high cooling rates increase the sensitivity of the clad and the HAZ to cracking, so precautions such as preheating might be necessary. Other disadvantages include expensive equipment, relatively poor energy efficiency (around 30% at best), the utilization efficiency of powder is less than 100%, there are a wide variety of process parameters, there is a health hazard due to laser radiation, and relatively low productivity – typical cladding rate is around 1.5–2 kg/h [5].

Powder utilization, i.e. “catchment” efficiency is a major issue in continuous powder feed systems for laser cladding. The nozzle geometry, the weld pool geometry, the travel speed, and the powder feed rate all influence the percentage of feedstock powder that contributes to the overall build-up of the cladding. Another potential challenge with laser cladding is that the process is much more sensitive to dirt than most conventional weld overlay processes. Typically, this involves mechanically cleaning the component with a pneumatic or electric wire brush followed by an acetone rinse to remove any oil residue [122].

The genesis of laser cladding can be traced back to studies by Gnanamuthu at Rockwell International Corporation in Thousand Oaks, California in the late 1970's [116] and studies of laser cladding have continued apace since then. According to Scopus, (the largest abstract and citation database) the number of publications about laser cladding stayed relatively low in the 80's but started to grow in the early '90, continuing until 2008 when there was a record 300 publications. Since then the number of publications on the topic has levelled out at around 300 a year. For 2017, Scopus lists a total of 353 references with the search term “laser cladding”. The number of laser cladding studies is difficult to compare with competing

technologies, like arc welding methods, since there is no single generic term for weld overlays made with arc methods.

However, even though laser cladding has been studied comprehensively and is an emerging technology for some industrial sectors, like the maintenance industry, it has still found only very limited, niche applications, for example in the production of wear resistant surfaces in the mining and mineral processing sectors in Canada [122]. However, the popularity of laser cladding has recently been given a boost by the additive manufacturing (AM) sector, both in terms of research and actual applications in industry. This is because one AM method, direct energy deposition with laser beam and powder and blown powder, is essentially the same process as is used in laser cladding.

1.11. Cladding with wire and arc

Welding with any method where the energy to heat up and melt both the feedstock and base material comes from an electric arc, namely arc welding, is a workhorse in the welding industry. There are a variety of arc welding methods and most of them are also used for weld overlays.

1.11.1. Wire and arc cladding processes

There are several welding methods that utilize wire feedstock and an electric arc to generate the heat needed to melt the feedstock and parent materials together. Most widely used among these methods are:

- Metal Inert/Active Gas welding – MIG/MAG, also called Gas Metal Arc Welding – GMAW.
- Tungsten Inert Gas welding – TIG, also called Gas Tungsten Arc Welding – GTAW.
- Manual Metal Arc welding – MMA, also called Shielded Metal Arc Welding – SMAW.
- Submerged Arc Welding – SAW.
- ElectroSlag Welding – ESW.

Of these methods, the Metal Inert/Active Gas welding (MIG/MAG, or GMAW) is perhaps one of the best known and is discussed in the following sections. The MIG/MAG process is a welding process in which an electric arc forms between the consumable wire electrode and the metal(s) in the workpiece. The arc heats the metals in the workpiece causing them to melt and coalesce [124]. According to the definition by European welding standard EN 14610 (*“Welding and allied processes. Definitions of metal welding processes”*), MIG is a process where shielding is provided by an inert gas, e.g. argon (Ar) or helium (He), whereas MAG is process where the shielding is provided by a chemically active gas [125]. However, the distinction between the shield gas being inert or active is not clear cut. The term GMAW is used for the same method in the US, and this term is very often used in welding research.

1.11.2. Transfer modes in the MIG/MAG process

There are some variations in the methods of how the filler material is transferred from the wire to the weld seam, or melt pool, in MIG/MAG welding. These methods are called transfer modes. The type of transfer is governed by various parameters, but mainly by the voltage between the wire and the base plate. According to the traditional classification of MIG/MAG

transition modes in standard EN ISO 4063 [126], there are four primary transfer modes of metal transfer and these are discussed below.

1.11.2.1. Short circuit transfer

Short-circuit transfer has traditionally been the MIG/MAG mode used for applications which only require low heat input, penetration depth and dilution. These applications include thin sheet welding, since no great penetration depth is needed, and overlay coating if low dilution is desirable. With the short-circuit mode, the current level is not sufficient to maintain an arc or to enable the transfer of droplets across the arc. The droplet forms on the end of the wire and is only transferred to the weld pool when the wire with the molten droplet is in contact with the weld pool. When this happens, an electrical short-circuit is created and the current spikes. The combination of surface tension forces and the magnetic pinch force created by the current spike cause the droplet to transfer to the weld pool and the arc is re-established. This process repeats itself about 100 times per second. The short-circuit process is usually characterised as having a high spatter level. The short-circuiting event causes high current values, peaks that make the molten droplet burst and spatter over the weld bead.

1.11.2.2. Globular transfer

MIG/MAG welding with globular metal transfer is considered the least desirable of the three major variations, because of its tendency to produce high heat, a poor weld surface, and spatter. The method was originally developed as a cost efficient way to weld steel using MIG/MAG, because this variation uses carbon dioxide, a less expensive shielding gas than Ar [124].

1.11.2.3. Spray transfer

Spray transfer was the first metal transfer method used in MIG/MAG, and is well-suited for welding aluminium and stainless steel while with an inert shielding gas. In this process, the weld electrode metal is rapidly passed along the stable electric arc from the electrode to the workpiece, essentially eliminating spatter and resulting in a high-quality weld finish. As the current and voltage increases beyond the range of short circuit transfer the weld electrode metal transfer transitions from large globules through small droplets to a vaporized stream at the highest energies. Since this vaporized spray transfer variation of the MIG/MAG weld process requires higher voltage and current than short circuit transfer, and because it needs higher heat input and a larger weld pool area (for a given weld electrode diameter), it is generally used only on thick workpieces of above about 6.4 mm (0.25 in) [124].

1.11.2.4. Pulsed-spray process

The pulsed spray process is a variation of the spray transfer mode. It is based on the same principles as spray transfer but uses a pulsing current to melt the filler wire and thus allows one small molten droplet to fall with each pulse. The use of pulses means that the average current is lower, which decreases the overall heat input and thereby decreases the size of the weld pool and the heat-affected zone. This means it is possible to weld thin workpieces. The pulse provides a stable arc and no spatter, since no short-circuiting takes place [124].

1.11.2.5. Newer classification of transfer modes in MIG/MAG welding

The four-class classification of transfer modes in MIG/MAG welding, as presented above, was established in 1976 by the International Institute of welding – IIW [127]. However, this classification does not encompass recent controlled-transfer types or metal transfer modes which can only be recognised with the latest sophisticated measurement technologies, such as oscilloscope and high-speed video camera imaging. Some attempts have since been made to better classify transfer modes with newer, advanced MIG/MAG processes using digital control.

Norrish [128] proposed extending the above-mentioned classification in 2003 by adding two more groups of modes, namely *Controlled Transfer Modes* and *Extended Operating Modes*. In 2012, Scotti et al. [129] suggested classification into three main classes as presented in Fig. 21, where the classification is based on classes, groups and modes.

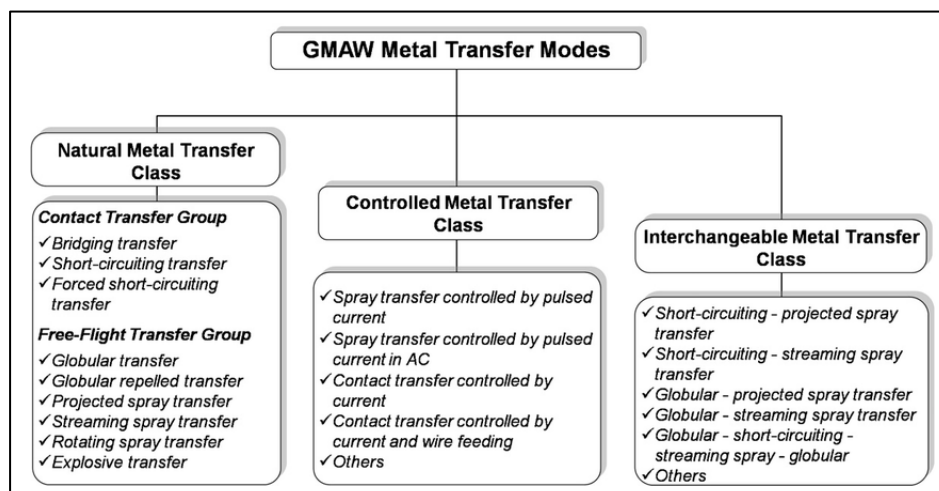


Fig. 21: MIG/MAG metal transfer classification based on hierarchical order, classes, groups and modes [129].

In this classification, the “normal”, or “pure” CMT process would belong to the class in the middle: *Controlled Metal Transfer* and in the mode *Contact transfer controlled by current and wire feeding*. However, the CMT process can also be in modes where there are pulsed and CMT process mixed together, so in that case the process would belong to the class *Interchangeable Metal Transfer*. In this study, all the experiments were done with the normal CMT process, since mixing with other processes do not bring any advantages to the overlay welding of Ni alloys.

In this study, the term “conventional” is used for a MIG/MAG welding process where the metal transfer is not digitally controlled, and it comes into the category “Natural transfer” in Fig. 21. There are many alternative terms for “conventional” in the literature, such as standard, normal, non-controlled, historic and many more.

There is also one new classification of controlling modes in MIG/MAG welding presented recently (2015) by the German Welding Society, DVS Verband. In this classification, called DSV 0973, “*Overview of process control variants for gas shielded metal-arc welding*” [130] there are a total of 10 controlling modes for MIG/MAG welding. The emphasis in this publication is not on the process modes themselves, but on how the process is controlled by

the software of the welding power source. There is also a category for cyclic wire movement process controls, as is used in the CMT process

The classification of the transfer mode is an important aspect for determining the heat input during welding, or arc power. Classic methods in determining heat input do not apply to a waveform-controlled process like CMT. This issue is discussed further in section 2.1 on page 67.

1.11.2.6. Brand names of advanced MIG/MAG processes

Cold metal transfer (CMT) is the brand name for a relatively new welding process developed and owned by the Austrian welding power source manufacturer Fronius GmbH. The CMT process differs from the traditional MIG/MAG process in that it relies on filler wire (electrode) short circuit and precise wire control for material transfer. The CMT process is one of the MIG/MAG-methods that use the direction of the wire feed as a one of the process parameters. Kapustka [131] called these methods “*Reciprocating wire feed gas metal arc welding (RWF-GMAW)*” methods. With the RWF-GMAW process the wire has a reciprocal motion in and out of the weld pool. The wire’s motion is synchronized with the current waveform to produce a weld that is characterized as having minimal if any spatter, closely controlled heat input, bead placement, and base metal dilution. In 2017 the manufacturers of RWF-GMAW equipment included Jetline Engineering (Controlled Short Circuit – CSC), Fronius (Cold Metal Transfer – CMT), SKS Systems (micro-MIG), and Panasonic (Active Wire Process – AWP). In addition, several, if not all, manufacturers have their own methods for controlled waveform MIG/MAG welding, although these methods do not have the capacity to repeatedly retract the wire, such as Surface Tension Transfer (STT) by Lincoln and Wise by Kemppi.

1.11.3. The CMT process

CMT is an abbreviation for Cold Metal Transfer and describes a welding process with a low heat input. CMT is a MIG/MAG welding process that utilizes short-circuit transfer, also known as the dip-transfer process. More detailed information about transfer modes in MIG/MAG welding are presented in section 1.11.2 on page 43. However, the CMT process includes a completely new type of droplet detachment, combined with the reversing wire electrode movement. The components of the CMT equipment are presented in section 2.1.2 on page 68. Schematic illustrations of conventional dip transfer and CMT process are shown in Fig. 22. In addition, some frame captures from high-speed video of the CMT process are presented in Fig. 26 on page 57.

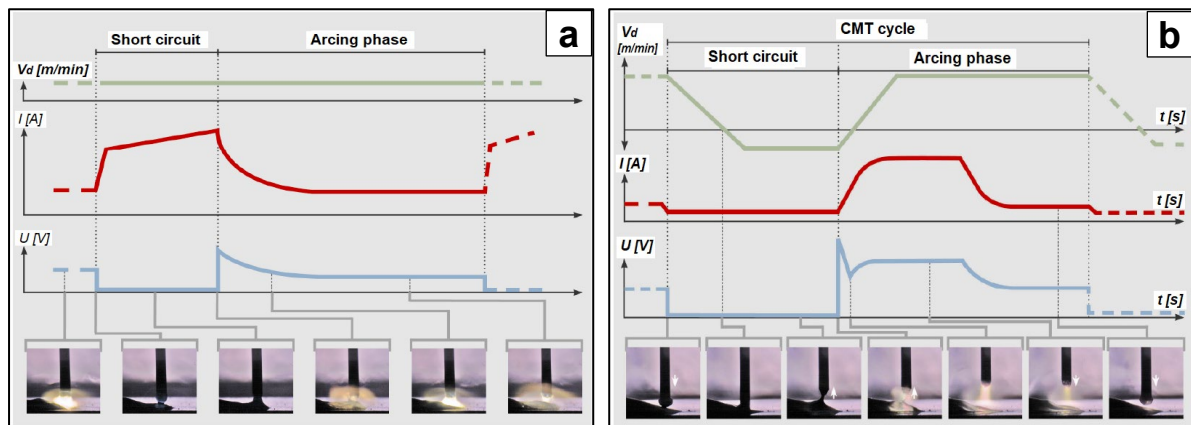


Fig. 22: Wire speed (top), current (middle) and voltage (bottom) graphs. a) Conventional dip transfer MIG/MAG arc process with stable wire feed. b) CMT process with reciprocating wire speed [157].

In the conventional dip transfer arc process (Fig. 22 a), the wire is fed continuously towards the workpiece. When the wire touches the workpiece, a short circuit occurs and the current increases since the electrical resistance between the wire and the workpiece has vanished. The sudden rise in current causes a large pinch effect, i.e. it vaporises the molten metal at the wire tip, and some of that metal is ejected from the wire tip. The wire is then no longer in contact with the melt pool, so the short circuit is broken. The rapid increase in current during the short circuit causes the molten metal to spatter, which is why welding with the conventional dip transfer mode is characterized by some amount of spatter and the accumulation of molten droplets close to the weld seam. The rise and fall in current can be optimised in the case of digitally regulated machines. However, the occurrence of spatter and arc re-ignition at relatively high current level is a physical necessity in the conventional dip transfer process.

With the CMT process (Fig. 22 b), on the other hand, droplet detachment and re-ignition are controlled by means of a backwards movement of the wire electrode. The wire is fed towards the workpiece until the arc is removed as the short circuit occurs. The direction of the wire's movement is then reversed, i.e. the wire is withdrawn from the melt pool. This breaks the short circuit and the arc is reignited. Then the wire moves forward again and the process is repeated. It is this reverse motion of the wire that withdraws it from the melt pool rather than the large current needed to break it free in the conventional process. This reversing motion occurs within a frequency range of 50 to 130 Hz, depending on the characteristics of the filler metal, the shielding gas, the diameter of the electrode and the synergic line. One characteristic feature of the CMT process, and of other controlled transfer modes (section 1.11.2.5, p. 45), is that both voltage and current are digitally controlled in every phase of the process. These controlling parameters are pre-determined by the so-called synergic line, which is designed for each filler wire and shield gas combination. A more detailed explanation of synergic lines follows in section 1.11.3.1.

1.11.3.1. Synergic lines

The conventional explanation of synergic line is that it is a linear mathematical relationship that determines the process controls for matching the voltage and amperage with WFS. In other words, the synergic line adjusts the welding power to the speed of the wire feed. Synergic lines are used in most modern MIG/MAG power sources to help the welder to choose

the appropriate combination of settings (WFS, current and voltage) for the welding power source. Suitable welding parameters, i.e. synergic lines, are pre-programmed into the power source. By inputting the filler metal, wire diameter and shield gas, the power source control unit will automatically set optimum voltage and other parameters (pulsing etc.) to fit to the set WFS. With a synergic line, a welder only needs to set the WFS and the power source control will do the rest. If need be, conventional MIG/MAG welding power sources can also be used also without a synergic line, by adjusting both the voltage and the WFS [160].

Fronius CMT MIG/MAG welding apparatus has fully digitally controlled parameters. In addition, the CMT process has to be operated with a synergic line, since the synergic line also determines the parameters for the wire retraction, and gives guideline values for current, voltage etc., in each phase of the cycle. There are a total of around 60 parameters that are controlled by a synergic line in the CMT process. A schematic diagram of a single cycle of the CMT process with explanations of some of the controlling parameters of the synergic line are presented in Fig. 23.

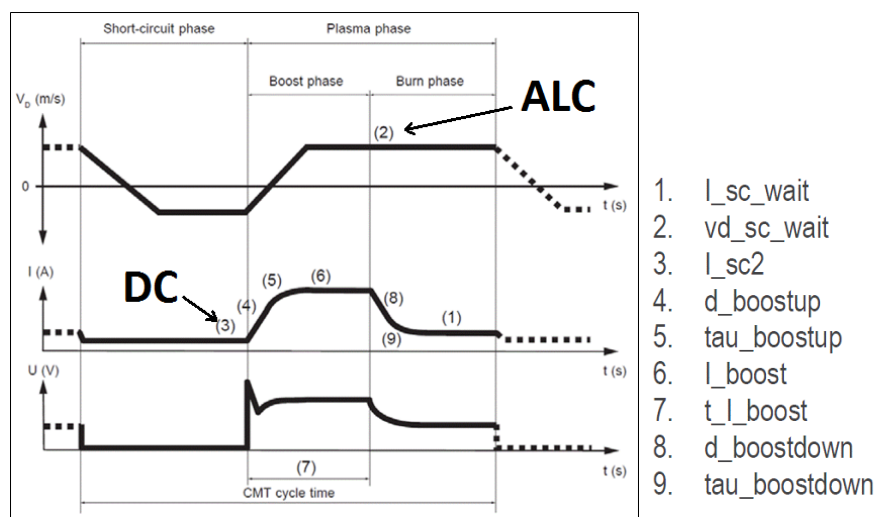


Fig. 23: The CMT process cycle and parameters inside the synergic line for each phase of the cycle [161].

In the CMT process, each synergic line has its own set of values for parameters 1–9 presented in Fig. 23, and the values for these parameters can be found from the RCU, the remote control unit. These parameters are also the ones that could be altered if one chooses to create a new synergic line. Table 8 shows the parameters for synergic line 1693 (NIBAS 625) and with a WFS set value of 8 m/min.

Table 8: Parameters for synergic line 1693 with WFS setting of 8 m/min (ALC: 0%, DC: 0.0) [162].

Parameter (No. in Fig. 23.)	Value with set WFS: 8 m/min
Slaghammer On_1/Off_0	1
I_ignition	200 A
t-ignition	12 ms
I_sc_wait (1)	100.5 A
Vd_sc_wait (2)	24.00 m/min
I_sc2 (3)	90.00 A
vd_boostup (4)	1000.0 A/ms
tau_boostup (5)	0.60 ms
I_boost (6)	330.0 A
t_I_boost (7)	4.00 ms
I_drop_melt	10.0 A
t_burnback	0.0
Current guideline value	180 ms (ex)
Guideline value for material	180 A
Voltage guideline value	15.6 V
Wirefeed speed	8 m/min

The values in Table 8 are dependent on the set value for WFS and the synergic line. Although not all of these parameters are available or adjustable with each synergic line, they are specific for each synergic line. For example parameters 8, *d_boostdown* and 9, *tau_boostdown* are not available for synergic line 1693.

In the CMT process, there are three parameters the user can alter inside the synergic line through the remote control unit (RCU), or in the control panel of the power source, without the need to alter the synergic line itself. These are:

1. Wire feed speed (WFS, primary)
2. Arc Length Correction (ALC, auxiliary)
3. Dynamic Correction (DC, auxiliary)

These three will be discussed in more detail in the following sections 1.11.3.2 and 1.11.3.3. The classification to primary (WFS) and auxiliary parameters (ALC and DC) is not standard, but is made by the author of this study.

1.11.3.2. Wire feed speed – WFS

The set value for the wire feed speed (WFS) governs the overall deposition rate and welding power according to the synergic line in use. The synergic line of the MIG/MAG process is designed so that, once the WFS is set, the welding power source supplies enough power, current and voltage, to melt the wire at the set WFS value. However, it turned out that in the CMT process, the actual WFS is not the same as the set one.

In a conventional MIG/MAG process, the WFS is set to be constant and the welding power source gives nearly constant voltage to the process. The adaptation of the process to

variations, like changes in distance from the workpiece or melt pool, as well as short-circuiting and arcing in the dip-transfer process, is made by changes in welding current. But since the wire feed direction in the CMT process changes at high frequency depending on the feedback to the controlling software, the actual WFS in the CMT process does not have to be constant or the same as the set value. Parameters ALC and DC also have an effect on the actual WFS rate. In studies by Almeida [164] it was found that the WFS set value of 4 m/min resulted in an actual WFS value of only 2.75 m/min with an ALC value of -30%, and an actual WFS value of 3.3 m/min with an ALC value of +30%.

1.11.3.3. Auxiliary parameters ALC and DC

The parameters Arc Length Correction (ALC) and Dynamic Control (DC) both have considerable influence on the CMT process, the welding energy and the properties of the resulting weld. However, only a few studies of the effects of these parameters in the CMT process have been published. Almeida [164] studied the effect of ALC and DC on single bead welding of Ø1.2 mm mild steel with a relatively low WFS of 4 m/min. In this study, only one of the two parameters was altered at a time, while the other was kept at a value of 0. Pépe [163] also studied the effect of ALC and DC on welding Ø1 mm mild steel and type 22-9-4 duplex stainless steel wires, and Pickin et al. [189] did the same with bead on plate welding with Ø1.2 mm aluminium wire. In the studies by Pickin et al. [189] it was found that the ALC value also affects the arcing's short-circuiting ratio and frequency. Changing the ALC from +10% to -30% resulted in a change in the short circuit duration from ~5 ms to ~10 ms, respectively. However, no systematic determination of the mutual effect of parameters ALC and DC in the CMT process has yet been published

Altering the ALC affects the second parameter in Fig. 23, vd_{sc_wait} . The ALC can be adjusted between -30% and +30%. With a conventional MIG/MAG process, the changes in arc length are effected by increasing or reducing the arc voltage. However, in the case of the CMT process, the effects of ALC are more complex. In the CMT process, the arc length is detected and adjusted mechanically via the back and forth movement of the wire with a frequency of 70–100 times per second and altering the ALC parameter affects the time or speed of the forward movement of the wire during the arcing phase. Increasing the ALC value decreases the wire's forward speed during the arcing phase and thus increases the arcing time and decreases the short circuiting time. Conversely, decreasing the ALC value increases the wire's forward speed and decreases the arcing time so the total process power is decreased. With synergic line 1693 and an ALC value of +30%, the wire forward speed during the arcing phase is set to 18 m/min and with an ALC value -30% this value is set to 30 m/min. More of these values are presented in Table 9.

Altering the DC affects the third parameter in Fig. 23, I_{sc2} . The DC parameter can be adjusted between -5.0 and +5.0 and it affects the inductivity, i.e. the level of current during the short circuiting phase. Low values for the DC result in higher current during the short circuit phase and, vice versa. Higher current during the short circuit can cause spatter to occur. On the other hand, higher current during the short circuit also causes the wire to melt faster without increasing penetration depth and dilution of the base material.

In summary, the set value for ALC affects WFS during the arcing period, when the wire moves forward at a high speed, and DC affects the level of current during the short circuiting phase. Some of these values for synergic line 1693 and a WFS set value of 8 m/min are presented in Table 9. Some explanations for these parameters have already been presented in section 1.11.3.1 on page 47.

Table 9: Set values of parameters ALC (2, Vd_sc_wait) and DC (I_sc2) for the synergic line 1693 and WFS set value of 8 m/min.

ALC	Parameter 2 Vd_sc_wait		DC	Parameter 3 I_sc2
-30%	30 m/min		-5.0	144 A
-15%	27 m/min		-2.5	117 A
0%	24 m/min		0.0	90 A
+15%	21 m/min		+2.5	63 A
+30%	18 m/min		+5.0	36 A

The effect of ALC and DC on the CMT process in cladding single beads is studied in section 3.2.3 on page 114.

1.11.3.4. CMT cladding studies

The CMT process is a relatively new method and relatively few studies have been published about its use in overlay welding. This is in contrast to laser cladding, about which thousands of research papers, have been published since the early '80s.

However, if the CMT process is to be classified as only one variation in the MIG/MAG arc welding process, then the MIG/MAG arc welding process has been widely studied in fusion welding, although less so in overlay welding. This is despite the fact that overlay welding with a manual MIG/MAG process, as well as other arc welding processes, are some of the most widely used methods in workshops around the world. One of the reasons for the apparent lack of publications dealing with arc overlay welding is probably the fact there is no one established term that covers all arc welding methods, unlike laser cladding, which is an overarching generic term for any processes that use laser radiation to weld a metal coating onto another metal surface.

The number of studies on cladding with the CMT process or examination of these claddings published during the past decade (2008→) can be counted in tens, rather than hundreds, the earliest being a study by Egerland and Helmholdt in 2008 [165]. Many of these studies have dealt with the cladding of boiler panels or boiler pipes (mild steel) with alloy 625, such as the studies published by Dutra et al. [144], Frei et al. [169], Egerland [165, 166,], Rutzinger [170, 171], Rozmus-Górnikowska et al. [172, 173, 174], Slania et al. [175, 176], Solecka et al. [177] and Pertzark et al. [178]. Other studies dealing with other Ni alloys have been conducted by Daniels [167] and McVicker [168] with M52 Ni-based alloy for nuclear power plant components, and Ola and Doern [179] and Benoit et al. [180] with alloy 718 wire on top of alloy 718 plate. Some studies have also been made on aluminium cladding on an aluminium substrate [190, 191], cladding with copper-silicon alloy (CuSi) on steel [196], Stellite (cobalt) alloy on steel [192, 193, 194, 195] and even magnesium on magnesium [197].

2.1 Arc power in MIG/MAG process

Determining the arc power, or in other words, the welding energy, is very important in fusion welding since the standards determine that welding should be performed with a specific welding energy, or heat input that is predetermined by the welding procedure specification (WPS). According to welding procedure specification standard EN ISO 15614-7:2016 for overlay welding [154], the actual arc energy should not vary more than $\pm 25\%$ from what has been used in welding tests for the welding procedure specification [132] and arc energy should be determined according to the technical report ISO/TR 18491 [139].

Arc power P_{arc} in arc welding is usually determined by the equation:

$$P_{arc} = I_{aver} \times U_{aver} \quad (3)$$

where P_{arc} is arc power (W), I_{aver} is average current (A) and U_{aver} is average voltage (V).

The heat input in arc welding is determined with a similar equation:

$$E = k \times \frac{I \times U}{TS} \quad (4)$$

where E is welding energy (J/mm), k is the process efficiency factor, I is average current (A) and U is average voltage (V) and TS is travel speed (mm/s) during welding and The efficiency factor is usually applied in determining the effective heat input in arc welding, since some of the energy brought to the process is lost by radiation or other effects, and is not used in heating and melting the wire or base material. According to standards, ISO/TR 17671-1 [140,] and EN 1011-1 [141], the value $k = 0.8$ is recommended for a MIG/MAG process. Some studies have concluded that process efficiency for CMT process in welding $\varnothing 1$ mm mild steel wire was around 85%, giving factor k of a value 0.85 [137]. Standards ISO/TR 17671-1, EN 1011-1, or even the standard EN 1011-6 for laser welding [142], do not state a value for the k factor value in the laser welding process. However, k factor values in the range 0.4–0.7 for the laser welding process have been proposed [143]. In this study, a k factor value of 0.5 was used for laser the cladding process and a value of 0.8 for MIG/MAG processes (including the CMT).

Current and voltage during the welding are usually determined by recording the average readings of these values on the control panel of the welding power source during welding, or from the memory of the power source after the weld is finished. These current and voltage values represent the average values during the weld.

However, while traditional methods produce relatively consistent results with high-energy processes such as spray transfer arc, the results are less consistent or accurate with controlled arc or pulsed modes due to the continually changing current and voltage. According to a study by Joseph [138], the most appropriate method for calculating the heat input for complex waveforms, as in the like short-arc or pulsed modes, is a method called Average Instantaneous Power (AIP), where current and voltage are recorded with a high frequency (> 1 kHz) data acquisition device (DAQ), and arc power, current x voltage, is determined from each data point during some sequence; thus allowing the average arc power to be the average of these values.

Average instantaneous power is calculated by the equation:

$$AIP = \frac{\sum_i^n U_i \times I_i}{n} \quad (5)$$

where AIP is instantaneous power, U_i is voltage and I_i current for each sample acquired by the data acquisition system, and n is the number of samples i.e. measurement points.

According to a quite recent (2015) technical report ISO/TR 18491 "*Welding and allied processes — Guidelines for measurement of welding energies*" [139], Instantaneous Power – IP, is a welding power determined by averaging the product of current and voltage measurements made over time at rapid intervals which capture brief changes in the welding waveform. This technical report states that when determining welding heat input, Instantaneous Power (IP) or Instantaneous Energy (IE) methods should be used for waveform-controlled welding methods, like CMT, since the conventional method by using the product of average current and voltage ($I \times U$) can introduce errors of up to 70% [139]. The technical reports goes on to state that both the sampling rate and the calculation rate should be sufficient to capture the changes in the welding waveform; typically, a sampling rate of at least 10 times the frequency of the waveform is used. So, for the CMT process, where the waveform frequency is around 70–100 Hz, the sampling rate in current and voltage measurements should be at least 1000 Hz. ISO/TR 18491 also states that in voltage measurements, the position of connectors should be located so that the first one is connected to the earth clamp on the workpiece and the second one to the welding head.

Examples of the differences that can arise in the results of arc power measurements are presented in studies by Dutra et al. [144], where AIP values were determined in the overlay welding of alloy 625 with pulsed DC, pulsed AC and CMT modes. The difference of the arc power values determined with $I_{aver} \times U_{aver}$ values vs. AIP values, was +12% in the pulsed DC mode, and around +20% in the pulsed AC and CMT modes. In other words, the AIP value in the CMT mode was 20% higher than the arc power value determined by the traditional method using average current and voltage ($I_{aver} \times U_{aver}$).

A useful tool for determining the relationship of process power and deposited metal, especially for overlay welding, is the term Power Ratio (PR). Power ratio is a relationship developed for gas tungsten arc welding (TIG) which considers the ratio of arc power ($U \times I$) over the amount of filler metal deposited per unit of distance travelled [100]. A simple definition of PR is presented below:

$$Power\ Ratio = \frac{Process\ power}{Cross\ sectional\ area\ of\ deposited\ filler\ metal} \quad (6)$$

If a wire is used as a feedstock material, the cross-sectional area of the deposited filler metal is linearly proportional to the input parameters WFS divided by travel speed (TS) multiplied by the cross sectional area of the filler wire that is fed into the process, so that PR can be determined with equation:

$$Power\ ratio = \frac{U \times I}{\frac{WFS}{TS} \times \pi r^2} \quad (7)$$

where U is average voltage, I is average current, WFS is wire feed speed TS is travel speed and r is wire radius. In this study, the arc power ($U \times I$) factor was replaced by the corresponding value of AIP when determining power ratio.

1.11.4. Shield gases in the welding of Ni-based alloys

Deciding on the appropriate shielding gas when welding alloy 625 with the MIG/MAG process is not always straightforward. There are sub-categories of the MIG/MAG process such as short circuiting or spray transfer which can have a large effect on the welding process, especially on heat input. The transfer mode is often neglected in shield gas recommendations. However, the Nickel Development Institute recommends 100%Ar shield gas for spray transfer mode, and mixtures of Ar and He, or Ar, He and CO₂ for short circuiting and pulsed arc modes [105].

Gases containing CO₂ produce a very stable arc, excellent out-of-position welding characteristics, and excellent Ni-base to carbon steel welding characteristics. However, because carbon dioxide is present, the bead surface will be highly oxidized, which can increase the possibility of incomplete fusion defects unless the oxide layer is removed from the surface before the next weld pass [145]. The alternative is only to use shielding gases with carbon dioxide for single pass welds [105].

It has often been stated that some carbon dioxide is needed, or is advantageous, to stabilize the arc in MIG/MAG welding. However, this stabilisation effect does not apply to the CMT process because of its inherent stability due to the CMT process's software-controlled voltage, current and wire feed. According to a newer classification of MIG/MAG transfer modes (Fig. 21, p. 45) CMT falls into the class of controlled metal transfer mode, where the metal transfer and the short circuiting are not just determined by the voltage, but also by other forces such as pinch force and melt surface tension, which can be affected by the shield gas. Due to the stability of the CMT process, it is even possible to weld mild steel wire with pure CO₂ shield gas [146]. With conventional arc welding, using a pure CO₂ shield gas has usually been avoided due to the arc's instability.

Some of the arc's heat is transferred to the workpiece via the plasma or gas flow. Especially at high temperatures, there are two components, He and H₂, which can significantly improve process efficiency. Good thermal conductivity has a positive effect on seam geometry, wetting, degassing of the molten pool and in the welding speed [147]. The thermal conductivities of shield gases are presented in Fig. 24.

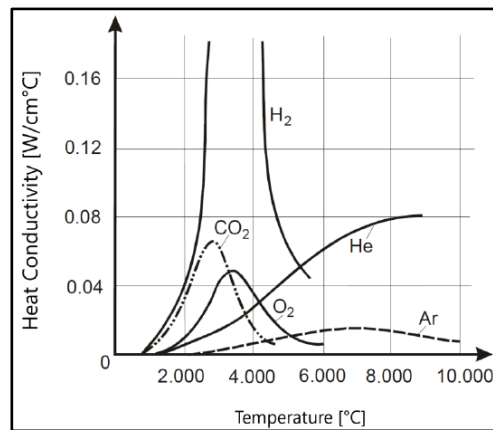


Fig. 24: Heat conductivity of shield gas constituents [147].

Ar-H₂ mixtures are often used for the gas-tungsten arc welding of Ni-base alloys to improve the wetting and flow characteristics of the weld metal. However, it has been observed that a loss in weld metal ductility may occur if the welding is conducted with shielding gases containing >1% hydrogen [14]. This loss in ductility is associated with the pick-up of hydrogen in the weld metal which results in hydrogen embrittlement. A study by Young et al. [149] showed that hydrogen levels as low as 5 ppm were sufficient to reduce the strength and ductility of a multipass tungsten inert gas (TIG) weld with alloy 625 wire.

The shielding gas supplier Linde AG has also developed a shielding gas CRONIGON® Ni10 specially for the MAG welding of Ni-based materials. The gas contains four components: Ar, He, H₂ and small amount of CO₂ to stabilize the arc [147]. However, this gas is not currently ordinarily available in Finland in regular size gas bottles, but only as special delivery in small bottles. The Finnish subsidiary of Linde, AGA, recommends the gases MISON® Ar and MISON® 30He for MIG/MAG welding of Ni alloys. The compositions of these shield gases are presented in Table 10.

Table 10: Recommended shielding gas mixtures for MIG/MAG welding of Ni alloys [147, 148].

	Ar%	He%	CO ₂ %	H ₂ %	N ₂ %
CRONIGON® Ni10	bal	30	0.05	2	–
CRONIGON® Ni20	bal	50	0.05	–	–
MISON® 30He	bal	30	–	–	0.03
MISON® Ar	bal	–	–	–	0.03

The characteristics feature in CMT welding is the low heat input which results in lower dilution and a cooler weld pool than pulsed or spray arc MAG processes. In a study by Dutra et al. [144] it was found that in overlay welding with a weaving motion with alloy 625, the CMT process needed 25% He in the shielding gas, compared to pulsed DC+ and pulsed AC processes, where wetting was sufficient with a mixture of Ar+2,5%CO₂. According to a study by Baixo and Dutra, it was shown that pure Ar only works in the spray transfer mode in MIG/MAG fusion welding of alloy 625. It was also found that poor results were obtained in short-circuit transfer welding, regardless of the shielding gas [150]. In a study by McVicker, shield gas that was called “tri-mix”, Ar-30%He-0.5%CO₂, was found to be the most suitable for overlay welding with the Ni alloy 52M in a CMT process using the synergic line 1393 and

a weaving motion. Other tested shield gases were 4.8 Ar (100%Ar), Ar-0.5%CO₂, Ar-25%He, and Ar-30%He-2%H₂-0.5%CO₂ [168].

1.11.5. Arc cleaning effect

In the arc welding process, when there is an electric arc present, the arc also affects the surface around the melt pool, which is cleaned by the arc. This cleaning effect happens in MIG/MAG welding with “normal” DCEP polarity (Direct Current, Electrode Positive) of the electrode, i.e. the feedstock wire is the positive anode and the substrate is the negative cathode. With this polarity, negative electrons travel to the positive wire and the positively charged shield gas ions travel to the negative surface of the workpiece. The reverse polarity option, DCEN (Direct Current, Electrode Negative) with negative wire, is seldom used in MIG/MAG welding processes.

A schematic illustration of a MIG/MAG welding system with a wire as a positive electrode is presented in Fig. 25. This figure illustrates a pulsed MIG/MAG process where the arc column is relatively long and wide so the molten material is transferred as relatively large droplets and the feedstock wire does not touch the melt pool.

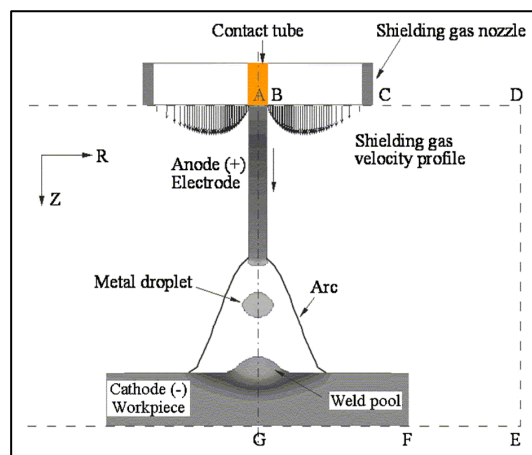


Fig. 25: A schematic representation of a MIG/MAG system and DCEP polarity including the electrode, the arc, and the weld pool (not to scale) [133].

In the following figure, Fig. 26, there are three frame captures from a high speed video of a single phase of the CMT process.

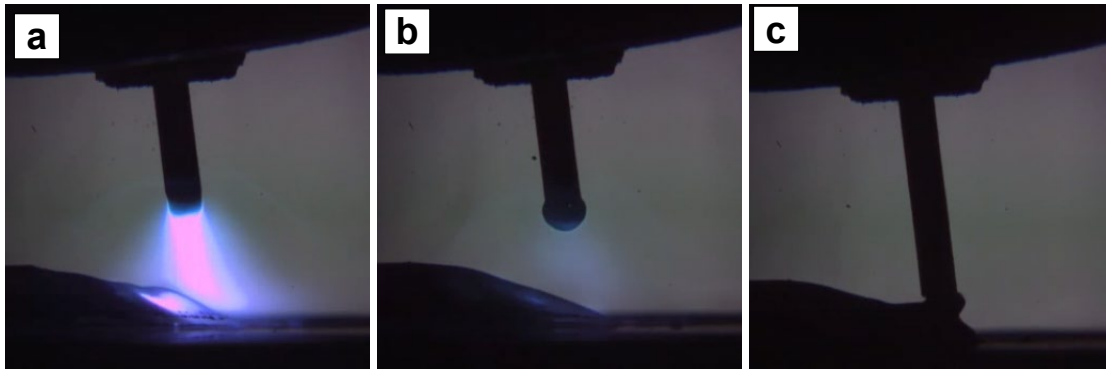


Fig. 26: Three frame captures from high speed video of a single phase of the CMT process. The direction of movement is from left to right [134]. a) Arcing phase when the wire is retracted to its uppermost position and the arc column is longest and widest. b) In the uppermost position, the arc is diminished and the wire starts to move towards the melt pool. c) The short circuiting phase when the wire touches the melt pool.

As can be seen from figures above, during the arcing phase (Fig. 26 a), the arc is relatively long, the area it affects is wide, and it affects ahead of the melt pool. The long arc length is related to the fact that the wire tip moves backwards during the arcing phase. The arcing and short circuiting phases alter with a frequency of 70 – 80 Hz and the arcing phase covers around half of the total duration of a single process cycle.

This “arc cleaning effect” is usually neglected in the welding of steels, but it is considered to be especially important in welding aluminium, since aluminium forms stable oxides on the surface that deteriorate the weld quality if they are left in the weld. The cathodic surface cleaning effect in variable polarity (AC) TIG welding of aluminium was studied by Sarrafi and Kovasevic [135]. They found that there are three regions on the arc-affected surface (Fig. 27): A) molten metal, B) a cleaned, smooth surface adjacent to the weld pool, where repetitive scanning by cathode spots caused smoothness, and C) a rough, porous, cleaned surface located farther from the arc centre, where craters are related to the locations of the cathode spots. Area D represents unaffected surface.

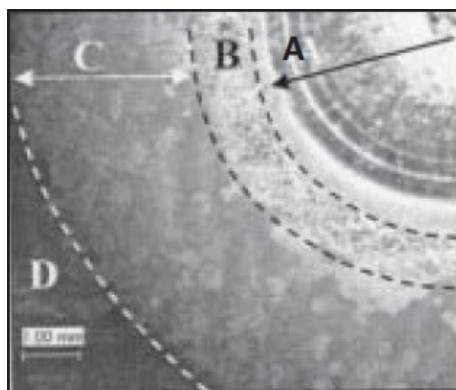


Fig. 27: Different areas formed on the aluminium surface after its melting by variable-polarity (TIG) arc. A – Molten pool; B – shiny, cleaned, smooth surface adjacent to the molten pool; C – rough, cleaned surface; D – not affected [135].

Sarrafi and Kovasevic [135], present three hypotheses for how the surface cleaning takes place during the electrode positive (DCEP) cycle of TIG AC welding of aluminium. According to the first hypothesis (1), the positive ions that are accelerated toward the aluminium cathode are assumed to “sputter” the surface oxide layer. Sputtering is the ejection of substrate atoms

due to the effect of the high-energy bombarding particles. In the second hypothesis (2), the surface oxides are assumed to be destroyed because of the dielectric breakdown phenomenon. In the third, most recent (2000) hypothesis (3), the evaporation of the oxide layers at the cathode spots of non-thermionic cathodes is a possible mechanism for cathodic cleaning [136].

An example of this cleaning effect in the MIG/MAG (CMT) process is presented in Fig. 28 a, where there is clearly a bright area ahead of the melt pool that cleans and heats up a thin layer of the substrate surface as the weld melt pool generates a metallurgical bond with the substrate. The situation is clearly different in laser cladding with blown powder. Fig. 28 b is an image from a high-speed video of single bead laser cladding where electric arc and thus substrate cleaning do not occur. On the contrary, a powder cloud can shadow the substrate so that the substrate surface does not melt and no metallurgical bond is created between the substrate and cladding.

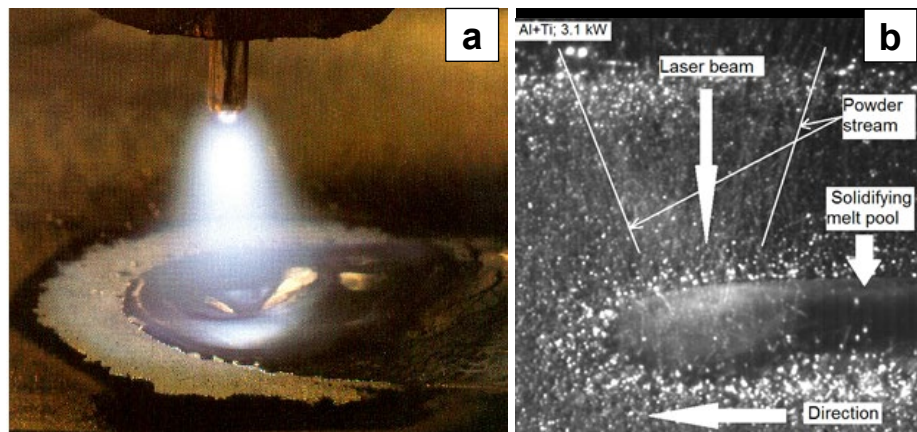


Fig. 28: High speed video image captures from single bead welding processes. a) Cleaning effect in MIG/MAG surface welding of steel using positive electrode [151]. b) Laser cladding process [99].

The situation in laser cladding presented in Fig. 28 b may lead to a lack of fusion between the substrate and the cladding. Some results of examinations on the base metal surface near the cladding bead of both laser and CMT claddings is presented in section 3.3.1 on page 136.

1.12. Cladding defects

This section presents some examples of typical defects found in both laser and CMT claddings. The defects are based on experience, rather than on standards or regulations about welding. Standard ISO 6520-1 [152] divides (fusion) welding defects into the following seven groups: cracks, cavities, solid inclusions, lack of fusion, low penetration, imperfect shape and dimensions, and miscellaneous imperfections. Standard ISO 5817 [153] defines acceptance levels for these defects in fusion-welded joints and standard ISO 15614-7 [132] also defines acceptance levels for defects in overlay welding.

1.12.1. Cracks

Cracks in weld material occur when the localized stresses exceed the tensile strength of the material. Hot cracks develop during solidification of the weld melt pool, or at elevated

temperatures, when weld material is reheated. Cold cracks, like hydrogen cracking, develop in low temperatures. Cracking is the most detrimental type of defect and according to welding standards [132, 153], cracks or other linear imperfections are not permitted.

According to experience [5], hot cracking is a relatively common defect in alloy 625 claddings. Hot cracking has been discussed in detail in previous section 1.6 above (p. 19) and some examples of hot cracks can be seen in Fig. 1 on page 2.

1.12.2. Lack of fusion and lack of inter-run fusion

Lack of fusion occurs when the molten weld metal fails to fuse completely with the substrate, or the previous weld bead, when it is called inter-run fusion. As with cracks, lack of fusion has a very detrimental effect on the quality of a weld, and both lack of fusion and lack of inter-run fusion are considered unacceptable by welding standards [132, 153]. An example of a lack of fusion defect in alloy 625 laser cladding is presented in Fig. 29 a, which shows a defect in which the laser power has not melted the substrate surface, so the weld consists of molten feedstock material which has solidified on top of substrate without any fusion between the two. Fig. 29 b shows an example of lack of inter-run fusion between the beads in alloy 625 CMT cladding.

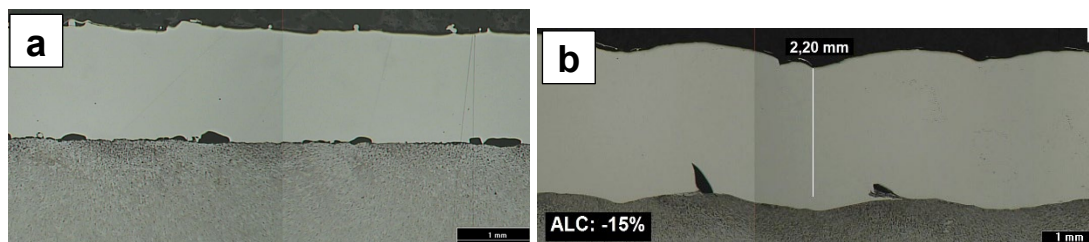


Fig. 29: Cross section alloy 625 claddings a) laser cladding with a severe lack of fusion between substrate and cladding, b) CMT cladding with some lack of inter-run fusion between cladding beads [5].

Lack of fusion can easily occur in laser cladding if the laser power is too low. However, with CMT this kind of defect is rare. In the arc welding process, the arc bombards the substrate surface with enough heat to melt the thin surface layer of the substrate, as illustrated in Fig. 28 on page 58, and this helps to create the fusion between the substrate and the cladding.

The laser cladding literature introduces a term for a very similar defect to lack of inter-run fusion, called inter-run porosity. This can be caused by the dimensions of the bead; a small contact angle between the bead and substrate and/or the large height/width ratio of the bead (Fig. 40, p. 81). However (fusion) welding standard EN ISO 6520-1 [152] (*Classification of geometrical imperfections in metallic materials*) does not recognise the inter-run porosity defect as it is difficult to distinguish from inter-run fusion.

1.12.3. Humping

In both cladding processes and in fusion welding processes, one way of increasing productivity is to use a higher travel speed (TS). In cladding, higher TS also serves to decrease the bead height. However, a fundamental problem in the use of higher travel speeds in a MIG/MAG process is phenomenon called humping.

Humping, or sagging as it is also known, can be described as a periodic undulation of the weld bead. Fig. 30 c shows a typical example of humping in an alloy 625 MIG/MAG single bead on a plate weld on mild steel. At both the valley and the hump, the depth of penetration is the same. However, there is a large accumulation of weld metal at the hump. The overall appearance of a humped weld suggests that its formation is a periodic physical phenomenon in an otherwise steady welding process. Humping occurs mainly in welding with stringer motion. Often, this problem of a sluggish melt and subsequent bead humping can overcome by weaving the torch.

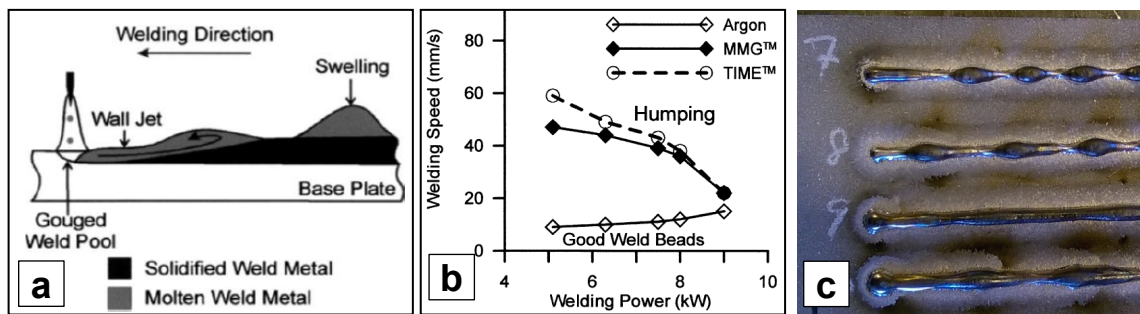


Fig. 30: a) Schematic presentation of humping phenomenon. b) Plot of limiting welding speeds vs. welding powers for varying shielding gas [155]. c) Example of severe humping of alloy 625 single bead on plate welds. TS 1200 mm/min, shielding gas 100%Ar, set WFS: 7, 8, 9 and 10 m/min.

The effect of the shielding gas is critical for the humping phenomenon, since shielding gas has large effect on the surface tension and hence the fluidity of the melt pool. In a study by Nguyen et al. [155] it was found that in MIG/MAG welding with $\varnothing 0.9$ mm mild steel wire reactive shielding gas (Ar-He-CO₂) could suppress the occurrence of humping and allowed up to 400% higher welding speeds than with pure Ar shielding gas.

Few studies have been published about humping in the CMT process. Adebayo, Mehnen and Tonnellier [156] studied the humping of mild steel wire in wire and additive layer manufacturing with the CMT process. They found that there is a tipping point with a TS of 600 mm/min after which humping starts to take place on both $\varnothing 0.8$ and 1.2 mm wire. They concluded that the backflow of molten metal inside the weld pool is responsible for the initial formation (which starts at the TS of 600 mm/min) and subsequent growth of the hump which is promoted by the high surface tension of the molten weld metal. No any studies have been found about the humping phenomenon in the welding of Ni alloys despite the fact that molten alloy 625 is very sluggish and is hence prone to humping.

1.12.4. Underfill

Underfill occurs when the molten weld metal fails to fill the joint. In cladding, this defect appears as holes or cavities on the cladding surface. The origin of an underfill-type defect is a viscous melt and the wrong ratio of filler metal to TS. Underfill can be avoided by reducing the travel speed, increasing the amount of feedstock material, a smaller track displacement, or making the melt less viscous by increasing the arc power or changing the shield gas to reduce the surface tension of the melt. Some examples of underfill defects in CMT test claddings are presented in Fig. 31.

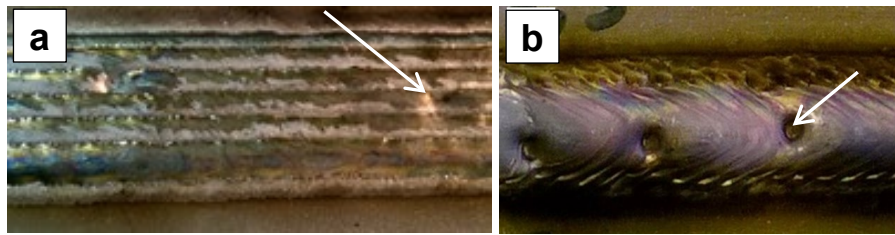


Fig. 31: Underfill-type defects in the surface of CMT test claddings, as shown by arrows. a) Adjacent beads with stringer motion, b) single bead with weaving motion [5].

Underfill defect is not common defect in laser cladding, but underfill-type of holes in the surface are quite typical defects in cladding with CMT process. This is probably related to the fact that melt pool is relatively cool and viscous in CMT process, especially with Ni alloys. Other reason is that to enable desired high coverage rates, TS values in overlay welding with CMT are on a high level. It happens also in practise, that underfill-type defect does not appear in the first bead, but in the second or third pass in CMT claddings.

1.12.5. Porosity

Porosity is the result of spherical or elongated pockets of gas getting trapped in the solidifying weld metal [158]. With a powder feedstock, the causes of porosity include: oxidized particles, too many small particles, hollow particles and moisture. Porosity is a problem in laser cladding with powder and is apparently caused by poor quality powder and a high solidification rate that does not leave time for the gas to escape from the melt pool.

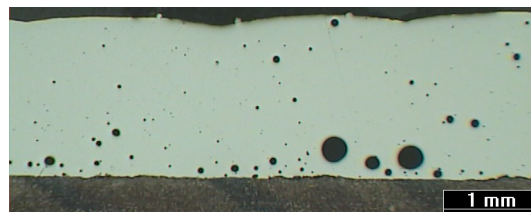


Fig. 32: Porosity in alloy 625 laser cladding caused by oxidized powder particles [5].

Porosity is not considered to be a serious threat to weld strength in normal loading, or even in fatigue conditions. The standard ISO 15614-7 [132] for overlay welding allows pores as large as of 2 mm in diameter in weld overlay.

1.12.6. Undercutting

Undercutting, a common weld defect, is usually associated with high speed welding, and often occurs with humping. Indeed, there is evidence that they are caused by similar mechanisms [190]. The origin of undercutting is a high welding current and arc pressure which gouges and melts the base material ahead of and around the melt pool. Due to high the TS or inadequate or sluggish filler material, the melt does not fill the groove at the edge of the weld melt pool as the melt solidifies.

However, undercutting is not a common defect in the CTM welding since the arc current and voltage values, and hence the arc pressure, are too low to generate gouging, i.e. the melting of the base material, at least at the edges of the weld bead. However, the combination of a high TS (1500 mm/min) and ALC (+30%) was able to produce some small intermittent

undercutting (Fig. 93, p. 128) in this study with the CMT process. This defect type is not common in laser cladding since there is no electric arc present to gouge the surface and the laser beam's intensity is at a low level in cladding. However, undercutting can happen in laser or laser hybrid welding [159].

1.13. Mechanical parameters

In the following sections, the effects of mechanical parameters: travel motion, travel speed (TS), track displacement (TD) as well as some parameter related features, like bead width and height, are discussed. The general rules for these parameters apply both in laser cladding with powder and cladding with arc and wire, but for example, the effect of bead shape on cladding quality is more pronounced in cladding with arc and wire.

1.13.1. Motion

There are two distinctive torch motion methods that are used to produce overlay welding, or overall welding: 1. stringer motion and 2. weaving motion.

Stringer motion is made by moving the welding electrode straightforward in a direction parallel to the axis of the bead, without any appreciable transverse oscillation. Weave or weaving motion is made with oscillations along the bead which are transverse to the length of the bead. Hence this motion is quite often called oscillation. The question as to whether to use a weaving motion instead of stringer motion is a very common issue in manual (fusion) welding. Some weaving is quite often applied in overlay welding to widen the bead.

The stringer motion produces the smallest heat input to the substrate and the highest solidification rate of the cladding melt pool, which is beneficial for cladding properties. The stringer motion is simpler than weaving, since the motion is straightforward, and the only variable parameter is the TS. Nevertheless, there are motion-related parameters that affect the process with stringer motion such as the work and travel angle and the contact tip to workpiece distance (CTWD). The work angle is the relationship between the weld joint and the torch parallel to the direction of motion. The travel angle is the relationship between the torch and substrate perpendicular to the motion. However, the effects of these parameters were not examined in this study.

Laser cladding is usually performed with a stringer motion, since weaving is not needed in order to achieve wider bead or good height/width ratio. So, the question of using stringer or weaving motion is usually not an issue in laser cladding. Cladding with arc welding methods, like CMT, is quite often done with an oscillating motion of the tool. Weaving is common in studies dealing with Ni-alloy claddings made with the CMT process [144, 165, 166, 167, 168, 169, 170]. However, even more of studies have been made with alloy 625 and the stringer motion [171, 172, 173, 174, 175, 176, 177, 178]. However, almost all of these studies (except 171) deal with cladding of boiler pipes and several deal with examination of alloy 625 cladding microstructure, rather than the cladding process. Some studies have been made with stringer motion and alloy 718 [179, 180] as well as with Al alloys [189, 190, 191].

However, the stringer motion has certain advantages over the weaving method, like lower heat input to the base material and faster solidification that yields a finer grain structure with higher hardness and lower segregation of elements, so CMT claddings with the stringer motion was used in this study. Another reason for choosing the stringer motion over the weaving motion for the CMT process was that since the tests with laser cladding were done with the stringer motion, doing the CMT cladding with the same motion would be better for comparison between the two processes.

1.13.2. Track displacement

Track displacement (TD) indicates the length of transverse movement between cladding passes. The term overlap, or overlapping ratio (OR) is quite often used to indicate this movement. The relationship between OR, TD and the width of the bead (W) can denoted by the equation:

$$OR = \frac{(W-TD)}{W} \quad (8)$$

The amount of overlap is usually stated as a percentage. However, the term overlap is not strictly accurate, since it does not indicate the actual movement between passes, so in this study, the term track displacement (TD) is used.

Productivity in terms of covered area vs. time, is a factor of TD and TS. Therefore, from the productivity point of view, it would be beneficial to use as large TD, as well as TS, as possible. However, as illustrated in Fig. 33, TD also affects penetration depth, dilution, smoothness of the cladding surface and the height of the second and following beads compared to the first one.

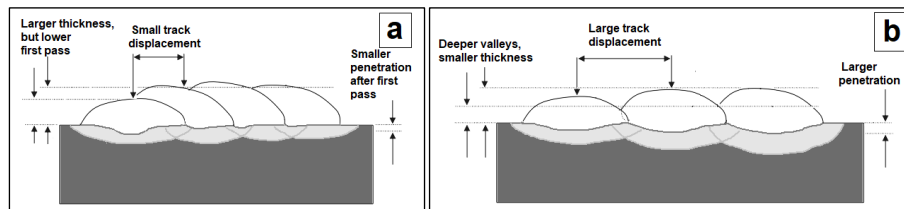


Fig. 33: The relation between track displacement, penetration, bead thickness, and depth of valleys. a) Small track displacement. b) Large track displacement.

If TD is smaller than 0.5 x bead width (W), the laser beam or arc hits mainly on the previous pass, the penetration depth and dilution are lower, the cladding thickness increases after the first pass, and the final surface is relatively flat (Fig. 33, a). With large TD values, the laser beam or arc hits on the base material surface, which increases penetration depth (Fig. 33, b). Therefore the easiest method to keep the average dilution at a low level, is to keep the TD value small so that laser beam or arc does not hit the substrate surface, but hits the previous pass. However, the drawback with this that it decreases the cover rate.

In additive manufacturing, surface smoothness and the predictability of the height of each layer are important features as the structure is build up layer by layer. Some models have recently been developed, to predict the single bead shape and the optimal value of TD in the wire and arc additive manufacturing process (WAAM) [182, 183], in the laser cladding process

[184, 185], or in the MIG/MAG overlay welding process [186]. For example in a study by Ding et al. [182], a tangent overlapping model (TOM) was developed to predict the optimum TD based on single bead width (W) for additive manufacturing. In this study by Ding et al. [182] it was concluded that in the WAAM process, a TD of $0.738 \times W$ optimises the material use, since little material removal (machining) is needed with this optimized TD. With a typical bead width (W) of 6.5 mm for CMT single bead, this equation would produce a TD of 4.8 mm. However, the effect of track displacement on penetration depth and dilution, as well as on cover rate, was not considered in these models, which were designed mainly for additive manufacturing.

1.13.3. Travel speed

From the productivity point of view, it is beneficial to use as high TS, as possible. Travel speed (TS) has a direct effect on heat input in welding, since TS is a divider in the equation in which the heat input is determined (eq. 4, p. 52). However, the term heat input and the equation to determine it were developed for fusion welding of structural steel in order to estimate the effect of welding on hardening and/or softening of parent metal (steel). Increasing the TS, assuming the arc power is kept the same, generally lowers the penetration depth and dilution, as well as the bead cross section area. However, the effect of TS on penetration depth is not straightforward. When the TS is slowed down, the melt pool acts as a barrier to the action of the arc on the base metal, decreasing the penetration depth and dilution. However, this does not happen except for relatively low values of TS (<400 mm/min) [151, 96].

In a manual (fusion) arc MIG/MAG welding process, TS values are normally in the range 100 – 400 mm/min and the physical difficulty of moving the welding torch faster is a limiting factor. In automatized MIG/MAG welding, the TS is normally in the range 500 – 800 mm/min with normal MIG/MAG equipment. If the speed goes higher, the stability of the welding process becomes poorer, the weld appearance deteriorates, and some defects such as undercut and humping may easily occur [187]. So, TS values exceeding 1000 mm/min can be regarded as belonging to the high speed welding category in MIG/MAG welding.

TS is also related to humping-defect, Adebayo et al. [188] studied humping with mild steel wire in additive manufacturing with the CMT process. They found that there is a limiting speed of 600 mm/min at which humping starts to take place with both $\varnothing 0.8$ and $\varnothing 1.2$ mm wire. A study by Rutzinger [171] in cladding with CMT and $\varnothing 1.2$ mm alloy 625 wire, used the same TS of 600 mm/min. However, in a study by Ola and Doern [179] with $\varnothing 1.2$ mm alloy 718 wire, high TS's of 900, 1500 and 2100 mm/min were used in CMT cladding tests, although in a study by Benoit [180], a TS of only 300 mm/min was used with the same alloy 718 wire.

In the laser cladding process with blown powder, there are fewer factors such as humping to limit the travel speed than there are in the arc MIG/MAG welding process, or the effect is less pronounced. In laser cladding, travel speeds exceeding 1000 mm/min are quite normal and it is possible reach travel speeds of 3000 mm/min [181].

1.13.4. Bead shape

The shape and dimensions of the cross section of a single bead are illustrated in Fig. 40 on page 81. When producing weld overlay coating, especially with adjacent stringer beads, the

shape of a single bead, as well as wetting of the melt or the contact angle between the base metal and the weld bead, are essential parameters for achieving high-quality defect-free coating.

With some weaving or oscillating motions, i.e. transverse motion of the welding torch, wide and flat bead is easier to achieve and hence the bead shape and wetting angle are less important. Wide and flat weld bead is preferable in order to increase the coated area and to minimize surface irregularities, contributing to increased productivity and a better-quality overlay. The geometrical parameter bead height/width (H/W) ratio indirectly evaluates the flatness, or convexity of the weld bead, as does the contact angle. Weld beads that are very convex, in other words, high and narrow, may hinder the overlap of subsequent passes, causing lack of fusion, or so called inter-run porosity (Fig. 29 b, p. 59) between the passes. In general, H/W ratios greater than 0.5 are an indication that the weld beads that are too convex [96]. Conversely, H/W ratios around or less than 0.3 are beneficial for overlay welding with adjacent beads.

The contact angle has also been shown to set a limit for cladding with stringer motion, and an angle of less than 90° is especially undesirable in that it results in non-uniformity of bead shape with a potential to allow voids between successive clad passes. When the contact angle is close to 90° , the arc becomes un-stable, with the arc jumping between the reinforcement and the base material, leading to lack of fusion between clads and, occasionally, overlapping of beads on top of one another. The contact angle should be greater than 115° for successive passes with stringer motion in CMT cladding with alloy 718, as suggested by Ola and Doern [179].

In summary, a low contact angle and/or a wide and relatively flat bead is beneficial in overlay welding since:

1. It decreases the possibility of lack of fusion or voids between beads.
2. If the arc hits the previous bead, or the root of the bead but not the base material, penetration depth and dilution are lower.
3. A high and narrow bead can lead to the arc jumping between the top of the previous bead and the base material, leading to a lack of fusion between clads and/or holes in the clad layer.
4. A wide bead allows larger track displacement (TD) between beads to be used, which increases cladding coverage rate.

2. Methods

This section describes the tests and examinations that were done in this study. The equipment used in the cladding test is presented in section 2.1, and the materials in 2.2. Cladding experiments with laser and alloy 625 powder are presented in section 2.3 and with MIG/MAG arc welding processes and alloy 625 wire in 2.4. The tests that were made to compare the laser and CMT processes and the resulting cladding properties are presented in section 2.5, and 2.6 presents the measurements and examinations that were done for the cladding test samples.

Most of the laser cladding tests were done with single beads to examine the effect of alloy 625 composition on the process and the hot crack sensitivity. However, some test claddings with adjacent beads were also done to compare the laser cladding process and properties with those of the CMT process.

The tests with the CMT process were mainly aimed at determining the CMT process properties and parameters, as well as the available process parameter in cladding with $\varnothing 1.2$ mm alloy 625 wire. No hot cracking tests were performed with the CMT welding process.

2.1. The equipment in the cladding tests

Tests were conducted both with laser cladding apparatus with a coaxial powder feed for the cladding head and with CMT arc welding (MIG/MAG) apparatus. Two different types of laser cladding devices were used, both with coaxial powder feeding. The test apparatuses are presented in the following sections.

2.1.1. Laser cladding equipment

Laser single bead test claddings on hot crack examinations were made with a diode-pumped 4.4 kW Rofin-Sinar Nd:YAG laser (DY044) with 600 μm fiber optics and with a Gaussian beam profile. The laser radiation had a wavelength of 1.064 μm . Other components of the cladding apparatus were a Motoman robot, Precitec YC50 coaxial cladding head and a Medicoat powder feeder. The robot and cladding head, as well as the beam profile of the laser determined with a beam diagnosis instrument (Primes FocusMonitor) are presented in Fig. 34.

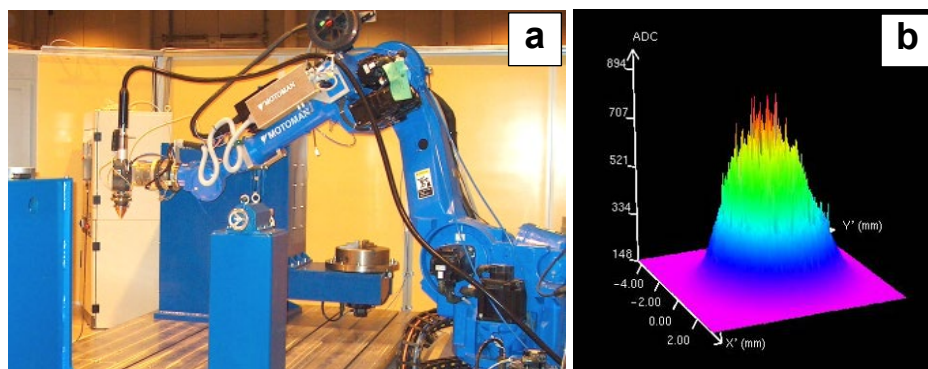


Fig. 34: a) Laser cladding apparatus diode-pumped 4.4 kW Rofin-Sinar Nd: YAG that was used in single bead hot cracking tests. b) Beam intensity profile of the laser.

The test claddings with adjacent beads for the comparison between laser and CMT claddings, were made with a fibre coupled diode laser with a wave length of 980 nm and maximum nominal output of 6 kW. This laser cladding equipment with its coaxial cladding head is presented in Fig. 35.



Fig. 35: Coaxial laser cladding head used to make test samples in comparison studies between laser and CMT.

2.1.2. CMT cladding equipment

The CMT welding equipment consists of a TransPuls Synergic 5000 power-source and wire feeder, wire liner 1, wire buffer, wire liner 2, Robacta Drive pulsing unit that contains the pulsating rolls that move the wire back and forth between the wire buffer and the torch (in the wire liner 2). The welding torch used in the tests was the RA TWIN Compact PRO 30°PA that is designed to be used in welding with two wires (TWIN mode), although all the tests presented in this study were done with one wire. The whole system consists of two separate CMT power source units to enable cladding with two wires in (TWIN mode). The welding power source was controlled with RCU 5000i remote control. The equipment is attached to an ABB IRB 2400L robot that was designed for industrial welding applications. The CMT and robot device with an explanations of the components are shown in Fig. 36.

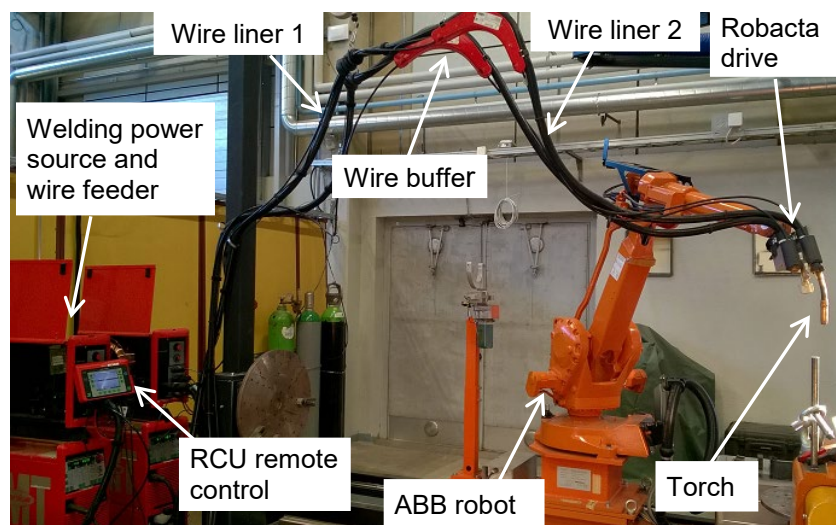


Fig. 36: CMT equipment. Fronius TransPuls Synergic 5000 CMT (2 units) and ABB IRB 2400L welding robot. The whole system consists of two CMT power source units to enable welding with two wires — the TWIN process.

2.2. Materials

2.2.1. Alloy 625 powders

A total of 11 powders from 6 manufacturers were chosen to be tested for the hot cracking susceptibility studies. The powders had some clear variations in composition according to the analyses certificates (Table 11). Some elements (P, S, Mn, Si, Al, Ti) that probably have some effect on hot-cracking, are highlighted in black when the value is high and grey when low. Boron (B) content was not mentioned in any of the certificates.

Table 11: Compositions of alloy 625 powders No. 1 – 11 according to analyses certificates.

Powder	C	N	O	Si	P	S	B	Al	Ti	Mn	Fe	Co	Cu	Mo	Cr	Nb
1	0.01	0.11	0.029	0.42	0.002	0.002	NA	0.16	0.29	0.43	0.77	NA	NA	9.22	22.14	3.57
2	0.02	0.14	0.026	0.43	0.021	0.004	NA	0.18	0.33	0.37	1.23	NA	NA	8.72	21.38	3.33
3	0.01	0.11	0.07	0.50	NA	NA	NA	0.03	0.02	0.40	1.15	NA	NA	9.1	21.6	3.58
4	0.01	0.14	0.23	0.50	0.015	0.002	NA	0.17	0.23	0.44	1.26	NA	NA	8.97	21.96	3.64
5	0.004	NA	NA	0.3	NA	NA	NA	0.01	<0.01	0.04	0.7	0.2	NA	8.2	20.9	3.74
6	0.01	NA	NA	<0.1	NA	NA	NA	0.3	0.3	0.04	0.7	0.2	NA	8.9	20.8	3.88
7	0.014	NA	NA	<0.1	NA	NA	NA	0.01	0.01	0.04	0.7	0.2	NA	8.6	20.4	3.70
8	0.003	NA	NA	0.11	NA	NA	NA	<0.005	0.011	0.04	0.7	0.2	NA	8.4	20.6	3.36
9	0.010	NA	NA	0.34	0.009	0.001	NA	<0.01	0.070	0.38	0.10	0.10	0.03	8.40	21.0	3.65*
10	0.010	0.09	NA	0.45	0.003	0.003	NA	0.00	0.006	0.41	3.6	NA	NA	8.2	21.9	3.48
11	0.02	NA	NA	0.27	NA	NA	NA	0.32	0.25	0.28	2.36	0.12	NA	9.00	21.82	3.85

NA: Not Available, content of this element was not mentioned in analyses certificate

* Ta+Nb

Notes about the analyses certificates and the components that are supposed to have an effect on hot cracking:

- Powder Nos. 1, 2, 4, 6 and 11 contained some amount of Al and Ti as alloying elements, while in powders No. 3, 5, 7, 8, 9 and 10 the Al and Ti content was kept as low as possible.
- Powder Nos. 6 and 7 had no Si as an alloying element and powder No. 8 had only a small amount of Si. All the other powders contained some amount of Si (0.3 to 0.5%).
- Powder Nos. 5 to 8 had very small Mn content while the others had Mn between 0.4 and 0.5%.
- The P and S contents of the powders were not mentioned in all certificates, even though those elements have a very strong effect on cracking. The sulphur contents were low, when mentioned, but powder Nos. 2, 4 and 9 had rather high P contents. Powder No. 2 had phosphor content above the compositional limit for alloy 625.
- B content, which presumably also has a very strong effect on hot cracking, was not mentioned in any of the analyses certificate.
- The content of some other hot cracking related elements: Cu, Zr and Pb were not mentioned in the certificates.
- The contents of O and N, which presumably can have some effect on the quality of cladding even if they don't affect hot cracking, were usually not mentioned in the certificates.

The results of the compositional analyses are presented in Table 28 on page 88 and SEM BE images of powder Nos. 1 – 11 are presented in Fig. 44 on page 90.

The analyses certificate for the composition of powder No. 12, which was used in the comparison tests between laser and CMT, is presented in Table 12. The analyses certificate for this powder No. 12 also stated its boron content.

Table 12: The chemical composition (wt%) of alloy 625 powder No. 12 used in laser vs CMT comparison tests according to analyses certificate.

Powder	C	N	O	Si	P	S	B	Al	Ti	Mn	Fe	Co	Cu	Mo	Cr	Nb
12	0.01	NA	NA	0.38	0.001	0.003	0.00	0.00	0.00	0.34	1.0	0.02	0.02	9.0	21.6	3.31

Composition of powder No 12 was not analysed more accurately in this study. SEM BE images of powder No. 12 are presented in Fig. 45 on page 90.

2.2.2. Composition modification of alloy 625 powders

Some of the alloy 625 powders were modified by adding some B, Al and Ti, to see how the addition of these elements affects the hot cracking sensitivity. Since it was not possible to use pure elements in alloying, compounds were used instead. These compound powders were chosen so that their particle size (50–150 μm) and melting temperature (1400°C) were as close as possible to that of alloy 625 powder. This was supposed to ensure melting and mixing in the melt pool during cladding. Other criteria for selection was that the alloying powder shouldn't contain any other elements that are not also present in alloy 625 (Ni, Cr, Si etc.).

Al and Ti were added as a form of alloy pre-cursor powders Ni50/Al50 and Ni60/Ti40. These powders were provided by Goodfellow – a well known supplier of materials for research and development. Ni-based, self-fluxing alloy NiCrBSi laser/PTA grade powder with a particle size of 50–150 μm was chosen as a source for boron. The compositions of these powders are presented in Table 13 and SEM BE images in Fig. 37.

Table 13: Compositions and melting temperatures of alloying powders (wt%) according to their analyses certificates.

Powder	C%	Si%	B%	Al%	Ti%	Fe%	Cr%	Ni%	Melting temp.
Ni50/Al50	–	–	–	50	–	–	–	50	1350 °C
Ni60/Ti40	–	–	–	–	40	–	–	60	1280 °C
NiCrBSi	0.26	3.65	1.65	–	–	2.55	7.66	bal	1050 °C

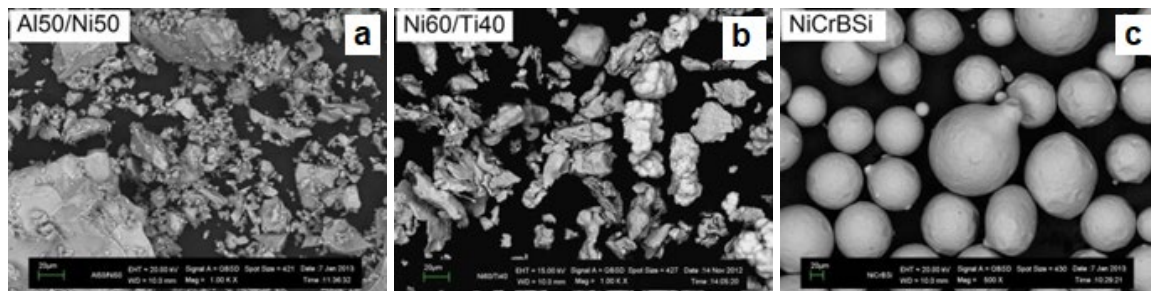


Fig. 37: SEM BE images of alloying powders. a) Al50/Ni50 pre-cursor powder, magnification 1000x, b) Ni60/Ti40 pre-cursor powder, magnification 1000x, c) NiCrBSi laser cladding/PTA powder, magnification 500x.

The amount of each mixing powder was calculated, weighted and mixed with small amount (300 g) of alloy 625 powder.

2.2.3. The alloy 625 wires

Alloy 625 wire with a diameter of 1.2 mm was used in the cladding tests with arc welding methods. The compositions of these wires according to their analyses certificate are presented in Table 14.

Table 14: The chemical composition (wt.%) of the alloy 625 wires used in this study according to analyses certificates.

Wire	C	Si	Mn	P	S	Cr	Mo	Ni	Nb	Cu	Ti	Al	Co	B	N	Fe
1	0.02	0.08	0.02	0.002	0.001	22.4	9.2	64.2	3.47	<0.01	0.18	0.10	0.03	NA	NA	NA
2	0.007	0.053	0.042	0.003	0.0005	22.17	9.16	63.8	3.66	0.03	0.233	0.076	0.018	NA	0.0137	0.49

Both wires originated from the same manufacturer and supplier, but they were from different production batches. The wires were spooled on a small spool with a weight of 5 kg.

2.2.4. Alloy 625 plate

Alloy 625 plate with a thickness of 20 mm was used in the corrosion tests as a reference material. The composition of this plate, according to its analyses certificate, is presented in Table 15.

Table 15: The chemical composition (wt.%) of alloy 625 plate used as a reference material in CPT tests according to the analyses certificate.

C	Si	Mn	P	S	Cr	Mo	Ni	Nb	Cu	Ti	Al	Co	N	Fe
0.006	<0.05	0.03	<0.005	0.0016	21.14	8.24	64.78	3.35	NA	0.050	0.075	0.19	NA	1.78

This plate was also used as a substrate in some preliminary hot cracking tests with laser cladding, to see if the tendency to crack existed if cladding was made on top of alloy 625 (Fig. 46 d, p. 91).

2.2.5. Cladding substrates

Most of the tests were made on top of mild steel plates with a thickness of 20 mm. The size of these substrates in laser cladding single bead tests with 11 powders was 100 x 150 mm. In the CMT tests and the laser cladding comparison tests the plates were 100 x 200 mm. The

grade of the steel plates was non-certified, several different batches were used, and no analyses certificates were available. However, Table 16 presents the composition of one of these steels analysed with the Metorex 930 mobile OES analyser.

Table 16: The chemical composition (wt.%) of mild steel substrates used in this study as analysed with OES method.

C	Si	Mn	P	S	Cr	Mo	Ni	Cu	Ti	Al	Co	N	B
0.22	0.22	0.90	0.0051	0.029	0.58	0.18	0.37	0.23	NA	0.0046	–	NA	NA

Single bead claddings in the comparison laser vs. CMT tests were made on top of Toolox 33 tempering steel to study the hardness of the heat affected zone (HAZ). The composition of this steel according to the analyses certificate and a carbon equivalent (CE_{IIW}) is presented in Table 17.

Table 17: The chemical composition (wt.%) and carbon equivalent (CE_{IIW}) of Toolox 33 substrates used in single bead comparison tests according to the analyses certificate.

C	Si	Mn	P	S	Cr	Mo	Ni	Cu	V	Ti	Al	Co	N	B	CE_{IIW}
0.22	1.08	0.81	0.009	0.001	1.06	0.206	0.05	0.01	0.100	0.013	0.009	NA	0.003	0.002	0.63

All the test surfaces were grit blasted and degreased with acetone prior to the tests.

2.3. Laser cladding tests

The laser cladding tests were mainly done with single beads to examine the hot crack sensitivity of alloy 625 powders. Some test claddings with adjacent beads were also done to compare the laser cladding process and properties to that of cladding with the CMT process (section 2.5, p. 78).

2.3.1. Hot cracking tests with 11 alloy 625 powders

The composition of the 11 powders according to their analyses certificates is presented in Table 11 on page 69. Experiments were made with a diode-pumped Nd:YAG laser (Rofin DY044) and a coaxial powder feeding system (section 2.1.1, p. 67). In order to get varying dilution rates, the laser power was varied in the range 2.5–3.9 kW. These laser power values are based on measurements with a laser power meter, not on the set values. The powder feed rate (PFR) was kept constant ~30 g/min in most cases, but in order to get excessive dilution with maximum laser power of 3.9 kW, PFR was decreased to values around ~20 g/min. The parameters are presented in the following Table 18.

Table 18: Parameters in laser cladding tests with 11 alloy 625 powders and single beads

Travel speed	1000 mm/min
Work and travel angle	Neutral, 0°
Laser spot size	6 mm
Distance of the cone to workpiece	13 mm
Powder feed rate	30 g/min (also ~20 g/min with 3,9 kW)
Shield gas flow rate	10 l/min (100%Ar)
Carrier gas flow rate	2 l/min (100%Ar)
Laser power levels	2.7 kW, 2.9 kW, 3.1 kW, 3.3 kW, 3.5 kW, 3.7 kW and 3.9 kW

The length of the single bead test samples was 70 mm. An example of a test sample is presented Fig. 48 on page 92. Single beads were used because it made examination and quantification of hot cracks simpler and faster. It was also assumed that this method would eliminate the risk of liquation cracking, which could be caused by the heat of the following pass. This meant that it was safe to assume that any cracks that appeared in the samples had been formed during solidification, not during remelting and resolidification caused by the heat from following passes (liquation cracking and/or microfissuring).

All the test samples were made on top of low-alloyed 20 mm steel sheet. A thick substrate doesn't heat up and allows the melt pool to cool rapidly. In addition, the residual tensile stresses that remain in the clad layer do not bend a thick substrate. The composition of the steel is presented in Table 16 on page 72. The substrate surfaces were grit blasted and degreased with a solvent prior to cladding.

2.3.2. Hot cracking tests with modified alloy 625 powders

Based on the findings of the hot cracking sensitivity comparison that was made for a total of 11 commercial alloy 625 powders, two alloy 625 powders were chosen in follow-up tests. These powders and the objectives of the tests were as follows.

- Powder No. 3 appeared to be very crack sensitive. The powder generated cracks with relatively low dilution levels of 15–20%. The powder was free of Al and Ti, but contained a relatively large amount of B (0.006%). Among the 11 tested powders there were some powders that had the same or higher B content, but none of these were as crack sensitive and these powders also contained some Al and Ti. The objective of the tests with powder No. 3 was to see whether the addition of Al and Ti decreases the hot cracking tendency.
- Powder No. 8 that was free of Al and Ti. The Si and Mn contents as well as contents of the impurity element (S, P, B) were also low. It was not possible to detect any B with the methods applied. This powder appeared to be almost immune to hot cracking. The objective of tests with powder No. 8 was to see whether the addition of B increases, and if the addition of Al and Ti to this B-containing powder again decreases the hot crack tendency.

The alloying powders that were used to add B, Al and Ti, are presented in section 2.2.2, (Table 13 and Fig. 37, p. 71). The powder mixtures in these tests are presented below in Table 19 and 20.

Table 19: Levels of Al and Ti additions in hot cracking tests with powder No. 3

Powder mixtures (wt%)	Resulting content (wt%)		Target
	Al%	Ti%	
No. 3	–	–	The effect of Al and Ti on solidification cracking sensitivity, dilution and microstructure
No. 3 + Al50/Ni50 and Ni60/Ti40	0.3	0.3	

Table 20: Levels of B, Al and Ti additions in hot cracking tests with powder No. 8

Powder mixtures (wt%)	Resulting content (wt%)			Target
	B%	Al%	Ti%	
No. 8	–	–	–	The effect of B on solidification cracking sensitivity
No. 8 + 0.25% NiCrBSi	0.004	–	–	
No. 8 + 0.5% NiCrBSi	0.008	–	–	
No. 8 + 1% NiCrBSi	0.016	–	–	
No. 8 + 2% NiCrBSi	0.033	–	–	
No. 8 + 2% NiCrBSi + 0.6% Al50/Ni50 + 0.8% Ni60/Ti40	0.033	0.3	0.3	The effect of B + Al and Ti on solidification cracking sensitivity

The powder mixtures were calculated, weighed and mixed with some amount (300 g) of alloy 625 powder by careful shaking. To vary the dilution rate, the actual laser power on the workpiece was varied between 2.7–3.9 kW. The PFR was around 30 g/min in the tests with powder No. 3 and Al+Ti addition (Table 19), and around 25 g/min in the tests with powder No. 8 and B addition (Table 20). Other parameters and settings were the same as in the hot cracking tests with the 11 powders (Table 18, p. 73).

2.3.3. High speed video imaging during single bead tests

The melt flow and melt pool behaviour during the cladding was captured visually with a high-speed video camera, the Citius Imaging C100 Centurio. The frame rate in the tests was ~1000 frames per second so the time between frames was ~1 ms. During the high speed imaging the melt pool was illuminated with Cavilux® HF light source with a wavelength of 810 nm and output power of 500 W. Test settings are presented in Fig. 38.



Fig. 38: Test settings in high speed video imaging tests.

High speed imaging was performed from the side of the melt pool and the direction of movement was from right to left. The powders in the tests and the objectives of the tests were:

- Powder No. 8 that was free of Al and Ti. Also Si and Mn content as well as impurity element (S, P, B) content was low.
- Powder No. 11 that contained some Al, Ti and Si (0.3%). The powder had very low content of impurity elements (S, P, B).

Tests were made with two laser power levels: low (3.1 kW) and high (3.9 kW) and with a PFR of 25–26 g/min. All other parameters and settings were the same as in the hot cracking tests (Table 18, p. 73).

2.4. Cladding with arc process and wire

Most of the cladding tests with the arc welding process (MIG) were done with the CMT process, but some tests were made also with conventional MIG and pulsed MIG processes to explore some process differences. These were mainly differences in arc power determined by both the conventional $I_{aver} \times U_{aver}$ method and the Average Instantaneous Power (AIP) method. All the tests were done with the same Fronius TransPuls Synergic 5000 CMT welding power source.

2.4.1. Comparison of conventional MIG, pulsed MIG and CMT processes

Tests were made to compare conventional MIG, pulsed MIG and CMT processes. The emphasis was especially on determining the actual arc power during the welding, both with the $I_{aver} \times U_{aver}$ and AIP methods (section 2.1, p. 52). The synergic lines and parameters used in these tests are presented in Table 21.

Table 21: Synergic lines and parameters used in the comparison of conventional MIG, pulsed MIG and CMT processes with single beads.

	Convent. MIG	Pulsed MIG	CMT
Synergic line	S538	P327	C1693
Wire that the synergic line was designed for	CrNi 19 12 3*	NIBAS 625**	NIBAS 625**
Shield gas that the synergic line was designed for	Ar+2.5%CO ₂	100% Ar	100% Ar
Wire feed speed set values	5 – 12 m/min	5 – 12 m/min	5 – 10 m/min
Shield gas	Ar-30%He (AGA Mison He30), 17 l/min		
Gas nozzle distance	12 mm (contact tube: 15 mm)		
Torch angle (travel and work)	0°		
Travel speed	1000 mm/min		
Motion	Stringer, single bead		
Substrate	Mild steel, thickness 20 mm, grit blasted		

* Type 316 austenitic stainless steel

** Alloy 625

Because there was no conventional MIG synergic line available for Ni alloys, line S538 that was designed for welding type 19-12-3 stainless steel (AISI 316) was used instead. The shield gas used in tests, Mison He30, was not the same as the gas that the lines were designed for.

Tests with conventional MIG and pulsed MIG were done up to a WFS of 12 m/min. The highest set WFS with the CMT process was 10 m/min, since the upper limit for WFS in CMT synergic line 1693 is 10.5 m/min and the process starts to get unstable above a feed rate of 8 m/min.

Current and voltage during welding were determined by oscilloscope measurements (section 2.6.6, p. 82) to determine arc power with the AIP method, and to compare voltage/current waveform in CMT process to conventional MIG and pulsed MIG processes. These tests were also used in determining the optimum WFS set value in the CMT process with alloy 625 wire and synergic line 1693 (section 3.2.2, p. 111).

2.4.2. CMT tests with single beads

Single bead tests with the CMT process were made to see the upper limit of TS and whether it is possible to lower the single bead height by increasing the TS. The other important part of this experiment was also to study the effect of auxiliary parameters ALC and DC on the process.

WFS setting of 8 m/min was chosen for these tests, because with this value the CMT process is spatter free, but produces a relatively high deposition rate of 4–5kg/h. Three TS values 1000, 1200 and 1500 mm/min were tested, and tests with a TS of 1000 mm/min were made both with Ar-30%He and 100%Ar shield gas, making a total of four test series. The test parameters are presented in Table 22 below.

Table 22: Parameters in cladding tests with CMT and single beads and varying TS and shield gas.

WFS set value	8 m/min
Synergic line	1693
Shield gas nozzle distance	12 mm
Travel and work and angle	0°
Shield gas flow rate	17 l/min
Travel speed and shield gas combinations	1. TS: 1000 mm/min, Ar-30%He (+ oscilloscope) 2. TS: 1000 mm/min, 100%Ar (+ oscilloscope) 3. TS: 1200 mm/min, Ar-30%He 4. TS: 1500 mm/min, Ar-30%He

The auxiliary parameters ALC and DC were varied with each travel speed and gas combinations (4). The parameter DC was varied with intervals -5.0, 0.0 and +5.0 with each DC value. The parameter ALC was varied with intervals of: -30%, -15%, 0%, +15% and +30%, so that the total number of tests was 60 (4 x 3 x 5). This test array is presented in Table 23.

Table 23: The array of auxiliary parameters ALC and DC in tests with single beads and varying TS and shield gas.

DC	ALC		DC	ALC		DC	ALC
-5.0	-30%		0.0	-30%		+5.0	-30%
	-15%			-15%			-15%
	0%			0%			0%
	+15%			+15%			+15%
	+30%			+30%			+30%

The tests with each DC value were made on the same substrate. The substrates were cooled with compressed air between each bead. In addition, an oscilloscope was used in the tests with TS of 1000 mm/min and both Ar-30%He and 100%Ar shield gas (section 2.6.6, p. 82). The data obtained with the oscilloscope was also used to determine average instantaneous power (AIP, p. 53), process frequency and the ratio between arcing and short circuiting in the process. The criteria for assessing whether the single bead was successful and if it could be used with adjacent beads included: bead outlook, height, width, contact angle, penetration depth and dilution values. Emphasis was also on bead integrity and the variation of bead height and width. The methods for these measurements are presented in section 2.6.4 on page 81.

2.4.3. CMT tests with adjacent beads

According to the experience from single bead tests, some tests were conducted with adjacent beads, mainly to determine the functional track displacement (TD) and travel speed (TS) range. The targets in these tests were to get flawless cladding with stringer motion with low dilution, high productivity (kg/h or m²/h), low heat input to the workpiece and low thickness (<2 mm). A work angle of 10° was used in all tests with CMT and adjacent beads since visual examination of the process indicated that this seemed to help prevent the arc from hitting at the top of the previous bead and/or melt pool accumulating on the previous bead.

Tests were made with three TS levels of 1000, 1200 and 1400 mm/min. The tests were made mainly with Ar-30%He shield gas, but some tests with TS of 1000 mm/min were done with 100%Ar shield gas. The common parameters for all the tests with CMT and adjacent beads are shown in Table 24.

Table 24: Common parameters in CMT cladding tests with adjacent beads

Synergic line	1693
WFS set value	8 m/min
Shield gas nozzle distance	12 mm
Travel angle	0°
Work angle	10°
Number of beads	6

Two combinations of auxiliary parameters ALC and DC were tested with TS 1000 mm/min to see if it is possible to produce sound cladding with a larger TD, when there is more arc power and feedstock material input with an “optimum” combination of auxiliary parameters ALC: +15%, DC: -5.0, compared to a “neutral” combination of ALC: 0%, DC: 0.0. This combination ALC: +15%, DC: -5.0 was found to be optimum in single bead test claddings with Ar-30%He

shield gas, since it produced a low contact angle value and large actual WFS at the same time when penetration depth and dilution values were low (section 3.2.4, p. 120). The parameters with a travel speed of 1000 mm/min are presented in Table 25.

Table 25: Parameters in CMT tests with adjacent beads and TS of 1000 mm/min

Travel speed	1000 mm/min
Shield gases and track displacements	- Ar-30%He: TD: 3.4, 3.6, 3.8, 4.0, 4.2, 4.4, 4.6 and 4.8 mm - 100%Ar: TD: 3.8 mm
Auxiliary parameters combinations	- ALC: 0%, DC: 0.0 - ALC: +15%, DC: -5.0

With Ar-30%He shield gas, TD values of 3.4–4.8 mm were tested, but with 100%Ar shield gas, only one TD value of 3.8 mm was tested since this value seemed to produce relatively smooth, underfill and hole-free cladding in tests with Ar-30%He shield gas even with a “neutral” combinationn of ALC: 0%, DC: 0.0.

Tests with higher TS of 1200 and 1400 mm/min (Table 26) were made with Ar-30% shield gas and an ‘optimum’ combination of auxiliary parameters: ALC: +15%, DC: -5.0.

Table 26: Parameters in CMT tests with adjacent beads and TS of 1200 and 1400 mm/min

Shield gas	Ar-30%He
Travel speeds and track displacements	- TS: 1200 mm/min: 3.5, 3.7 and 4.0 mm - TS: 1400 mm/min: 3.0 mm
Auxiliary parameter combination	ALC: +15%, DC: -5.0

Three TD values 3.5, 3.7 and 4.0 were tested with a TS value of 1200 mm/min, and one TD value of 3.0 mm was tested with TS of 1400 mm/min.

2.5. Laser vs. CMT – comparison

The differences between the laser and CMT cladding processes, as well as the differences in the resulting cladding properties of alloy 625 were tested with both single and adjacent bead cladding tests. The single bead tests were made on top of Toolox 33 temper-hardened steel and the tests with adjacent beads were made on top of mild steel, both with a thickness of 20 mm. The dimensions of the Toolox 33 test piece was 115 x 75 mm and the mild steel test piece was 100 x 200 mm. The compositions of both the steel plates used in the tests are shown in Table 16 and 17 on page 72.

The objectives of the single beads tests on the temper-hardened steel Toolox 33 was to study the effect of the cladding process on: 1) the cladding microstructure and any defects; 2) the hardening of heat affected zone in the base material; and 3) the penetration, dilution and other dimensions that can be measured form the single bead cross section.

The objectives of the adjacent bead tests on mild steel were to study: 1) the energy consumption and heat input to the base material; 2) the cladding microstructure and any defects; and 3) the corrosion properties with CPT measurements. The test cladding area was 150 x 55 mm and the number of cladding passes was chosen so that the width of the cladde

area would be the same. The tests were done twice mainly to ensure the statistical reliability of the measurements of energy consumption and substrate temperature during cladding (section 2.6.7, p. 83). The test parameters for the comparison tests are presented in Table 27.

Table 27: Parameters in laser vs. CMT comparison tests

	Laser cladding	CMT cladding
Substrates	Single bead: Toolox 33, adjacent beads: mild steel	
Laser power set value	4200 W	–
Feedstock set value	40 g/min (PFR)	8 m/min (WFS)
Feedstock material	Powder No. 12	Wire 2
Synergic line	–	1693
Auxiliary parameters	–	ALC: 0%, DC: 0.0
Shield gas	100%Ar	Ar-30%He
Shield gas flow	NA	17 l/min
Travel speed	1500 mm/min	1000 mm/min
Track displacement	1.5 mm	3.8 mm
Overlap ratio	68% (bead width: 4.7 mm)	46% (bead width: 7.1 mm)
Number of passes	34	14
Travel angle	0°	0°
Work angle	30°	10° ⁽¹⁾
Shield gas nozzle distance	NA	15 mm
Nom. deposition rate ⁽²⁾	2.4 kg/h	4.4 kg/h
Coverage rate ⁽³⁾	0.14 m ² /h	0.23 m ² /h

1) In the single bead test the work angle was 0°

2) Laser: PFR x 60 min, CMT: calculated based on WFS set value and a density of 8.4 g/cm³

3) Travel speed x track displacement

NA: Not available

The laser cladding tests were done with 6 kW fibre coupled diode laser (Fig. 35, p. 68) and the cladding parameters represent the actual parameters used in production. However, it should be noted that the CMT cladding parameters had not been proved to produce consistent quality in production as they had only been proved to produce low-dilution claddings on a rather small test samples. So it is possible that some defects, for example underfill or inter-run fusion could exist in some circumstances with these parameters.

2.6. Measurements and examinations

The methods for examining the results of the test cladding and the test cladding properties are presented in below.

2.6.1. Analysis of the alloy 625 powders

Powder Nos. 1–11 were analysed to get the precise content of all elements. The methods used for the compositional analyses of the powders were: the infrared absorption method after combustion in an induction furnace according to ISO 15350 for C and S; the infrared absorption method according to EN 10276-2 for O and N; and, inductively coupled plasma

atomic emission spectroscopy (ICP-OES) according to ISO 13898-1-4 for the rest of the elements (Al, Ti, Cr, Ni, Mo, Nb, etc.).

2.6.2. Hot crack measurement

In order to determine the amount of hot cracks in the single bead laser claddings, the test claddings were ground and polished close to the original substrate surface level (~0.1 mm). Cracks could then be seen with a low magnification optical microscope (Fig. 39). The total length of all the cracks on the bead was measured. It was assumed that this method would reveal most, if not all, of the cracks in the bead.

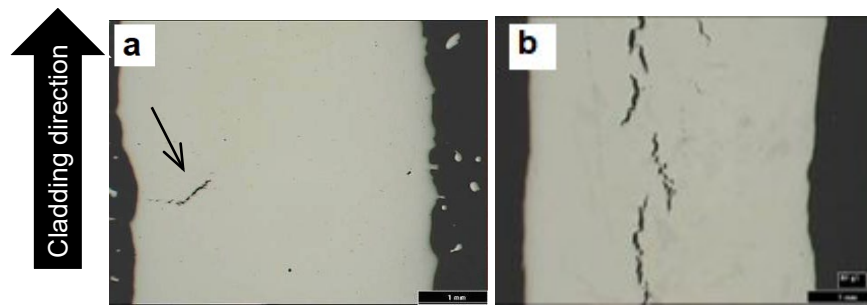


Fig. 39: Ground and polished surfaces of the single bead laser test claddings. Magnification 7x. The width of the bead: ~4 mm. a) some small cracks (arrow), b) continuous line of cracks at the bead centreline.

This kind of self-restraint or representative method is simple and is assumed to give a more realistic assessment of hot cracking susceptibility than simulative methods like the Varestreint tests, because this test represents the actual configuration and restraint level in cladding.

2.6.3. Metallography and microscopy

In order to examine the macro and microstructure of the test samples, cross sections, or microsections were prepared perpendicularly to the cladding direction, from the middle of the total length of the test piece.

The cross section surfaces were etched with:

1. Nital (ethanol + 2% HNO_3) to etch the base metal (mild steel) and to examine the penetration depth and dilution of the single bead test claddings (following section 2.6.4) and to detect any defects in the adjacent bead claddings (base material etched condition).
2. A fresh mixture of 5 ml HCL, 5ml HNO_3 and 5 ml CH_3COOH to etch alloy 625 cladding in order examine the alloy 625 phase and micro-structure. The base material was protected with adhesive tape during these etchings (alloy 625 etched condition).

The cross sections were examined to detect defects in the structure like hot cracks, lack of fusion, porosity and inclusions, and also to examine the solidification structure, the phases present and to measure the average primary dendrite arm spacing. The surfaces of the cross sections of the test claddings were examined with an optical (metallography) microscope, Olympus CK40M, an optical (stereo) microscope, Euromex and a scanning electron microscope (SEM), the Zeiss EVO 50VP equipped with a Röntec XFlash EDS analyser.

In addition to the test claddings done with laser and CMT cladding methods, some microstructure examinations were done for alloy 625 cladding samples made with Plasma Transferred Arc (PTA) method. The aim of these tests was to compare how the microstructure of PTA cladding with its high dilution level and slow solidification differs from the less-diluted and rapidly-solidified laser and CMT claddings. The results of these tests are presented in Fig. 127 on page 151.

2.6.4. Single bead dimension

The geometrical dilution, penetration depth and HAZ depth of single beads of both laser and CMT claddings were measured with the same method from Nital etched (base material etched) cross sections as presented in Fig. 40 below.

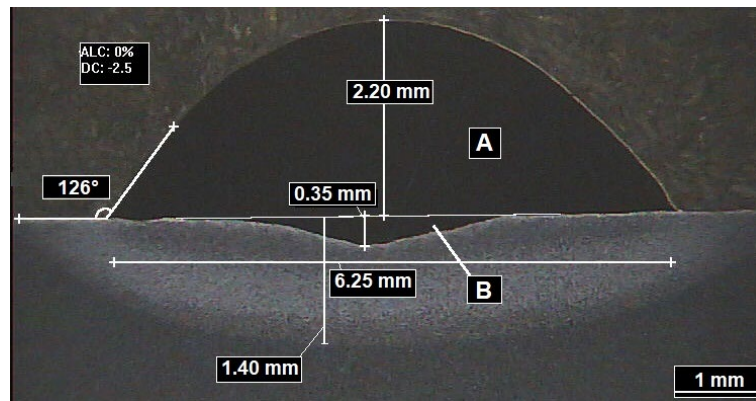


Fig. 40: CMT single bead cross section. Dimensions. Contact (toe) angle: 126°, penetration depth: 0.35 mm, HAZ depth: 1.40 mm, bead height: 2.2 mm, bead width: 6.25 mm, height/width: 0.35, A: 9.6 mm² (bead area), B: 0.53 mm² (melted base metal area), dilution: 5%.

Geometrical dilution was determined from the cross section with the equation:

$$Dilution \% = \frac{B}{A+B} \times 100 \% \quad (9)$$

where B is the melted base material area below the original substrate surface and A is the bead area above the original substrate surface.

The bead thickness and the width of the single bead CMT test claddings were measured from the bead's outer surface, not from the cross section, since there was a large variation in both the width and height of the beads and one cross section only represents the dimensions in that one single location. The same applies for penetration and dilution, which were measured from the cross section, but it was assumed that there was less variation in these parameters especially in penetration. The thickness of a CMT single bead was determined with around 20 measurements along the length of the single bead. These measurements were done with a calliper with a digital display. The width of the CMT single bead was determined with 20–30 measurements from a low magnification optical (stereo) microscope image. These measurements were taken on three images along the bead, with each image covering around 20 mm of the bead length. The emphasis in both the height and width measurements was particularly on finding the largest and smallest values. This may have affected the statistics in determining the average value. However, the average value of both height and width was

determined based on these measurements and the ratio between height and width (H/W) was then calculated from these average values. The results of the height and width measurements presented in this study are rounded up with a resolution of 0.05 mm.

2.6.5. Hardness measurements

The hardness measurements were performed on the cladding cross sections with a Buehler 1900-2104 Vickers hardness measurement device. Measuring weights of both 5 kg and 1 kg were used. The measurements were done on the microsection surfaces where the base material was etched with Nital.

2.6.6. Current and voltage measurements in arc welding tests

High-speed variations in welding can not be measured or examined with an ordinary clamp-on current meter and voltmeter. Instead, the current and voltage during the welding process with high were measured using an oscilloscope. The measurement points were stored, and subsequent analysis of the stored data proved to be very useful tool for understanding the welding process. An oscilloscope graph, showing voltage and current measured with high frequency, reveals many variations and disturbances in the welding process. In a waveform controlled process, like CMT, the oscilloscope graph shows the current and voltage waveforms and the regularity of the process particularly well. One further essential feature in current and voltage measurements with an oscilloscope is that the average instantaneous power (AIP) can be determined based on the high-frequency current and voltage measurements (eq. 5, p. 53).

The welding current and voltage during the arc welding processes (conventional MIG, pulsed MIG and CMT) with the single beads was monitored with a PicoScope 3424 oscilloscope (Fig. 41 a). The welding current for the oscilloscope was measured with a Pico TA167 current clamp which gave the output signal to the oscilloscope. The current clamp was connected to the negative cable of the welding power source (Fig. 41 c). The voltage was measured between the contact tip and the cladding substrate. A copper wire (plus) was soldered to a hole that was bored into the contact tip and a second wire (minus) was connected to a hole bored into the substrate. These wires were connected directly to the oscilloscope.

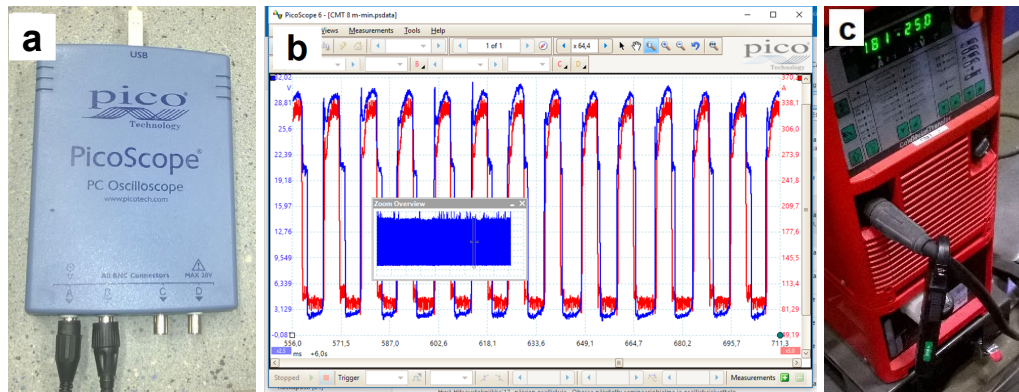


Fig. 41: Instruments for the current and voltage measurements. a) PicoScope oscilloscope, b) print screen image from PicoScope software with a period of 150 ms, c) Pico TA167 clamp meter on grounding cable output of welding power source.

The sampling rate for the measurements was 50 kS/s (50 000 Hz) and the measurement points from the oscilloscope were transferred and processed in an Excel worksheet. These voltage and current values were used to determine:

1. Arc power by the AIP method that was determined from between 4 to 8 seconds of the total welding time of around of 9 to 10 seconds. This period of 4 seconds contained a total 200 000 data samples. Determination of the AIP is presented in equation 5 on page 53.
2. Ratio between arcing and short circuiting was determined from the voltage data from the oscilloscope so that voltage values below 5 V were defined to as representing short-circuiting and values over 5 V were defined as representing arcing.
3. Process frequency determined with the PicoScope 6 oscilloscope software from the current graph of the total weld duration of around of 9 to 10 seconds.
4. The effect of parameters ALC and DC on the process and process stability was examined from the the shape of voltage and current graphs.
5. Power ratio, based on AIP results, according to equation 7 on page 53.

Average voltage, current and actual WFS values during the process were recorded by the Fronius Xplorer software that was connected to the CMT power source. This software does not control the welding process itself, but records the data during welding, like voltage, current and actual WFS values at minimum intervals of 0.1 s.

2.6.7. Cladding substrate temperature

In order to compare the heat input to the substrate with laser and CMT cladding, the substrate temperature was measured in the laser vs. CMT cladding tests. The measurement was made with one K-type sensor below the last cladding bead. A Fluke T3000 was used to record the temperature at intervals of 1 s. The temperature sensor was inserted in a hole that was drilled horizontally into the steel substrate at a depth of 3 mm below the surface, so that the end of the probe hits the HAZ of the last cladding pass, as shown in Fig. 42.

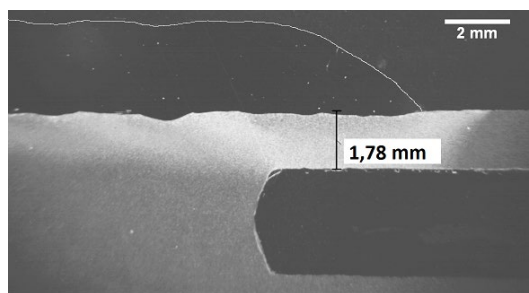


Fig. 42: Cross section from the location of the temperature sensor below the last pass of CMT cladding test sample.

This location, below the laser cladding pass, is supposed to be the hottest, since the heat accumulates here toward the end of the process. However, some error in temperature measurements may have occurred due to the fact there was some inaccuracy in the positioning of this hole.

2.6.8. Measurements of corrosion properties

Corrosion resistance as the critical pitting corrosion temperature (CPT) of samples was measured by a modified ASMT G150 method. In the standard method, the sample surface is exposed to sodium chloride (NaCl) solution with a concentration of 1M. The sample surface is set to a potential of 700 mV and the test temperature is increased at a rate of 1 °C/min. The current through the sample surface is measured, and when there is a sudden rise in the current, this indicates the occurrence of pitting corrosion and the test temperature at this stage is called the pitting potential temperature. With the standard method using 1M NaCl solution, it was found that the critical pitting temperature of alloy 625 is around or above the boiling temperature of water (100 °C), or the potential applied (700 mV vs. SCE) was too close to the transpassive potential of alloy 625. So, using the standard method with high quality claddings would not record any sudden rise in the current before the test solution reached a temperature of 95 °C, so pitting corrosion would not occur and it would not be possible to determine the CP temperature.

Therefore, in the tests of this study, 3M sodium bromide (NaBr) solution was used instead of 1M NaCl. The solubility of NaBr in water is much higher than NaCl, so it is possible to use a much more concentrated solution. Both the higher concentration and corrosivity of NaBr lowers the CPT. According to a study by Johansson et al. at Avesta Research Centre [202], an average CPT of 52.2 °C was obtained with this method for alloy 625 plate with a thickness of 3 mm.

In the standard ASTM G150 test, crevice corrosion is prevented by feeding distilled water through the filter paper so that it acts as a sealing surface, as presented in Fig. 43 a. This arrangement ensures that the NaBr (or NaCl) concentration between the seal, filter paper, and sample surface is very low compared to the concentration in the actual solution in the cell, and pitting corrosion occurs before crevice corrosion.

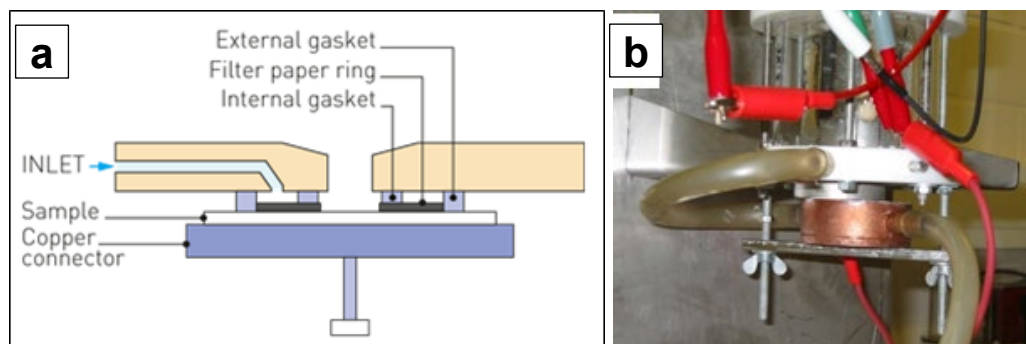


Fig. 43: Avesta CPT corrosion test cell. a) Schematic presentation of flushing on the test surface in the Avesta test cell. b) Image of the test cell with copper heating element under the sample.

CPT tests were made for three samples:

- 1. Alloy 625 plate, thickness 20 mm
- 2. Laser cladding with blown powder and adjacent beads
- 3. CMT cladding with wire and adjacent beads

The composition of the alloy the 625 plate is presented in Table 15 on page 71. The laser and CMT cladding parameters are presented in Table 27 on page 79, and the test claddings are presented in section 3.3.2 on page 140.

The samples in the corrosion tests were cut to a size of 50 x 50 mm with a thickness of 10 mm. They were heated from below during the test with a copper heating element as shown in Fig. 43 b. The heating water went through this copper element, but it was electrically insulated from the sample. The test surfaces were ground flat and the final grinding was done with P800 SiC grinding paper. After the CPT test, the test surfaces were examined visually and with optical microscopy to detect the presence of pitting corrosion. The the SEM EDS method was also used to analyse the composition of the surface, especially the iron content in the surface layer.

3. Results

The results are divided into three main parts:

1. The results of the laser cladding studies. The emphasis in this part is on the single bead tests and hot cracking (section 3.1, p. 87).
2. The results of the CMT cladding studies (section 3.2, p. 106). The emphasis in this part is on the CMT cladding parameters and properties. These tests are done with both single and adjacent beads.
3. The results of the comparison studies of the laser and CMT cladding processes, and the properties of the resulting cladding (section 3.3, p. 136).

3.1. The results of the laser cladding studies

Laser cladding studies started with preliminary tests with adjacent beads during which it turned out that one batch of alloy 625 powder was particularly sensitive to hot cracking. In order to get reliable quantitative results of hot crack sensitivity, the single bead method was chosen for the follow-up tests with 11 powders. Dilution was varied by varying the laser power. The laser cladding tests results are divided into the following sections:

1. Powder appearance and composition of the total of 12 alloy 625 powders used in the cladding tests.
2. Preliminary tests with one powder batch (No. 3) and adjacent beads.
3. Single bead tests with 11 alloy 625 powders: hot cracking and dilution.
4. Single bead tests with two alloy 625 powders with modified composition: hot cracking and dilution.
5. Single bead tests with two alloy 625 powders: melt pool behaviour.

In addition, laser cladding tests with powder No. 12 were done both with single and adjacent beads to compare the laser cladding process and properties to those of CMT cladding.

3.1.1. Laser – composition and appearance of the alloy 625 powders

A total of 11 powders were chosen to be tested with single bead laser cladding tests. The compositions of these powders according to their analyses certificates are presented in Table 11 on page 69. In order to determine the precise composition, these 11 powders were analysed with methods that are presented in section 2.6.1 on page 79. The results are presented in Table 28. The results of the hot crack measurements (Fig. 49, p. 93) are presented in the extreme right column of this table with a four-level evaluation. The elements that are supposed to be related to hot cracking (P, S, B etc.) are highlighted in grey when the content is low and black when the content is relatively high.

Table 28: Analysed compositions of powders No. 1 – 11 and hot cracking results.

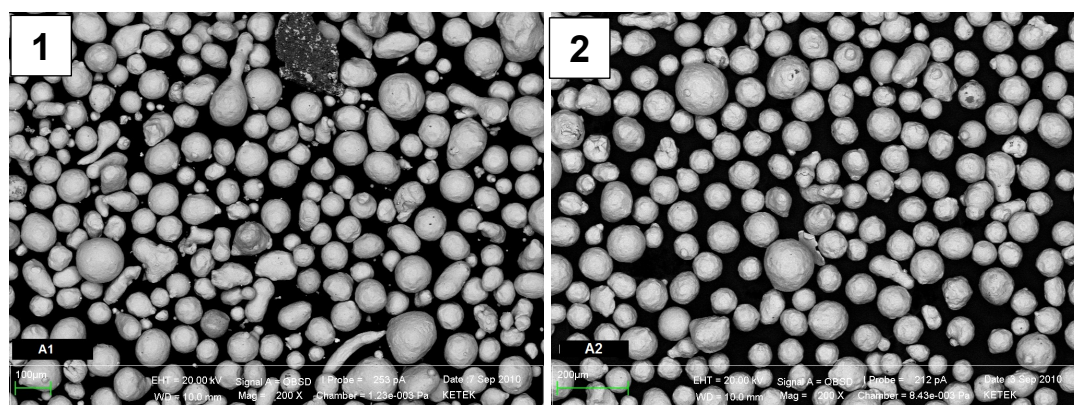
Powder	C%	P%	S%	Si%	B%	Al%	Ti%	Mn%	Mo%	Fe%	Cr%	Cu%	O%	N%	Nb%	Cracks
1	0.016	0.0009	0.0034	0.43	0.012	0.15	0.25	0.41	8.65	0.97	21.50	0.005	0.042	0.115	3.57	2
2	0.019	0.02	0.004	0.412	0.02	0.188	0.323	0.35	8.50	1.65	20.10	0.02	0.025	0.151	3.21	2
3	0.014	0.006	0.0027	0.47	0.006	0.02	0.02	0.38	9.02	1.14	21.02	0.002	0.066	0.108	3.37	3
4	0.02	0.003	0.0037	0.47	0.006	0.12	0.17	0.41	8.60	1.37	21.19	0.01	0.027	0.13	3.46	2
5	0.006	–	0.002	0.121	–	0.007	0.004	0.034	8.50	1.12	19.70	0.01	0.015	0.09	3.52	0
6	0.0108	0.001	0.0021	0.075	0.001	0.3	0.35	0.04	8.54	0.74	21.24	0.001	0.0095	0.0129	3.97	1
7	0.018	0.001	0.0024	0.08	0.001	0.008	0.01	0.04	8.45	0.74	20.94	0.001	0.03	0.029	3.66	1
8	0.005	–	0.005	0.112	–	0.001	0.02	0.033	8.44	1.08	19.90	0.01	0.063	0.153	3.41	0
9	0.013	0.001	0.0014	0.31	0.001	0.009	0.08	0.37	9.10	0.47	21.35	0.004	0.034	0.03	3.60	2
10	0.013	–	0.004	0.47	–	0.001	0.006	0.415	8.0	4.11	20.7	0.03	0.013	0.105	3.41	2
11	0.018	–	0.002	0.268	–	0.272	0.28	0.22	9.11	3.07	21.4	0.01	0.008	0.106	4.04	2

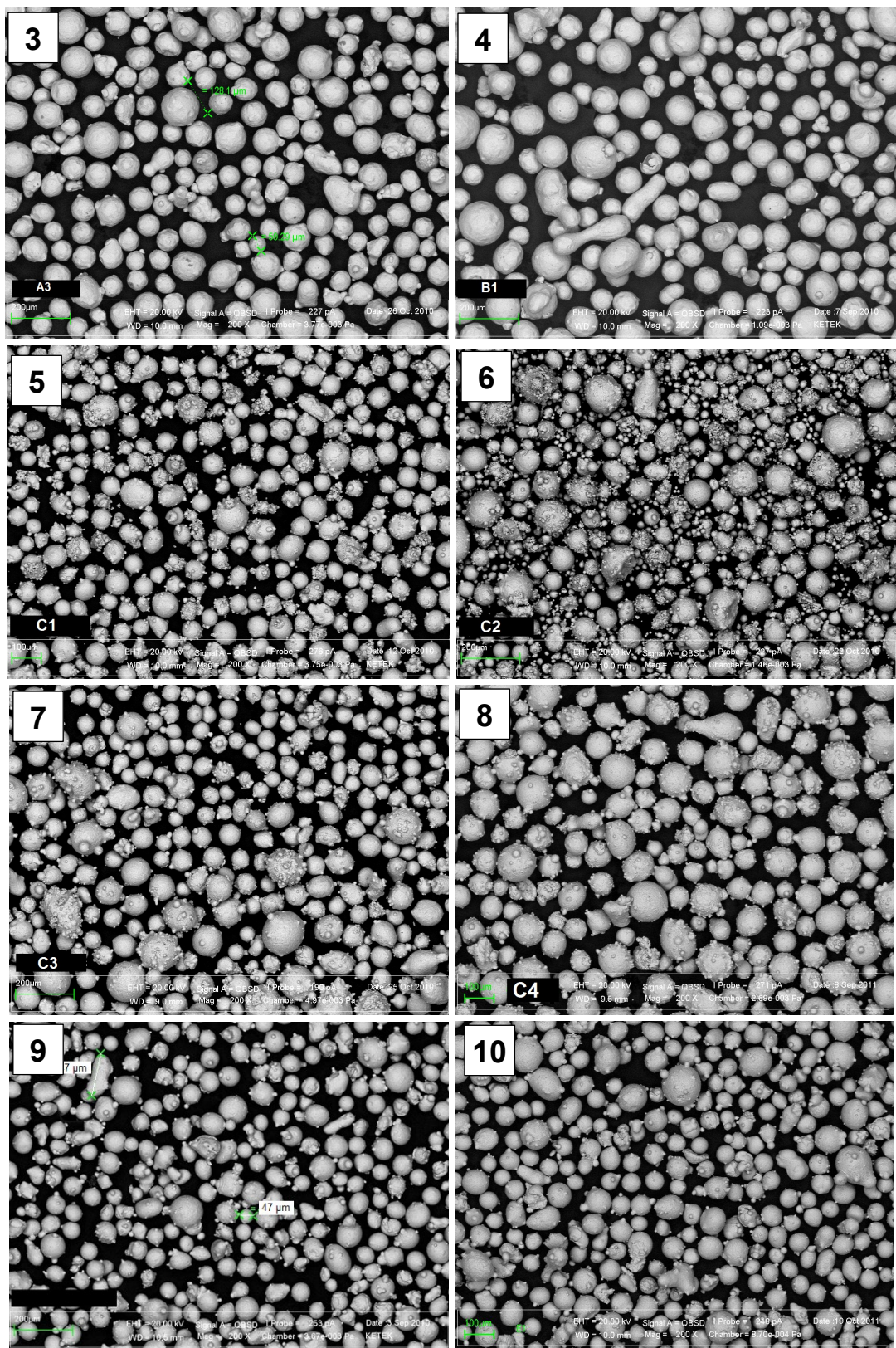
Composition	Evaluation of cracks
Relatively low content	0 = No cracks
Relatively high content	1 = Some cracks with very high dilution > 50%
	2 = Cracks with high dilution ~20 – 40%
	3 = Cracks with relatively low dilution ~20%

The analysed compositions in Table 28 show that the impurity (C, S, P, B) content of all the powders was quite low. However, some differences did exist with P and B, but there were no notable differences in the C and/or S contents. Powders 2, 3 and 4 did have slightly more P than the other powders, but the percentage was still low. Powders 1, 2, 3 and 4 also had more B (0.006–0.02%) than the other powders (< 0.001%). The other powders either had a very low B content or no B was detected. Powders 1, 2, 3, 4, 9, 10 and 11 had some Si (~0.3–0.5%) while in powders 5, 6, 7 and 8, the Si content was low (<0.01%). It was the same for the Mn content.

There was some variation in the Nb content of the powders (3.2–4%), but this variation can be regarded as slight so no further attempts were made to see Nb's effect on hot cracking.

SEM BE images of powders used in hot cracking tests (No. 1–11) are presented in Fig. 44 and the powder used in the laser vs. CMT comparison tests (No. 12) in Fig. 45.





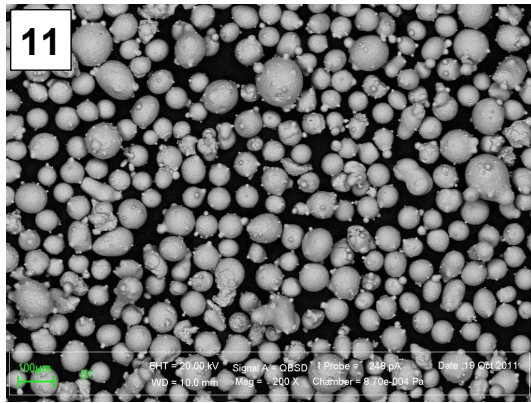


Fig. 44: SEM BE images of powder Nos 1 – 11 that were used in hot cracking tests. All with a same magnification of 40x.

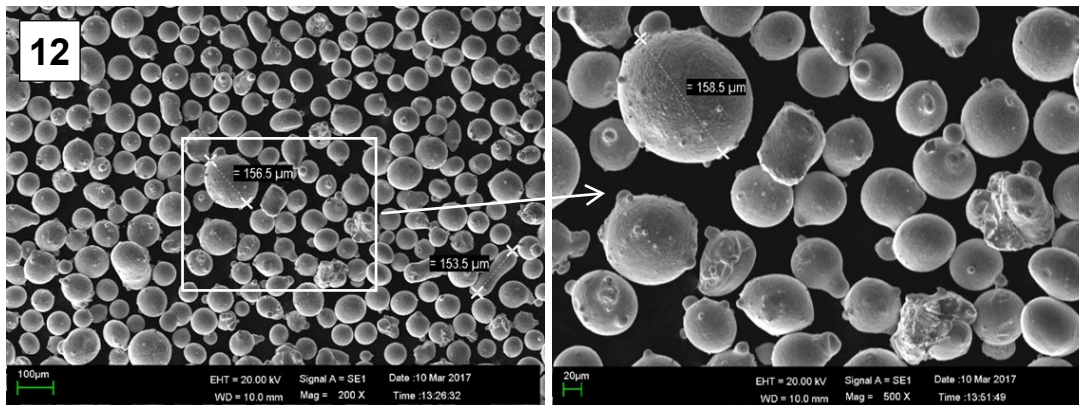


Fig. 45: SEM BE images of powder No. 12 that was used in the laser cladding vs. CMT comparison tests. Magnifications: left 40x, right: 100x.

The most notable feature of the powders' appearance as presented in the SEM images is that powder No. 6 (Fig. 44, 6) had a higher proportion of small $<10\ \mu\text{m}$ particles. The presence of so many small particles apparently caused porosity in the test claddings, as will be discussed later. Quite a few of the powders also contained some satellites, i.e., smaller particles that had already adhered to larger ones during the atomization process.

3.1.2. Laser – preliminary hot cracking test results

According to experience of several years in laser cladding with alloy 625, it was found that hot cracking sensibility seems to vary strongly between powder batches. Further evidence of this came up when a new batch of powder (No. 3) was tested with adjacent beads on top of 20 mm thick mild steel plate. The cladding tests with this batch resulted in very poor quality whose defects could be seen with the naked eye from the machined surface. This powder batch, (No. 3), which was supposed to be top quality, with limited (less than 0.1%) content of Al and Ti was chosen for further tests. These tests were performed on different base materials such as mild steel, 42CrMo4 quenched and tempered steel bar and alloy 625 plate. Alloy 625 plate with a thickness of 20 mm was chosen as a one of the test substrate materials to see if the reason for cracking is changes in the composition of the weld caused by diluted elements from the steel substrate.

The laser power in the tests was varied in order to get varying dilution rates. The PFR was kept constant at 30 g/min. Some cross section images of these test claddings are presented

in Fig. 46. These cross sections were etched with Nital, except for the test cladding on top of alloy 625 plate (d), which was etched with Kallings No. 1 reagent.

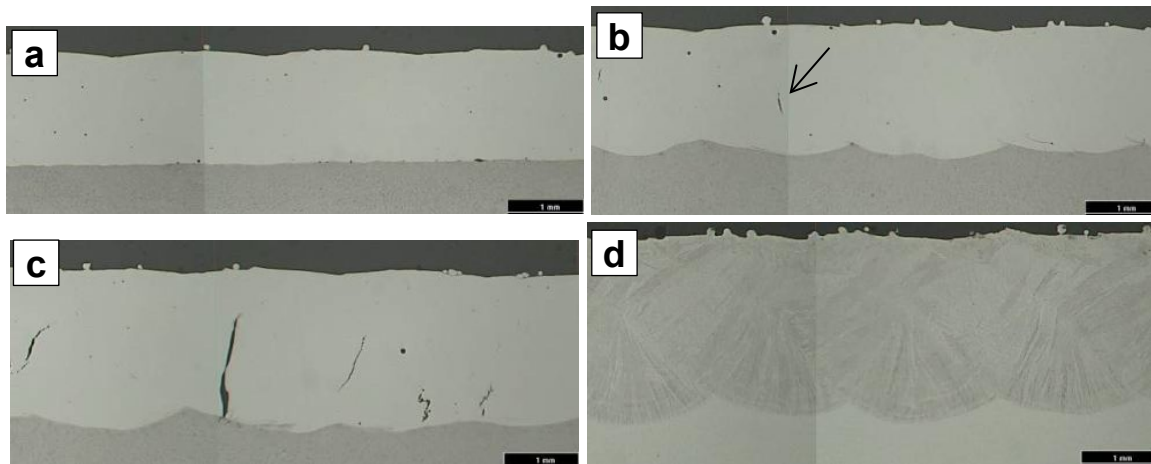


Fig. 46: Laser cladding tests with adjacent beads and powder No. 3.

- a) On top of mild steel. Laser power 2.5 kW. Very low dilution, no cracks.
- b) On top of mild steel. Laser power 3.0 kW. Moderate dilution. Fe content on the surface of the cladding: 7.2%. Some cracks (arrow) starts to appear.
- c) On top of mild steel. Laser power 3.5 kW. High dilution. Severe cracking.
- d) On top of alloy 625 plate. Laser power 3.5 kW. High dilution. No signs of cracks.

The tests showed that this powder batch (No. 3) already produced cracks with a relatively low level of dilution. The measured Fe content on the cladding surface was only 7.2% in the test cladding where cracking started to appear (Fig. 46 b).

One laser cladding sample from powder No. 3 containing hot cracks was fractured to reveal the fracture surface. SEM images from this fractured surface are presented in Fig. 47.

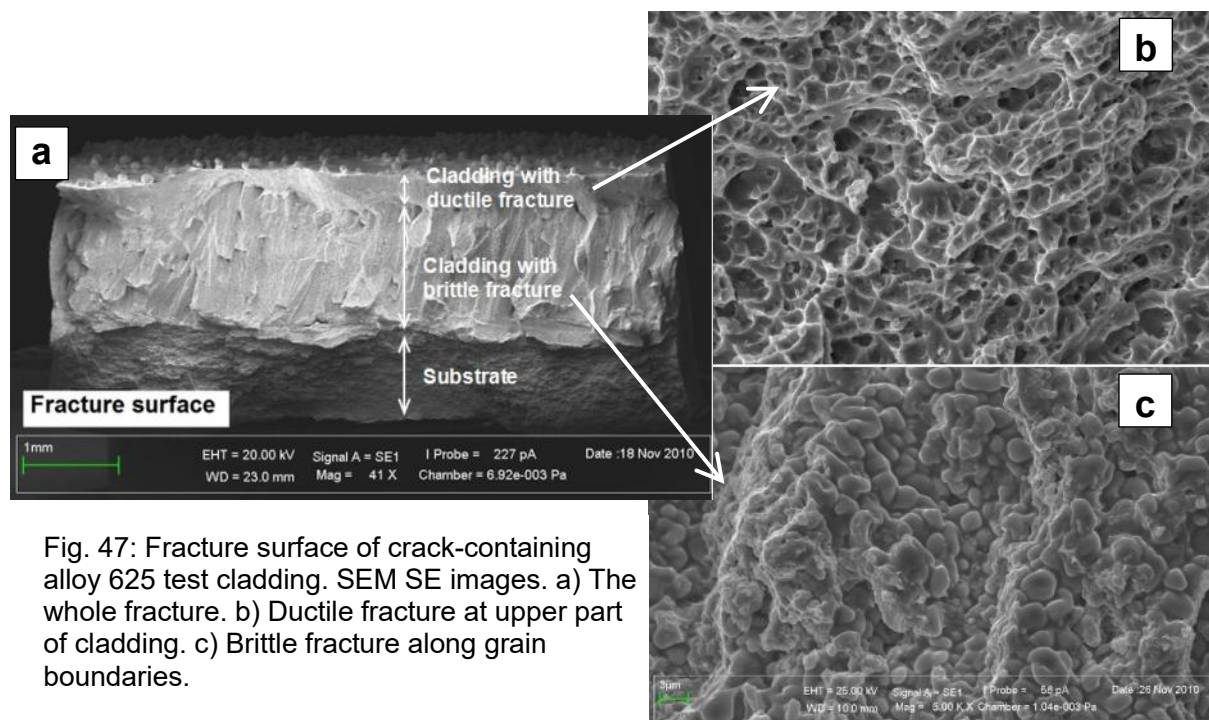


Fig. 47: Fracture surface of crack-containing alloy 625 test cladding. SEM SE images. a) The whole fracture. b) Ductile fracture at upper part of cladding. c) Brittle fracture along grain boundaries.

The fracture surface (Fig. 47 a) reveals that most of the cracking at the fracture surface has occurred between grain boundaries (Fig. 47 c). There was clearly evidence that a liquid film was present when the fracture (hot crack) had occurred. No plastic deformation could be seen

in the grain surfaces, in contrast with the ductile fracture with dimples in the grains (Fig. 47 b). However, it turned out to be difficult or impossible to detect any possible impurity elements (P, S, B) from the fracture surface with EDS because the last-to-solidify layer where the impurities would have remained is very thin, only a few nanometres. EDS is not sensitive enough to analyse such a thin layer, because the electron beam penetrates relatively deep into the material, up to a depth of one micron, and X-rays are generated in this whole penetration depth. The overlapping of the X-ray peaks also hinders the detection of both S and P. The peak of S overlaps with a peak of Nb and ditto for P and Mo. It was not possible to detect B with the used instrument (Röntec Quantax) either because the B content is very low and the spectrum peak of B has such low energy (0.183 keV) that it does not pass through the window of the detector and/or the B content was simply below the detectable limit. In addition, overlapping X-ray peaks of Nb and Mo would also hinder the detection of B.

3.1.3. Laser – Hot crack results with 11 alloy 625 powders

The solidification cracking sensitivity of the 11 powders was tested with single bead test claddings. The laser cladding test settings are presented in section 2.3.1 on page 72. One photograph of a test sample with 7 single bead laser cladding tracks is presented in Fig. 48.



Fig. 48: Single bead tests with powder No. 3. Laser power increases from 2.7 kW to 3.9 kW looking from left to right.

Cross sections were prepared from the middle of the test cladding and dilution and penetration values were measured (section 2.6.4, Fig. 40, eq. 9, p. 81). The hot cracks were measured after the test cladding beads had been ground down close to the original substrate surface (section 2.6.2, Fig. 39, p. 80).

The results of the hot crack length versus geometrical dilution values are plotted on a graph shown in Fig. 49. The values for the crack lengths are presented on a logarithmic scale where value 1 means no cracks and value 1000 ($\mu\text{m}/\text{mm}$) means a continuous line of cracks along the weld centreline. Some of the threshold values for dilution where cracks start to appear are also presented in Table 29.

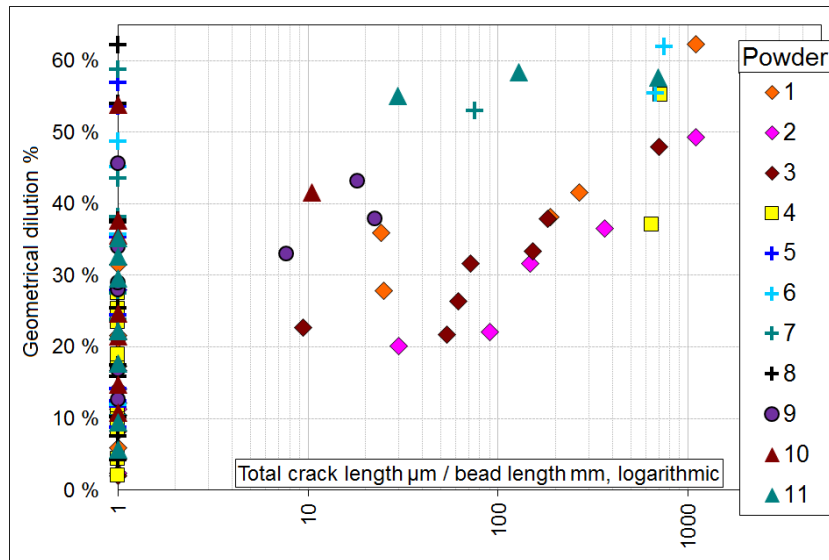


Fig. 49: Relation between dilution and measured crack length in the tests with laser single beads and 11 alloy 625 powders.

Table 29: Threshold dilution values for cracks to appear.

Powder	Highest dilution rate without cracks	Lowest dilution rate for cracks to appear
1	22%	28%
2	17%	20%
3	10%	22%
4	27%	37%
5	57%	—
6	49%	56%
7	44%	53%
8	62%	—
9	29%	33%
10	28%	42%
11	35%	55%

As can be seen from Fig. 49 and the Table 29, powder Nos. 1, 2, and 3 generated cracks with far lower dilution values than the other powders. Powder Nos. 5 and 8 did not show any cracks at any dilution level and powders 6 and 7 showed some cracks with high dilution rates (45 – 55%).

Some of the hot cracking results in Fig. 49 were gained by decreasing the PFR from the normal 30 g/min to as low as 15–20 g/min. Therefore, Fig. 50 shows some of the same hot crack length results as in Fig. 49, but all of these results were made with a PFR of 30 g/min, and the vertical axis shows laser power, not dilution. The no-crack test results have also been erased from this graph.

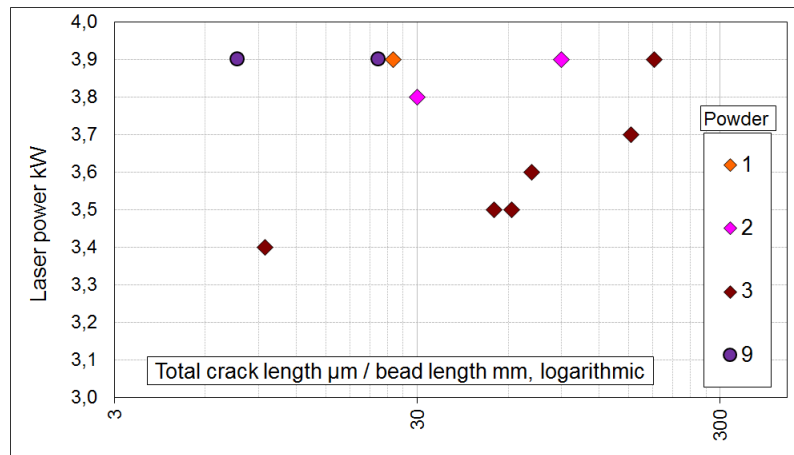


Fig. 50: Relation between laser power and crack length between 11 alloy 625 powders with PFR of 30 g/min.

As can be seen from the hot crack length measurement results in Fig. 50, powders Nos. 1, 2, 3, and 9 generated cracks with a PFR of 30 g/min and powder No. 3 generated cracks with lower laser power than the other powders.

The hot crack tests with 11 alloy 625 powders showed that there was considerable variation in both measured geometrical dilution and penetration depth values. When all the results of geometrical dilution values vs. laser power were plotted on the same graph (Fig. 51 a) it is apparent that those powders that were free of Al and Ti showed substantially higher average dilution values than those powders that contained some Al and Ti (0.25–0.5%).

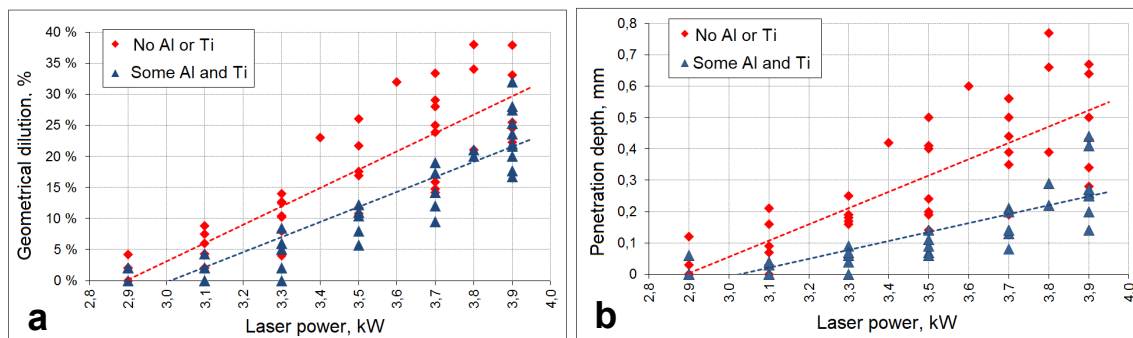


Fig. 51: The results of laser cladding single bead tests with 11 powders. a) Geometrical dilution vs. laser power. b) Penetration depth vs. laser power.

This difference between the average dilutions of Al-and-Ti-free powders and Al-and-Ti-containing powders was around 5–8% percentage units. When laser power is plotted against penetration depth values, as shown in Fig. 51 b, this difference is even larger, around 0.1–0.2 mm, and increases in line with the laser power. The dilution and penetration depth values from Fig. 51 are also in Table 30 below. Powder Nos. 3, 5, 7, 8, 9 and 10, which were free of Al and Ti, are highlighted in the table.

Table 30: Dilution (%) and penetration depth (mm) values of test claddings with laser power levels 3.1–3.9 kW.

Powder	Laser power, kW				
	3.1	3.3	3.5	3.7	3.9
1, Some Al and Ti	2%, 0.03 mm	6% 0.09 ,mm	12%, 0.14 mm	17%, 0.21 mm	22%, 0.20 mm
2, Some Al and Ti	0%, 0 mm	2%, 0.04 mm	11%, 0.07 mm	14%, 0.13 mm	17%, 0.14 mm
3, No Al or Ti	4%, 0.09 mm	10%, 0.19 mm	22%, 0.40 mm	33%, 0.56 mm	38%, 0.67 mm
4, Some Al and Ti	4%, 0.04 mm	8%, 0.07 mm	10%, 0.11 mm	19%, 0.20 mm	25%, 0.25 mm
5, No Al or Ti	9%, 0.16 mm	13%, 0.16 mm	12%, 0.20 mm	14%, 0.20 mm	24%, 0.34 mm
6, Some Al and Ti	2%, 0.03 mm	5%, 0.06 mm	8%, 0.09 mm	12%, 0.14 mm	24%, 0.27 mm
7, No Al or Ti	2%, 0 mm	4%, 0.05 mm	10%, 0.19 mm	24%, 0.44mm	27%, 0.43 mm
8, No Al or Ti	8%, 0.21 mm	10%, 0.25 mm	18%, 0.41 mm	16%, 0.39 mm	25%, 0.5 mm
9, No Al or Ti	6%, 0.07 mm	13%, 0.17 mm	17%, 0.24 mm	28%, 0.5 mm	33%, 0.64 mm
10, No Al or Ti	2%, 0.03 mm	14%, 0.19 mm	11%, 0.14 mm	15%, 0.19 mm	22%, 0.28 mm
11, Some Al and Ti	0%, 0 mm	0%, 0 mm	6%, 0.05 mm	9%, 0.09 mm	18%, 0.26 mm

This difference in dilution and penetration can be seen in the cross in section images presented in Fig. 52 with power levels of 3.1 kW, 3.5 kW and 3.9 kW.

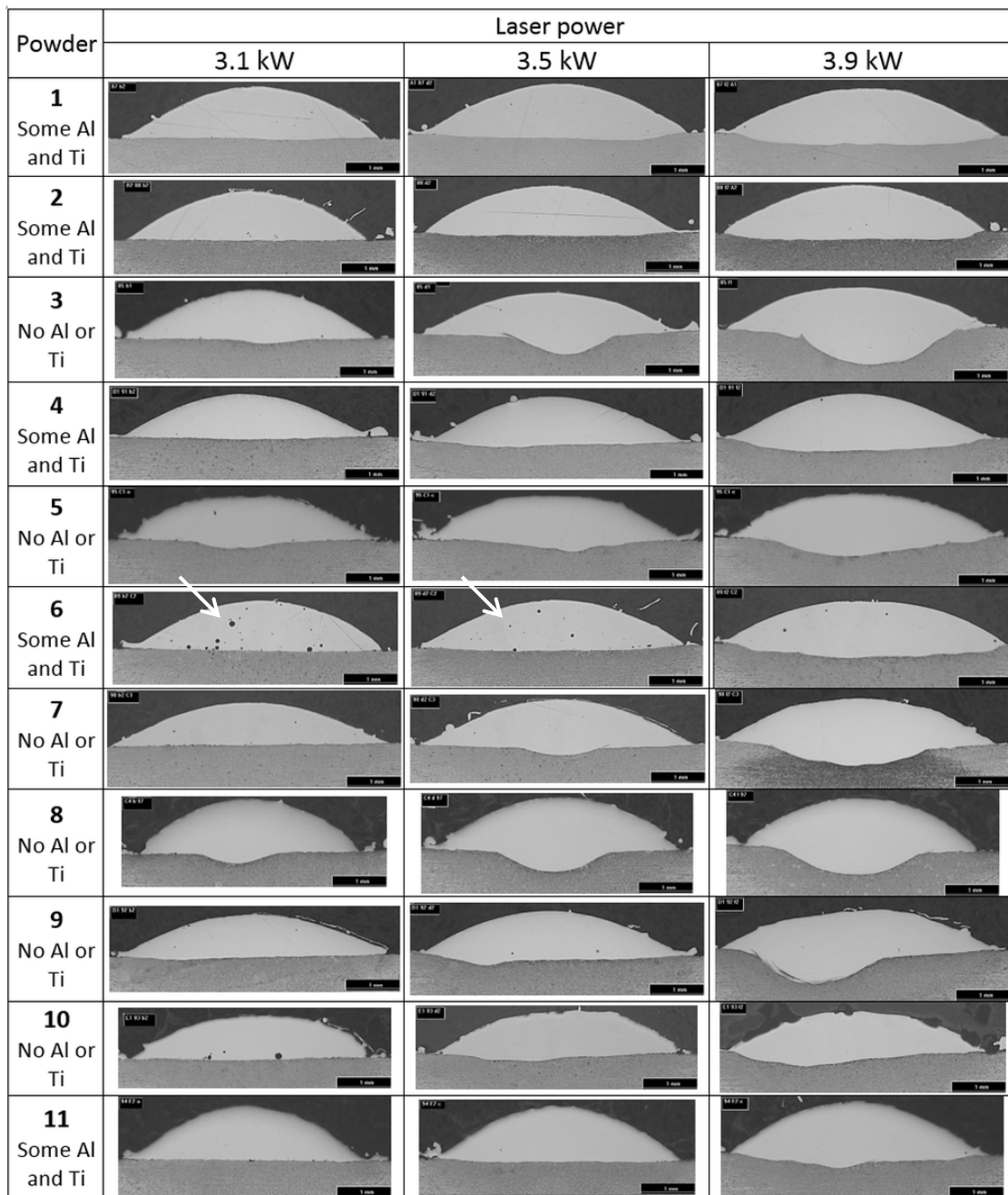


Fig. 52: Cross section images of laser cladding single bead tests with laser power levels of 3.1 kW (left), 3.5 kW (middle) and 3.9 kW (right). Some porosity is pointed out with the arrows.

More detailed information from the cross sections of the single bead test claddings that were made with the same parameters but with No-Al-or-Ti in the powder (No. 10) and some-Al-and-Ti in the powder (No. 11), are presented in Fig. 53 and 54.

Powder: **10**
 Al content: 0.001%
 Ti content: 0.006%
 Si content: 0.47%
 Laser power: 3.7 kW
 PFR: 28.2 g/min
 Geometrical dilution: 15%

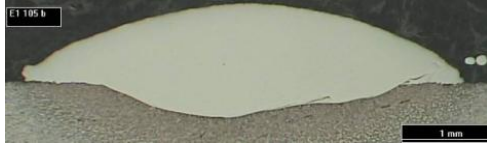


Fig. 53: Powder No. 10, single bead, cross section image

Powder: **11**
 Al content: 0.27%
 Ti content: 0.28%
 Si content: 0.27%
 Laser power: 3.7 kW
 PFR: 28.4 g/min
 Geometrical dilution: 9%



Fig. 54: Powder No. 11, single bead, cross section image

This same effect of Al and Ti on penetration and dilution can also be seen from the cross section surfaces of the tests claddings made with adjacent beads in Fig. 55 and 56. These two test cladding were made only half an hour apart with identical parameters in the same session on the same day. The presence or absence of Al and Ti also affected the bead surface appearance and composition.

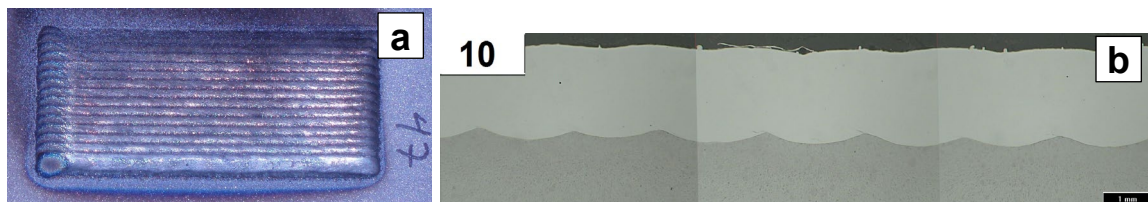


Fig. 55: Powder No. 10, no Al or Ti. Laser cladding with adjacent beads. Laser power: 3.8 kW, PFR: 30.0 g/min. a) Test sample outlook, photograph. b) Cross section, OM image, magnification 6x. Relatively large dilution.

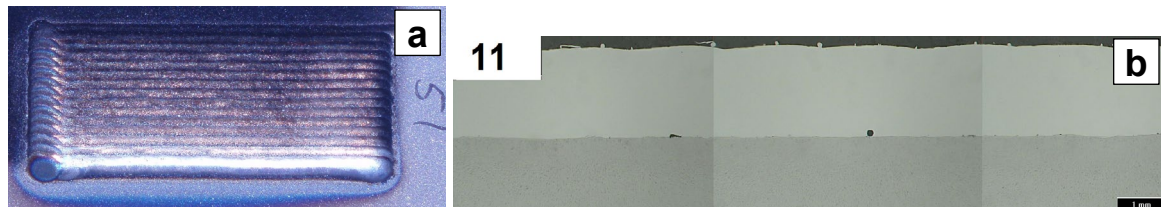


Fig. 56: Powder No. 11, some Al and Ti. Laser cladding with adjacent beads. Laser power: 3.8 kW, PFR: 29.2 g/min. a) Test sample outlook, photograph. b) Cross section, OM image, magnification 6x. Low dilution.

In Fig. 57 and 58 show images of single bead test cladding surfaces and EDS mapping results on surfaces made with these same powders, Nos. 10 and 11. EDS point analyses results to the surface are presented in Table 31. The EDS mapping and point analyses were aimed at examining the composition of the slag on the bead surface.

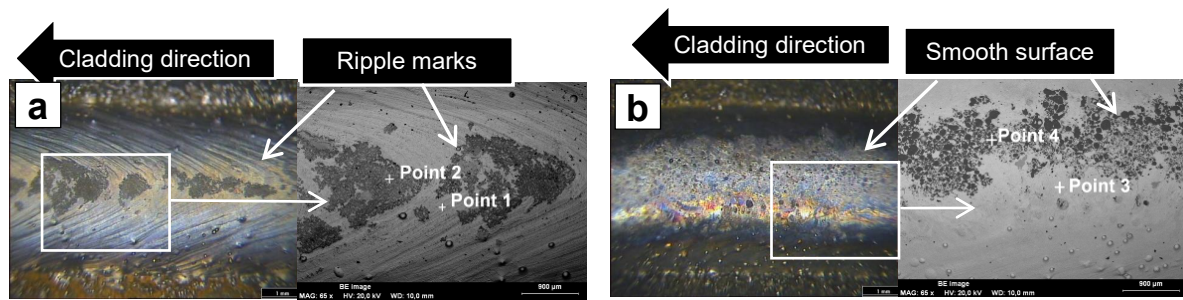


Fig. 57: Laser single bead test cladding surfaces. OM and SEM BE images. a) Powder No. 10, no Al or Ti, b) Powder No. 11, some Al and Ti.

Table 31: The results of EDS point analyses on the surface of single bead test with powder No. 10 and 11.

Powder No. 10, Fig. 57 a (wt%)											Powder No. 11, Fig. 57 b (wt%)										
Point	C	O	Al	Si	Cr	Mn	Fe	Ni	Nb	Mo	Point	C	O	Al	Si	Ti	Cr	Fe	Ni	Nb	Mo
1	5	32	–	1.5	13	–	12	29	3.4	3.4	3	2.4	34	14	0.2	1.6	11.5	9	24	1.5	2.2
2	5	59	0.4	0.7	12	5.3	5	10	1	1	4	1.1	69	29	–	0.5	0.6	0.2	0.3	–	–

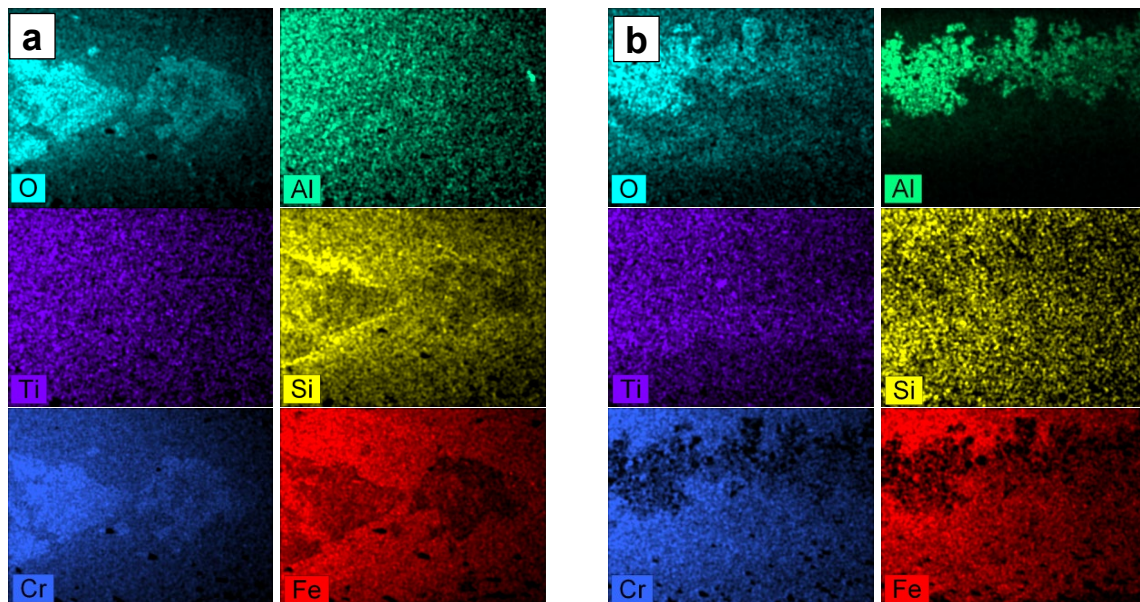


Fig. 58: EDS mapping images for elements: O, Al, Ti, Si, Cr and Fe. The same field of view as in the previous images (Fig. 57). a) Powder No. 10 (no Al or Ti), b) Powder No. 11, (some Al and Ti).

As can be seen from the EDS results on the single bead test cladding surface, with Al and Ti-free powder No. 10 (Fig. 58 a), the oxide island on the surface consists mainly of elements O, Cr and Mn; no Al is present. With powder No. 11 containing some Al and Ti (Fig. 58 b) the oxide islands on the surface consist of the elements O and Al, but hardly any Cr could be detected.

At this point, it appeared that the effect of Al and Ti on dilution is most probably related to surface oxidation. Without the presence of Al and Ti as a minor alloying element, the melt pool surface is probably more prone to oxidise. On the other hand, when there is some Al, it forms compounds with the oxygen – oxides – on the surface. These oxides seem to gather in clusters on the surface so that the rest of the melt pool remains less oxidized. When there is no Al in

the powder, Cr and Mn oxides form instead. This phenomenon is studied in more detail with high-speed video examinations (section 3.1.5, p. 103).

One feature of the single bead cross sections with 11 alloy powders is that the test claddings with powder No. 6 contained some porosity as indicated by the arrows in the middle of Fig. 52 (page 96). The total amount of porosity decreased as the laser power increased from 3.1 kW to 3.9 kW. This is because gas has more time to escape from the melt if the solidification gets slower. The origin of the porosity is related to the large amount of small ($<10\text{ }\mu\text{m}$) powder particles (Fig. 44, 6, p. 90).

In conclusion the tests with the 11 alloy 625 powders indicate that powders (Nos. 1 – 4), which had a high tendency for solidification cracking, had a relatively high B content, the highest percentage being 0.02% (Table 28). The most crack-sensitive powder (No. 3) of the powders containing B was the one that was free of Al and Ti. Generally, Al and Ti-containing powders also showed lower dilution values than Al and Ti free powders (Fig. 51). The powders that were least sensitive to cracking had a very low B content. The powders that showed the best resistance to cracking were also free of Si.

In order to investigate the effects of elements B, Al and Ti on cladding, some amounts of these elements were added in a powder form to the alloy 625 powder, as described in section 2.3.2 on page 73. The results from these tests are presented in the following section, 3.1.4.

3.1.4. Laser – hot crack results after modification of the alloy 625 powders

The most crack-sensitive powder, No. 3, which had no Al and Ti, was alloyed with 0.3% (wt) of Al and Ti to see if this could cure its hot-cracking sensitivity. In addition, powder No. 8, which appeared to be crack resistant, was alloyed with some boron. The alloying powders are presented in section 2.2.2 on page 70 and the alloying tests are explained in section 2.3.2 on page 73. The total length of the hot cracks in the single bead test claddings were determined in the same way as in the tests with the 11 powders as explained in section 2.6.2 on page 80.

The hot-cracking measurement results of the claddings made with powder No. 3, both with and without the addition of Al and Ti, are presented in Fig. 59.

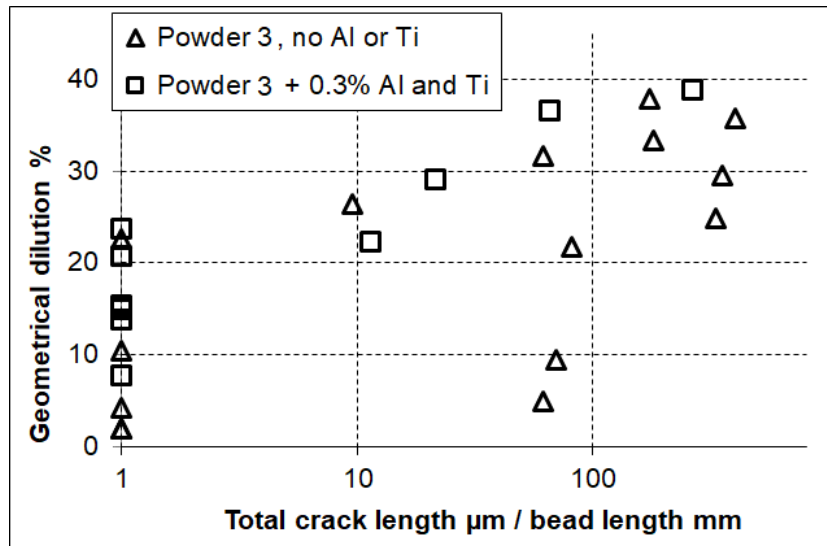


Fig. 59: The results of hot cracking tests with Al and Ti addition to powder No. 3.

The results show that a small addition (0.3%) of Al and Ti to the crack-sensitive powder No. 3 decreased its cracking sensitivity. With the addition of Al and Ti addition the threshold dilution value when cracks start to appear rose to above 20%, while without Al and Ti some cracks were detected with dilution values of only 5–10%.

When hot-crack resistant powder No. 8 was alloyed with boron (B), the effect of B on hot crack density was also clear. The hot-crack measurement results of powder No. 8 with the addition of the B-containing NiCrBSi self-fluxing alloy are presented in Fig. 60.

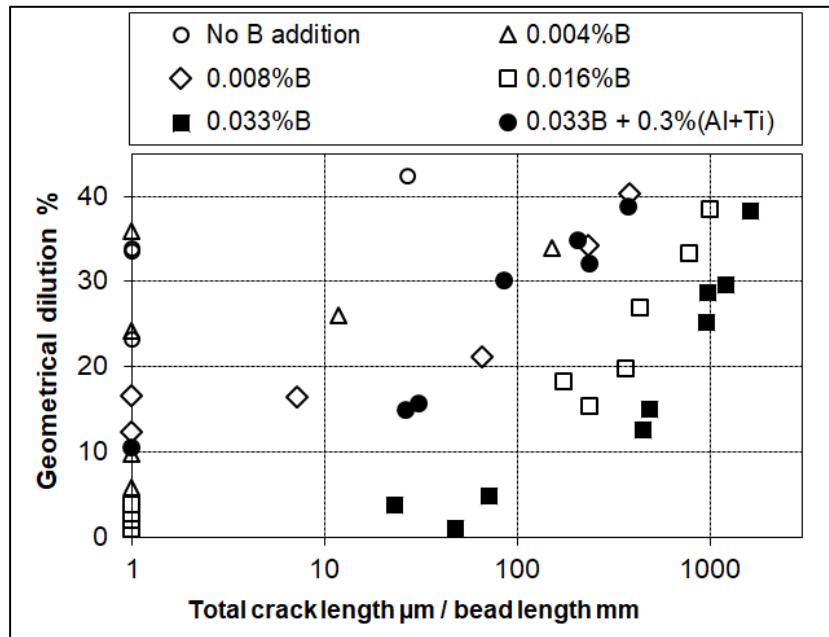


Fig. 60: The results of hot cracking tests with B, Al and Ti addition to powder No. 8. (Note, different X-axis than in Fig. 59).

When the powder No. 8 was alloyed with 0.033% B, some solidification cracks already appeared at a very low dilution level and even a 0.016% B content had a clear effect on measured the hot crack density. With even lower B levels of 0.004% and 0.008%, the effect on crack length was less clear. However, when a powder blend with a high proportion of B (0.033%) and with the same amount (0.3%) of both Al and Ti as was used with powder No. 3,

the crack sensitivity was decreased again. The addition of Al and Ti also substantially decreased penetration and dilution, as can be seen clearly from the cross section images presented in Fig. 61. These cross section images also show how hot cracks start to appear in test claddings made with Al and Ti free powder with a laser power of 3.7 kW.

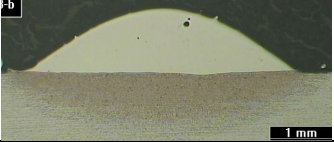
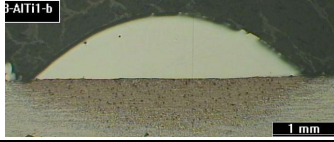

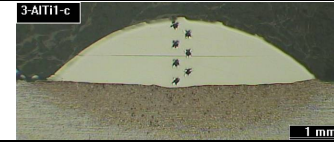
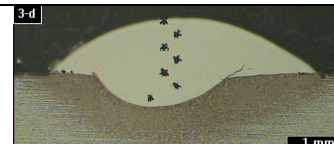

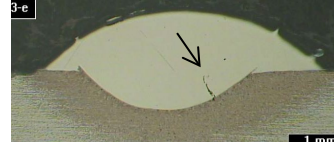
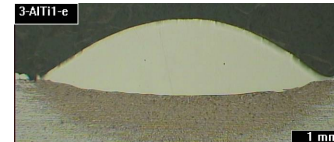
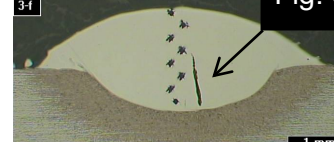
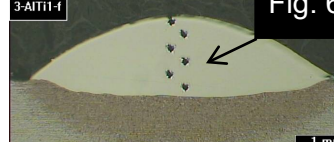
Laser Power	Powder No. 3, no Al and Ti	Powder No. 3 + 0.3% Al and Ti addition
3.1 kW		
	Penetration depth: 0.06 mm Dilution: 5% Fe content: 4%	Penetration depth: 0.03 mm Dilution: 3% Fe content: 4,5%
3.3 kW		
	Penetration depth: 0,22 mm Dilution: 10% Fe content: 10% Hardness: 244 HV ₁	Penetration depth: 0,12 mm Dilution: 8% Fe content: 9% Hardness: 246 HV ₁
3.5 kW		
	Penetration depth: 0.53 mm Dilution: 25% Fe content: 21% Hardness: 234 HV ₁	Penetration depth: 0.16 mm Dilution: 14% Fe content: 16% Hardness: 238 HV ₁
3.7 kW		
	Penetration depth: 0.63 mm Dilution: 30% Fe content: 26% Hot cracks	Penetration depth: 0.25 mm Dilution: 21% Fe content: 20%
3.9 kW		
	Penetration depth: 0,71 mm Dilution: 36% Fe content: 31% Hardness: 209 HV ₁ Hot cracks	Penetration depth: 0,27 mm Dilution: 22% Fe content: 23% Hardness: 226 HV ₁

Fig. 61: Cross section images and some measurement values from laser cladding single bead tests with powder No. 3 and laser power of 3.1–3.9 kW. TS: 1000 mm/min, PFR: 30 g/min. On the left: tests without the addition of Al or Ti. On the right: tests with the addition of 0.3% Al and Ti. Some hot cracks are indicated with the arrows. Some of the cross sections contain hardness measurement indentations.

Images of alloy 625 etched cross section surface of test claddings with laser power of 3.9 kW (bottom row in Fig. 61) are shown in the following images in Fig. 62 and 63.

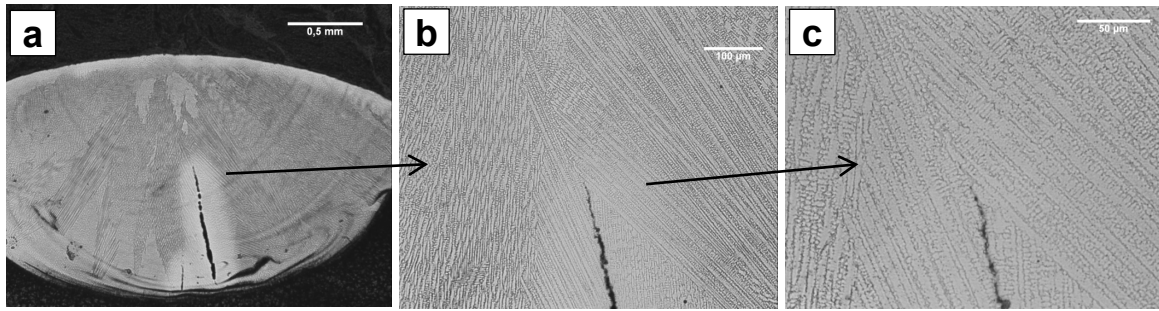


Fig. 62: Laser cladding single bead test with powder No. 3. Laser power: 3.9 kW. Alloy 625 etched microsection surface. OM images, magnifications: a) 20x, b) 80x, c) 200x. Small variation in solidification direction – columnar solidification. Hot crack at the centre-line.

These cross section images show that the solidification mode is columnar with the Al-and-Ti-free powder, No. 3 (Fig. 62). This is an indication that the thermal gradient G (Fig. 10, p. 24) was higher during solidification. During solidification, impurities have been pushed along with the last-to-solidify liquid towards the weld centreline and a solidification crack has formed at the centreline.

When the powder No. 3 was modified with some Al and Ti, the solidification has transformed to go in more directions, or in other words the solidification is equiaxed (Fig. 63).

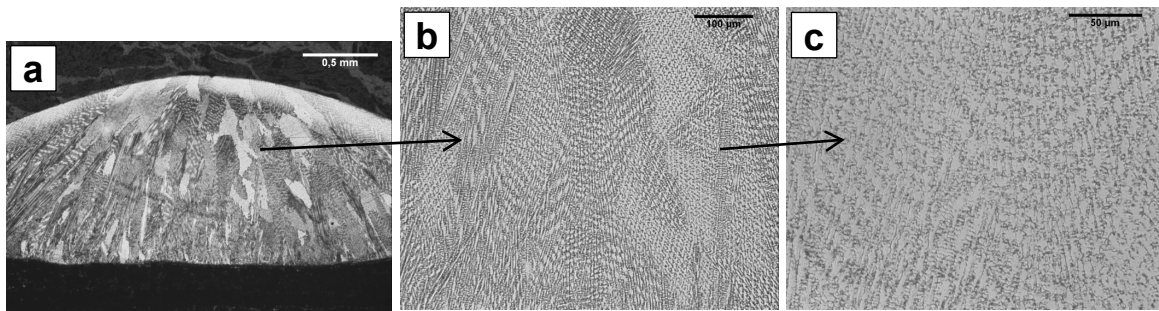


Fig. 63: Laser cladding single bead test with powder No. 3 and with addition of Al+Ti. Laser power: 3.9 kW. Alloy 625 etched microsection surface. OM images, magnifications: a) 20x, b) 80x, c) 200x. Large variation in solidification direction. No cracks.

The following images, Fig. 64 a and b, are OM images from the bead surface of single bead test claddings made with powder No. 3 without (a) and with (b) addition of Al+Ti.

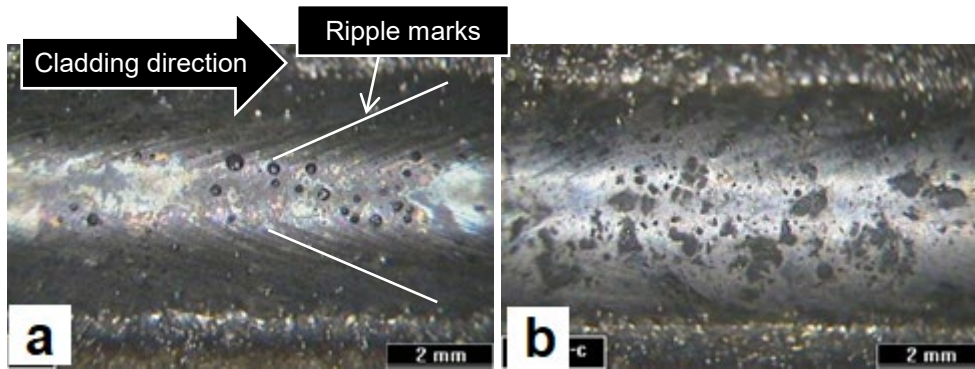


Fig. 64: Bead surface appearance of test claddings made with laser power of 3.3 kW. a) Al and Ti-free powder No. 3. b) Powder No. 3 with addition of 0.3% Al and Ti. In image (a) V-shaped ripple marks can clearly be seen on the surface made with Al and Ti-free powder No 3.

V-shaped ripple marks are quite clearly visible on the beads made with Al and Ti free powder No. 3 as shown in Fig. 64 a. These ripple marks indicate that the melt pool was teardrop shaped during the process as depicted in Fig. 9 on page 23. However, there was no sign of any ripple marks on the surface when there was some Al and Ti present (Fig. 64 b). The appearance and composition of bead surface was very similar to the test claddings made with Al and Ti-free powder, No. 10, and powder containing Al and Ti powder No 11, shown in Fig. 57 on page 98.

In conclusion of the tests with modified alloy 625 powders, the hot cracking tests showed that the hot-crack density of the crack-sensitive powder No. 3 was decreased with the addition of some Al and Ti (0.3%). In the case of Al and Ti-free powder, No. 8, which was originally hot crack resistant, a small addition of B substantially increased the hot-crack density. Crack density was decreased still further when some Al and Ti was added together with B.

3.1.5. Laser – melt pool behaviour

The melt flow on the melt pool surface Heiple's model for Marangoni convection, is dependent on the surface tension gradient as shown in Fig. 12 on page 30. Surface tension is dependent on so-called surfactants, elements such as O, Al and Ti that affect surface tension.

The melt pool behaviour, i.e. the direction of the melt pool surface flow, was captured by high speed-video imaging, done with the settings presented in section 2.3.3 on page 74. One side-view image from the high-speed video camera with some explanation is presented in Fig. 28 on page 58. Some images from the high-speed video camera with two laser power levels: low; 3.1 kW and high; 3.9 kW and with Al and Ti-free powder No. 8 and Al and Ti-containing powder No. 11, are presented below.

The direction of motion in the images is from the right to the left. The melt pool, powder stream and melt pool surface appearance can be seen quite clearly. The laser beam itself is not visible in the images. Quantitative data about melt pool temperature or direct temperature gradient or distribution is not available from the image. However, it can be assumed that the brightly areas in the images are the hottest areas. Because of the constant stream of glowing powder particles, it is rather difficult to distinguish the movement on the melt pool surface from the trajectories of the powder particles.

With the low laser power of 3.1 kW the melt pool surface is quite stable and similar for both powders, the Al and Ti-free powder No. 8 (Fig. 65 a) and the Al and Ti-containing powder No. 11 (Fig. 65 b). No movement in the melt pool can be detected. The frames are taken with the interval of 1 ms.

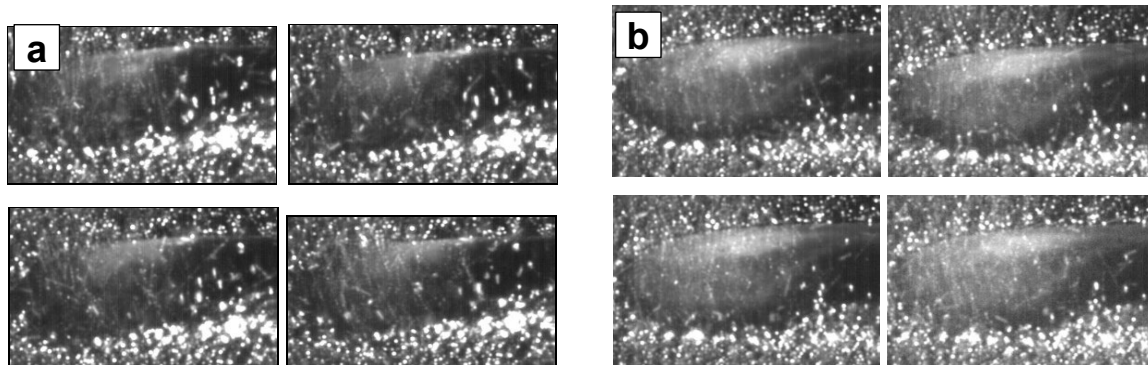


Fig. 65: Four sequential frames from test with with laser power of 3.1 kW. a) Al and Ti free powder No. 8. b) Al and Ti containing powder No. 11.

With the higher laser power of 3.9 kW, the behaviour of the melt-pool surface was different for the two powders, Nos. 8 and 11. With the Al and Ti-free powder No. 8, there was a large brighter area in the middle of the melt pool and it was thus possible to see some inward movement on the melt pool surface (Fig. 66 a). In the four sequential image captures in Fig. 66 a, the bright spot indicated by the arrow moves towards the bright centre of the melt pool. It can be seen how some small elongated areas that appear bright move from the edge of the melt pool to the bright centre.

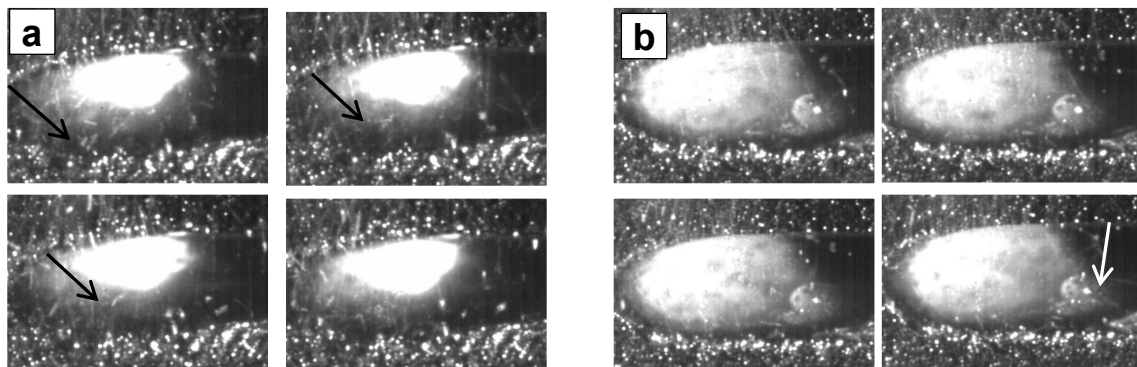


Fig. 66: Four sequential frames from tests with a laser power of 3.9 kW. a) Al and Ti-free powder No. 8. Bright area indicated by arrow moves from the edge of the bead to the bright area on the centre. b) Al and Ti-containing powder No. 11.

With high laser power of 3.9 kW and the Al and Ti-containing powder No. 11 (Fig. 66 b), there is no clear movement from the middle towards the outer edges of the melt pool and/or this movement cannot be shown with still images in the way it can with the inward movement from powder 8 in Fig. 66 a. However, it seems that there is some rotation on the melt pool surface and oxides seem to gather at the side of the melt pool as indicated by the arrow in Fig. 66 b. In addition, the bright area on the melt pool surface is larger but it is quite stable compared to that of the tests with Al and Ti free powder No. 8 (Fig. 66 a).

The bright area in the middle of the melt pool is smaller and located further back with the Al and Ti-free powder No. 8 than it is with the Al and Ti-containing powder No. 11. The smaller size of this bright area indicates a steeper temperature gradient in the melt pool. There is also some fluctuation in the size and location of the bright area. One example of this fluctuation motion is presented in Fig. 67.

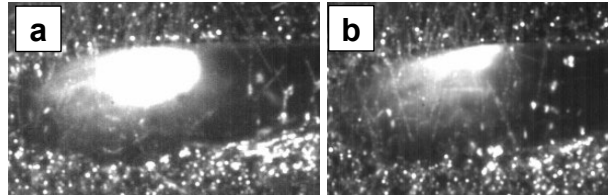


Fig. 67: Two frames from test with powder 8 and with a laser power of 3.9 kW. Frames were taken with an interval of 80 ms.

In Fig. 67 a, the size and location of the bright area is “normal”, but in Fig. 67 b, taken after 80 ms later, the bright area is smaller and has moved backwards. After this, the images show that the size and location of the bright area returns to “normal” again after a few milliseconds. In tests with Al and containing powder No. 11 this fluctuation of the melt pool was not detected.

The same fluctuating effect can also be seen from the longitudinal cross sections in Fig. 68 b and Fig. 69 b. With the Al and Ti-free powder No. 8 there is clear variation in the penetration depth (Fig. 68 b). With powder 11 containing some Al and Ti, the penetration depth is very stable even with a high laser power of 3.9 kW (Fig. 69 b).

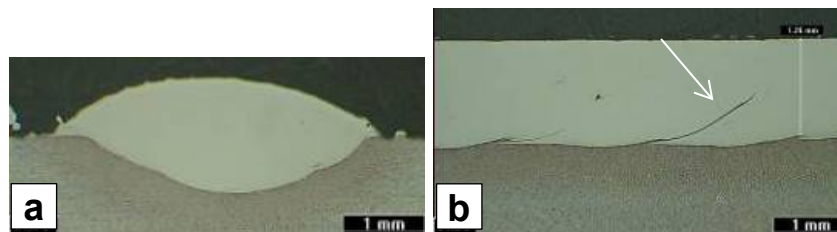


Fig. 68: Powder No. 8 (no Al or Ti). High-speed video test samples with laser power of 3.9 kW. Cross sections taken in a) perpendicular and b) parallel direction to the cladding motion. OM images. Geometrical dilution: 45%. Penetration depth: 0.6–0.7 mm.

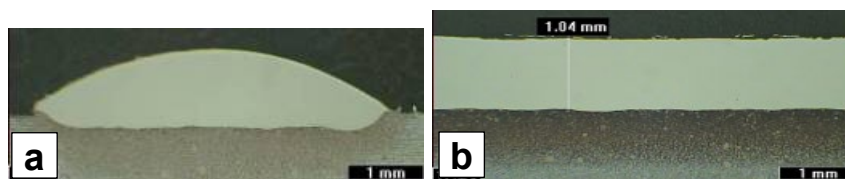


Fig. 69: Powder No. 11 (some Al and Ti). High-speed video test samples with laser power of 3.9 kW. Cross sections taken in a) perpendicular and b) parallel direction parallel direction to the cladding motion. OM images. Geometrical dilution: 25%. Penetration depth: 0.24 mm.

It could be assumed that this variation is due to the fluctuation of the melt pool surface shown in Fig. 67. Large dilution and melt-pool instability also generate iron-containing phases that were affected by etching. These can be seen as a wave crest pattern indicated by the arrow in Fig. 68 b. If these phases reach the surface of the cladding, they can destroy the anti-corrosion properties of alloy 625.

3.1.6. Laser – cladding with adjacent beads

Laser cladding tests with adjacent beads were mainly done for the laser vs. CMT comparison. These results are presented in section 3.3, on page 136. The SEM BE images of powder No 12, which was used in these tests, are presented in Fig. 45 on page 90.

3.2. Results from cladding tests with arc and wire

This section presents the results of the tests that were performed with Ø1.2 mm alloy 625 wire and arc (MIG) welding methods. Most of the tests were done with the CMT process, but some stringer single bead tests were also made with conventional MIG and pulsed MIG processes to characterize the differences between the processes. The cladding tests with arc and wire are divided into five main parts:

1. Single bead tests with three processes: conventional MIG, pulsed MIG and CMT (3.2.1)
2. Wire feed speed (WFS) in the CMT process (3.2.2)
3. CMT single bead tests – the effect of shield gas and auxiliary parameters ALC and DC on the process (3.2.3).
4. CMT single bead tests – the effect of shield gas and travel speed (3.2.4).
5. CMT tests with adjacent beads – the effect of track displacement and travel speed (3.2.5)

3.2.1. Conventional MIG, pulsed MIG and CMT processes – comparison

In order to illustrate the characteristic features of the CMT process, and to compare the CMT process properties with conventional MIG and pulsed MIG processes, some single bead tests were made with these all processes by varying the set WFS values. All of the parameters and other settings in these tests are presented in section 2.4.1, Table 21 on page 75. The emphasis in these tests was in determining the actual process power. Current and voltage during welding were measured with oscilloscope at 50 kHz to determine the voltage/current graph and the average instantaneous power (AIP) as presented in section 2.1 on page 52.

In order to illustrate the characteristics of the different processes, in the following images (Fig. 70) are presented the voltage/current graphs acquired with oscilloscope during welding with three processes: conventional MIG, pulsed MIG and CMT with a set WFS of 8 m/min.

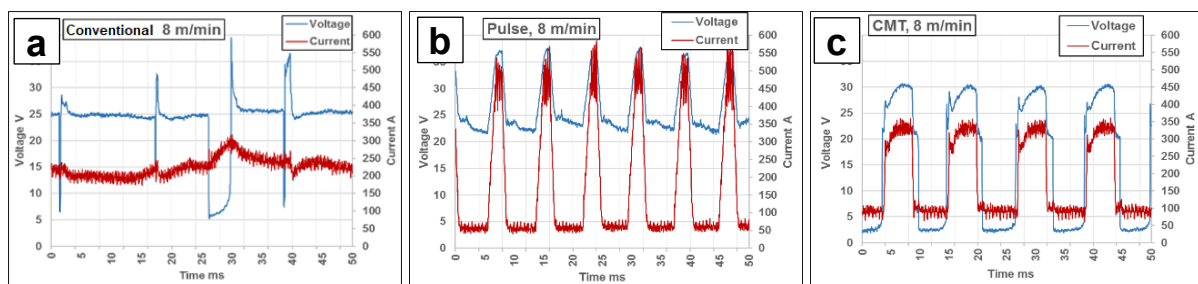


Fig. 70: Oscilloscope voltage/current graphs from processes: a) conventional MIG, b) pulsed MIG, and c) CMT (set WFS: 8 m/min, Ar-30%He shield gas).

As can be seen in Fig. 70, the shape of the voltage/current waveform in the CMT process differs from that of both the conventional and pulse processes. The voltage/current graphs

from the oscilloscope also show that the CMT process is very stable and regular, at least when compared to the conventional short-circuiting MIG process. With both pulsed MIG and the CMT process, the waveform of the current and voltage is regular and they are in the same phase shift, meaning that during high-phase, both voltage and current are high, and vice versa, during low-phase. In the conventional MIG process, there is no clear shift between the phases, but there is an irregular, abrupt short circuit when the wire tip touches the melt pool. As a consequence, the voltage drops and the current rises as can be seen in the middle of Fig. 70 a, between 25 and 30 ms. The irregularity was probably so prominent because in this case, with a WFS value of 8 m/min, the conventional MIG process fell in a globular transfer mode, somewhere between short circuit transfer and spray transfer.

In the pulsed MIG process the current reaches around 500 A and the goes to over 35 V during the high current and voltage phase, while in the CMT process, the corresponding values are around 330 A and 30 V. In a low current and voltage phase, the current and voltage levels are around 50–60 A and 23–24 V for the pulsed MIG process, and around 100 A and 2–3 V for the CMT process.

However, these phases, high and low, also have different names in the conventional, pulsed and CMT processes, since the processes are so different. The levels of current and voltage during the different phases of the pulsed MIG and CMT processes also differ from each other. Current and voltage values during phases in conventional, pulse and CMT process with WFS set value 8 m/min are presented also in Table 32 below.

Table 32: Current and voltage values during the conventional, pulse and CMT processes, as determined with an oscilloscope (WFS set: 8 m/min, shield gas: Ar-30%He).

Process	Phase	Current	Voltage
Conventional MIG	Re-ignition (high)*	NA	35 – 50 V
	Short-circuiting (low)*	200–300 A	5–7 V
	Average**	200 A	24.5 V
Pulsed MIG	Pulse (high)*	450–500 A	35–37 V
	Background (low)*	50–60 A	22–24 V
	Average**	175 A	26 V
CMT	Arcing (high)*	300–350 A	25–30 V
	Short-circuiting (low)*	90–105 A	2–3
	Average**	182 A	15.5 V

* Values were determined from the oscilloscope graph (Fig. 70)

** Values from the Fronius Xplorer software

The higher peak and average current and voltage levels in the pulsed MIG process produce higher average process power. This differences in arc power values are illustrated in Fig. 71, where the arc power values (AIP) based on current and voltage measurements with the oscilloscope are presented along with the power values using the conventional $I_{aver} \times U_{aver}$ method. The AIP was determined with equation 5 on page 53. It should be noted that Y-axis (power) in Fig. 71 b for the pulse process, has a different scale than the scales for the conventional (a) and CMT processes (c).

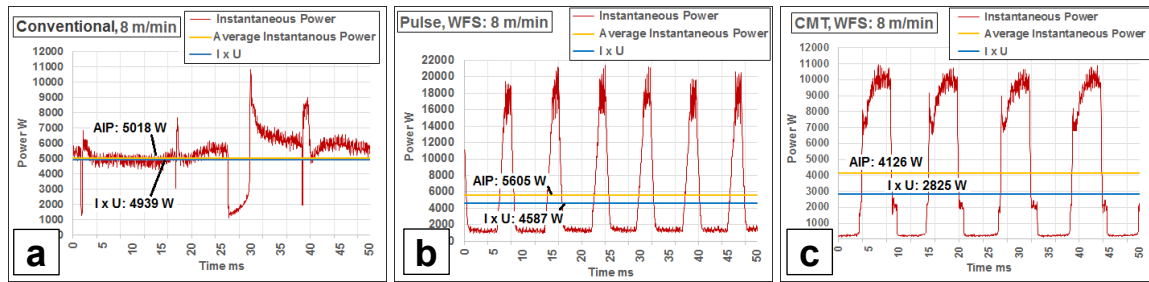


Fig. 71: Arc power values (IP, AIP and $I \times U$) based on current and voltage measurements with an oscilloscope (Fig. 70) for the three processes: a) conventional MIG, b) pulsed MIG and c) CMT (set WFS: 8 m/min, Ar-30%He shield gas).

The red line, instantaneous power (IP), indicates the power value ($I_i \times U_i$) at any moment of time, as an outcome from the current and voltage values presented in the previous image (Fig. 70). In this case, since the sampling frequency was 50 kHz, the calculation was made 50 000 times in one second. The orange line, AIP, indicates the average of the IP (red line) values and the blue line indicates the average power value determined with the conventional $I_{aver} \times U_{aver}$ method. These average current and voltage values during welding were recorded by Fronius Xplorer software.

The results of arc power determination with each WFS set value are presented in Table 33–35 and in Fig. 72–74. The average current and voltage values (I_{aver} and U_{aver}) recorded by Fronius Xplorer software are also presented along with the values determined with the oscilloscope (I_{mean} and U_{mean}).

Table 33: Conventional MIG process, electrical parameters.

WFS m/min	Average I and U			Oscilloscope			diff: $I \times U$ vs. AIP
	I_{aver} A	U_{aver} V	$U \times I$ W	I_{mean} A	U_{mean} V	AIP W	
5	122	20.9	2538	125	18.9	2019	-21%
6	130	24.1	3124	136	20.0	2346	-25%
7	184	21.7	4007	185	21.9	3922	-2.1%
8	203	24.4	4939	204	24.6	5018	1.6%
9	214	25.8	5511	218	25.1	5462	-0.9%
10	229	25.3	5793	230	25.6	5885	1.6%
11	243	26.1	6354	242	26.4	6399	0.7%
12	265	27.5	7277	262	27.3	7139	-1.9%

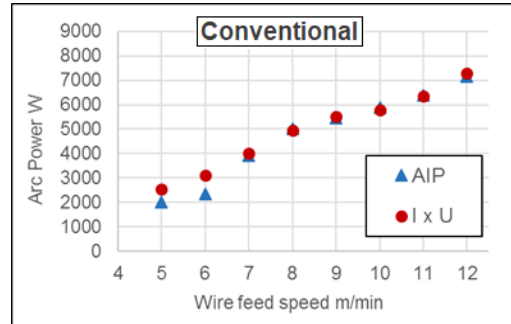


Fig. 72: Conventional MIG process. WFS set value vs. arc power.

Table 34: Pulsed MIG process, electrical parameters

WFS m/min	Average I and U			Oscilloscope			Diff: I x U vs. AIP
	I _{aver} A	U _{aver} V	U x I W	I _{mean} A	U _{mean} V	AIP W	
5	105	24.0	2508	107	24.2	3271	30%
6	128	24.3	3102	129	24.7	3970	28%
7	153	25.2	3846	155	25.7	4800	25%
8	175	26.3	4587	178	26.8	5605	22%
9	197	27.3	5374	200	27.8	6419	19.4%
10	223	28.0	6247	227	28.4	7278	16.5%
11	240	29.2	6996	243	29.8	8081	15.5%
12	261	29.0	7567	262	29.8	8661	14.5%

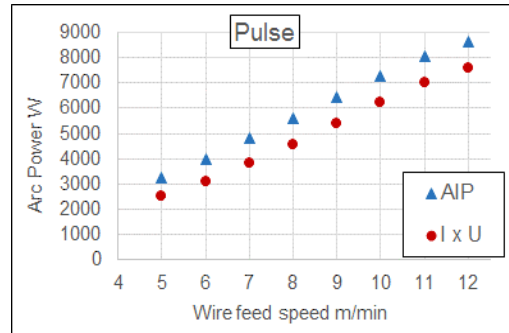


Fig. 73: Pulsed MIG process. WFS set value vs. arc power.

Table 35: CMT process, electrical parameters

WFS m/min	Average I and U			Oscilloscope			Diff: I x U vs. AIP
	I _{aver} A	U _{aver} V	U x I W	I _{mean} A	U _{mean} V	AIP W	
5	123	14.5	1784	126	14.4	2474	39%
6	139	15.3	2115	141	15.3	2936	39%
7	153	15.9	2437	155	15.8	3333	37%
8	182	15.5	2825	186	15.6	4126	46%
9	205	17.9	3665	207	18.0	4946	35%
10	218	18.1	3928	219	17.8	5134	31%
11							
12							

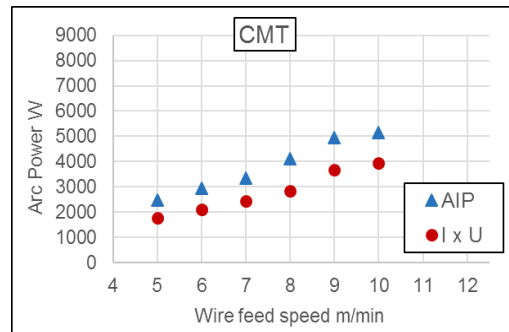


Fig. 74: CMT process. WFS set value vs. arc power.

As the above tables and images show, the average current and voltage values determined with both methods, from the welding powder source via Fronius Xplorer software, and from the oscilloscope, are very close to each other. This indicates that both methods give reliable results in measuring average values of current and voltage.

However, the arc power measurement results show that while the conventional method to determine arc power by multiplying $I_{aver} \times U_{aver}$ gives the same values as the AIP method with the conventional MIG process, the situation is different with the pulsed MIG and CMT processes. With the pulsed MIG process, there is a 25–30% difference between the arc power values provided by the $I_{aver} \times U_{aver}$ method and the AIP methods, although the relative difference gets smaller as the WFS is increased.

With the CMT process, the difference between the arc power values provided with the $I_{aver} \times U_{aver}$ and the AIP methods was even larger than it was with the pulsed MIG process, the highest measured difference being 46% with a WFS set value of 8 m/min. Nor was there any clear indication that the difference would get smaller as the WFS set value increases. The average value for this difference with WFS set values between 5 and 10 m/min was 37%. This value is used later in determining actual arc power in CMT test claddings with adjacent beads (Table 52, p. 144). However, it is shown later (section 3.2.3, p. 114), that altering the auxiliary

parameters ALC and DC can lead to a situation where this difference in the arc power can be as high as 70%.

Some of the results from the tests with conventional MIG, pulsed MIG and CMT processes are presented in Table 36 and some bead appearance and cross section images from the single-bead-on-plate tests are presented in Fig. 75.

Table 36: Comparison data from tests with conventional, pulse and CMT process WFS setting of 8 m/min.

Parameter	Conventional MIG	Pulsed MIG	CMT
Average voltage (Fronius Xplorer)	24.4 V	26.3 V	15.5 V
Average current (Fronius Xplorer)	203 A	175 A	182 A
Arc power ($I_{aver} \times U_{aver}$)	4939 W	4587 W	2825 W
Average instantaneous power (AIP)	5018 W	5605 W	4126 W
Heat input ⁽¹⁾	240 J/mm	269 J/mm	198 J/mm
Actual fire feed rate ⁽²⁾	8.1 m/min	8.1 m/min	8.8 m/min
Power ratio ⁽³⁾	548 W/mm ²	612 W/mm ²	415 W/mm ²
Bead cross section area ⁽⁴⁾	9.5 mm ²	10.0 mm ²	10.4 mm ²
Penetration depth ⁽⁴⁾	1.5 mm	1.3 mm	0.5 mm
Geometrical dilution ⁽⁴⁾	36%	25%	10%
Melted base material + HAZ area	16.2 mm ²	16.2 mm ²	10.7 mm ²

1) Eq. 4, vs. AIP (not $I \times U$), $k = 0,8$

2) Fig. 78, p. 113

3) Power ratio: eq. 7, p. 53.

4) Measured from one cross section, Fig. 40, p. 81

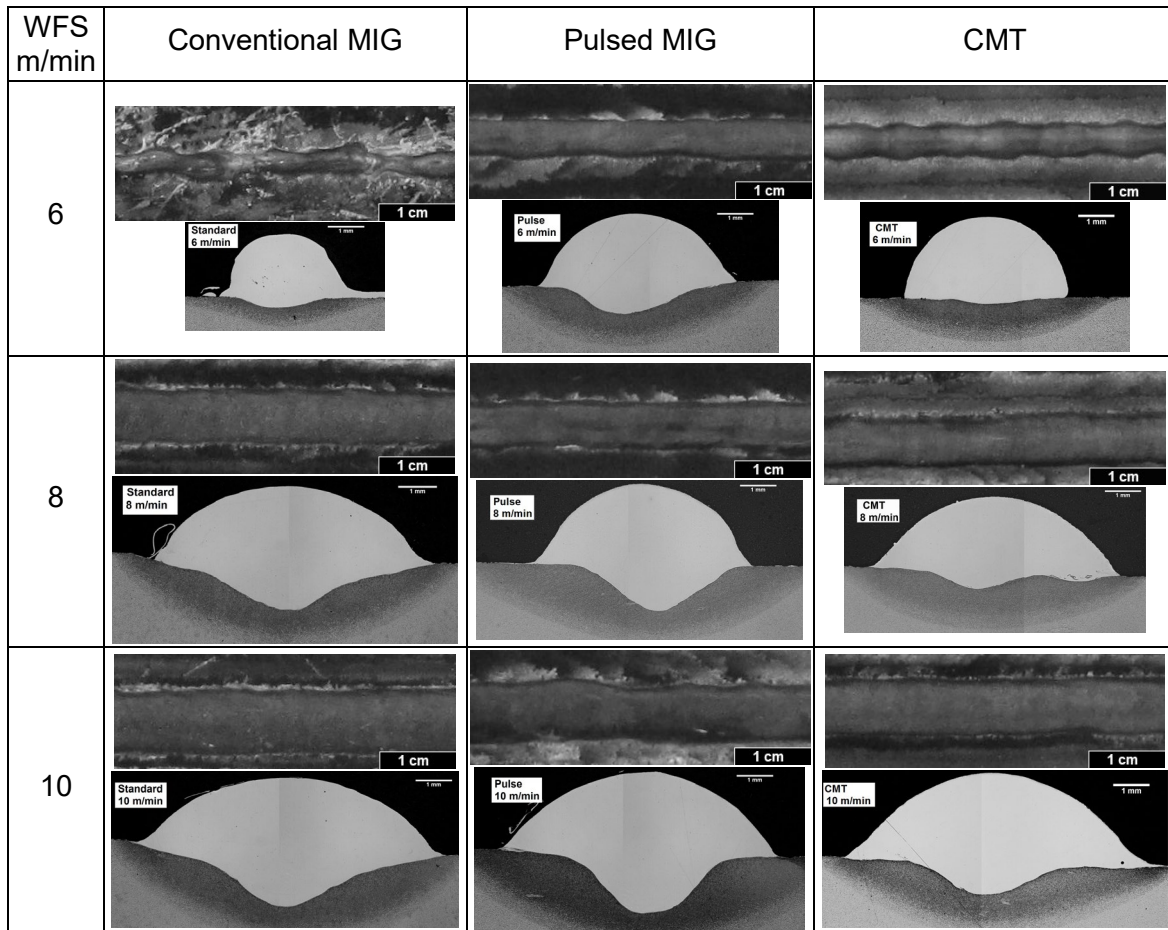


Fig. 75: Bead appearance and cross section images of single bead test samples with set WFS of 6, 8 and 10 m/min, from top to bottom, respectively. Left column: conventional MIG process. Middle column: pulsed MIG process. Right column: CMT process.

One essential feature that can be seen from the values in Table 36 and the cross section images in Fig. 75, is that both penetration and dilution are lower with the CMT process, than they are with the other two processes. The heat input to the base metal during welding can also be derived or estimated from the size of the HAZ and the amount of melted base material from the cross section. These results are presented in the last row of Table 36. For the conventional and pulsed MIG processes this area was 16 mm² while for the CMT process it was only 10 mm². It is also worth noting that even though the WFS setting was 8 m/min, the actual wire feed rate in CMT process was slightly higher, 8.8 m/min, which produces slightly larger reinforcement of the cross section area. This feature, that the actual wire feed is higher than the set value, is typical for the CMT process. In the tests for this study, the actual WFS in the CMT process was typically around 10% higher than the set value.

3.2.2. CMT – wire feed speed

In order to examine the effect of WFS set value in the oscilloscope voltage/current graph and to determine the optimum WFS, oscilloscope graphs of single bead tests made with the CMT process, set WFS of 5–10 m/min and with Ar-30%He shield gas were examined. The tests were the same as on the previous process comparison section (3.2.1) and the parameters are as presented in Table 21 on page 75.

Oscilloscope graphs with the CMT process and WFS set values of 5, 6 and 7 m/min are presented in Fig. 76, and those with set WFS values of 8, 9 and 10 m/min in Fig. 77.

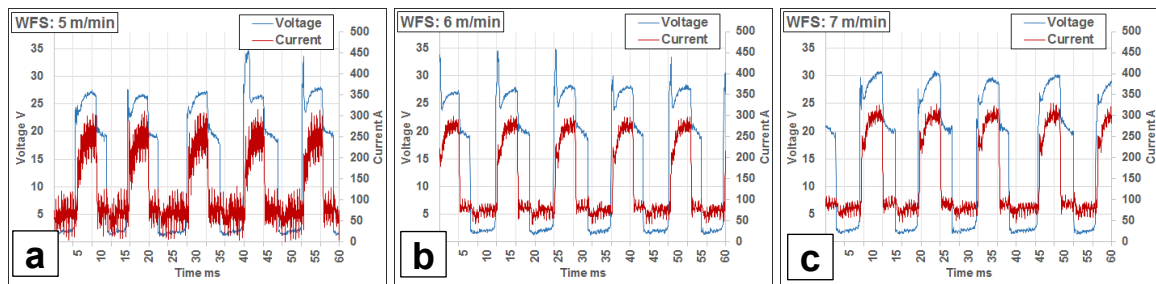


Fig. 76: Oscilloscope voltage/current graphs of the CMT process with a set WFS of a) 5, b) 6 and c) 7 m/min (Ar-30%He, ALC: 0%, DC: 0.0).

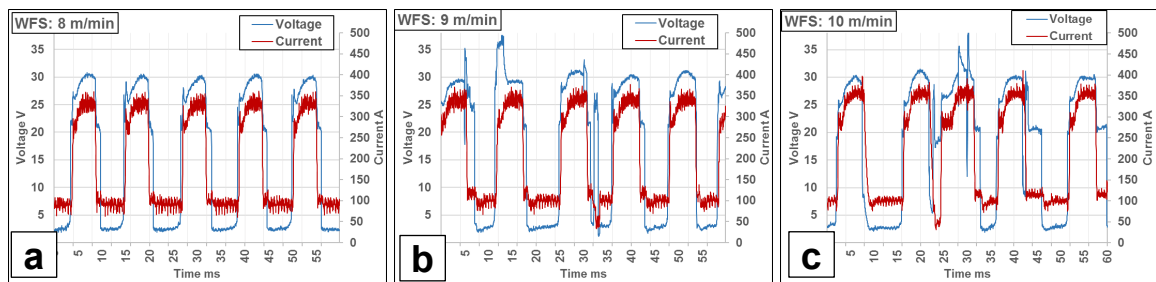


Fig. 77: Oscilloscope voltage/current graphs of the CMT process with a set WFS of a) 8, b) 9 and c) 10 m/min (Ar-30%He, ALC: 0%, DC: 0.0).

Some results from tests with varying WFS set values and CMT process are collected below in Table 37.

Table 37: Results from tests with CMT process and set WFS of 5–10 m/min

Parameter	WFS set value					
	5 m/min	6 m/min	7 m/min	8 m/min	9 m/min	10 m/min
Average voltage ⁽¹⁾	14.5 V	15.3 V	15.9 V	15.5 V	17.9 V	18.1 V
Average current ⁽¹⁾	123 A	139 A	153 A	182 A	205 A	218 A
Arc power $I_{aver} \times U_{aver}$	1784 W	2115 W	2437 W	2825 W	3665 W	3928 W
AIP (oscilloscope) ⁽²⁾	2474 W	2936 W	3333 W	4126 W	4946 W	5134 W
Heat input	119 J/mm	141 J/mm	160 J/mm	198 J/mm	237 J/mm	246 J/mm
Actual fire feed rate ⁽⁴⁾	5.5 m/min	6.4 m/min	7.3 m/min	8.8 m/min	10.3 m/min	11.0 m/min
Power ratio ⁽⁵⁾	398 W/mm ²	406 W/mm ²	404 W/mm ²	415 W/mm²	425 W/mm ²	413 W/mm ²

1. Average values from welding power source via Fronius Xplorer software.

2. AIP: eq. 5, p. 53.

3. Eq. 4, p. 52 vs. AIP, $k = 0.8$.

4. Measured by Fronius Xplorer.

5. Power ratio: eq. 7, p. 53.

As can be seen from the oscilloscope graphs in Fig. 76 and 77 and the results in the Table 37:

1. With the CMT process, when the voltage is dropped during the short-circuiting phase, a current drop follows immediately. The same happens when the phase shifts again from the short circuiting to the arcing phase. There are no signs of any abrupt rise in current that would cause spattering, as in the oscilloscope graph of the conventional MIG process (Fig. 70 a, p. 106).

2. There is relatively large fluctuation in the current with a set WFS of 5 m/min.
3. As the WFS setting is increased from 5–8 m/min, the voltage during the arcing phase increased from around 25 V to 30 V, and the current relatively more, from around 250 A to 320 A.
4. The voltage and current graphs are totally regular and the variation between the arcing and short-circuit phase is constant up to a set WFS of 8 m/min (Fig. 77, a).
5. When the set WFS is increased further, to 9 m/min (Fig. 77 b) and to 10 m/min (Fig. 77 c), the voltage and current levels during the arcing phase are not increased, but the process clearly becomes unstable. The voltage/current graph is not totally regular, and there is a clear irregular shifting between the arcing and short circuiting phases.

However, it should be noted that synergic line 1693 used in the test was designed for 100%Ar shield gas, and these tests were done with Ar-30%He shield gas because 100%Ar shield gas did not seem to work properly with a stringer motion, producing relatively narrow beads with large height and width variations. In other words, with 100%Ar shield gas the melt did not spread well and the beads suffered from the humping effect. This is discussed more in sections 3.2.3 and 3.2.4. With some He (30%) in the shield gas the melt spreads better and He also increases the arc voltage as can be seen from the oscilloscope graphs in Fig. 80 (page 115) taken from tests with both Ar-30%He and 100%Ar shield gases.

The control software of the CMT power source measures several parameters during the welding process. Fronius Xplorer software records and shows some of these parameters. One of these is actual wire feed speed (vD mean) that is recorded and showed with a frequency of 10 Hz. These values apparently show the rotation speed of the wire feed rolls that are next to the wire spool.

Fig. 78 a shows plots of the actual WFS (vD mean), or wire feed roll rotation values recorded by the Fronius Xplorer during 10 s of a single bead welding test, with the conventional MIG and pulsed MIG processes (and with ALC: 0%, DC: 0.0). Fig. 78 b shows these same (vD mean) values with the CMT process and the two auxiliary parameter combinations of ALC: 0%, DC: 0.0 and ALC: +15%, DC: -5.0. These results were acquired from conventional-pulse-CMT comparison tests (section 3.2.1, p. 106).

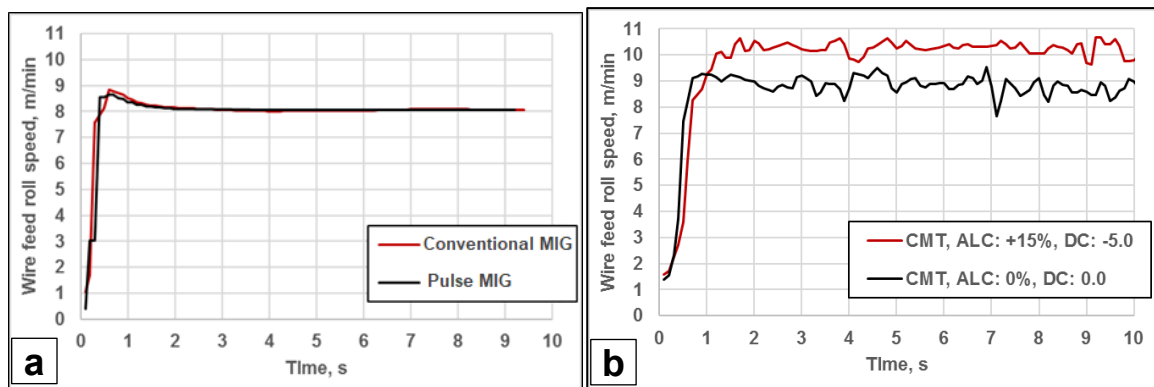


Fig. 78: Wire feed roll speed values with WFS set value of 8 m/min. a) Conventional MIG and pulsed MIG process (ALC: 0%, DC: 0.0). b) CMT process with ALC: 0, DC: 0.0 and ALC: +15%, DC: -5.0 (Ar-30%He shield gas).

Fig. 78 a shows clearly that with both the conventional MIG and pulsed MIG processes, wire feed roll rotation is constant and the same as the set WFS value.

As can be seen in Fig. 78 b from the CMT process, while the set WFS value is 8 m/min, there is a clear fluctuation in the actual WFS values. Values are around 8–9 m/min with ALC: 0%, DC: 0.0, and around 10 m/min with ALC: +15%, DC: -5.0. So the actual average WFS is around 10% higher than the set value when the values of ALC and DC are both 0, as was shown earlier in Table 37 on page 112. And this difference is even larger (~20%) with combination ALC: +15%, DC: -5.0, which has a greater effect on the actual deposition rate and on resulting cladding, as is shown in Fig. 84 on page 119.

3.2.3. CMT – the effects of shield gas and the auxiliary parameters

Current and voltage were measured with an oscilloscope during the tests with single beads presented in section 2.6.6 on page 82 in which the auxiliary parameters ALC and DC were varied, so the effects of these parameters were examined from the oscilloscope graphs. Tests were made with both Ar-30%He and 100%Ar shield gas to examine the effect of the shield gas had on the bead's appearance, and on the electrical parameters. The DC value was varied at three levels: -5.0, 0.0 and +5.0 and the ALC was varied at five levels: -30%, -15%, 0%, +15% and +30%. This yielded a total of 30 tests (2 x 3 x 5). These tests were made with a TS value of 1000 mm/min and with a WFS set value of 8 m/min. Test parameters are presented in Table 22 and 23, on page 76.

The effect of shield gas to the voltage/current waveform is presented in Fig. 79 from the tests with auxiliary parameter combination ALC: 0%, DC: 0.0.

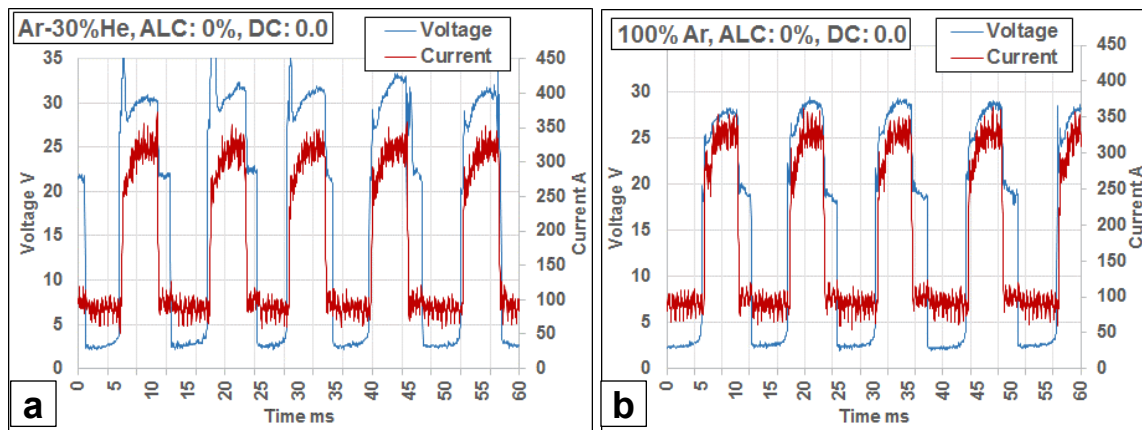


Fig. 79: Oscilloscope voltage/current graphs of CMT process.

- a) Shield gas: Ar-30%He, I_{aver} : 177 A, U_{aver} : 16.0 V, $I \times U$: 2922 W, AIP: 4005 W.
 - b) Shield gas: 100%Ar, I_{aver} : 178 A, U_{aver} : 15.4 V, $I \times U$: 2701 W, AIP: 3778 W.
- (WFS set: 8 m/min, TS: 1000 mm/min).

As can be seen from average voltage (U_{aver}) values recorded by the welding power source (Fronius Xplorer) presented in the caption for Fig. 79, the addition 30% He to the shield gas only increases the average voltage by ~0.6 V (16 V vs. 15.4 V), but the effect on voltage during the arcing phase is clearly larger, around 1.5–2.5 V. This rise in voltage is illustrated in more detail in Fig. 80 a with oscilloscope graphs from one arcing phase with Ar-30%He and 100%Ar shield gases.

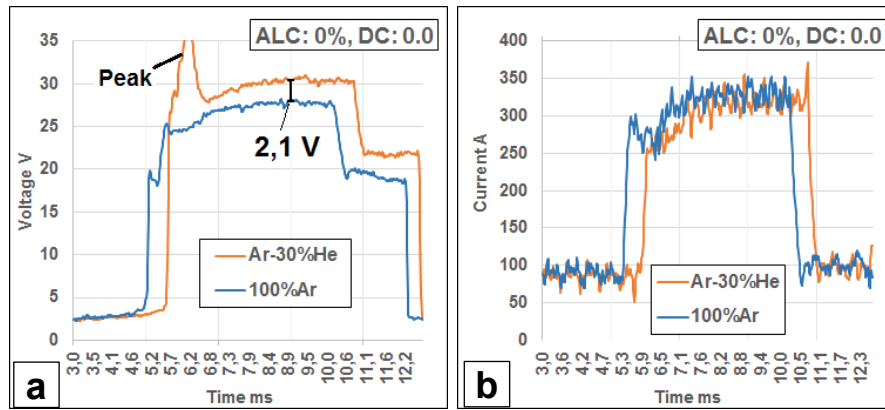


Fig. 80: Oscilloscope graphs of CMT process. a) voltage, and b) current of a one arcing phase with Ar-30%He and 100%Ar shield gases (WFS set: 8 m/min, TS: 1000 mm/min).

Unlike with the voltage (Fig. 80 a), the shield gas does not seem to have an effect on current, or if so it is negligible (Fig. 80 b). Average current (I_{aver}) values (177 A vs. 178 A) as well as the current during both the short circuit and arcing phases seem to be on the same level.

Current and voltage graphs from the oscilloscope for the single bead tests with Ar-30%He shield gas and with varying ALC and DC values are presented in Fig. 81 and 82.

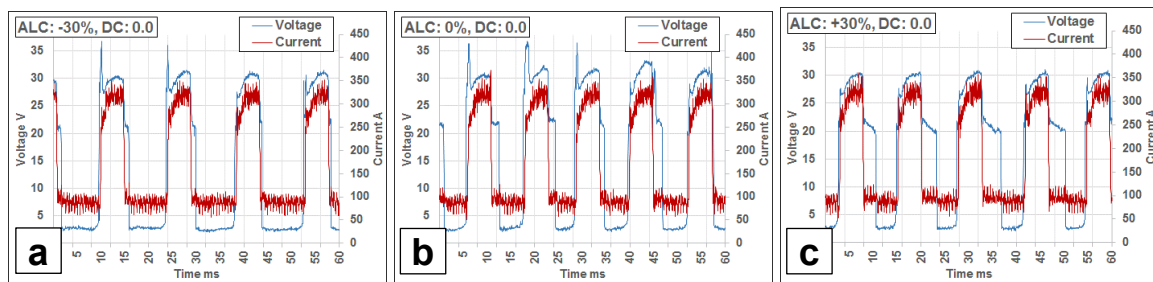


Fig. 81: Oscilloscope voltage/current graphs of the CMT process with varying ALC values. a) ALC: -30%, b) ALC: 0%, c) ALC: +30%. (Ar-30%He shield gas, DC: 0.0, set WFS: 8 m/min).

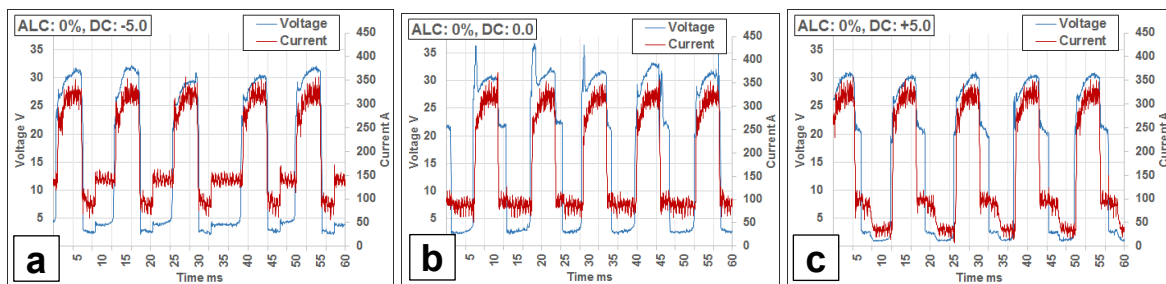


Fig. 82: Oscilloscope voltage/current graphs of the CMT process with varying DC values. a) DC: -5.0, b) DC: 0.0, c) DC: +5.0. (Ar-30%He shield gas, ALC: 0%, set WFS: 8 m/min).

A smaller section of the voltage and current graphs from the oscilloscope with varying ALC values (-30% – +30%) and DC: 0.0 are presented in Fig. 83 a to illustrate the effect of ALC on the process. Correspondingly, current oscilloscope graphs with varying DC values (-5.0, 0.0, +5.0) are presented in Fig. 83 b.

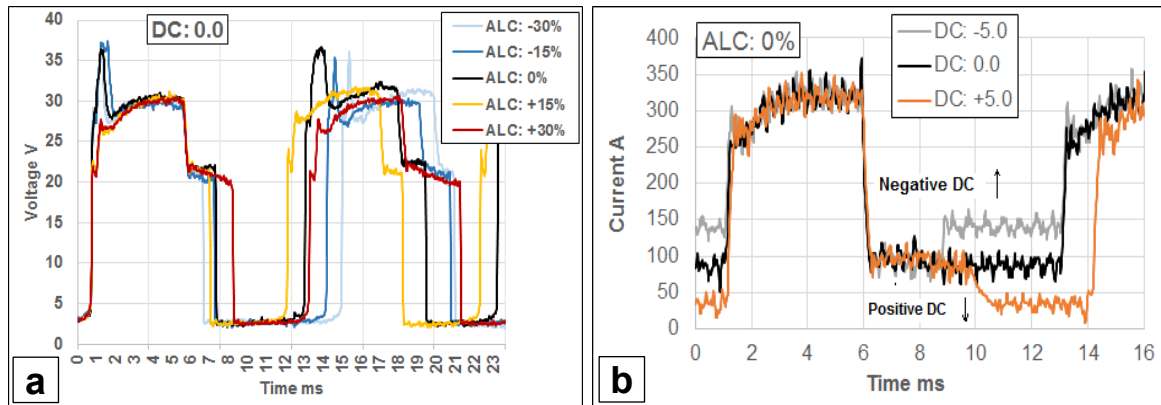


Fig. 83: Oscilloscope graphs of CMT process. a) The effect of ALC on the voltage with ALC values: -30%, -15%, 0%, +15% and +30%. (DC: 0.0, time span 25 ms). b) The effect of DC on the current with DC values: -5.0, 0.0 and +5.0 (ALC: 0%, time span 16 ms). (Ar-30%He shield gas, set WFS: 8 m/min).

As can be seen in Fig. 83 a, varying the ALC parameter has only a slight effect on voltage during the arcing phase. However, with small values of ALC: -30%, -15% and 0%, there is a voltage peak at the beginning of the arcing phase, although this does not happen with ALC: +15% and +30%. This spike was also not seen in the tests with 100%Ar shield gas (Fig. 79 and 80). So, the variation in ALC affects mainly on the length of the arcing phase, making it longer.

As can be seen in Fig. 83 b, negative DC values increase the current and positive DC values decrease it during the second half of the short circuiting phase. These current values during short circuit measured from the one phase presented in Fig. 83 b, are presented in Table 38, together with corresponding guideline values, AIP and actual WFS values.

Table 38: CMT process. Current values during the second half of a short circuit phase and corresponding AIP values and actual WFS values. (ALC: 0%, Ar-30%He shield gas, ALC: 0%, set WFS: 8 m/min).

DC	Current in 2 nd half of short circuit phase ⁽¹⁾			Guideline value ⁽²⁾	AIP ⁽³⁾	Actual WFS ⁽⁴⁾
	I _{min}	I _{max}	I _{aver}			
-5.0	124 A	164 A	~140 A	144 A	4307 W	9.8 m/min
0.0	61 A	110 A	~87 A	90 A	4005 W	8.8 m/min
+5.0	8 A	49 A	~34 A	36 A	3788 W	8.2 m/min

1) Values determined from the oscilloscope graph (Fig. 83 b).

2) Synergic line 1693 guideline values (Table 9, p. 51).

3) AIP: eq. 5, p. 53

4) Fronius Xplorer, vD mean

These average current values fit well with the guideline values presented earlier in Table 9 on page 51. Since the voltage/current graph is very similar with varying DC values, except for the change in short-circuit voltage, it can be said that the rise that the negative DC (-5.0) brings to the arc power is a result of the rise in short-circuiting current, which brings more resistive heating to the process, and thus makes it possible to melt more wire. So, the actual WFS increases even though the set WFS value remains the same, as presented in right-hand column in Table 38.

All the electrical parameters for the single bead tests with Ar-30%He shield gas are presented in Table 39 and with 100%Ar shield gas in Table 40. The highest values for power, actual WFS and frequency are highlighted in red colour and the lowest in blue. The auxiliary parameter combinations ALC: 0%, DC: 0.0 and ALC: +15%, DC: -5.0 are highlighted in grey colour in Table 39. These combinations of parameters were further examined in tests with adjacent beads. Corresponding single bead measurements results from the tests with Ar-30%He are presented in Table 41 on page 117 and with 100%Ar shield gas in Table 42 on page 124.

Table 39: Ar-30%He shield gas. CMT process. Results from the current and voltage measurements with an oscilloscope (set WFS: 8 m/min, TS: 1000 mm/min).

ALC	DC	Average I and U			Oscilloscope			Differ. I x U vs. AIP	Actual WFS m/min	Power Ratio ⁽¹⁾	Arcing %	Short- circuit %	Freq. Hz
		I _{aver} A	U _{aver} V	I x U W	I _{mean} A	U _{mean} V	AIP W						
-30%	-5.0	194	15.0	2909	190	14.9	3805	31%	9.3	362	53	47	74
	0.0	167	13.7	2295	163	13.6	3414	49%	7.9	382	56	44	71
	+5.0	142	12.8	1819	138	12.8	3182	75%	7.2	391	55	45	69
-15%	-5.0	197	15.9	3126	194	15.9	4043	29%	9.5	376	47	53	80
	0.0	173	14.9	2589	169	14.9	3717	44%	8.3	396	51	49	76
	+5.0	150	14.1	2122	147	14.1	3447	62%	7.6	401	49	51	74
0%	-5.0	200	16.9	3389	197	16.9	4307	27%	9.8	389	42	58	85
	0.0	181	16.2	2922	177	16.0	4005	37%	8.8	402	46	54	82
	+5.0	160	15.5	2488	157	15.3	3788	52%	8.2	408	46	54	80
+15%	-5.0	202	18.4	3709	199	18.5	4617	24%	10.2	400	35	65	89
	0.0	185	17.5	3231	179	17.4	4210	30%	9.1	409	38	62	85
	+5.0	171	16.7	2854	167	16.7	4121	44%	8.7	419	42	58	86
+30%	-5.0	199	19.7	3912	191	19.5	4553	16%	9.8	411	28	72	85
	0.0	183	18.5	3380	179	18.4	4249	26%	8.9	422	32	68	83
	+5.0	177	18.8	3320	171	18.8	4352	31%	8.8	437	32	68	84

1) Calculated from AIP power

Table 40: 100%Ar shield gas. CMT process. Results from the current and voltage measurements with an oscilloscope (set WFS: 8 m/min, TS: 1000 mm/min).

ALC	DC	Average I and U			Oscilloscope			Differ. I x U vs. AIP	Actual WFS m/min	Power Ratio ⁽¹⁾	Arcing %	Short- circuit %	Freq. Hz
		I _{aver} A	U _{aver} V	I x U W	I _{mean} A	U _{mean} V	AIP W						
-30%	-5.0	194	13.9	2702	196	13.8	3587	33%	9.2	345	51	49	74
	0.0	168	13.2	2216	169	13.0	3291	49%	8.1	359	54	46	71
	+5.0	142	12.4	1757	143	12.0	3051	74%	7.2	375	55	45	69
-15%	-5.0	197	15.4	3032	198	15.3	3930	30%	9.6	362	45	55	80
	0.0	173	14.3	2475	174	14.3	3567	44%	8.4	375	47	53	75
	+5.0	151	13.6	2053	152	13.4	3367	64%	7.7	387	49	51	74
0%	-5.0	197	16.4	3230	198	16.2	4083	26%	9.6	376	39	61	83
	0.0	176	15.3	2701	178	15.4	3778	40%	8.6	388	43	57	78
	+5.0	157	14.7	2309	159	14.6	3610	56%	8.0	399	45	55	77
+15%	-5.0	196	17.2	3371	198	17.0	4229	25%	NA	NA	35	65	85
	0.0	179	16.3	2908	180	16.2	3928	35%	8.8	395	39	61	80
	+5.0	145	14.5	2098	145	14.4	3151	50%	7.3	382	39	61	63
+30%	-5.0	188	17.9	3360	187	17.6	4020	20%	9.0	395	30	70	75
	0.0	170	16.7	2844	167	16.4	3547	25%	8.0	392	33	67	71
	+5.0	150	15.9	2383	148	15.7	3300	38%	7.3	400	34	66	61

1) Calculated from AIP power

The results show that there is a large difference in the arc power values determined with the conventional method of multiplying average current and voltage ($I_{aver} \times U_{aver}$) and with the AIP value. The measured values of this difference were around 20–70% with both Ar-30%He and 100%Ar shield gas, even though AIP values with the same settings in tests with 100%Ar shield gas were around 5–25% lower compared to the AIP values with Ar-30%He shield gas.

With Ar-30%He shield gas and using the $I_{aver} \times U_{aver}$ method (Table 39), the largest arc power value of 3912 W with a combination ALC: +30%, DC: -5.0, was twice that of the lowest arc power value of 1819 W with ALC: -30%, DC: +5.0. However, with the AIP method, the corresponding power values were 4553 W and 3182 W, respectively, so the difference was only ~40%. So, it is reasonable to assume that the AIP method gives more reliable results.

The proportion of the arcing phase grows as the ALC value gets smaller and vice versa, i.e. with large ALC values, the arcing gets smaller and the short circuiting phase gets larger. The frequency is higher with an ALC value of +15% and lowest with ALC -30%. DC only has a slight effect on frequency.

However, from the point of view of productivity, actual WFS and bead width, which would make it possible to clad adjacent beads with large TD and also relatively small penetration and dilution values, the auxiliary parameters ALC: +15%, DC: -5.0 seem to be the optimum combination (with Ar-30%He shield gas). With this combination, both AIP power and actual WFS were largest, 4617 W and 10.2 m/min, respectively, but power the ratio, which indicates process power in relation to feedstock import, was at the level of 400 W/mm², as it was with combination ALC: 0%, DC: 0.0. The effect of 'neutral' auxiliary parameter combination: ALC:

0%, DC: 0.0 and 'optimum': ALC: +15%, DC: -5.0 on the oscilloscope graph and the appearance and cross section dimensions of single bead are presented in Fig. 84, below.

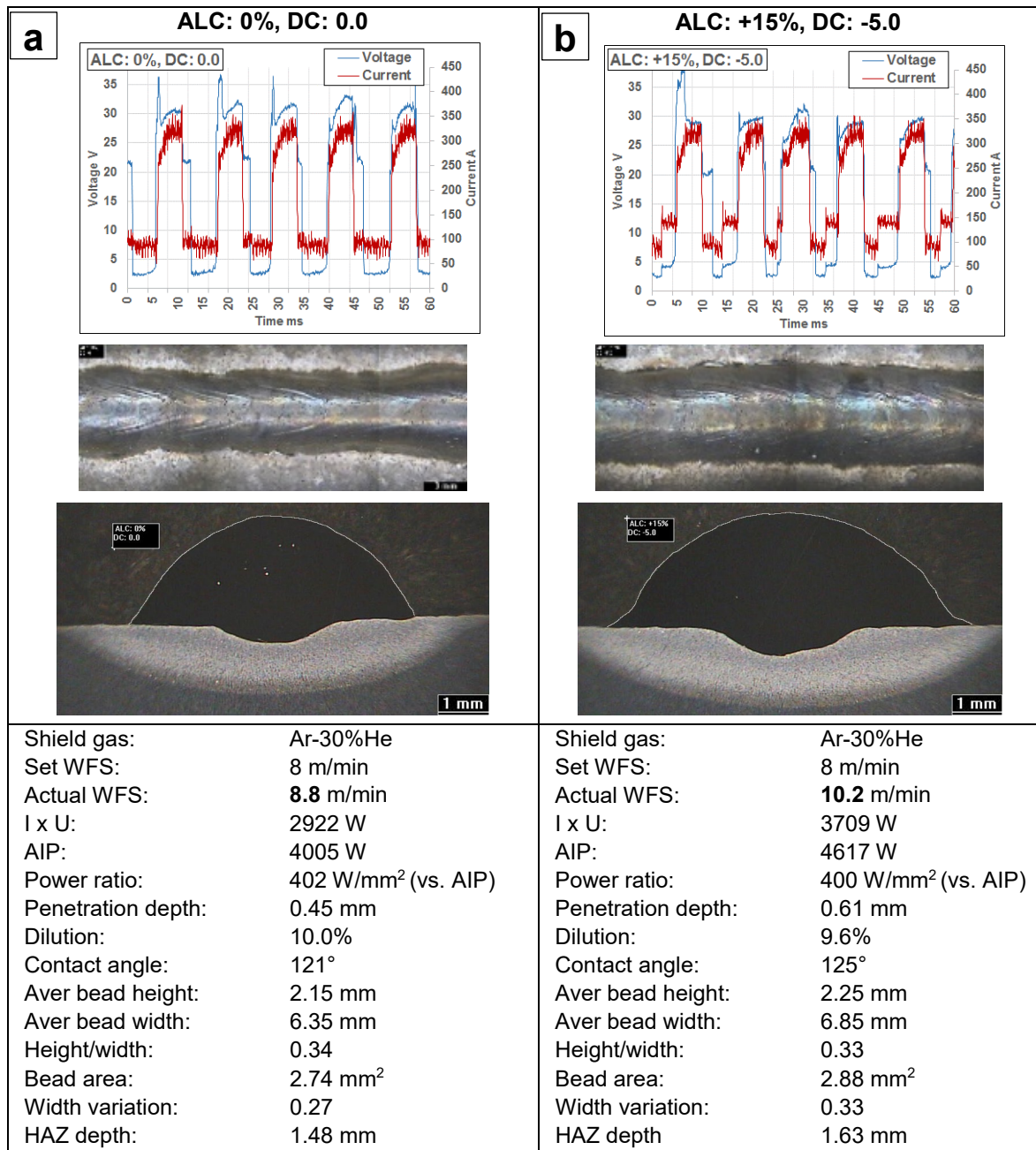


Fig. 84: Comparison of CMT single bead test samples with auxiliary parameter combinations of a) ALC: 0%, DC: 0.0, and b) ALC: +15%, DC: -5.0 (Ar-30%He shield gas, TS: 1000 mm/min, set WFS: 8 m/min).

The larger arc power and feedstock material input with combination ALC: +15%, DC: -5.0 produces a slightly wider bead even though the variation in bead width was slightly higher. However, the power ratio value, which indicates the relation between arc power, WFS and TS (eq. 7, p. 53), does not increase with ALC: +15%, DC: -5.0. Penetration is slightly larger with ALC: +15%, DC: -5.0, around 0.6 mm compared to 0.45 mm with ALC: 0%, DC: 0.0, but there is no difference in the geometrical dilution values (~10%), since the reinforcement (bead) area is larger with ALC: +15%, DC: -5.0. These two combinations, ALC: 0%, DC: 0.0 and ALC: +15%, DC: -5.0 as presented in Fig. 84 were used in cladding tests with adjacent beads and the results of these tests are presented in section 3.2.5 on page 130.

3.2.4. CMT – results with single beads

All the test parameters and settings in the CMT single bead tests are presented in section 2.4.2 (Table 22 and 23, p. 76). The tests with a TS 1000 mm/min were made with two the shielding gases: Ar-30%He and 100%Ar. These tests were used to examine whether it is possible to affect the bead shape and dilution by varying the auxiliary parameters ALC and DC, and also to examine the current and voltage with the oscilloscope during the process with varying ALC and DC values. The results from these oscilloscope measurements are presented above section 3.2.3 on page 114. Some tests were done with Ar-30%He shield gas and TS of 1200 and 1500 mm/min to see if the bead thickness could be decreased and productivity increased by using a higher TS.

The bead surfaces from the tests with TS at 1000 mm/min and with Ar-30%He shield gases are presented in Fig. 85 and the cross section images in Fig. 86. The measurements made on the bead surface and cross section images are presented in Table 41. The corresponding electrical parameters and process power measurement values from these tests are presented in Table 39 on page 117.

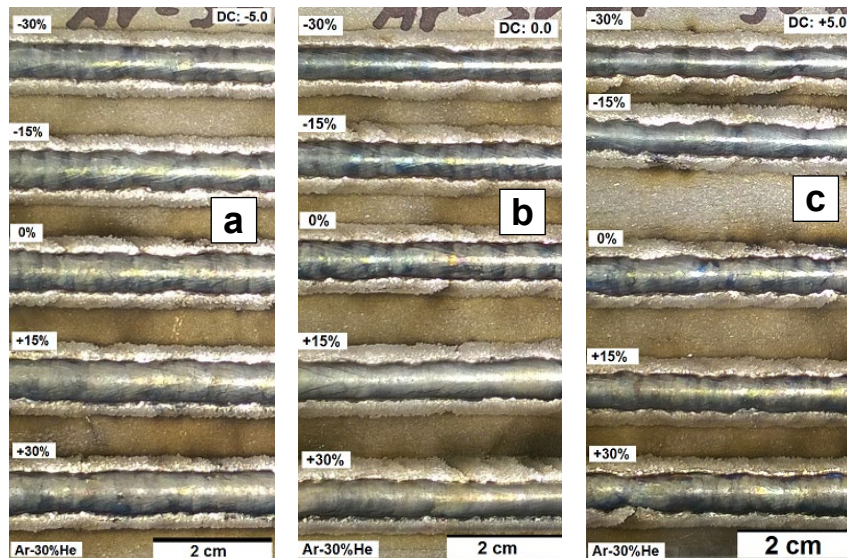


Fig. 85: Photographs of CMT single bead tests. Ar-30%He shield gas, TS: 1000 mm/min. ALC from top to bottom: -30%, -15%, 0%, +15% and +30%. DC from left to right: -5.0, 0.0 and +5.0 (set WFS: 8 m/min).

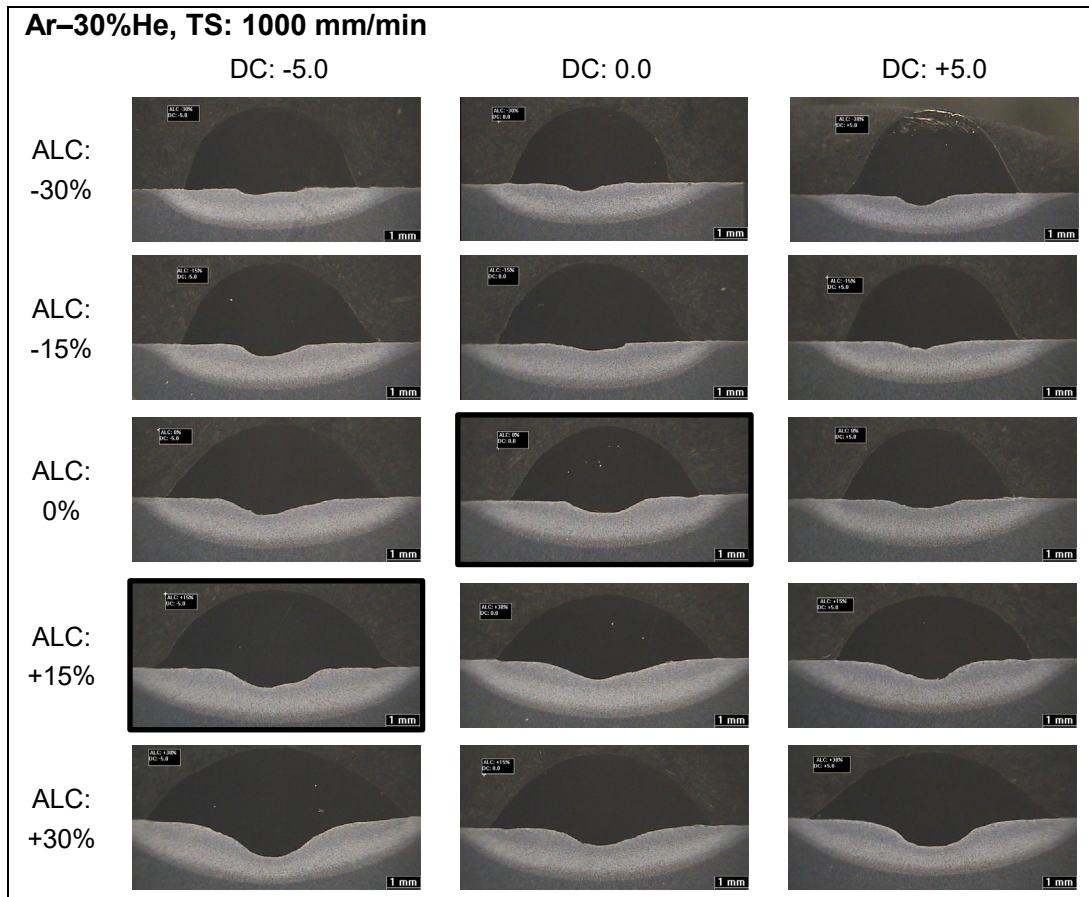


Fig. 86: Cross sections of CMT single bead tests. Ar-30%He shield gas, TS: 1000 mm/min. ALC from top to bottom: -30%, -15%, 0%, +15% and +30%. DC from left to right: -5.0, 0.0 and +5.0 (set WFS: 8 m/min).

Table 41: Cross section and bead surface measurement results of CMT single bead tests (Ar-30%He shield gas, TS: 1000 m/min, set WFS: 8 m/min).

ALC	DC	Penetr. depth [mm] ⁽¹⁾	A area [mm ²] ⁽¹⁾	B area [mm ²] ⁽¹⁾	HAZ depth [mm] ⁽¹⁾	Dilution ⁽¹⁾	Contact angles ⁽¹⁾		Bead height [mm] ⁽²⁾			Bead width [mm] ⁽²⁾			H/W ratio ⁽³⁾
									Min	Max	Aver	Min	Max	Aver	
-30%	-5.0	0.20	6.60	0.25	1.20	4%	110°	110°	2.25	2.45	2.35	5.50	6.80	6.15	0.38
	0.0	0.20	8.25	0.25	1.10	3%	116°	99°	2.05	2.30	2.20	4.85	6.35	5.65	0.39
	+5.0	0.35	8.90	0.45	1.05	5%	118°	116°	2.00	2.45	2.20	3.90	5.80	5.05	0.43
-15%	-5.0	0.40	9.75	0.55	1.25	5%	115°	125°	2.05	2.35	2.25	5.55	7.20	6.40	0.35
	0.0	0.25	9.70	0.35	1.25	5.5%	114°	115°	2.05	2.35	2.15	5.60	6.80	6.10	0.35
	+5.0	0.25	8.40	0.30	1.15	3.5%	114°	118°	1.95	2.35	2.15	4.30	6.10	5.35	0.40
0%	-5.0	0.50	9.80	1.00	1.45	9.5%	132°	125°	1.90	2.45	2.20	5.55	7.50	6.65	0.33
	0.0	0.45	8.35	0.90	1.40	10%	123°	119°	1.95	2.30	2.15	5.65	6.70	6.35	0.34
	+5.0	0.25	7.40	0.60	1.40	7%	120°	122°	1.85	2.30	2.10	5.40	6.80	6.20	0.34
+15%	-5.0	0.60	11.20	1.20	1.55	9.5%	127°	123°	2.10	2.40	2.25	6.25	7.40	6.85	0.33
	0.0	0.60	9.80	1.25	1.55	11%	127°	125°	2.00	2.45	2.15	5.40	7.25	6.45	0.34
	+5.0	0.60	8.05	1.20	1.45	13%	119°	118°	1.95	2.25	2.10	5.00	6.85	6.15	0.34
+30%	-5.0	1.15	11.10	3.30	1.70	23%	130°	138°	2.00	2.35	2.15	6.60	7.70	7.10	0.30
	0.0	0.60	8.65	1.55	1.65	15%	132°	130°	1.90	2.40	2.15	5.65	7.35	6.50	0.33
	+5.0	0.85	9.25	2.05	1.60	18%	139°	137°	1.75	2.30	2.10	5.10	7.70	6.45	0.32

1) Measured from one cross section, Fig. 40, p. 81.

2) Measured from bead outer surface with ~20 measurements (section 2.6.4, p. 81)

3) Average height / average width of the bead.

Images from the bead surface (Fig. 85) show that a TS of 1000 m/min and Ar-30%He shield gas produced relatively flat and wide beads with a smooth surface. The bead cross section images and measurements and the bead surfaces (Table 41) confirm these results.

The auxiliary parameter combinations ALC: 0%, DC: 0.0 and ALC: +15%, DC: -5.0, are highlighted in grey colour in Table 41. These combinations for auxiliary parameters were further examined in tests with adjacent beads.

The bead surfaces from the tests with 100%Ar shield gas and a TS of 1000 mm/min are presented in Fig. 87 and the cross section images in Fig. 88. The measurements of the bead surface and cross section images are presented in Table 41. The corresponding electrical parameters and process power measurement values from these tests are presented in Table 40 on page 118.

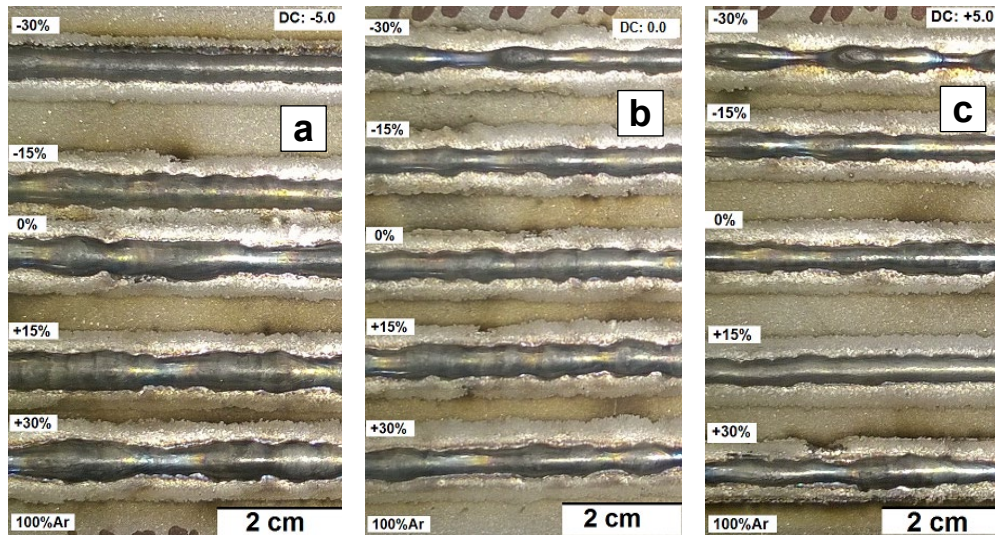


Fig. 87: Photographs of CMT single bead tests surfaces. TS: 1000 mm/min. 100%Ar shield gas, a) DC: -5.0, b) DC: 0.0, c) DC: +5.0. ALC from top to bottom: -30%, -15%, 0%, +15% and +30%. (set WFS: 8 m/min).

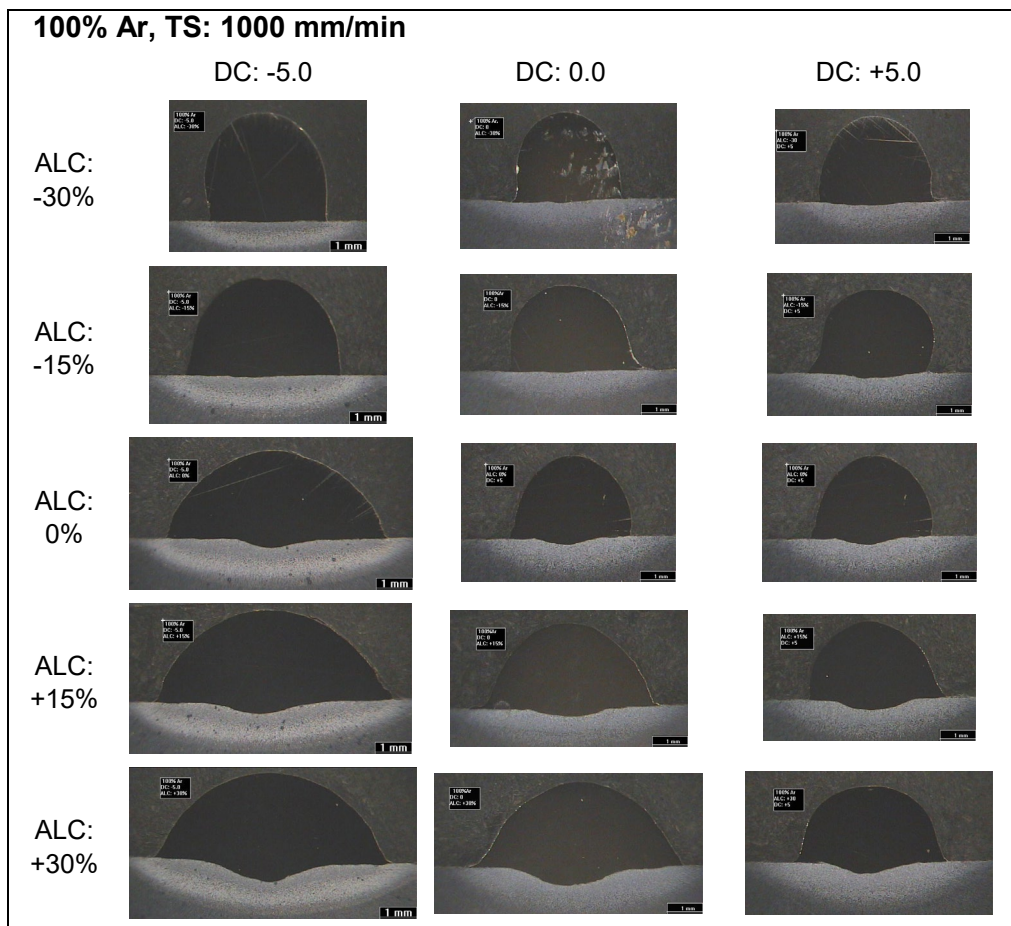


Fig. 88: Cross section images of CMT single bead tests. TS: 1000 mm/min. 100%Ar shield gas, ALC from top to bottom: -30%, -15%, 0%, +15% and +30%. DC from left to right: -5.0, 0.0 and +5.0 (set WFS: 8 m/min).

Table 42: Cross section and bead surface measurement results of CMT single bead tests (TS: 1000 mm/min, 100%Ar shield gas, set WFS: 8 m/min).

ALC	DC	Penetr. depth [mm] ⁽¹⁾	A area [mm ²] ⁽¹⁾	B area [mm ²] ⁽¹⁾	HAZ depth [mm] ⁽¹⁾	Dilution ⁽¹⁾	Contact angles ⁽¹⁾		Bead height [mm] ⁽²⁾			Bead width [mm] ⁽²⁾			H/W ratio ⁽³⁾
									Min	Max	Aver	Min	Max	Aver	
-30%	-5.0	0.05	NM	~0	0.90	~0%	81°	90°	2.65	3.10	2.85	4.10	4.70	4.40	0.65
	0.0	0.10	NM	~0	0.85	~0%	90°	95°	1.65	4.00	2.80	2.40	4.80	3.45	0.81
	+5.0	0.10	5.75	0.15	1.0	3%	93°	88°	1.25	4.40	2.70	2.00	4.30	3.35	0.81
-15%	-5.0	0.05	NM	~0	1.15	~0%	106°	95°	2.30	3.05	2.60	4.35	5.95	5.15	0.50
	0.0	0.05	NM	~0	0.90	~0%	90°	107°	2.25	3.15	2.65	3.40	4.90	4.15	0.63
	+5.0	0.15	5.80	0.20	1.0	4%	120°	71°	2.10	3.10	2.50	3.25	4.90	4.10	0.61
0%	-5.0	0.25	11.35	0.50	1.40	4%	109°	109°	2.10	3.05	2.50	4.00	6.40	5.25	0.48
	0.0	0.30	7.15	0.50	1.25	7%	94°	76°	1.95	2.85	2.50	4.05	5.85	4.95	0.51
	+5.0	0.20	5.50	0.20	1.10	3%	105°	93°	1.70	3.25	2.50	3.60	5.65	4.60	0.54
+15%	-5.0	0.30	12.40	0.90	1.45	7%	106°	125°	1.90	2.75	2.35	4.50	6.60	5.75	0.41
	0.0	0.25	7.55	0.34	1.10	4%	111°	111°	2.15	2.80	2.40	3.85	6.20	5.15	0.46
	+5.0	0.35	5.60	0.45	1.15	7%	95°	113°	2.20	2.45	2.35	3.75	4.95	4.30	0.55
+30%	-5.0	0.60	11.60	1.40	1.55	11%	120°	112°	1.90	2.85	2.40	4.10	6.90	5.40	0.44
	0.0	0.50	8.50	1.10	1.30	11%	120°	122°	1.85	2.95	2.50	3.20	5.65	4.15	0.60
	+5.0	0.30	6.20	0.45	1.30	7%	105°	107°	1.80	3.40	2.35	3.25	5.50	4.15	0.56

1) Measured from one cross section, Fig. 40, p. 81

2) Measured from bead outer surface with ~20 measurements (section 2.6.4, p. 81)

3) Average height /average width of the bead.

NM Not measured

Single beads made with 100%Ar shield gas (Fig. 87 and 88) appeared narrower and there was more variation in both the bead width and height, than in the tests with Ar-30% shield gas (Fig. 85). The results in Table 42 only confirm this discovery. However, the auxiliary parameter combination of ALC: +15%, DC: -5.0, which was found to be 'optimum' with Ar-30%He shield gas, also showed relatively good results with 100%Ar shield gas. In fact, measured bead height/width ratio was the lowest (0.41) with this combination of ALC: +15%, DC: -5.0, and this combination was further tested in cladding with 100%Ar shield gas and adjacent beads (Table 46, p. 133).

Higher TS of 1200 and 1500 mm/min were tested only with Ar-30%He shield gas, mainly to see if it would be possible to achieve lower bead thickness and if this would improve productivity in terms of square meters per hour.

The bead surfaces from the tests with TS at 1200 mm/min (Ar-30%He shield gas) are presented in Fig. 89 and the cross section images in Fig. 90. The measurements of the bead surface and cross section images are presented in Table 43.

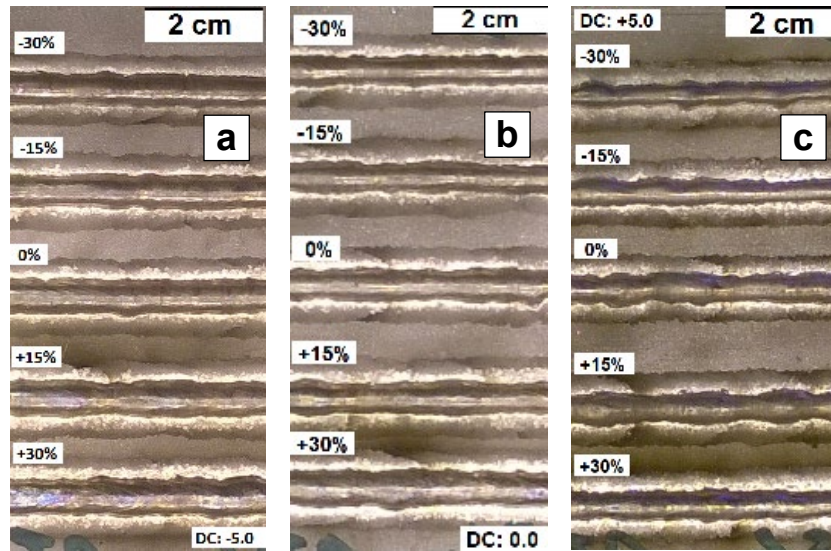


Fig. 89: Photographs of CMT single bead tests surfaces. TS: 1200 mm/min. Ar-30%He shield gas, a) DC: -5.0, b) DC: 0.0, c) DC: +5.0. ALC from top to bottom: -30%, -15%, 0%, +15% and +30%. (set WFS: 8 m/min).

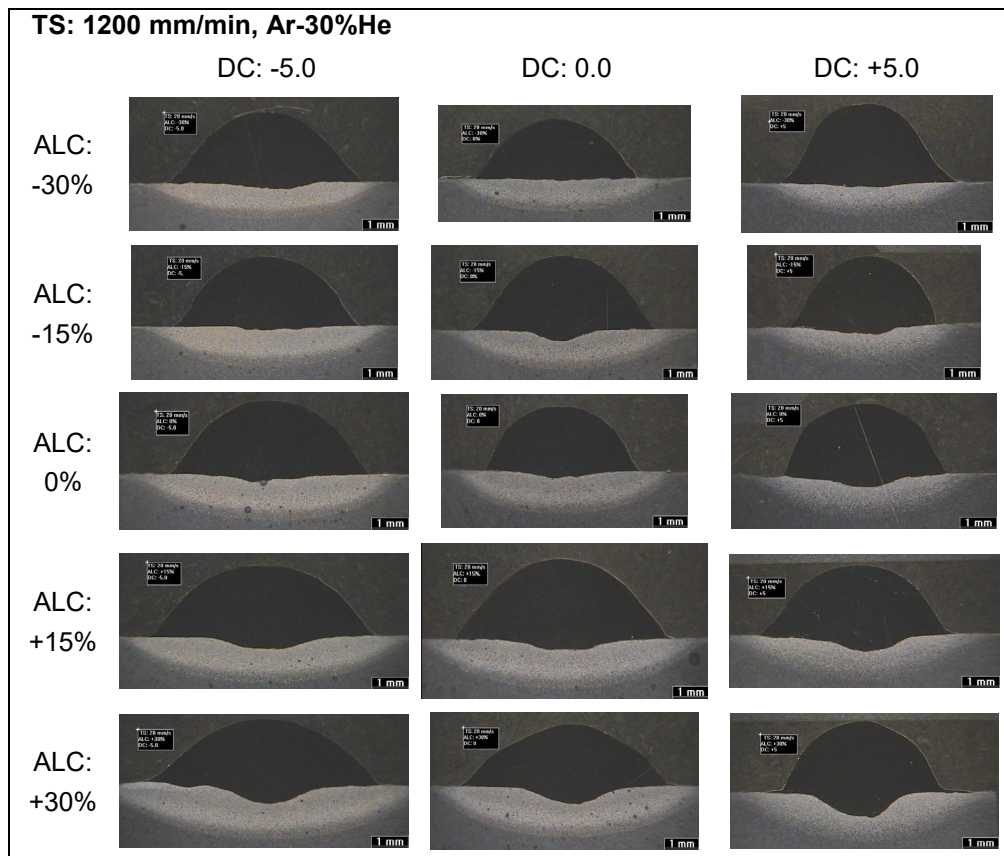


Fig. 90: Cross section images of CMT single bead tests. TS: 1200 mm/min, Ar-30%He shield gas. ALC from top to bottom: -30%, -15%, 0%, +15% and +30%. DC from left to right: -5.0, 0.0 and +5.0 (set WFS: 8 m/min).

Table 43: Cross section and bead surface measurement results of CMT single bead tests (TS: 1200 mm/min, Ar-30%He shield gas, set WFS: 8 m/min).

ALC	DC	Penetr. depth [mm] (1)	A area [mm ²] (1)	B area [mm ²] (1)	HAZ depth [mm] (1)	Dilu- tion (1)	Contact angles (1)		Bead height [mm] (2)			Bead width [mm] (2)			H/W ratio (3)
									Min	Max	Aver	Min	Max	Aver	
-30%	-5.0	0.15	7.31	0.35	1.00	5%	129°	131°	1.95	2.20	2.10	4.95	5.75	5.25	0.40
	0.0	0.10	5.51	0.12	1.00	2%	124°	121°	1.75	2.05	1.90	4.25	5.40	4.75	0.40
	+5.0	0.15	7.33	0.28	0.90	4%	120°	123°	1.90	2.70	2.25	3.10	4.75	3.90	0.58
-15%	-5.0	0.10	7.07	0.23	1.10	3%	127°	122°	2.00	2.20	2.10	4.75	6.10	5.50	0.38
	0.0	0.30	7.61	0.47	1.10	6%	127°	124°	1.80	2.20	2.00	4.35	5.95	4.95	0.41
	+5.0	0.25	5.59	0.38	0.85	6%	120°	99°	1.85	2.25	2.00	3.40	5.50	4.25	0.47
0%	-5.0	0.25	7.63	0.39	1.20	5%	126°	122°	2.05	2.30	2.15	5.25	6.40	5.90	0.37
	0.0	0.20	6.02	0.35	1.15	6%	117°	118°	1.80	2.25	2.00	4.65	6.10	5.50	0.36
	+5.0	0.40	6.95	0.74	1.15	10%	111°	117°	1.65	2.32	2.05	3.85	5.95	5.00	0.41
+15%	-5.0	0.35	8.95	0.79	1.30	8%	128°	125°	1.90	2.30	2.15	5.30	6.65	6.05	0.35
	0.0	0.30	8.75	0.69	1.30	7%	130°	128°	1.85	2.30	2.05	4.80	6.80	5.65	0.36
	+5.0	0.50	7.08	0.97	1.25	12%	125°	120°	1.60	2.35	2.05	4.00	6.15	5.15	0.40
+30%	-5.0	0.55	7.85	1.33	1.55	15%	139°	129°	1.90	2.30	2.10	6.00	7.10	6.55	0.32
	0.0	0.50	7.37	1.08	1.45	13%	136°	131°	1.80	2.05	2.00	5.70	7.00	6.20	0.32
	+5.0	0.75	7.11	1.33	1.45	16%	117°	115°	1.70	2.80	2.10	4.10	6.60	5.05	0.41

1) Measured from one cross section, Fig. 40, p. 81

2) Measured from bead outer surface with ~20 measurements (section 2.6.4, p. 81).

3) Average height /average width of the bead.

Both the appearance of the single bead in Fig. 89 and the measurements in Table 43 show that as TS was increased, the height of a single bead only decreases slightly compared to a TS of 1000 mm/min.

The bead surfaces from the tests with TS 1500 mm/min (Ar-30%He shield gas) are presented in Fig. 91, and cross section images in Fig. 92. The measurements of the bead surface and the cross section images are presented in Table 44.

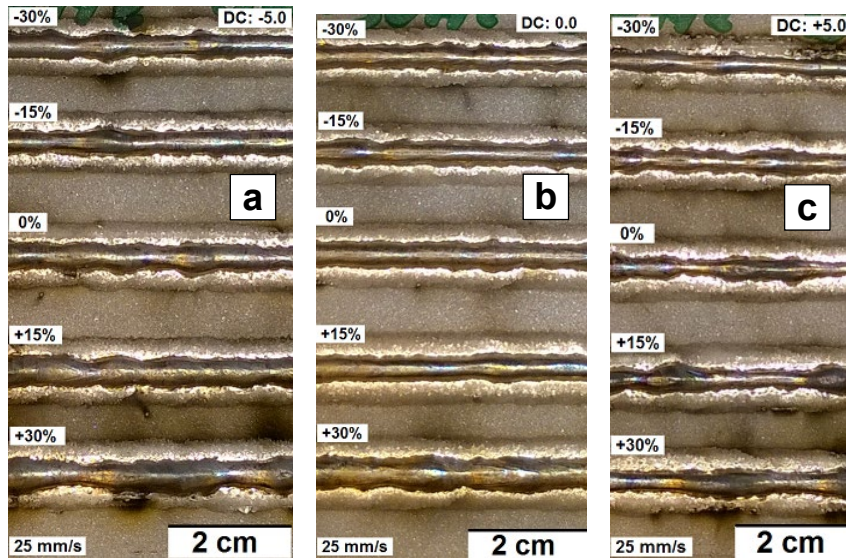


Fig. 91: Photographs of CMT single bead tests surfaces. TS: 1500 mm/min, Ar-30%He shield gas, a) DC: -5.0, b) DC: 0.0, c) DC: +5.0. ALC from top to bottom: -30%, -15%, 0%, +15% and +30%. (set WFS: 8 m/min).

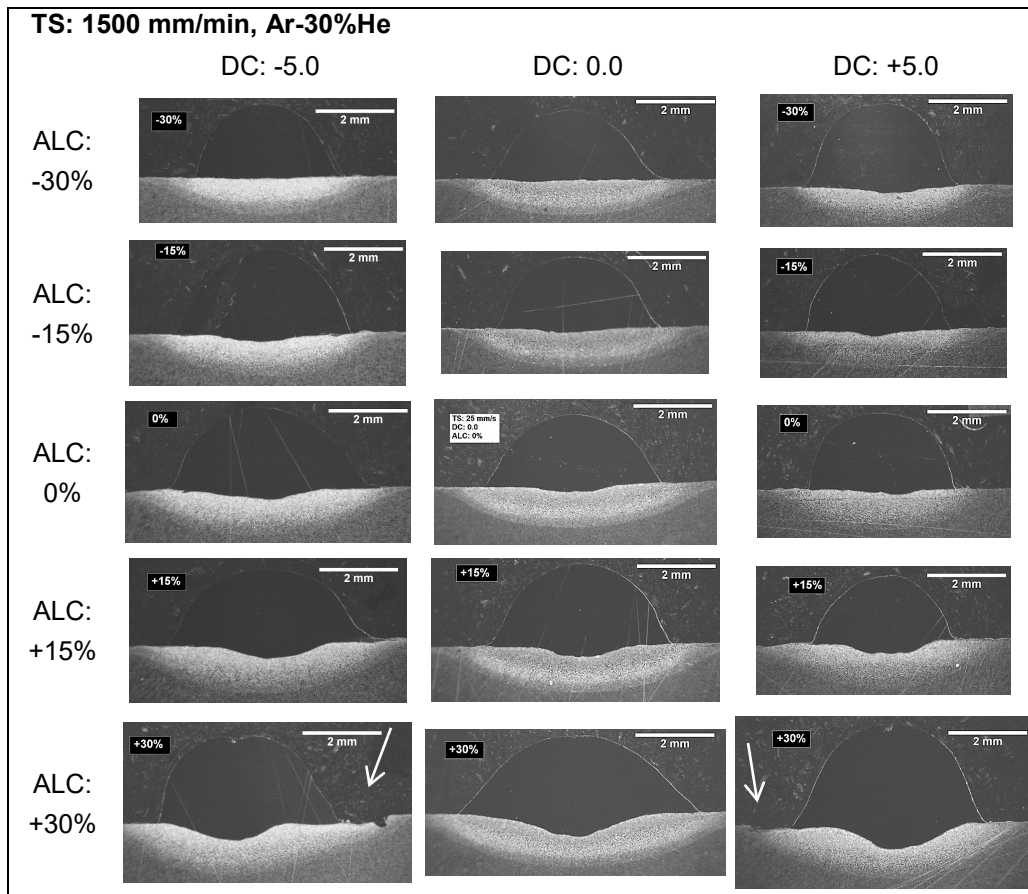


Fig. 92: Cross section images of CMT single bead tests. TS: 1500 mm/min, Ar-30%He shield gas. ALC from top to bottom: -30%, -15%, 0%, +15% and +30%. DC from left to right: -5.0, 0.0 and +5.0 (set WFS: 8 m/min).

Some undercutting defects were detected in the cross sections of the test samples made with a TS of 1500 mm/min and ALC: +30%. Some of these are shown by arrow in Fig. 92 and a higher magnification image of this is presented in the following image on Fig. 93.

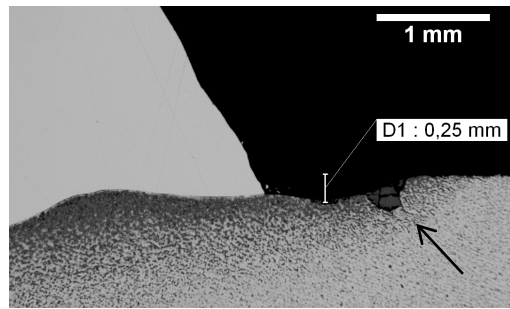


Fig. 93: Higher magnification of undercutting defect shown by the arrow in the previous image (Fig. 92). ALC: 30%, DC: -5.0. (Ar-30%He, TS: 1500 mm/min, set WFS: 8 m/min).

However, the undercut is so small, ~0.25 mm, that it could not be detected from the outer surface of the sample. The reason for the undercutting is probably the combination of a high TS and a large ALC. Large value of ALC (+30%) increases the duration of the arcing period and also the arc length, which both increase the arc pressure and arc column width.

Table 44: CMT single bead cross section and bead surface measurement results (TS: 1500 mm/min, Ar-30%He shield gas, set WFS: 8 m/min)

ALC	DC	Penetr. depth [mm] (1)	A area [mm ²] (1)	B area [mm ²] (1)	HAZ depth [mm] (1)	Dilution (1)	Contact angles (1)		Bead height [mm] (2)			Bead width [mm] (2)			H/W ratio (3)
									Min	Max	Aver	Min	Max	Aver	
-30%	-5.0	~0	NM	~0	1.0	~0%	106°	122°	1.80	2.35	2.00	3.30	5.10	4.05	0.50
	0.0	0.05	NM	~0	0.95	~0%	120°	121°	1.60	1.85	1.75	3.65	5.35	4.35	0.40
	+5.0	0.15	5.65	0.20	1.0	4%	107°	111°	1.65	2.35	1.95	2.75	4.40	3.40	0.57
-15%	-5.0	0.2	6.95	0.35	1.1	5%	114°	108°	1.85	2.40	2.10	3.40	5.25	4.30	0.49
	0.0	0.1	NM	~0	1.0	~2%	114°	117°	1.65	2.00	1.85	3.90	5.05	4.35	0.42
	+5.0	0.15	5.00	0.14	0.9	3%	101°	107°	1.50	2.05	1.85	3.45	4.95	4.15	0.44
0%	-5.0	0.3	7.20	0.55	1.35	7%	119°	117°	1.65	2.40	2.05	3.90	5.45	4.65	0.44
	0.0	0.2	5.45	0.30	1.15	5%	118°	118°	1.60	1.95	1.80	4.10	5.85	4.70	0.39
	+5.0	0.15	5.55	0.15	1.0	3%	98°	104°	0.95	3.45	2.00	2.40	5.20	3.75	0.52
+15%	-5.0	0.4	6.75	0.75	1.3	10%	118°	116°	1.65	2.25	1.95	3.95	6.05	4.95	0.39
	0.0	0.3	6.50	0.50	1.2	7%	116°	116°	1.80	2.25	1.95	4.15	5.80	4.65	0.42
	+5.0	0.3	4.25	0.50	1.25	10%	114°	110°	0.90	3.05	2.05	2.75	5.25	3.90	0.53
+30%	-5.0	0.5	7.95	0.95	1.55	11%	100°	122°	1.40	2.60	2.00	3.55	6.35	4.95	0.40
	0.0	0.55	7.90	1.25	1.5	14%	131°	136°	1.45	2.10	1.85	4.40	6.45	5.50	0.33
	+5.0	0.65	8.65	1.20	1.45	12%	116°	109°	1.45	2.65	1.90	3.55	6.60	4.55	0.42

1) Measured from one cross section, Fig. 40, p. 81

2) Measured from bead outer surface with ~20 measurements (section 2.6.4, p. 81)

3) Average height /average width of the bead.

NM Not measured

Single bead cross sections and the measurement results with a TS of 1500 mm/min do not have too much relevance, since it is quite obvious from the appearance of the beads (Fig. 91) that the success of cladding with this TS and adjacent beads would be uncertain. The beads are too narrow and there is clearly too much variation in bead height, width and straightness. Some test claddings appear good in the cross section images (ALC: +30%, DC: 0, Fig. 92 bottom row, middle), but it should be remembered that a single cross section represents only one single randomly chosen sample along the welding pass. However, one test with adjacent

beads and a slightly lower TS of 1400 m/min was made. The results of this test are presented in Table 48 and Fig. 101 on page 136.

Some images and measurements from single bead tests with auxiliary parameters ALC: 0%, DC: 0.0 and with TS of 1000, 1200 and 1500 mm/min are collected below in Fig. 94. The variations in bead width are illustrated clearly in these images.

a TS: 1000 mm/min ALC: 0%, DC: 0.0	b TS: 1200 mm/min ALC: 0%, DC: 0.0	c TS: 1500 mm/min, ALC: 0%, DC: 0.0
<div>min max aver</div> <div>Width 5.6 mm 6.7 mm 6.4 mm</div> <div>Height 2.0 mm 2.3 mm 2.2 mm</div>	<div>min max aver</div> <div>Width 4.6 mm 6.1 mm 5.5 mm</div> <div>Height 1.8 mm 2.3 mm 2.0 mm</div>	<div>min max aver</div> <div>Width 4.1 mm 5.9 mm 4.7 mm</div> <div>Height 1.6 mm 2.0 mm 1.8 mm</div>
<div>Width stdev: 0.27</div> <div>Height stdev: 0.08</div> <div>Height/width: 0.34</div> <div>Penetration: 0.5 mm</div> <div>HAZ depth: 1.25 mm</div> <div>Contact angle: ~121°</div>	<div>Width stdev: 0.45</div> <div>Height stdev: 0.13</div> <div>Height/width: 0.36</div> <div>Penetration: 0.2 mm</div> <div>HAZ depth: 1.15 mm</div> <div>Contact angle: ~118°</div>	<div>Width stdev: 0.47</div> <div>Height stdev: 0.11</div> <div>Height/width: 0.39</div> <div>Penetration: 0,2 mm</div> <div>HAZ depth: 1.15 mm</div> <div>Contact angle: ~118°</div>

Fig. 94: CMT single bead surface appearance (top), bead cross section (middle) and measured dimensions (bottom). TS values of: a) 1000 mm/min, b) 1200 mm/min, and c) 1500 mm/min (Ar-30%He shield gas, set WFS: 8 m/min).

As can be seen from the bead surfaces, the cross section images and the measurements presented in Fig. 94, a higher travel speed mainly affects the bead width, but not its height. However, penetration and dilution also decrease as TS increases.

The results of bead height and width measurements with TS values of 1000 mm/min, 1200 mm/min and 1500 mm/min, and with DC: 0.0 are collected in the graphs in Fig. 95 below.

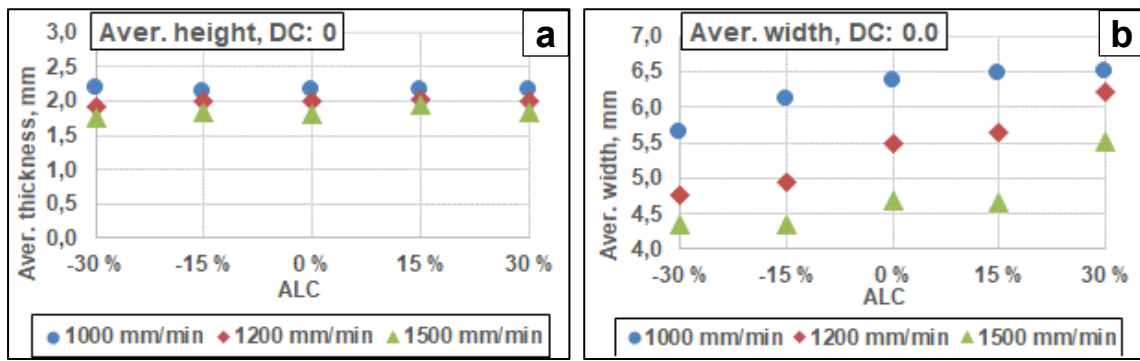


Fig. 95: CMT single bead dimensions with TS values of 1000 mm/min, 1200 mm/min and 1500 mm/min. a) Single bead average height, b) Single bead average width. (Ar-30%He shield gas, set WFS: 8 m/min, DC: 0.0).

The scale on the Y-axis of the graphs is the same, 3 mm. This shows that there is a small decrease in bead height, in the order of less than 0.5 mm (Fig. 95 a) when TS is increased from 1000 to 1500 mm/min, resulting in ~1.5 mm loss in average bead width (Fig. 95 b). As the TS gets higher, the bead gets slightly lower and a lot narrower and the contact angle decreases. However, the most distinctive feature of an increasing TS, bead unevenness, is not revealed in these graphs. Furthermore variations in the bead width clearly leads to humping type defects in extreme cases with a high TS and/or incorrect combination of the auxiliary parameters ALC and DC.

3.2.5. CMT – results with adjacent beads

In order to achieve higher productivity in terms of cover rate (the area covered in relation to time), there are basically two approaches: to increase track displacement (TD), or to increase travel speed (TS). The results from cladding tests with adjacent beads are presented below, where these two parameters, TD and TS, were varied to find the optimum values.

Most of the tests claddings with adjacent beads were done with Ar-30%He shield gas, since the single bead tests had shown that some He is needed in the shield gas to make the melt less viscous and to get a wider bead with a larger contact angle. However, some tests were also done with 100%Ar shield gas, a TS of 1000 mm/min and a TD of 3.8 mm (Fig. 99, p. 134) to see if it is possible to produce successful cladding with a stringer motion and 100%Ar shield gas.

First, a series of test claddings with a TS of 1000 mm/min, Ar-30%He shield gas and adjacent beads were made with the 'neutral' combination of ALC: 0%, DC: 0.0, and the 'optimum' combination of ALC: +15%, DC: -5.0. These combinations were selected based on the results from the single bead tests and the main aim was to see if it would be beneficial to use ALC: +15%, DC: -5.0 instead of the neutral combination, ALC: 0%, DC: 0.0. The TD was varied between 3.4–4.8 mm to find the optimum and limiting values. All the other parameters were the same as in the tests with single beads except for the fact that the torch work angle was 10°, since this seemed to help with visual checking during the process to prevent the arc from hitting the top of the previous bead and/or the melt pool accumulating on the previous bead. The cross section images from these test samples are presented in Fig. 96 and 97. These images were taken both with optical stereo (Fig. 96) and inverted (metallographic) microscopes (Fig. 97). Some cladding surface images (photographs) are also presented from

the test claddings to show that with larger TD values, some holes or underfill-type defects started to appear on the surfacer.

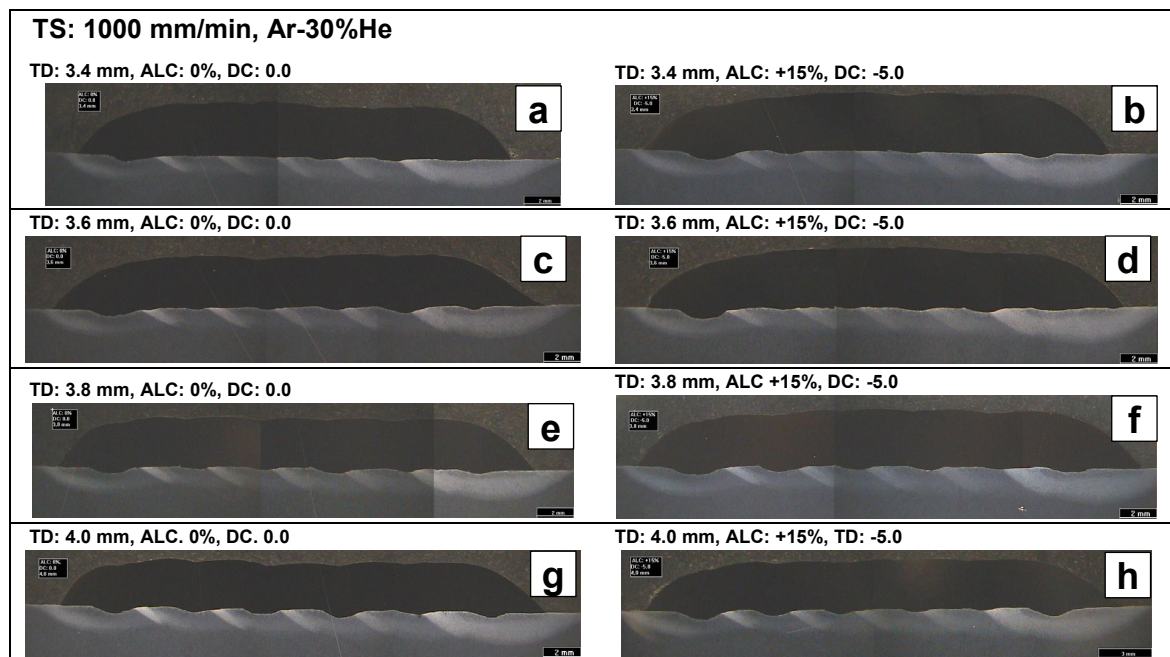


Fig. 96: CMT test claddings with adjacent beads. TD: 3.4–4.0 mm. Auxiliary parameter combinations: ALC: 0%, DC: 0.0 (a, c, e, g) and ALC: +15%, DC: -5.0 (b, d, f, h). Stereo microscope images from base material etched cross sections (set WFS 8: m/min).

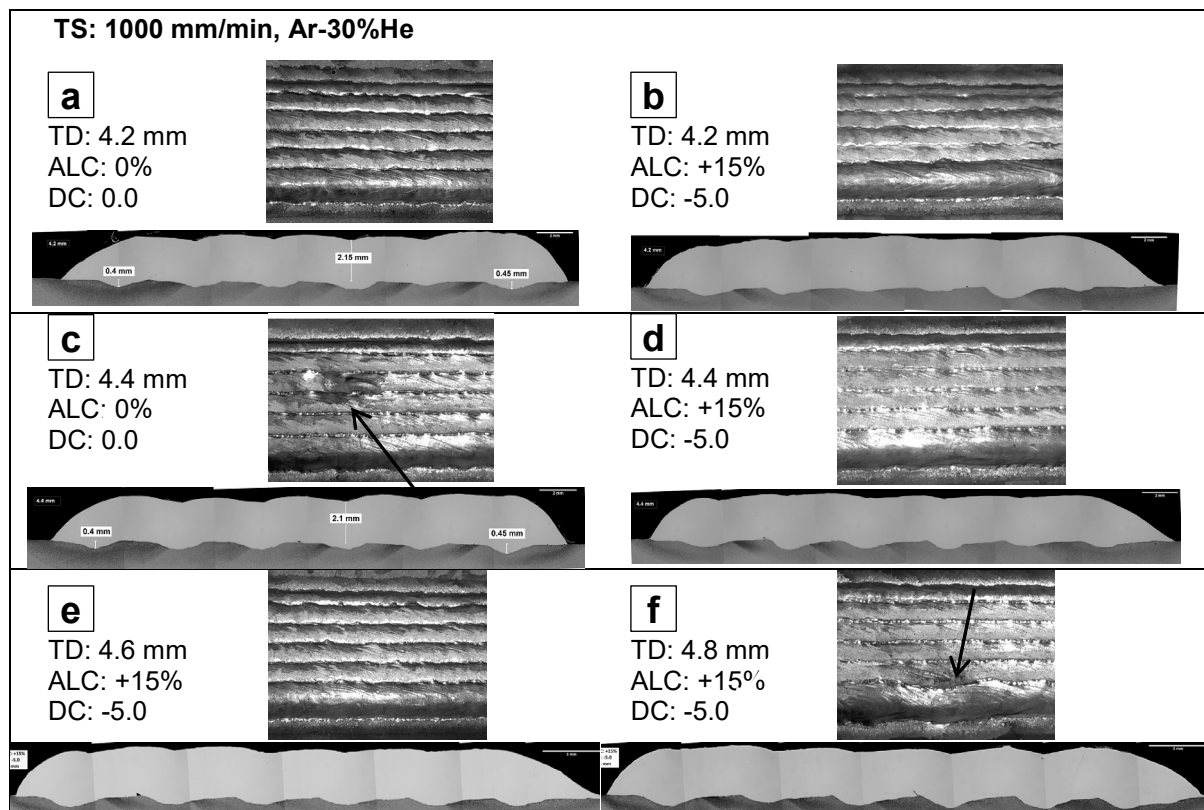


Fig. 97: CMT test claddings with adjacent beads. TD: 4.2–4.8 m. Ar-30%He, TS: 1000 mm/min. Cladding surface appearance and right: cross section, inverted microscope images, magnification: 2,5x. a) and c) ALC: 0%, DC: 0.0. b), d), e) and f) ALC: +15%, DC: -5.0. Arrows (Fig c and f) point to holes that started to form on the surface (set WFS 8: m/min).

The combination ALC: 0%, DC: 0.0 started to generate holes in the cladding surface already with a TD of 4.0 mm so no further tests with TD 4.6 and 4.8 mm and ALC: 0%, DC: 0.0 were made, since it seemed obvious that these tests would not be successful.

The penetrations of each bead (6 pcs) were measured from the cross section images and both the maximum and average values of these measurements are presented in Table 45.

Table 45: CMT test claddings with adjacent beads. Results from the measurements on cross sections (Ar-30%He shield gas, TS of 1000 mm/min, set WFS: 8 m/min).

TD mm	Cover. rate ⁽¹⁾ m ² /h	ALC	DC	Arc power W ⁽²⁾	Penetr. depth		Thickness ⁽⁴⁾		Test cladding appearance
					max mm	aver. ⁽³⁾ mm	min mm	max mm	
3.4	0.20	0%	0.0	2809	0.42	0.19	2.5	2.9	OK
		+15%	-5.0	3615	0.55	0.21	2.2	3.1	OK
3.6	0.22	0%	0.0	2838	0.44	0.29	2.4	2.7	OK
		+15%	-5.0	3626	0.63	0.28	2.3	3.1	OK
3.8	0.23	0%	0.0	2926	0.38	0.25	2.3	2.7	OK
		+15%	-5.0	3666	0.46	0.26	2.2	3.0	OK
4.0	0.24	0%	0.0	2883	0.44	0.32	2.1	2.5	OK
		+15%	-5.0	3638	0.60	0.37	2.5	3.0	OK
4.2	0.25	0%	0.0	2884	0.44	0.37	2.0	2.6	OK
		+15%	-5.0	3678	0.68	0.38	2.3	2.8	OK
4.4	0.26	0%	0.0	2892	0.49	0.39	2.0	2.5	Holes, underfill
		+15%	-5.0	3650	0.51	0.42	2.1	2.5	OK
4.6	0.28	0%	0.0	–	–	–	–	–	Test not made
		+15%	-5.0	3657	0.54	0.46	2.1	2.6	OK
4.8	0.29	0%	0.0	–	–	–	–	–	Test not made
		+15%	-5.0	3648	0.68	0.57	2.1	2.5	Unsteady, not straight bead

1) TS x TD.

2) $I_{\text{aver}} \times U_{\text{aver}}$

3) Average of 6 beads

4) Min and max values from valley bottom between and at the centre of the beads.

The maximum and average penetration values are also presented in the following Fig. 98, where the TD value is plotted on the X-axis.

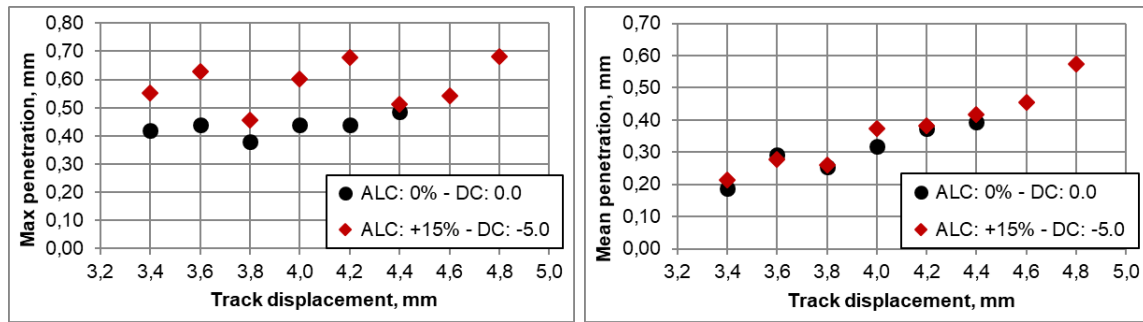


Fig. 98: CMT tests with adjacent beads. Results from measurements on cross sections. Maximum (left) and average (right) penetrations of six adjacent beads with settings ALC: 0%, DC: 0.0 and ALC: +15%, DC: -5.0 (Ar-30%He shield gas, TS: 1000 mm/min, set WFS: 8 m/min).

The statistical reliability of these penetration measurements is rather poor, but nevertheless it seemed that penetration started to increase with a TD of 4.0 mm and above, while penetration seemed to be low up to a TD of 3.8 mm. Therefore, this TD value (3.8 mm) was chosen for the CMT test claddings in the laser vs. CMT cladding comparison. The same TS of 1000 mm/min was also used in these comparison tests (section 3.3.2, p. 140). and the settings in these tests are highlighted in Table 45.

The auxiliary parameter combination ALC: +15%, DC: -5.0, which had been found to produce higher actual WFS and wider beads than the neutral combination of ALC: 0%, DC: 0.0 in the single bead tests, seemed to produce higher maximum penetration depth (Fig. 98 a), but the effect on average penetration was slight (Fig. 98 b).

The minimum thickness, i.e. the thickness that was measured in the valley between the beads did not fall below 2 mm on any of the test claddings. It should be also pointed out that this minimum thickness at the valley bottom would get smaller if the TD were increased, but this leads to an uneven cladding surface. If the final surface has to be levelled by machining, that leads to material waste, but the uneven cladding surface is left as it is, it would decrease the corrosion resistance. It would also be best to keep machining to a minimum because alloy 625 is hard to machine.

Cladding with 100%Ar shield gas and adjacent beads was tested with a TD of 3.8 mm and with two auxiliary parameter combinations: 'neutral' ALC: 0%, DC: 0.0 and 'optimized' ALC: +15%, DC: -5.0. The results are presented in Table 46 and photographs of the surface appearance and cross section images from these tests are presented in Fig. 99, below.

Table 46: CMT test claddings with adjacent beads. 100%Ar shield gas and TS of 1000 mm/min. Results from the measurements of the cross sections (set WFS: 8 m/min)

TD mm	Cover. rate ⁽¹⁾ m ² /h	ALC	DC	Arc power W ⁽²⁾	Actual WFS m/min ⁽³⁾	Penetration		Thickness ⁽⁵⁾		Test cladding appearance
						max mm	aver. ⁽⁴⁾ mm	min mm	max mm	
3.8	0.23	0%	0.0	2585	8.5	0.36	0.28	2.11	2.57	Underfill
		+15%	-5.0	3100	9.1	0.33	0.27	2.12	2.76	Ok

1) Travel speed x track displacement

2) $I_{\text{aver}} \times U_{\text{aver}}$

3) Recorded by Fronius Xplorer

4) Average of 6 beads

5) Min and max values from valley bottom between and at the centre of the beads.

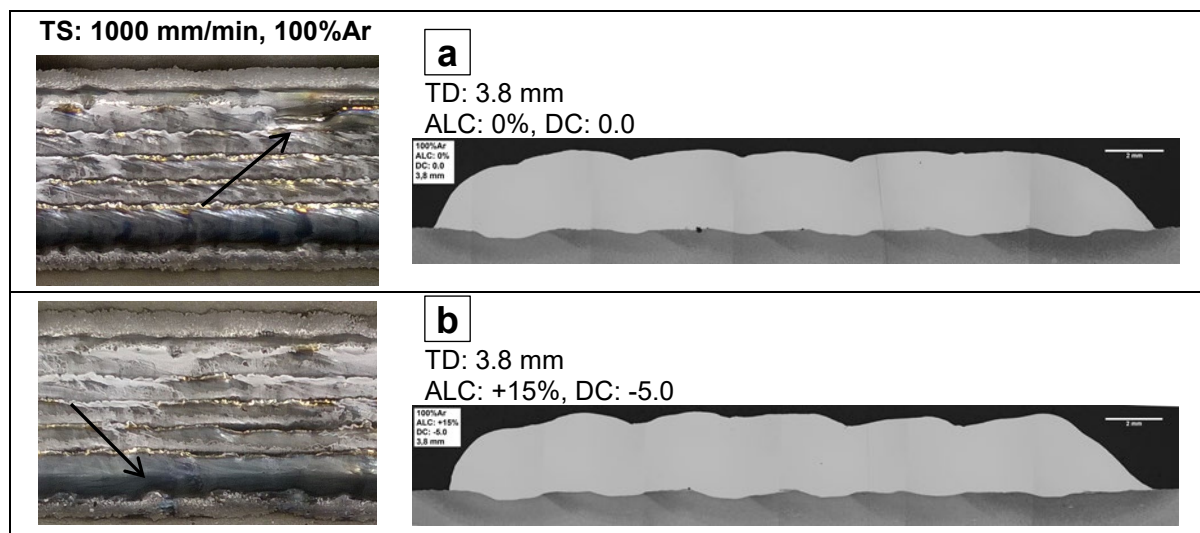


Fig. 99: CMT test claddings with adjacent beads. 100%Ar shield gas, TD: 3.8 mm, TS: 1000 mm/min. Left: cladding surface appearance, right: cross section, magnification: 4x. a) ALC: 0%, DC: 0.0, b) ALC: +15%, DC: -5.0 (set WFS: 8 m/min)

The auxiliary parameter combination ALC: 0%, DC: 0.0 produced some holes or underfills in the surface, as shown by the arrow in Fig. 99 a (left). In test with ALC: +15%, DC: -5.0 there were no signs of this defect due to the higher arc power and actual WFS. However, this test did show that even though 100%Ar shield gas did not produce good results with on tests with single beads (Fig. 87 and 88, and Table 42, p 123), cladding with adjacent beads seemed to be possible with relatively large TD value of 3.8 mm. It seems that bead gets kind-of support from the previous pass and this attenuates bead width and height variation.

Some tests with Ar-30%He shield gas and adjacent beads were also made with a TS of 1200 and 1400 mm/min to see if a higher TS could increase productivity. The tests were made with the 'optimum' auxiliary parameter combination of ALC: +15%, DC: -5.0 that had been found to produce larger actual WFS and larger bead width than the neutral combination ALC: 0%, DC: 0.0.

The tests with a TS of 1200 mm/min were made with three TD values of 3.5, 3.7 and 4.0 mm. The results are presented here in Table 47 and the cross section images in Fig. 100.

Table 47: CMT test claddings with adjacent beads. Ar-30%He shield gas, TS: 1200 mm/min. Results from the measurements of the cross sections (set WFS: 8 m/min).

TD mm	Cover. rate ⁽¹⁾ m ² /h	ALC	DC	Arc power W ⁽²⁾	Penetr. depth		Thickness ⁽⁴⁾		Test cladding appearance
					max mm	aver ⁽³⁾ mm	min mm	max mm	
3.5	0.25	+15%	-5.0	3558	0.48	0.30	2.0	2.4	Ok
3.7	0.27	+15%	-5.0	3401	0.65	0.56	1.8	2.5	Ok
4.0	0.29	+15%	-5.0	3380	0.55	0.49	1.9	2.5	Holes, underfill

1) TS x TD

2) $I_{aver} \times U_{aver}$

3) Average of 6 beads

4) Min and max values from valley bottom between and at the centre of the beads.

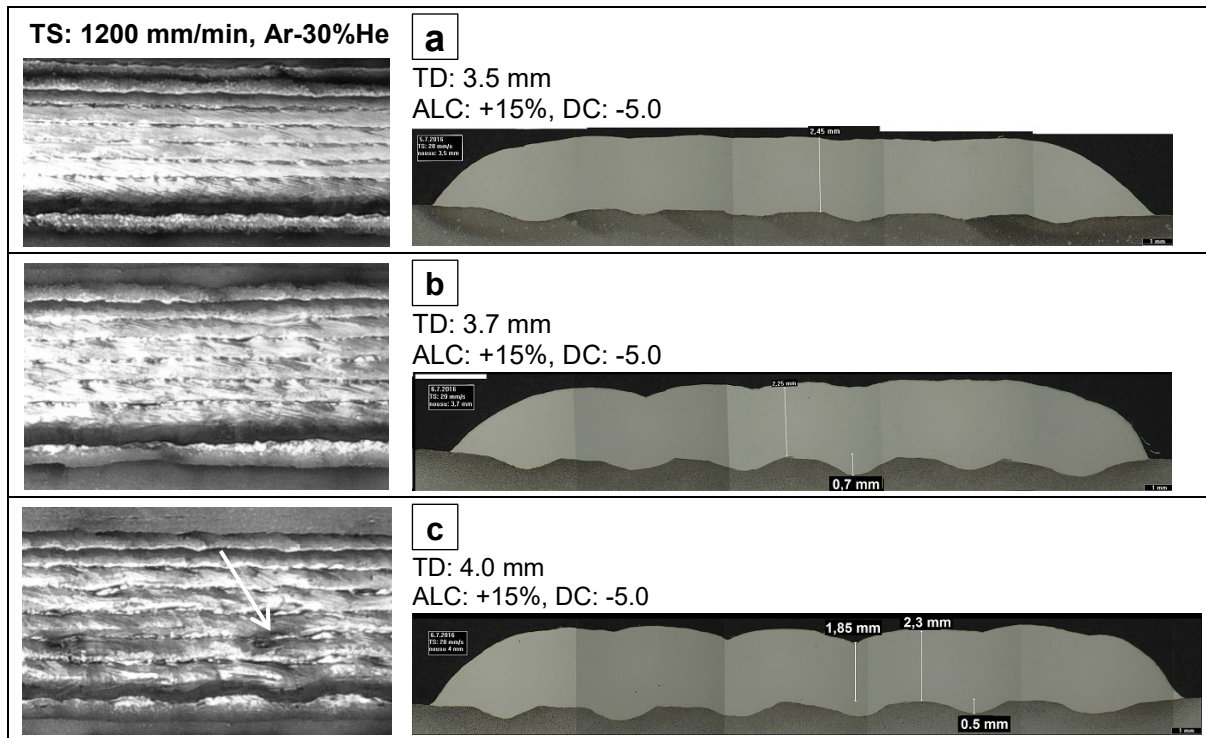


Fig. 100: CMT test claddings with adjacent beads. Ar-30%He shield, TS of 1200 mm/min. Left: cladding surface appearance, right: cross section, magnification: 4x. a) TD: 3.5 mm, b) TD: 3.7 mm, c) TD: 4.0 mm. Some holes or underfill-type defects appeared with TD 4.0 as shown by the red arrow (c) (set WFS: 8 m/min).

The cross section images show that penetration and dilution with a TS of 1200 mm/min are higher than in the tests with a TS of 1000 mm/min with similar TD values (3.6–4.4 mm, Fig. 96 and 97). This is due to fact that as the bead gets narrower, the arc hits on the base metal, rather than the edge of the previous bead when the following bead is welded. The penetration depth is already relatively large, over 0.5 mm, with TD value of only 3.7 mm. There are no signs that penetration would get lower as cladding proceeds, but instead it stays the same.

Furthermore, some holes or underfill-type defects started to appear on the test cladding with a track displacement of 4 mm, as shown by the arrow on the left of Fig. 100 b. The reason for this defect, the fact that the melt pool does not spread evenly, creates an uneven cladding surface. The cladding thickness was slightly lower with a TS of 1200 mm/min than it was in the claddings with a TS of 1000 mm/min, and the minimum thickness fell below 2 mm with a TD of 3.7 and 3.8 mm, but it seemed that this improvement was achieved at the expense of surface smoothness.

There was only one test with the highest TS value of 1400 mm/min and adjacent beads with a TD of 3.0 mm. This produced a cover rate of 0.25 m²/h, which is the same cover rate as with the lower TS setting of: 1000 mm/min; TD: 4.2 mm and TS: 1200 mm/min; TD: 3.5 mm. Tests were not continued to larger TD values, since there were clearly some fluctuation on bead width or formation that would probably produce defects, mainly holes in a longer run, even with this TD rate. The cladding surface appearance and a cross section image are presented in Fig. 101.

Table 48: CMT process. Results with adjacent beads and TS of 1400 mm/min. Ar-30%He shield gas (set WFS: 8 m/min)

TD mm	Cover rate ⁽¹⁾ m ² /h	ALC	DC	Arc power W ⁽²⁾	Penetr. depth		Thickness ⁽⁴⁾		Test cladding appearance
					max mm	aver ⁽³⁾ mm	min mm	max mm	
3.0	0.25	+15%	-5.0	3300	0.57	0.32	1.95	2.60	Ok (some irregularity)

1) Travel speed x track displacement

2) $I_{aver} \times U_{aver}$

3) Average of 9 beads

4) Min and max values from valley bottom between and at the centre of the beads

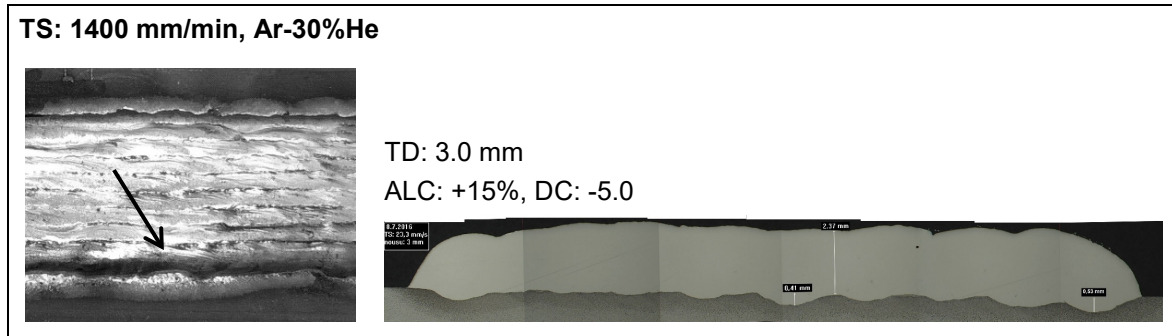


Fig. 101: CMT test claddings with adjacent beads. Ar-30%He shield gas, TS: 1400 mm/min, 9 beads. Left: cladding surface appearance, right: cross section (set WFS: 8 m/min).

As shown in Fig. 101, the CMT process and a TS of 1400 mm/min produced defect-free test claddings with a relatively high cover rate of 0.25 m²/h, but it seems that the melt pool was not stable which results in an uneven bead toe line, as shown by the arrow in the left-hand image of Fig. 101. However, the test was more successful than had been expected from the results with the single bead tests and at a TS of 1500 mm/min (Fig. 91, 92, and Table 44, p. 128), in which the single beads suffered from humping. It seems that when cladding adjacent beads, the melt pool gets some support from the previous bead which mitigates the melt pool's instability. The melt pool is also hotter and solidification slower with adjacent beads, since there is some preheating provided by previous passes.

3.3. Results of comparison: laser vs. CMT cladding

Both the process and resulting cladding properties of the laser with powder and the CMT processes were studied in cladding tests with both single and adjacent beads. The test objectives and parameters are presented in section 2.5 on page 78.

3.3.1. Laser vs. CMT – arc cleaning effect

The substrate surfaces of the single bead test claddings on Toolox 33 steel were examined with optical microscopy and SEM EDS methods. There is a distinct difference in the appearance of the substrate surface by the cladding bead in laser cladding and in CMT cladding (Fig. 28, p. 58). In laser cladding, there is only a thinner dark stripe on the substrate surface beside the laser-clad bead as shown in Fig. 102. This is in contrast to the CMT single bead, where there is wider bright area by the bead (Fig. 106, p. 138). The cross sections of these single bead test claddings are presented in Fig. 110 on page 140.

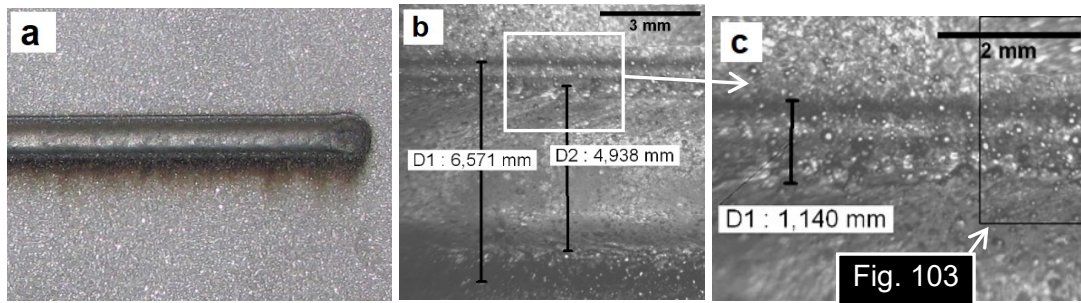


Fig. 102: Laser cladding, single bead surface. a) a photograph, b) OM image (stereo), magnification 4x, c) OM image (stereo), magnification 9x.

The dark stripe beside the laser-clad is around 1 mm wide. However, although the stripe is visible with the naked eye or with an optical microscope (Fig. 102), it did not show up in the examination with the electron microscope (SEM), as can be seen in the SEM SE images in Fig. 103, even though the examination was made with a relatively low accelerating voltage of 5 kV in SEM. This low acceleration voltage of electrons meant that the energy and penetration depth of the electrons is lower than it is with a normal accelerating voltage, in the range of 15–20 kV, and so the examination is focused more on a very thin layer on the surface. The drawback of this operation mode is that only the low energy X-ray peaks, energies less than around 3 keV, can be seen and analysed with EDS. This same 5 kV acceleration voltage was used also to examine the CMT test cladding (Fig. 107–109).

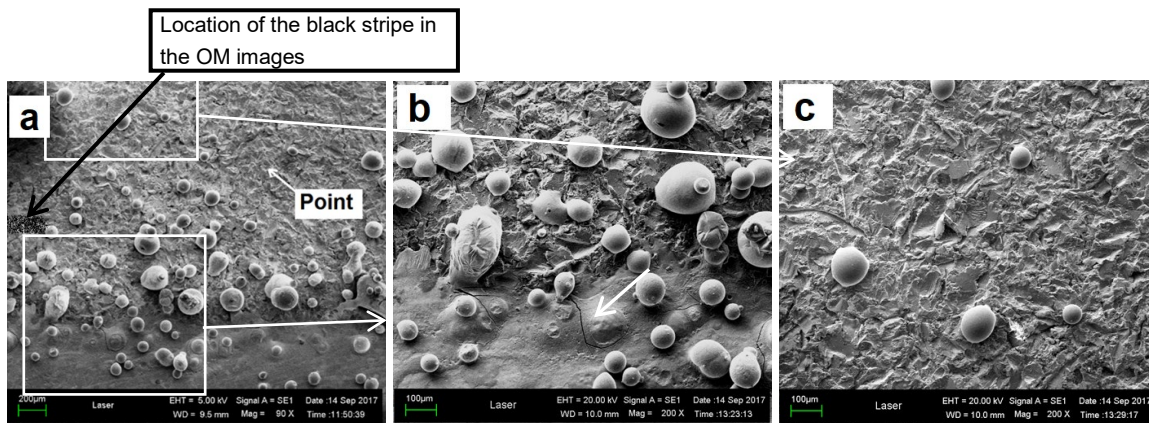


Fig. 103: Laser single bead surface. SEM SE images. a) Lower magnification (20x) from the area as shown in OM image (Fig. 102, c). b) No signs of surface melting near the bead toe, magnification: 40x. c) Unaffected, rough surface roughened by grit blasting, magnification: 40x.

As can be seen from the SEM images in Fig. 103, there is no sign of the substrate surface having melted in the close vicinity of the clad bead, unlike with the CMT clad bead in Fig. 107. There appeared to be some cracks at the bead toe, indicated by arrows in Fig. 103, but these cracks probably only formed in the thick and brittle oxide layer on the surface.

Some EDS point analyses, as well as EDS mapping examinations were made on the area close to the laser clad bead to determine the composition of this area. One EDS point analysis result is presented below in Fig. 104 and the EDS mapping results in Fig. 105.

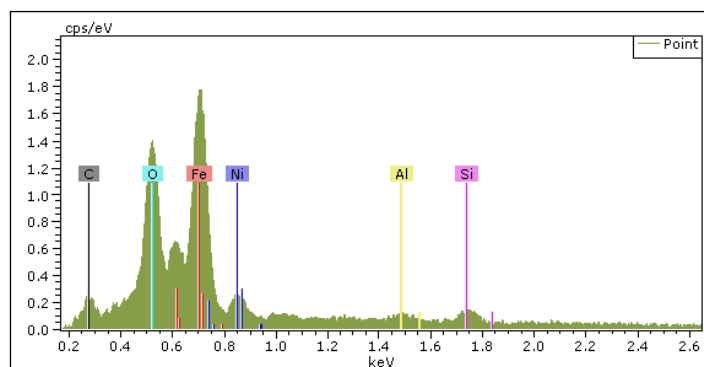


Fig. 104: Laser cladding EDS Point analysis spectrum from the melted area near the bead (Fig. 103). Accelerating voltage 5 kV (lower than on SEM images). The L α peak of Ni at 0,85 keV is low but distinguishable.

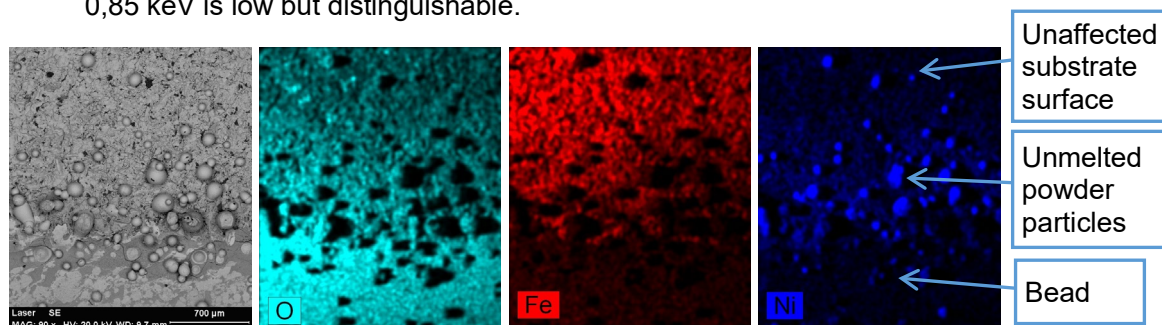


Fig. 105: Laser single bead surface. From left to right: SEM BE image and EDS mapping images for oxygen (O), iron (Fe) and nickel (Ni).

The dark stripe by the laser clad bead that was visible to the naked eye and in the OM images (Fig. 102), could not be seen in the EDS mapping images in Fig. 105. Furthermore, hardly any Ni could be detected from the EDS mapping images of the bead surface, marked with a darker blue colour on the right in Fig. 105. Most of the Ni is detected from the unmelted alloy 625 particles left on the substrate surface, but not on the alloy 625 bead or the substrate surface. This is probably due to the relatively thick oxide layer on the bead's surface. The peak for Ni is also low in the EDS point analysis image in Fig. 104, although it is distinguishable.

The CMT arc welding process leaves an arc-affected area on the substrate surface on both sides of the weld bead and in front of the melt pool, as illustrated earlier in Fig. 28 a on page 58. This area has a total width of around 2 mm, consisting of a duller, sharp edged area, and a bright area, with a width of 0.5 to 1 mm (Fig. 106, c). A cross section of this test cladding is presented in Fig. 110 b.

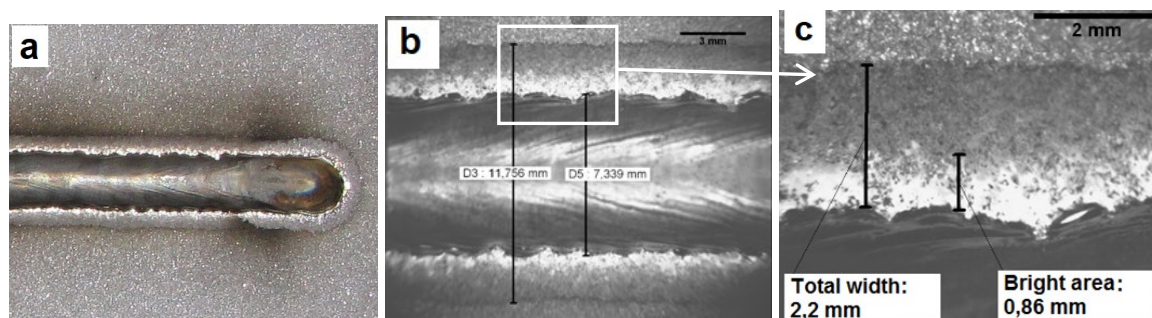


Fig. 106: CMT single bead. a) a photograph, b) OM image (stereo), magnification 3x, c) OM image (stereo), magnification 8x.

This area, which is affected by the surface cleaning effect of the arc, appears not only at the sides of the bead, but also ahead of the melt pool, as shown in Fig. 28 on page 58. It is quite obvious that this cleaning effect of the arc column prepares the substrate surface for the melt to spread over it and to create a metallurgical bond between substrate and the weld, even when the penetration depth is very low.

A more detailed examination of the arc-affected-surface by the bead with the SEM EDS method shows that some Ni has been transferred to this area, as shown in the SEM image in Fig. 107, as well as in the EDS point analysis in Fig. 108 and the EDS mapping images in Fig. 109.

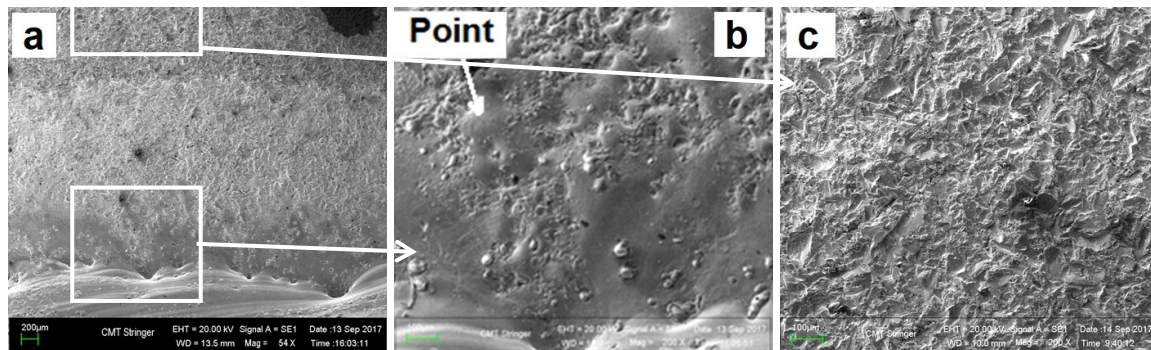


Fig. 107: CMT stringer single bead. SEM SE images from the substrate surface beside the bead. a) The same field of view as in the previous image (Fig. 106, c), magnification 12x. b) Smooth surface shows that this layer has been melted during the process, magnification 40x. c) Unaffected surface roughened by grit blasting, magnification 40x.

EDS point analyses spectra taken with 5 keV from the smooth molten area in Fig. 107, is presented in the following Fig. 108.

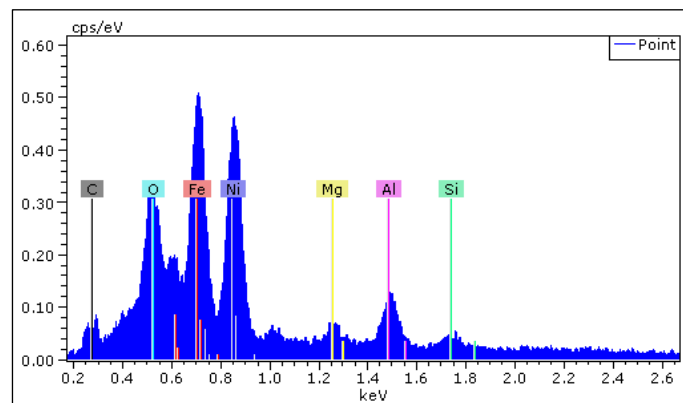


Fig. 108: CMT cladding. EDS Point analyses spectrum from the melted area near the bead (Fig. 107, b). Accelerating voltage 5 kV. The $L\alpha$ peak of Ni at 0,85 keV is very strong.

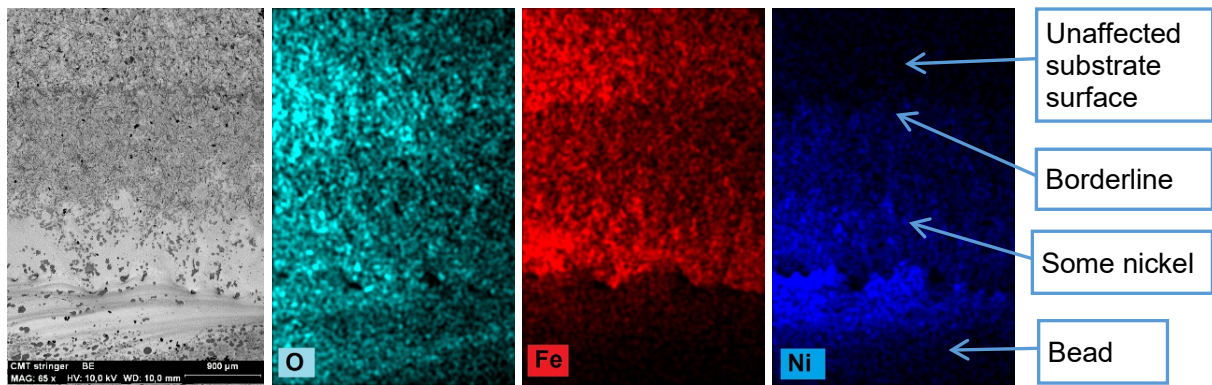


Fig. 109: CMT stringer single bead. From left to right: SEM BE image and EDS mapping images for oxygen (O), iron (Fe) and nickel (Ni).

The EDS point analysis spectra in Fig. 108, as well as the EDS mapping images in Fig. 109, show that Ni is strongly present in this location. The $L\alpha$ spectrum peak of Ni at 0.85 keV was almost as high as the peak of Fe at 0.7 keV in Fig. 108.

3.3.2. Laser vs. CMT – cladding appearance and cross sections

Cross section images of the single bead test claddings on Toolox 33 steel are presented in Fig. 110. The surface appearance of these single bead tests are presented in the previous section 3.3.1.

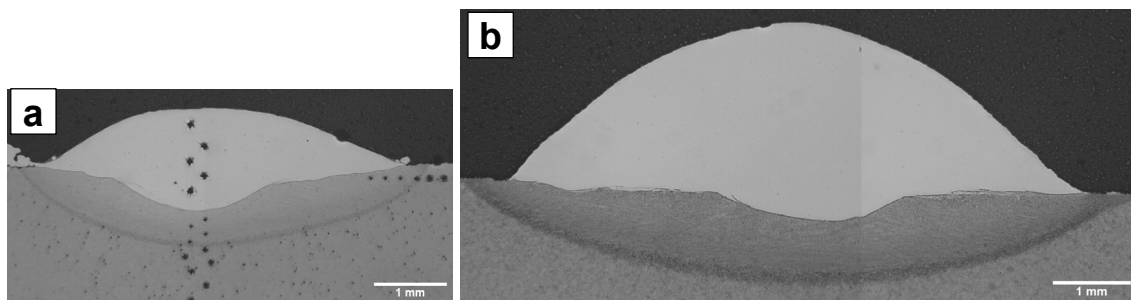


Fig. 110: Single bead cross sections, base material etched condition. OM images, magnification of 10x. a) Laser cladding, relatively large penetration depth (0.6 mm) compared to total height (0.75 mm), large dilution (~30%). b) CMT cladding, moderate penetration depth (0.5 mm) compared to total height (2.1 mm), small dilution (~10%).

The magnification of the cross section images in Fig. 110 is the same, so that the relative difference in the cross section area of a single bead is clearly illustrated. This difference is directly related to productivity, but it must be borne in mind that productivity or cover rate is also related to the travel speed (TS), and in this case the laser cladding had a 50% higher TS of 1500 mm/min compared to the CMT's TS of 1000 mm/min.

Some results of single bead dimension and hardness measurements from single cross section are presented below in Table 49.

Table 49: Results of measurements from single bead cross sections

Feature	Laser	CMT
HAZ max hardness	504 HV ₁	519 HV ₁
Cladding average hardness	222 HV ₁	241 HV ₁
Bead cross section area	2.5 mm ²	9.7 mm ²
Melted base material area	1.3 mm ²	1.05 mm ²
Geometrical dilution	34%	10%
Penetration	0.6 mm	0.5 mm
HAZ depth	1.1 mm	1.2 mm
HAZ + melted base material area	4.4 mm ²	7.4 mm ²
Bead height	0.75 mm	2.1 mm
Bead width	4.7 mm	7.1 mm
Bead height to width ratio	0.16	0.30

The results show that there is no great difference in the HAZ maximum hardness between claddings made with laser and CMT, although CMT showed a slightly higher max HAZ hardness (519 HV₁) than laser (504 HV₁). The hardness of the CMT cladding was also slightly higher (241 HV₁) than that of laser (222 HV₁). The hardness profiles in both the vertical and horizontal directions are presented in Fig. 111. The horizontal hardness profiles were made at a depth of 0.2 mm from the substrate surface and the vertical profiles at the middle of the bead. The location of the hardness profiles can be seen above in Fig. 110.

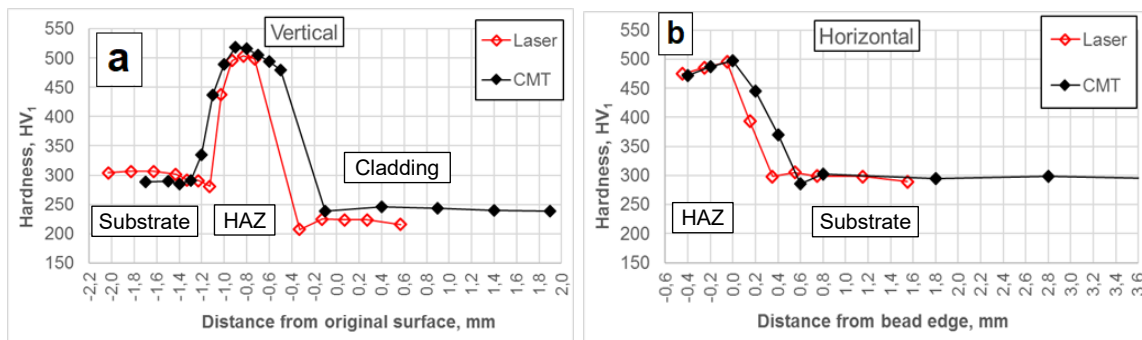


Fig. 111: Laser and CMT single bead cladding on top of Toolox 33. Hardness profiles. a) Vertical and b) horizontal direction.

The HAZ thickness, or depth, is slightly higher with CMT than with laser cladding. The higher HAZ depth in the CMT process is obvious, since the actual effective process power in CMT process is greater and the TS is slower than in laser cladding. The lower hardness of laser cladding is probably related to the larger dilution, i.e. the higher Fe content in the alloy 625 cladding material. However, with adjacent beads, this order was reversed and laser cladding showed slightly higher hardness (Table 50).

Two test samples with both methods, laser and CMT, were made with adjacent beads, but only one sample was taken for cross section and microstructure examination. The tests were made twice to improve the statistical reliability especially for the substrate temperature measurements. The corrosion test samples for the CPT tests (section 3.3.5, p. 152) were also taken from these test claddings. Photographs of the cladding samples with adjacent beads are presented in Fig. 112, and the cross section images in Fig. 113 and 114.

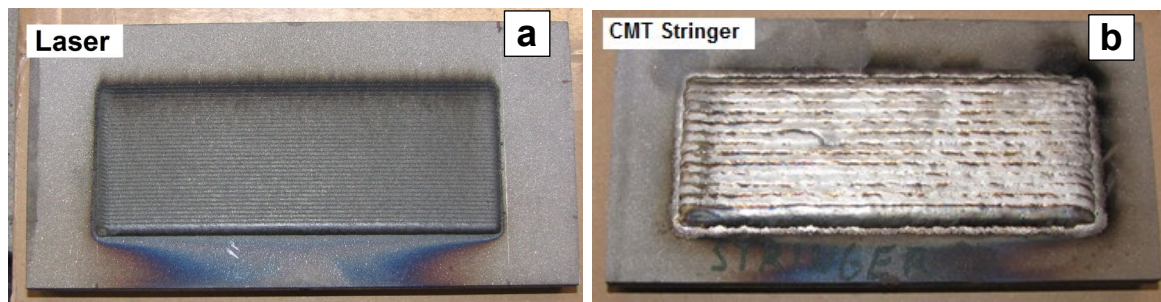


Fig. 112: Appearance of cladding test samples in laser vs CMT comparison tests with adjacent beads. a) Laser cladding tests sample with 34 beads. b) CMT cladding tests sample with 14 beads.

The surface of the laser cladding is clearly darker and more oxidized than the CMT test claddings. Some estimation of the heat input and substrate temperature during cladding can be deduced from the substrate colour, the so-called tempering colour, and its area. This area on the base material shows where the temperature has reached the level where the steel surface starts to oxidize. As the temperature is increased, the iron oxide layer grows in thickness and changes colour. In the area where the substrate has turned dark blue, the surface temperature has reached around 300 °C. This dark blue area is slightly larger in the laser cladded test sample.

Cross sections from base material etched (Nital) test claddings with laser and CMT are presented in Fig. 113 and 114. Neither of the tests claddings, laser or CMT, showed any macro-scale defects, but a microscale examination with a higher magnification revealed some defects, like small hot cracks in laser cladding (Fig. 118, p. 146).

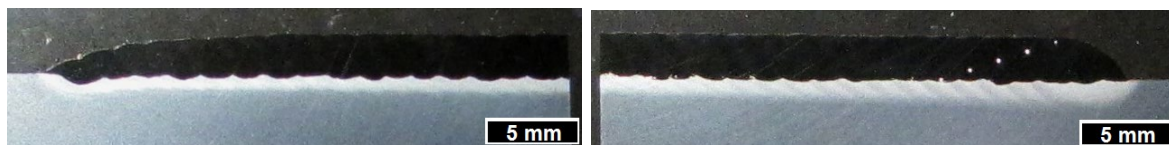


Fig. 113: Laser cladding cross section. Base material etched condition.

The laser cladding (Fig. 113) shows relatively large penetration depth (compared to total thickness) on the first bead (0.5 mm), but it decreases in the following passes, since the laser beam hits the previous pass, not the base material. The Fe content in the first bead is 32%, in the second 15% and only 9% in the last bead. The HAZ depth increases from 1 mm to 1.5 mm as the cladding proceeds. The hardness measurement indents are visible on the right side of the cross section.

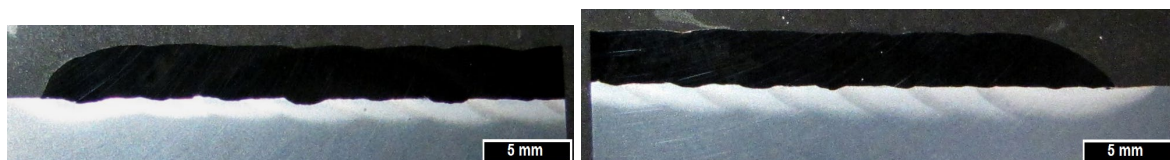


Fig. 114: CMT cladding cross section. Base material etched condition.

The CMT cladding (Fig. 114) shows relatively small penetration depth of 0.4 mm in the first bead, and the depth decreases as cladding proceeds. This is a consequence of the substrate heating up and a less viscous melt pool that spreads better so that the arc hits more in the previous pass. Furthermore, the Fe content decreases slightly. The Fe content in the first bead

is 9% and is only 7% in the last bead. HAZ depth increases from 1.5 to 2 mm as the cladding proceeds. In contrast to single bead test claddings (Table 49, p. 141), laser cladding showed slightly higher hardness of 234 HV₅ than CMT cladding, 220 HV₅. Penetration, HAZ depth, Fe content and hardness measurements on test claddings are shown also in Table 50.

Table 50: Laser vs. CMT with adjacent beads. Measurements to cross sections.

	Cladding thickness	Location	HAZ depth	Penetration depth	Fe content ⁽¹⁾	Cladding hardness
Laser cladding	1.9–2 mm	First bead	1.1 mm	0.5 mm	32%	–
		Second bead	1.0 mm	0.25 mm	15%	–
		Last bead (34 th)	1.6 mm	0.2 mm	9%	234 HV ₅ ⁽²⁾
CMT cladding	2.5–2.8 mm	First bead	1.5 mm	0.4 mm	9.0%	–
		Last bead (14 th)	2.0 mm	0.1 mm	7%	220 HV ₅ ⁽²⁾

1) SEM EDS method. At the middle of the bead, at the depth of 1–2 mm from the surface.

2) Hardness measurements on 15° angle to the fusion line starting from the last bead

3.3.3. Laser vs. CMT – process power and energy consumption

The same effect that is seen from the substrate colour in Fig. 112 on page 142, can be seen from substrate temperature measurement graphs that are presented in Fig. 115 and the measured max temperatures in Table 51. The tests and measurements were done twice to improve statistical reliability of measurements.

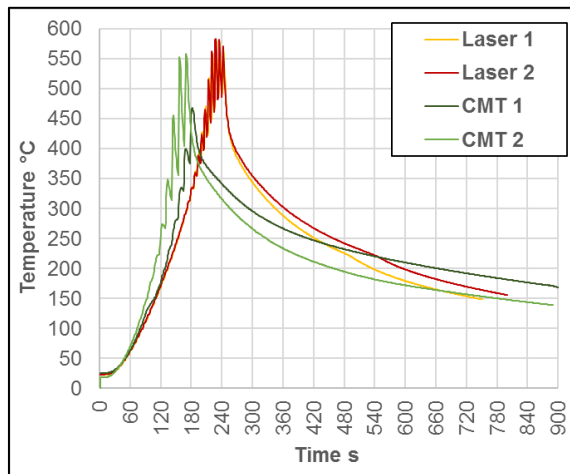


Fig. 115: Laser vs. CMT with adjacent beads. Temperature measurements from the HAZ of the last cladding pass.

Table 51: Laser vs. CMT with adjacent beads. Maximum measured temperatures.

Method	Test	Max temp.
Laser cladding	1	580 °C
	2	583 °C
CMT cladding	1	468 °C
	2	560 °C

The substrate of laser cladding showed slightly higher maximum temperature than the CMT cladding. However, the variation in the results of CMT cladding was large: 468 and 560 °C. The reason for this variation may be related to, for example, variation in the location of temperature sensor or probe below the last pass (Fig. 42, p. 84). The effect of separate passes to temperature can also be seen in the graphs of both the laser and CMT cladding.

The comparative values for process power and energy consumption are collected in Table 52. These values are the average values of the measurements of two tests. The values for average current and voltage, as well as the actual WFS and cladding mass, were quite close to each other for both two tests.

Table 52: Laser vs. CMT with adjacent beads. Results of power and energy determination.

	Laser cladding	CMT cladding
Process set power ⁽¹⁾	4200 W (set value)	2830 W
Actual power ⁽²⁾	3800 W ⁽²⁾	3880 W ⁽³⁾
Wall plug power ⁽³⁾	14 000 W (30% effic.)	4220 W (92% effic.)
Heat input ⁽⁴⁾	114 J/mm	186 J/mm
Power ratio ⁽⁵⁾	1520 W/mm ²	400 W/mm ²
Total laser or arc-on time	197 s	126 s
Total cladding time	240 s	170 s
Energy input ⁽⁶⁾	749 kJ	490 kJ
Total energy input ⁽⁷⁾	2 800 kJ	532 kJ
Cladding mass	134 g	168 g
Actual feedstock feed rate ⁽⁸⁾	41 g/min, 2.4 kg/h	83 g/min, 4.8 kg/h
Actual wire feed rate	–	8.9 m/min ⁽⁹⁾
Coverage rate	0.14 m ² /h	0.23 m ² /h
Total energy consumption per m ² of cladding	373 MJ/m ² , 104 kWh/m ²	66 MJ/m ² , 18.4 kWh/m ²
Total energy consumption per kg of cladding	20.6 MJ/kg, 5.7 kWh/kg	3.2 MJ/kg, 0.88 kWh/kg

1) Average values of two tests. Laser: set power. CMT: average current x voltage

2) Laser: estimated actual power on the workpiece surface. CMT: Estimated AIP power based on oscilloscope measurements with single beads: $I_{aver} \times U_{aver} \times 1.37$.

3) Estimated wall plug power. Estim. effic. of laser power source: 30% and CMT power source: 92%.

4) Eq. 4, vs Actual power. Laser: $k = 0.5$. CMT: $k = 0.8$.

5) Power Ratio: actual power / bead cross section area in the single bead tests.

6) Actual power x laser or arc-on time (CMT).

7) Actual wall plug power x arc-on time.

8) Calculated from cladding mass vs actual arc-on time.

9) Actual WFS measured by the Fronius Xplorer.

Total cladding time was longer (240 s) with the laser cladding than with the CMT (170 s), although the TS was high with laser cladding (25 mm/s) the TD was small (1.5 mm) and more passes (laser: 34, CMT: 14) were needed to cover the width of ~50 mm. More passes means also more return motions without laser beam or arc, since the cladding tests were done in one direction only. The powder feed was also on during these return motions in the laser cladding process.

The oscilloscope was not used in these test, so it was not possible to determine average instantaneous power (AIP) for the CMT process. The actual power for the CMT process was based on the AIP results determined with the oscilloscope and single bead tests (Table 35, and 39, p. 117). These tests had shown that a reliable estimate for the difference between arc power determined with $I_{aver} \times U_{aver}$ and AIP methods was around 37%. So the actual arc power with CMT was evaluated by multiplying the arc power determined with the $I_{aver} \times U_{aver}$ method by a factor 1.37. The actual laser power was assumed to be 3800 W with a set value of 4200 W. Once again, this roughly 10% difference between the set value and actual value on the workpiece had been measured in the single bead tests with fibre coupled Nd:YAG laser (Fig. 34, p. 67). Comparison graphs of productivity and energy consumption are presented below in Fig. 116.

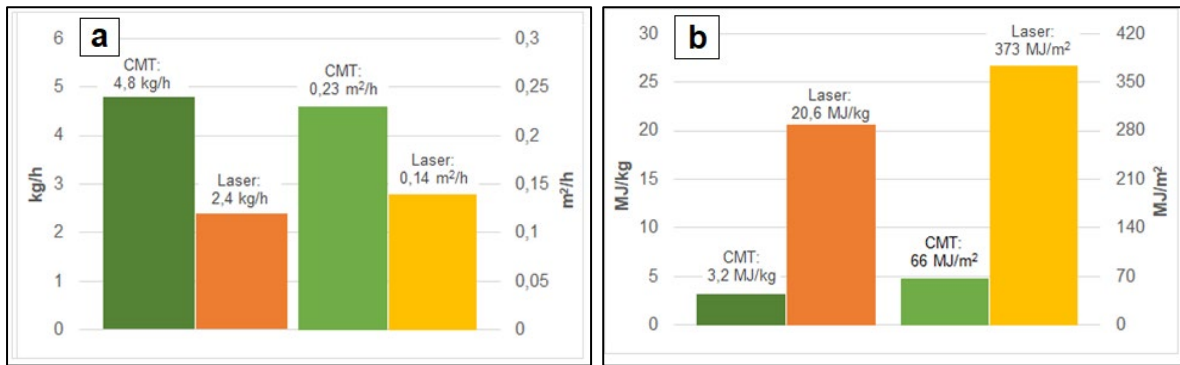


Fig. 116: Laser and CMT processes, comparison graphs of a) productivity in terms of kg/h and m²/h, and b) energy consumption in terms of MJ/kg and MJ/m².

The columns in Fig. 116 a illustrates that productivity both in terms of kg/h and m²/h was clearly higher for CMT than it was for the laser cladding process. This difference was even greater in the comparison of energy consumption in Fig. 116 b. According to the comparison values in Fig. 116 b, the total wall plug electrical energy consumption of the CMT process, 66 MJ/m², is only one-sixth (~17%) of that of the laser cladding process, which consumed 373 MJ/m².

This comparison does not take account the energy needed to produce the filler material, (alloy 625 powder or wire). However, wire filler material in the CMT process has a better utilisation rate than powder in laser process in any case, nearly 100%, since the amount of weld spatter is very small in the CMT process and almost all of the melted wire ends up in cladding. In the laser cladding process with powder, some portion of the powder is not melted by the laser beam does not end up to the cladding.

3.3.4. Laser vs. CMT – microstructure

The microstructures were examined from the tests made both with single and adjacent beads. Examinations were made on the cross section surfaces that had either the base material, or the alloy 625 cladding material etched. These examinations were done with an optical microscope (OM) and a scanning electron microscope (SEM) and EDS analyser.

3.3.4.1. Laser cladding microstructure

Laser single bead cross sections in the alloy 625 etched condition are presented in Fig. 117. The same cross section is presented for the base material etched condition in Fig. 110.

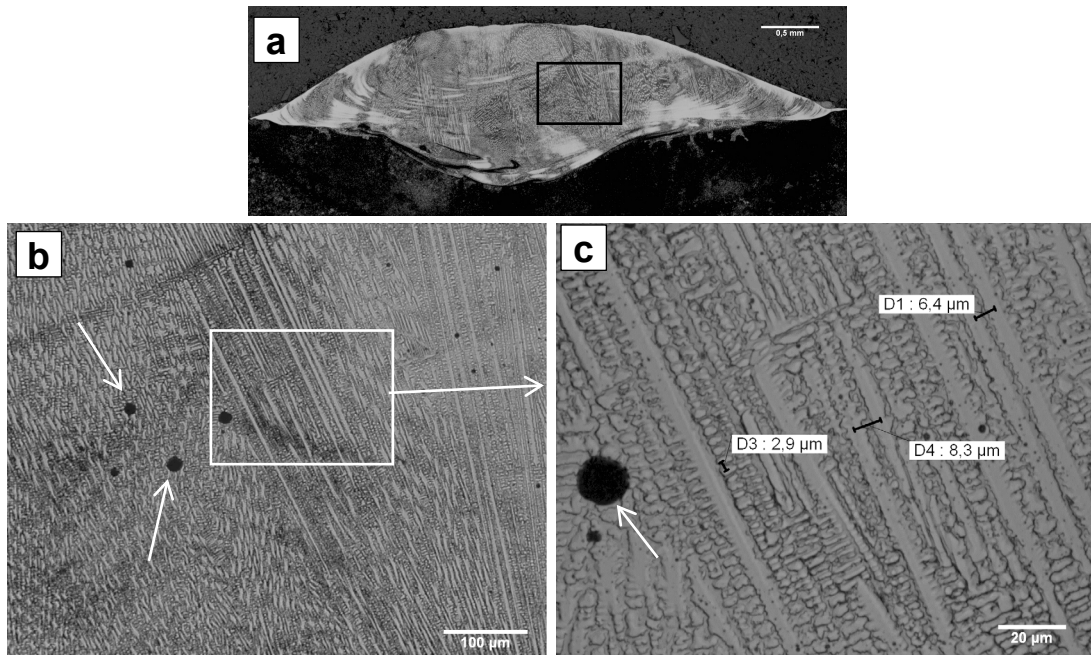


Fig. 117: Laser cladding with single bead, alloy 625 etched condition. OM images, magnifications: a) 14x, b) 90x, c) 375x. The same magnifications as in Fig. 122 for CMT cladding.

The OM images in Fig. 117 show that solidification pattern is columnar dendritic. The primary dendrite arm spacing in the area where the solidification is planar is around 5–9 μm and the secondary dendrite arm spacing is around 3 μm . Microstructure contained also some spherical dark spots that are pointed by the arrows in Fig. 117. Quite similar inclusions were found also from the tests claddings with adjacent beads (Fig. 118 and 119).

OM images from the base material etched microsection of laser cladding with adjacent beads that reveals better some defects, like the non-metallic inclusions, is presented in Fig. 118.

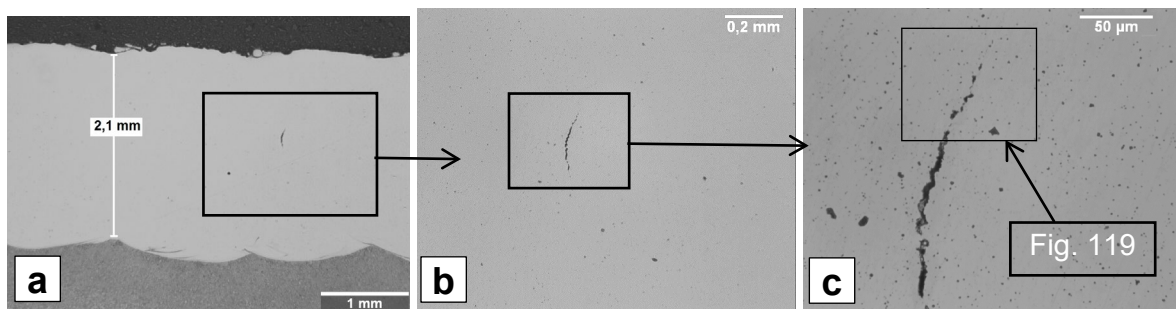


Fig. 118: Laser cladding with adjacent beads, base material etched condition. OM images, magnifications: a) 11x, b) 40x, c) 180x. Small hot crack with a length of 0.2 mm. Microstructure contains relatively large amount of inclusions that appear dark in the images.

OM images of adjacent bead test cladding in Fig. 118 show a small (0.2 mm) hot crack. A total of 2–3 similar cracks were found from the whole cross section. High-magnification OM image in Fig. 118 c show that there appears to be a large amount of dark inclusion in the microstructure. The SEM BE images and the EDS point analyses results from the inclusions around the same hot crack as in Fig. 118, are presented in Fig. 119.

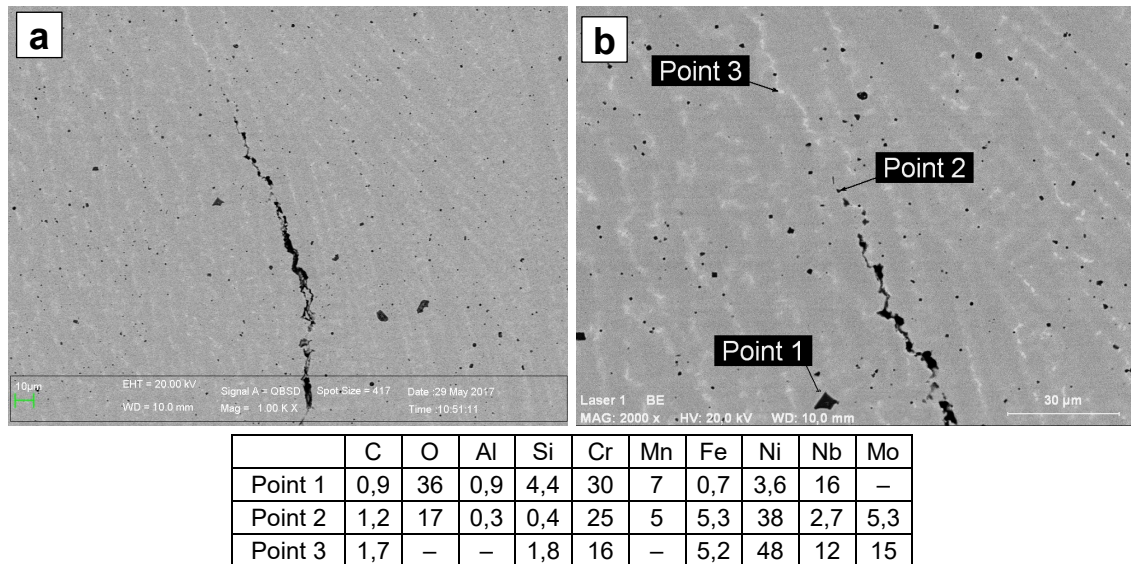


Fig. 119: Laser cladding with adjacent beads, base material etched condition. The same hot crack as in the previous OM images (Fig. 118). SEM BE images, magnifications: a) 250x, b) 500x. On bottom: quantitative results of EDS point analyses in mass percent.

EDS point analyses results (Fig. 119, Point 1 and 2) show that dark inclusions consisted mainly on elements O and Cr. These O- and Cr-containing inclusions were found all over the cross section of the laser cladding test sample and were relatively large, maximum length being around 20 μm . The existence of these inclusions is probably related to the fact that the feedstock powder had a very low content of the elements Al, Ti, Si and Mn (Table 14, p. 71) that could act as an oxygen binder in the melt.

The same hot crack as shown in Fig. 118 and 119, is presented in the alloy 625 etched condition in Fig. 121 below, where the solidification and the phase structure of alloy 625 is revealed.

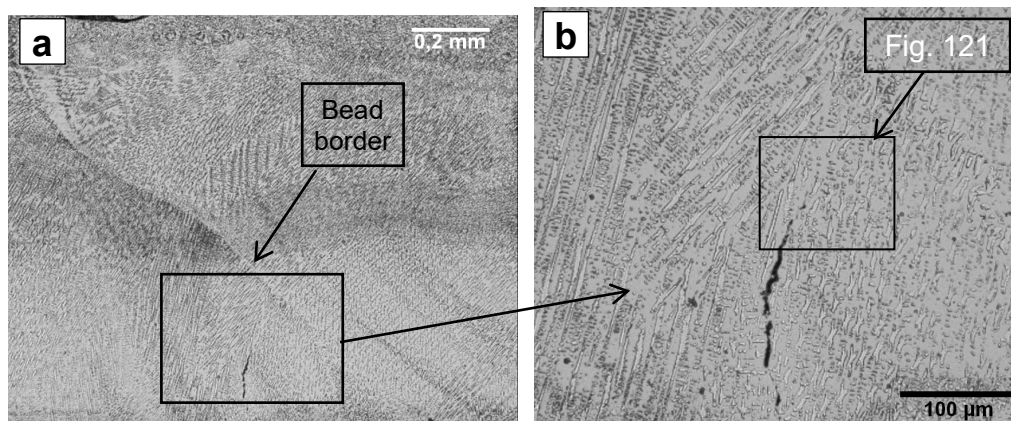


Fig. 120: Laser cladding with adjacent beads, alloy 625 etched condition. OM images, magnifications: a) 50x and b) 150x. Hot cracking is very close to the border of subsequent bead.

The etching of alloy 625 reveals that the crack has appeared very close to the interface of the following bead (Fig. 121 a), as indicated by the arrow, meaning that it is probably a liquation crack; such cracks being formed when the subsequent cladding pass has heated the previous pass close to its melting temperature. Some low-melting point phases must have liquefied and the tensile stresses have torn the crack open.

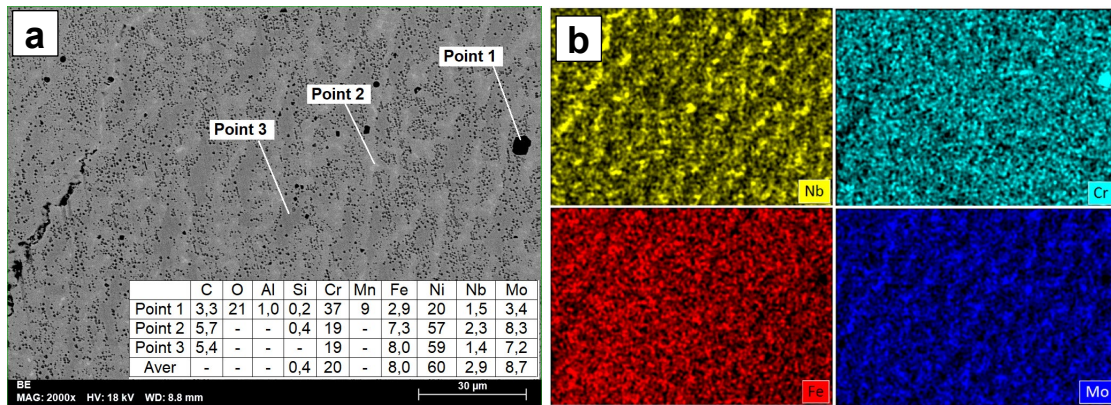


Fig. 121: Laser cladding with adjacent beads, alloy 625 etched condition. a) SEM BE image, magnification: 500x and quantitative results of EDS point analyses in mass percent, average Fe content 8%. b) EDS mapping images for elements Nb, Cr, Fe and Mo, the same field of view as in image a.

Both the SEM BE image in Fig. 121 a, and EDS mapping images in Fig. 121 b show some segregation of elements in laser cladding. Especially elements Nb (yellow) and Mo (blue) show some segregation between the dendrites in mapping images. The EDS analyses that were made of this alloy 625 etched show also some O- and Cr- containing inclusions (Fig. 121 b, Point 1), as was shown in some previous images (Fig. 118 and 119). In addition, the etched microsection showed some microporosity that appears as large amount of small dark spots in Fig. 121 a. These pores were formed during the etching with the mixture of HCL, NH_4OH and 5 CH_3COOH . However, the formation mechanism of these pores was not examined further.

3.3.4.2. CMT cladding microstructure

Optical microscope images from the CMT single bead cross section in alloy 625 etched condition are presented in Fig. 122. The same cross section was presented in the base material etched condition in Fig. 110.

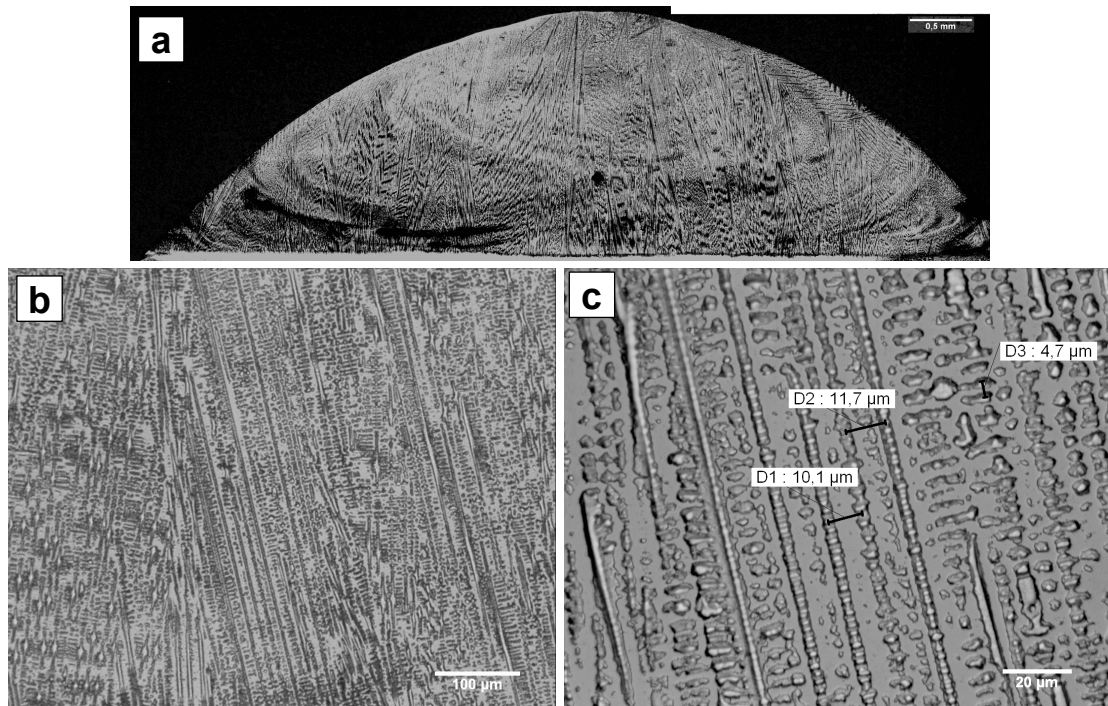


Fig. 122: CMT cladding with single bead, alloy 625 etched condition. OM images, magnifications: a) 14x, b) 90x, c) 375x. The same magnifications as in Fig. 117 for laser cladding.

The solidification pattern of the CMT single bead is columnar dendritic. The microstructure appears quite similar to that of the laser cladding (Fig. 117), but there were no any visible inclusions and the dendrite arm spacing was slightly larger. The primary dendrite arm spacing of the CMT cladding was around 10–12 μm and the secondary arm spacing 4–5 μm .

Cross section of CMT cladding with adjacent bead in base material etched condition is presented in Fig. 123.

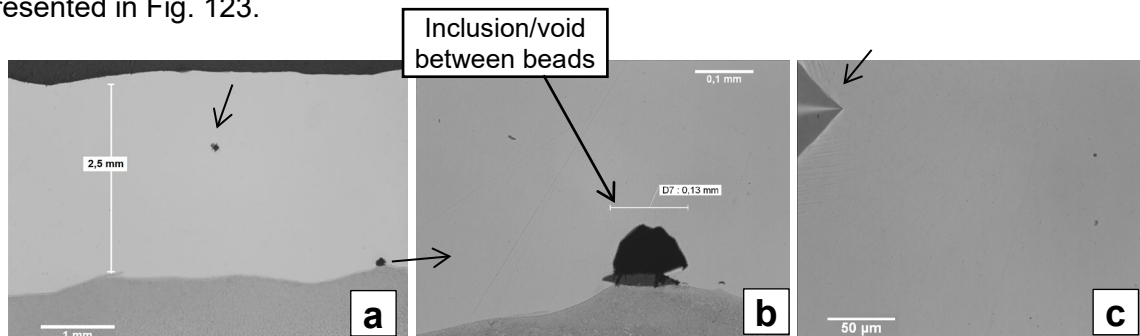


Fig. 123: CMT cladding with adjacent beads, base material etched condition. OM images Magnifications: a) 9x, b) 100x, c) 180x. Hardness indent was made to the middle of the clad to find the same location in the SEM examination (a and c).

As can be seen from the OM images in Fig. 123, the CMT cladding did not contain any defects, except one inclusion between the beads at the cladding-substrate interface (Fig. 123 b). Also in SEM examination of the base material etched condition, there appeared be clearly fewer inclusions in the microstructure than in the laser cladding (Fig. 119). However, some dark spots were detected on the SEM image as presented in Fig. 124 below.

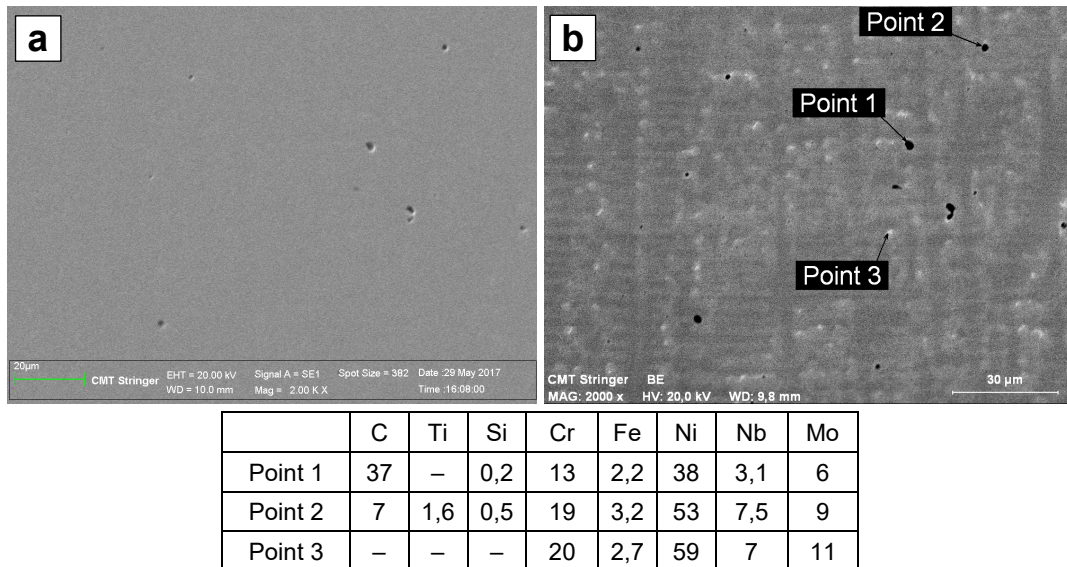


Fig. 124: CMT cladding, adjacent bead, base material etched condition. a) SEM SE image, b) SEM BE image. The same magnification (500x) and the field of view in both images. On bottom: quantitative results of EDS point analyses in mass percent.

Some of these few dark spots in Fig. 124 were analysed with EDS (Point 1 and 2) and they did not contain any O, but some C. It is possible that this C is a residue from the sample preparation – grinding of the microsection. The location in Point 3, the eutectic between dendrites, shows only slightly higher Nb and Mo content, but very low Si content.

The cross section of CMT cladding with adjacent beads in alloy 625 etched condition is presented in Fig. 126.

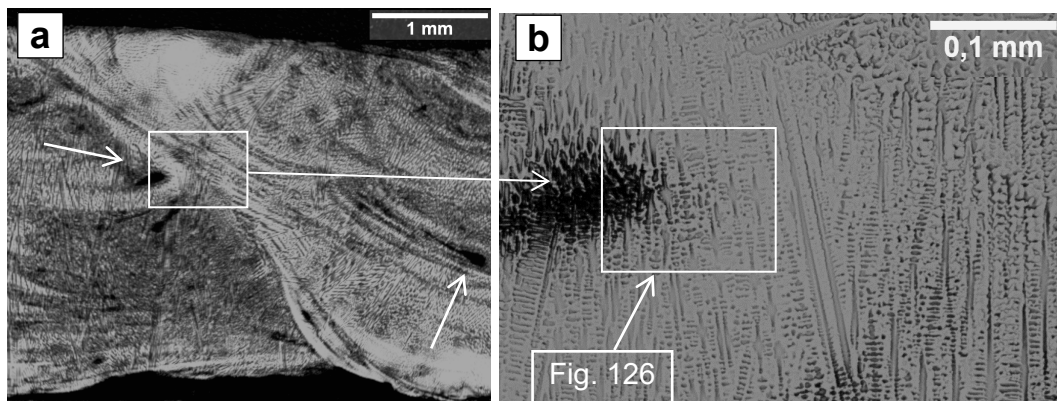


Fig. 125: CMT cladding with adjacent beads, alloy 625 etched condition. OM images, magnifications: a) 12.5x, b) 140x. The area that was affected more by etching is shown with an arrow.

Etching of alloy 625 cladding material revealed some areas, as indicated by the arrows in Fig. 126 a, that were more affected by the etching and contain more Fe than surrounding areas. Similar areas were not detected from the alloy 625 etched cross section of laser cladding (Fig. 121). However the Fe content that was analysed from one of these areas (Fig. 126 a, Point 1) was only 16%.

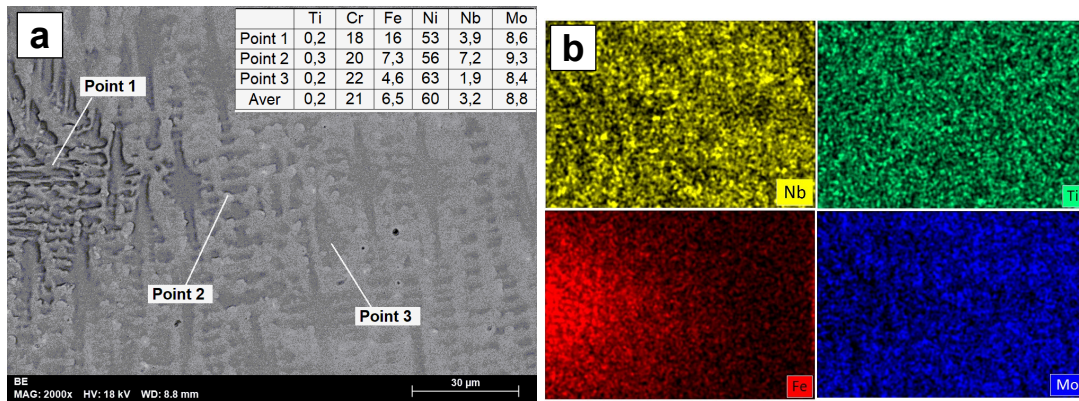


Fig. 126: CMT cladding with adjacent beads, alloy 625 etched condition. a) SEM BE image, magnification: 470x and quantitative results of EDS point analyses in mass percent, average Fe content 6.5%. b) EDS mapping images for elements Nb, Ti, Fe and Mo, the same field of view as in image a.

As can be seen both from the SEM BE (Fig. 126 a) and EDS mapping images (Fig. 126 b), the segregation of the elements in the microstructure in CMT cladding is relatively low level, and the last-to-solidify phases are not clearly distinguishable from the etched cross section.

However, to facilitate this comparison between the laser and CMT cladding microstructures, the following images (Fig. 127) present a microstructure of slowly solidified and highly diluted cladding made with the PTA (Plasma Transferred Arc) method, using a weaving motion and powder as the feedstock material. Neither the process parameters, nor the composition of the feedstock material of this alloy 625 powder were known, but the cladding was around 15 mm wide and 3 mm thick. The average composition of the PTA cladding as measured by EDS was as follows: Ni: 48%, Cr: 16%, Mo: 7%, Nb: 3%, Fe: 24%, Si: 0.7%, Al: 0.1%, Ti: 0.3%.

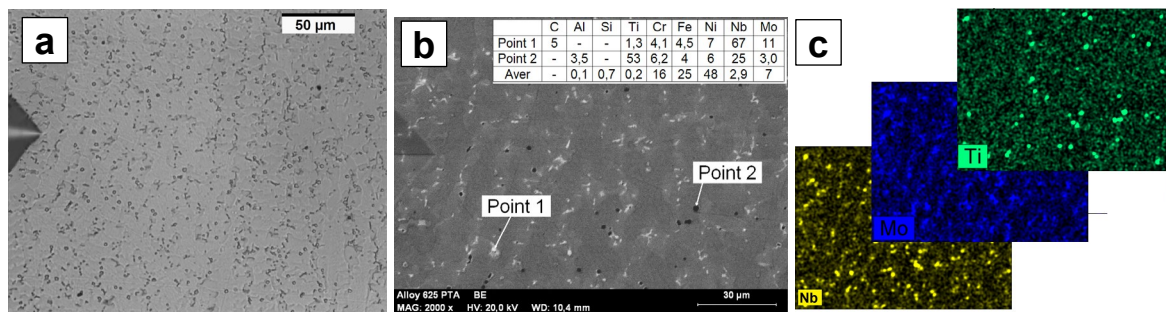


Fig. 127: Alloy 625 PTA cladding. Alloy 625 etched condition. a) OM image, magnification 200x b) SEM BE image, magnification 350x and quantitative results of EDS point analyses in mass percent, average Fe content 25%. c) EDS mapping images for elements Nb, Mo and Ti, the same field of view as in image b.

The phase structure of PTA cladding is clearly different than that of laser and CMT claddings. There is clearly more segregation of elements in the last-to-solidify phase as segregation of elements Nb, Mo and Ti is clearly visible in EDS mapping images (Fig. 127 c). The quantitative results of EDS point analysis (Point 1) shown in the Fig. 127 b, shows that max Nb content at the last-to-solidify eutectic between the dendrites reaches to a max of 60–70(wt)%. The Nb content indicates the presence of NbC. This microstructure is quite similar as the one presented in Fig. 7 on page 19 that was found by Guo et al. [57] from alloy 625 cladding made with a pulse TIG method. Furthermore, there is no sign of a columnar structure in the PTA cladding, as there was in the laser and CMT claddings. Instead, the solidification structure is

equiaxed dendritic, which indicates a slower cooling rate compared to the laser and/or CMT claddings.

3.3.5. Laser vs. CMT – corrosion resistance

The corrosion resistance of alloy 625 sheet and laser vs. CMT comparison test samples were determined with modified ASTM G150 pitting corrosion tests in a 3M NaBr solution. The pitting corrosion test settings are presented in section 2.6.8 on page 84.

A total of four tests were made for each sample. The results are presented in Table 53 and a corrosion test curve from a one test is presented in Fig. 128.

Table 53: Critical pitting corrosion temperature (CPT) measurement results.

Test	Alloy 625 plate	Laser cladding	CMT cladding
1	52 °C	46 °C	51 °C
2	51 °C	44 °C	50 °C
3	51 °C	50 °C	51 °C
4	53 °C	52 °C	54 °C
Average	52 °C	48 °C	51.5 °C

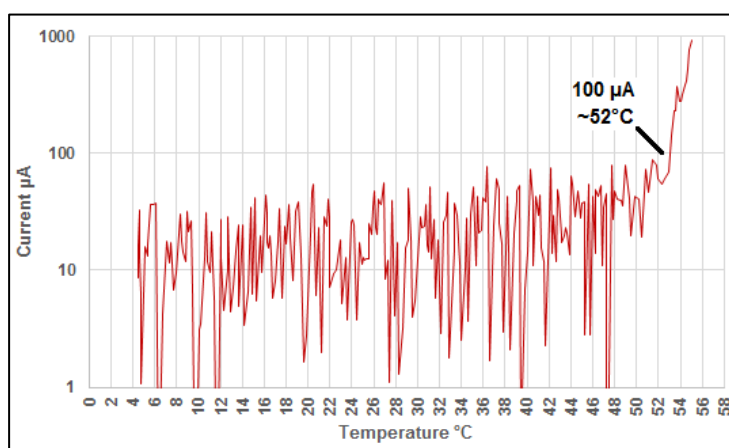


Fig. 128: One CPT test curve. The pitting temperature, the temperature when current reaches 100 μ A, was \sim 52 °C in this test. The current on the vertical axis is presented in a logarithmic scale.

With alloy 625 plate, the critical pitting temperature of all the claddings was around the same level, \sim 50 °C. However, the laser cladding showed a slightly lower average pitting corrosion temperature than the alloy 625 plate and CMT cladding. In addition, the lowest test result for the laser cladding (44 °C) was clearly lower than that of alloy 625 plate (51 °C) and CMT stringer cladding (50 °C).

The average compositions of the CPT test surfaces are presented in Table 54 showing that all the test cladding surfaces had a low iron content. The measurements were done with SEM EDS by scanning the larger area of 4.5 x 3 mm on a test surface (Fig. 129–131).

Table 54: Average composition of CPT surfaces (EDS, normalised mass percent).

	Ni%	Cr%	Mo%	Fe%	Nb%	Si%	Al%	Ti%
Alloy 625 plate (3)	66	21	8.3	1.5	3.1	0.2	–	–
Laser cladding (2)	61	20	8.3	6.9	3.2	0.5	–	–
CMT cladding (1)	62	21	8.5	5.1	3.4	0.2	0.1	0.2

Even though all the claddings showed low dilution values, meaning that the average Fe content was very low, around 5% or less, there appeared to be some variation in the Fe content of the test surface. The iron content of the CPT test surfaces was determined with SEM EDS mapping and linescan functions. The images of the CPT test surfaces and the EDS mapping and line analyses results are presented in Fig. 129–131. The purpose of the EDS line scan was to discover quantitative differences for Fe content in the particular site on the surface where the corrosion pits had occurred. On the EDS mapping images, the relative amount of Fe is shown in red, meaning that the areas with a larger Fe content are redder than the surrounding areas.

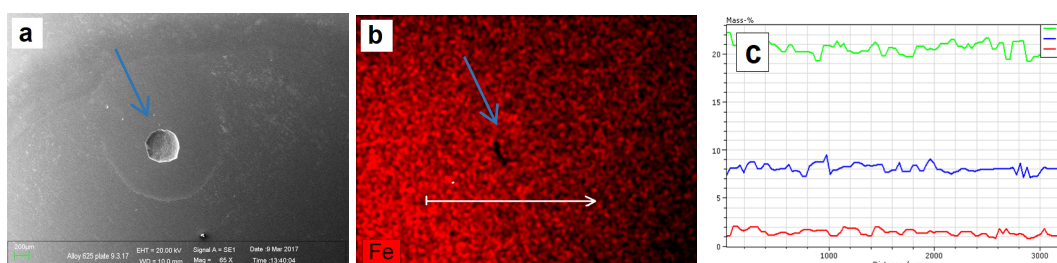


Fig. 129: Alloy 625 plate. Images from CPT test surface (test 1). a) SEM SE image. b) EDS mapping for Fe. c) EDS linescan graph (Cr: green, Mo: blue, Fe: red). Fe values of linescan: Min: 0.4%, max: 3%, average: 1.5%.

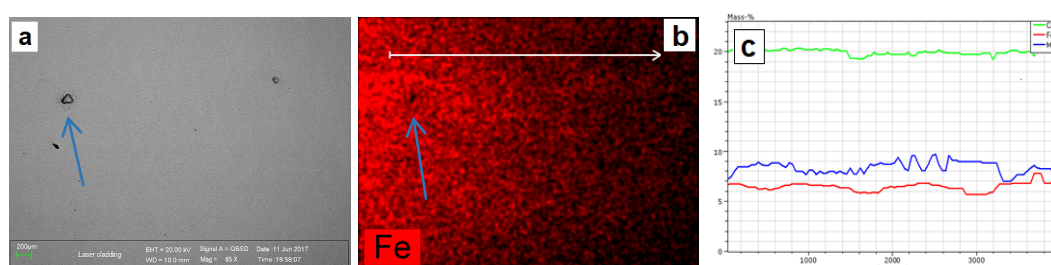


Fig. 130: Laser cladding. Images from CPT test surface (test 2). a) SEM SE. b) EDS mapping for Fe. c) EDS linescan graph (Cr: green, Mo: blue, Fe: red). Fe values of linescan: Min: 5.9%, max: 7.7%, average: 6.6%.

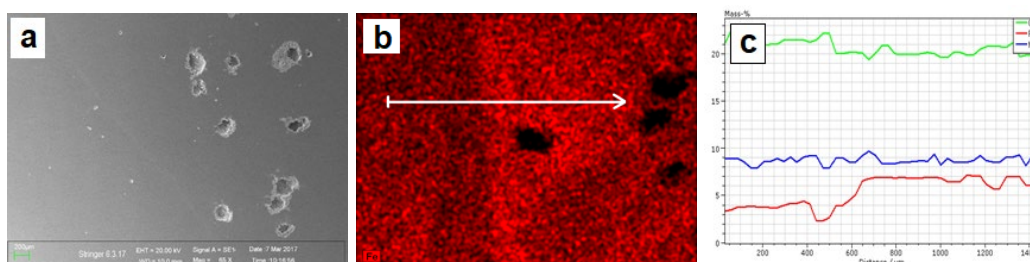


Fig. 131: CMT cladding. Images from CPT test surface (test 1). a) SEM SE image. b) EDS mapping for Fe. c) EDS linescan graph (Cr: green, Mo: blue, Fe: red). Fe values of linescan: Min: 2.5%, max: 7%, average: 5.5%.

As can be seen both from the EDS mapping images and the EDS linescan images, the CMT cladding showed some variation in the iron content on the surface, while the Fe seemed to be evenly distributed with no variation in the alloy 625 plate and in the laser cladding.

It can also be seen that there are more and larger corrosion pits in the CMT cladding surface, but in this case, the size or number of corrosion pits is not necessarily a reliable indicator of corrosion resistance. This is because pits start to grow rapidly once the pitting corrosion temperature has been reached, and not all the tests were continued for as long as each other.

4. Discussion

4.1. Cladding with laser and powder

4.1.1. Laser cladding – powder morphology

The most remarkable feature of the alloy 625 powders' appearance and grain size was that powder No. 6 contained so many small $<10\mu\text{m}$ particles (Fig. 44, 6, p. 90). This large proportion of small particles apparently increased porosity in the test claddings (Fig. 52, 6, p. 96). The large amount of small particles was not mentioned in the analyses certificate, so it could not be estimated or foreseen without microscopy or particle size measurement procedures. However, no further attempts were made to examine the effects of powder morphology or particle size distribution on the laser cladding process.

4.1.2. Laser cladding – parameters

The laser cladding process parameters were not the main focus of this study. The hot cracking studies were made with the parameters (TS: 1000 mm/min, PFR: ~ 30 g/min), which are well suited for the equipment used in the tests (section 2.1.1, Fig. 34, p. 67), particularly the laser beam and the powder feeder. The laser cladding parameters in the laser vs. CMT comparison tests were conducted with another laser cladding apparatus and with other parameters (TS: 1500 mm/min, PFR: ~ 40 g/min), once again, because these process parameters had been proved to produce constant quality in actual production with that apparatus.

4.1.3. Laser cladding – hot cracks and powder impurities

It was proved in this study that the origin of hot cracking comes from the impurity element content, mainly boron (B) in the powder. At the time when most of alloy 625 powders in this study were manufactured (2010–2011), the B content of the powder was not mentioned in any of the analyses certificates, since there was no specified limit for B in any of the specifications or standards. It seems apparent that the upper limit for the B content of alloy 625 feedstock material (powder or wire) used in the cladding process should exist and it should be on the low level, for example the same as for alloy 718, that is to say 0.006%. It was found in this study that the B content of powder sometimes exceeds this value and these powder batches are prone to hot cracking. Recently, (2016–2017) some powder manufactures have introduced alloy 625 powders designed especially for additive manufacturing (AM) purposes. These powders pay special attention to the requirements for additive manufacturing, and have an upper limit of 0.010% for boron [16, 17].

However, the latest alloy 625 powder batch, No. 12, used in this study in the laser vs. CMT comparison tests, was manufactured in 2017. The B content in the analyses certificate for this batch was stated to be 0.00% (Table 12, p. 70). The content should have been and presented more accurately, to three decimals points. In any case, this powder No. 12 produced some small hot cracks in cladding tests with adjacent beads (Fig. 118, p. 146). It seems that the cracks may have been formed when the subsequent cladding pass has heated the previous pass close to its melting temperature, and some low-melting point phases had liquefied and

the tensile stresses had opened up the liquid-containing space between the dendrites. The formation of the cracks may also have been related also to the lack of the oxide-forming elements Al, Ti, Si, and Mn in the powder. These cracks are discussed in more detail below, on page 166.

Furthermore, the laser cladding test samples made with powder No. 12 also contained a relatively large number of inclusions, which appeared dark in both the OM (Fig. 118) and SEM images (Fig. 119). These inclusions are discussed further on page 165.

4.1.4. Laser cladding – the effect of aluminium and titanium in the powder

The aluminium (Al) and titanium (Ti) content of alloy 625 powder was proved to have a significant effect on both dilution and hot cracking laser cladding.

Among the tested 11 alloy 625 powders, the single bead test claddings made with powders that contained some small amount of Al and Ti (0.3%) clearly showed a lower but wider penetration profile than the test claddings made with Al and Ti-free powders (Fig. 51, p. 94).

The hot cracking tests showed that the hot crack density of crack-sensitive powder No. 3 was decreased with the addition of some (0.3%) Al and Ti (Fig. 59, p. 100). In the case of the Al and Ti-free powder No. 8, which was originally hot crack resistant, the addition of a small quantity of B substantially increased the hot crack density. The crack density was then decreased again when some Al and Ti were added together with B to powder No. 8 (Fig. 60, p. 100).

The deeper and sharper penetration of the cross section indicates that the heat gradient in the melt pool is steeper with the powder without Al and Ti (Fig. 62 and 63, p. 102) than powder with some Al and Ti. Shallower and more uniform penetration, indicating a shallower heat gradient, helps to reduce the occurrence of solidification cracks. This effect of Al and Ti is related to the melt pool surface tension and the direction of melt flow in the melt pool. The penetration and heat gradient are dependent on melt flow or convection in the laser cladding melt pool.

Because there is no electric arc or current present in laser cladding, it can be concluded that the dominant convection mechanisms of the melt flow are the Marangoni forces (Fig. 12, p. 30), with buoyancy force being the other mechanism. In arc welding, however, there are also some other mechanisms which affect the melt pool, as explained in section 1.7 on page 29. The explanation for Marangoni convection, the surface tension-driven convection, is that the low content of surface active elements, mainly Al and Ti but also Si, Mn and Ca, raises the surface tension in the melt pool, which causes inward convection. With a relatively high content of surface active elements, more than 0.2–0.3%, the melt pool surface tension is lower and the direction of the convection is reversed to outward.

The direction of the melt flow can be seen from the appearance of a single bead. An inward melt flow leaves V-shaped ripple marks on the bead's surface, while with some Al-and-Ti present in the powder, the bead surface is smoother and there are no ripple marks (Fig. 57, p. 98 and 64, p. 103). In addition, with an inward flow in the melt pool, the solidification pattern is columnar. This leads to the situation where the last-to-solidify eutectic liquid, which consists

of impurities and has a lower solidification temperature, remains at the weld centreline, and hot cracks will form occasionally (Fig. 62 p. 102). On the other hand, after the alloy 625 powder was doped with some Al and Ti, an outward melt flow produced equiaxed solidification, and solidification occurred more smoothly throughout the whole melt pool (Fig. 63 p. 102).

The melt pool surface movements were also examined with a high-speed video camera. From these images (Fig. 65 and 66, p. 104), it was sometimes possible to detect some of the movements on the melt pool surface. When there was no Al or Ti present in the feedstock powder or in the melt pool, some inward movement towards the melt pool surface could be detected with high laser power of 3.9 kW. With Al and Ti present in the feedstock powder, no such inward movement was detected. Instead, it was detected that oxides generated on the surface gathered behind the melt pool. In addition, it was quite evident that the laser cladding melt pool was more stable when there was some Al or Ti present in the alloy 625 powder, than in the case of Al and Ti-free powder (Fig. 67, p. 105).

In the CMT process, both pressure caused by the electric arc and the reciprocating wire tip have an effect on the melt pool movement, so the movement is not only driven by Marangoni forces and surface tension as it is in laser cladding. However, melt pool convection or oxides on the bead surface were not examined in the case of CMT cladding, even though it is obvious that the oxides and also have an effect to the melt pool convection in the CMT process, as was studied recently (2016) by Ahsan et al [203].

4.2. Cladding with CMT process and wire

In contrast to the laser cladding studies, the emphasis in the CMT cladding studies was on the process and the process parameters themselves. No hot cracks were detected, intentionally made, or studied.

4.2.1. CMT – arc power

Arc power during the single bead tests was determined both with the conventional $I_{aver} \times U_{aver}$ method and the AIP (average instantaneous power) method, as explained in section 2.1 on page 52. The measurement settings are presented in section 2.6.6 on page 82. These measurements were made with:

1. Conventional MIG, pulsed MIG and CMT processes with varying the set WFS between 5–12 m/min. The values of the auxiliary parameters ALC and DC were both 0. The shield gas was Ar-30%He.
2. The CMT process with a constant set WFS of 8 m/min and varying the values of ALC and DC. The tested ALC values were: -30%, -15%, 0%, +15% and +30%, and the DC values: -5.0, 0.0 and +5.0, Both Ar-30%He and 100%Ar were used as shield gas. which together yielded a total of 30 tests (2x5x3)

When comparing conventional MIG, pulsed MIG and CMT processes, the results show that in both the pulsed MIG and CMT processes, the AIP method gave higher arc power values than the conventional $I_{aver} \times U_{aver}$ method with all set WFS values. The greatest difference for CMT process in these tests was 46%, and the difference was always over 30% with every WFS

tested. Also with pulsed MIG process, the AIP method gave higher results so that the difference was between 15–30%. However, with conventional the MIG process both methods, $I_{aver} \times U_{aver}$ and AIP, gave quite similar results for arc power (Table 33, 34 and 35, p. 109).

In the tests with the CMT process and varying auxiliary parameters ALC and DC, the AIP method gave higher arc power values, than $I_{aver} \times U_{aver}$ method, with every tested combination of the ALC and DC parameters. The difference was the highest, over 70%, with the combination ALC: -30%, DC: +5.0. (Table 39 and 40, p. 118).

Although it is still not a clearly established fact that the AIP method gives correct results for the process power in the arc welding process, it does seem that it gives more reliable results than the conventional $I_{aver} \times U_{aver}$ method, certainly for the pulsed MIG and CMT processes. According to the latest standards, the AIP is the method of choice when determining the arc power in waveform-controlled welding processes, like the CMT. These standards include the European ISO/TR 18491:2015, the German DSV 0973 and the American QW-409.1 of ASME IX.

In practice the the $I_{aver} \times U_{aver}$ method is quite often the only available option to determine arc power and heat input of the process. Using the AIP method with the power source used in the tests (Fronius TransPuls Synergic 5000 CMT, from 2015), needs some external high-frequency measurement device like an oscilloscope. However, the newest power sources are capable of determining arc power or welding energy with the AIP method by themselves, since the control software of the latest welding power sources senses current and voltage with a high frequency and is able the determine the arc power or the equivalent arc energy.

4.2.2. CMT – wire feed speed

The CMT process was able to produce consistent, scatter-free weld beads with low dilution and a relatively large deposition rates. The wire feed speed (WFS) in the most of the tests for this study was set to 8 m/min, but the actual WFS was usually between 8.5–9 m/min, which yields around 5 kg/h deposition rate. The set WFS was not at its maximum value (10.5 m/min), but was set at a level where the process seemed to be stable and scatter free visually, and according to the regular sound during the process. In addition, the voltage/current graphs from the oscilloscope were also stable with the set WFS of 8 m/min. Some instability started to appear in the oscilloscope graphs when the WFS was set to 9 or 10 m/min (Fig. 77, p. 112).

However, the CMT process could probably be performed just as successfully with a slightly higher set WFS than 8 m/min. The available WFS range is also particularly related to the synergic line in use, which was 1693 in the tests for this study, and this synergic line was designed to operate with 100%Ar shield gas. The synergic line could be modified, especially for Ar-30%He shield gas, overlay welding or for welding with a weaving motion where the melt pool is large, for example. It also seemed that the high short circuiting current that was achieved with the negative Dynamic Control (DC) value of -5.0 was beneficial in terms of increasing deposition rate without increasing penetration and dilution, or causing spattering. Therefore in the newer versions of CMT, the available range of this DC has been further decreased to -10 on some synergic lines [205].

In the CMT process, the actual WFS is not the same as the set one. According to the results of this study, it seems that the actual WFS is usually around 10% higher than the set one, when the auxiliary parameters ALC and DC are both 0. In fact, the difference is even larger (~20%) with a combination ALC: +15%, DC: -5.0, as in this case the actual WFS was measured to be around 10 m/min with a set WFS value of 8 m/min. However, as can be seen in Table 39 (p. 117) and Table 40 (p. 118), the actual WFS can also be lower than the set one, with the negative DC values. For example with a combination of ALC: -30%, DC: +5.0, the actual WFS was 7.2 m/min, i.e. around 10% lower than the set value. With the conventional MIG or pulsed MIG processes, it was also shown (Fig. 78 a, p. 113) that with the same power source, same settings, and the same wire, the actual WFS was stable and the same as the set one (8 m/min).

The fluctuation and above-set-value of the actual WFS (Fig. 78 b, p. 113) is a characteristic feature of the CMT process. These values were measured by the software of the CMT power source, which controls the rotation wire feed rolls that are located next to the wire spool, and the values were recorded by the Fronius Xplorer software. However, the actual WFS at the melt pool can be assumed to be rather stable, since successful single beads (Ar-30%He shield gas, TS: 1000 mm/min) had even height and width that indicates a constant and stable wire feed. Any irregularities in bead width and height that were detected, especially with 100%Ar shield gas (Fig. 87, p. 123), or with higher TS (Fig. 91, p. 127), are an indication of a sluggish melt pool, not an uneven feedstock feed.

The total route of the welding wire has several sections in the CMT process (Fig. 36, p. 68). After the wire feed rolls there is a wire liner 1 (longer, few meters), the wire buffer, a wire liner 2 (shorter, ~2 m), the CMT Robacta Drive unit that contains the pulsating rolls, and finally the welding torch. The wire is reciprocating, moving back and forth in the CMT process, between the wire buffer and the torch. The virtual fluctuation in the actual WFS in the CMT process is a consequence of the closed loop adjustment process between the wire buffer and the feed rolls. The wire buffer contains a sensor that senses the (small) amount of wire that is stored in the buffer. The wire feed rolls increase or decrease the rotation speed and wire feed based on the feedback from that sensor in the wire buffer, but the actual feedstock feed at the melt pool remains quite stable. With the conventional MIG and pulsed MIG processes, this closed loop control does not exist and the rotation speed of the wire feed rolls is constant.

In summary, the CMT process adjusts the wire feed rate to match the wire melting rate at the weld pool, and the actual melting rate is dependent on the auxiliary parameters, especially on DC – dynamic control. Thus the set WFS value is a kind of guideline value. In conventional MIG and pulsed MIG processes, WFS is fixed and the actual is the same as the set value (Fig. 78, p. 113), and the process is adjusted to fit the wire melting rate to the constant WFS by other means, by varying the current. This fact, that the actual WFS differs from the set value, is not really dealt with in the CMT process brochures and descriptions.

4.2.3. CMT – shield gas

According to both the oscilloscope graphs and the audio-visual evaluation during the process, the process itself was quite stable with both Ar-30%He and 100%Ar shield gas. However,

100%Ar shield gas produced a narrow bead with a steep contact with the substrate and single beads also suffered from humping-type defects that make bead uneven. However, it was shown that it is possible to produce low-dilution claddings with the CMT process and stringer motion, but cladding is more successful and reliable if there is He in the shield gas. With 100%Ar shield gas the melt is too sluggish and the bead is narrow with an uneven toe-line, and cladding with adjacent beads can cause blowholes. On the other hand, a weaving motion would help to widen the bead and make the contact to the substrate less steep even with 100%Ar shield gas. However, the results from the tests with a weaving motion are not presented in this study.

4.2.4. CMT – travel speed and track displacement

The available travel speed (TS) range with CMT process was determined first with single bead tests and TS values of 1000, 1200 and 1500 mm/min. The focus was to determine if the productivity in terms of covered area could be increased by increasing TS. When TS is increased, the height of single bead does not get lower, but bead gets narrower, as illustrated in Fig. 95 on page 143. In addition, and especially with the highest tested TS of 1500 mm/min with single beads, the fluctuations in bead height and width, the so called humping effect, started to take over. Some undercut defects started to appear with this 1500 mm/min TS, too. Nevertheless, this TS of 1500 mm/min can be used in the laser cladding process without any obvious difficulties, although it is still possible that the high TS affected the formation of inclusions (page 165) and the small track displacement (TD) may have affected the hot crack formation (page 166) in the laser-clad microstructure.

It was proved that cladding with the CMT process and adjacent beads, it is possible to use a travel speed (TS) of 1000 mm/min, which is relatively high for the arc welding method. In fact, even a higher TS of 1200 mm/min with a shield gas containing 30%He, seemed to be able to produce good quality claddings with a good productivity, low penetration and dilution (Table 47 and 100, p. 134). However, when the TS was further increased with adjacent beads to 1400 mm/min, the beads get narrower, the following pass hits more of the surface of the base material which was not covered in the previous pass, which means that both penetration and dilution increase.

The optimum value of track displacement (TD) in the CMT was tested with adjacent beads tests that were made mainly with TS of 1000 mm/min, Ar-30%He shield gas, and with two combinations of auxiliary parameters: ALC: 0%, DC: 0.0 and ALC: +15%, DC: -5.0. Some results from these tests are shown in Table 45 and Fig. 98 (p. 133). The 'optimum' combination of auxiliary parameters ALC: +15%, DC: -5.0, seemed to produce slightly higher maximum penetration depth, compared to the 'neutral combination' ALC: 0%, DC: 0.0, but the effect on average penetration was slight.

It seemed that both penetration starts to increase, and some underfill-defect may appear when the value of TD is above 4.2 mm. This combination of TS (1000 mm/min) and TD (4.2 mm) produces a cover rate of 0.25 m²/h. However, the combination of a TS of 1200 mm/min and a TD of 3.5 mm produced the same cover rate of 0.25 m²/h with slightly lower penetration depth (Table 47 and Fig. 100, p. 135).

However, to be on the safe side, in the comparison tests of the laser and CMT cladding, a TS of 1000 mm/min and a TD of 3.8 mm producing a cover rate of 0.23 m²/h, with a 'neutral' combination of ALC: 0%, DC: 0.0, were used. This combination of parameters avoided defects that may appear with higher values of TS or TD, mainly underfill-type holes in the cladding.

4.2.5. CMT – hot cracks

No hot cracks were detected from any of the alloy 625 claddings made with the CMT method. It is assumed that the reasons for this are related to:

1. Alloy 625 feedstock material has a higher purity level in its wire form. The same alloy 625 wires that are used in overlay welding are used extensively in fusion welding of Ni alloys or stainless steels. Thus, the quality requirements are very stringent, since no cracks can be permitted in fusion welds. The wire is also manufactured specifically to be used as a feedstock material in MIG/MAG welding. This is in contrast to the powders, which also have other uses than laser cladding. Furthermore, even though the boron content of the alloy 625 wire was not revealed in the analyses certificates, the other impurity elements S, P and Si are at a very low level.
2. The CMT process is a low heat input process and the electrical parameters are controlled by the synergic line (section 1.11.3.1, p. 47). Thus, it is virtually impossible to reach the higher (excessive) process power values that were utilized in laser cladding test to assist the formation of hot cracks. The highest dilution values that were reached with the single bead tests with Ar-30%He shield gas were around 20% (Table 41, p. 122). These dilution values were only reached when the ALC and DC parameters were set to their extreme limits (ALC: +30%, DC: -5.0), and which produced the highest arc power values.
3. According to some studies [83, 84] the stirring of the melt pool which occurs with the oscillation of the arc can be beneficial in reducing the hot cracking tendency by grain refinement. The reciprocating motion of the wire in the CMT process could also be considered to be a form of oscillation, i.e. a motion whose effect bring an additional stirring movement to the melt pool that prevents the formation of hot cracks. Stirring the melt pool by arc oscillation is discussed more in section 1.6.2.10 on page 26.

4.2.6. CMT – applicability of the process to cladding

The CMT cladding process itself turned out to be very flexible and the process is able to apply itself so that the average WFS is the same as the melting rate of the wire by the melt pool. This WFS is not the same as the set one. This feature has been designed by the manufacturer, Fronius, and is further governed by the synergic line.

Another feature of the CMT process, as well as other MIG/MAG processes, is that the wire is always pointed at the spot where the higher energy density is and where the melting occurs. This is because it is the wire itself that creates the heat in the form of electric arc. This is in contrast to laser cladding, with wire as a feedstock material, or laser-MIG-hybrid cladding, where there are a number of difficult issues, two of which are the proper alignment of the wire to the laser beam and melt pool, and the synchronisation of the WFS to the actual melting rate

[120]. Also in laser cladding with blown powder, the alignment of the powder stream and laser beam can be an issue.

Another typical defect in laser cladding with both powder and wire as a feedstock material, is lack of fusion between the base material and the cladding. In cladding with CMT, even though the penetration and dilution values are low, lack of fusion between the base material and the weld rarely seems to be a problem. This is probably because in an arc welding process such as CMT, the arc plasma affects the surface of the base material in front of the moving melt pool. Therefore, any oxides and impurities are cleaned off and a thin surface layer is even melted, which better prepares the surface to interact with the molten feedstock material of the melt pool, and thus creates a good metallurgical bond. This arc-affected area ahead and beside the melt pool is about 2 mm wide (Fig. 106, p. 138). This issue is discussed more in the following section, 4.3.1.

However, some small inclusions or interrune-type defects were detected from the substrate-cladding interface of CMT claddings. An example of this defect is presented in Fig. 123 on page 149. The origin of this type of defect probably lies in the curved shape of the weld toe line, or the border of the bead. In other words, there is variation in the bead width, and due to this variation, some oxide inclusion are occasionally trapped between beads. However, single beads that were made with Ar-30%He shield gas exhibited a relatively straight weld toe-line compared to the one made with 100%Ar shield gas, but in either case the toe line was less smooth and straight than it was for laser cladding.

4.3. Laser cladding vs. CMT cladding

4.3.1. Laser vs. CMT – surface cleaning

The results of the examination of the substrate surface of a single bead from both laser and CMT claddings are presented in section 3.3.1 on page 136. The surface cleaning effect of the electric arc, whether the positive electrode is the wire in MIG/MAG welding, or the tungsten in TIG welding, is an essential feature in welding aluminium. This cleaning effect is the reason why alternating current (AC) is used in the TIG welding of aluminium. The phase when the tungsten electrode is the positive pole cleans the oxides off the surface, while the other phase in which the tungsten is the negative pole, gives the electrode time to cool down, since most of the heat load is directed at the positive electrode.

Sarrafi and Kovasevic [135] identified three arc-affected areas on the surface of aluminium, A, B and C in TIG (AC) welding. These are presented in Fig. 27 on page 57. These same areas were detected in this study near the bead of CMT cladding, and are presented in Fig. 106 on page 138. It was also detected that a thin layer of Ni was formed on the smooth molten surface area (B) close to the weld bead (Fig. 107–109, p. 139).

Although it is recognised in welding aluminium, this cleaning effect is usually neglected in the welding of steels, and also in overlay welding using arc welding methods. It can be assumed that there are basically at least three reason for this. 1. Iron oxide melts at a lower temperature than aluminium oxide (Table 4, p. 33), so the iron oxide rises and floats on top of the melt pool, which means that welding defects caused by oxide inclusions in steel welds are not

usually an issue. 2. In the (fusion) welding of steel, high voltages are used that generate greater penetration that melts the mating surfaces to a relatively high depth of a few millimetres. The welding of steels is quite often done on plates with a hot-rolled surface and a relatively thick oxide layer, but this oxide does not normally cause welding defects due to the high welding voltage and the easy-to-melt iron oxide. 3. MAG welding of steel is normally done with shield gas containing CO₂ and this oxidises the surface anyway.

As has been stated, the plasma arc column of the CMT welding process heats up a very thin layer of the substrate, both ahead of and beside the melt pool. On the other hand, the effect of the arc on the substrate surface can be harmful. The tests showed that with a high TS of 1500 mm/min and higher values of the auxiliary parameter ALC (+15% and +30%), some undercutting defects started to appear by the bead (Fig. 93, p. 128). This is quite a common defect in arc welding with a high TS, but it does not appear in laser cladding.

4.3.2. Laser vs. CMT – coating thickness

The most significant difference between the two methods, laser cladding with powder and CMT cladding with wire, is that with laser cladding it is possible to achieve relatively thin coatings, while in CMT cladding, the minimum height of a single bead is around 2 mm with a Ø1.2 mm wire. It was not possible to decrease the height of a single bead by increasing the TS, since this leads to narrower and uneven beads and humping defect (Fig. 95, p. 130).

As the single bead laser cladding tests in the laser vs. CMT comparison showed, it is possible to produce a laser cladding with high TS of 1500 mm/min and with a low single bead height of 0.75 mm, thus producing a low height to width ratio of 0.16 (Table 49, p. 141). This low height to width ratio can be advantageous in producing overlapping adjacent passes. In contrast, CMT single bead cladding in the laser vs. CMT comparison produced a height to width ratio of 0.30 (H: 2.1 mm, W: 7.1 mm). This seemed to be the minimum of the achievable range since no lower values were measured in any of the CMT single bead test claddings (Table 41, p. 122).

In laser cladding, TD is quite often kept at a low level, meaning that the overlapping is large. With a large overlap, the next cladding pass mainly hits the previous pass, thus decreasing penetration and dilution. This proved to be the case in this study, too. The laser cladding test samples in laser vs. CMT comparison were made with a track displacement of 1.5 mm (68% overlap) in order to reduce penetration and dilution. Consequently, although the penetration and Fe content (dilution) of the first pass were 0.5 mm and 32% respectively, the dilution decreased in the subsequent passes and by the last pass the penetration was only 0.2 mm and the Fe content 9% (Table 50, p. 143).

In the case of CMT cladding, there is less need to use small value of TD to decrease penetration and dilution. In the laser vs. CMT comparison tests, a TD of 3.8 mm (~46% overlap) was used for CMT test claddings, which is on the safe-side. Slightly larger values could probably have been used without increasing penetration or causing too much 'waviness' in the cladding surface. In the CMT cladding, penetration and dilution (Fe-%) were already low in the first pass (0.4 mm and 9% Fe respectively) and they decreased slightly in the subsequent passes (Table 50, p. 143).

The use of larger TD (3.8 mm) in the CMT cladding clearly produced a higher coverage rate ($0.23 \text{ m}^2/\text{h}$) than that of laser cladding ($0.14 \text{ m}^2/\text{h}$) with TD of 1.5 mm, even though the TS was 50% higher in the laser cladding (1500 mm/min) than in CMT (1000 mm/min). If productivity is measured in terms of produced cladding mass per hour, the productivity of CMT cladding (5.1 kg/h) was over two and a half times greater than it was for laser cladding (2 kg/h). However, the fact that CMT cladding produces thicker coatings, compensates this difference in productivity.

4.3.3. Laser vs. CMT – process energy and heat input

The process power and energy values for the laser cladding and CMT processes are presented in Table 52 on page 144.

In the single bead CMT tests, the actual arc power in the CMT process using the AIP method was estimated to be approximately 37% higher than the arc power determined with the conventional $I_{\text{aver}} \times U_{\text{aver}}$ method (Table 35 and 39). In laser vs. CMT comparison tests, the $I_{\text{aver}} \times U_{\text{aver}}$ method produced arc power of 2830 W for CMT process. Therefore, the actual process power (AIP) CMT cladding was estimated to be 37% higher, 3880 W. The actual process power at the workpiece in laser cladding was estimated to be 3800 W with a laser power set value of 4200 W.

Total laser-on time or arc-on time was clearly higher for laser cladding (197 s) than for CMT (126 s), since laser cladding needed more passes to cover the same area. Based on actual power values and total arc-on time, the energy input to the process, to heat and melt the thin layer of substrate and filler material, was calculated to be 750 kJ for laser cladding and around 490 kJ for CMT cladding when the cladding sample size was 150 x 50 mm. This difference is relatively small, but it must also be remembered that although the test samples covered were the same size, the thickness and mass of the CMT cladding was larger.

If these energy values above are multiplied with the process efficiency values, the difference between the laser and CMT processes is much larger. It was estimated that the wall-plug efficiency of the laser power source was 30%, meaning that in order to produce 4200 W of nominal power from the laser beam source, 14 000 W of power had to be drawn from the grid. The wall-plug efficiency for CMT process was estimated to be 92%, so to produce 3880 W of actual arc power (AIP), only 4220 W electrical power is needed from the grid. This kind of computation puts the efficiency difference between laser and CMT on a whole other level. The electrical energy to produce one square meter of alloy 625 cladding with laser takes 373 MJ, while it is only 66 MJ with the CMT process (Table 52, p. 144). According to this determination, the electrical energy consumption of the CMT process is only 18% of that of the laser cladding process. This difference is even larger (15.5%) if the comparison is made based on the deposition rate in terms of kg/h, which gives comparable values of 20.6 MJ/kg for laser cladding and only 3.2 MJ/kg for CMT (Fig. 116, p. 145).

The substrate plate heated to a slightly higher temperature in laser cladding than in CMT process (Fig. 115 and Table 51, p. 143). On the other hand, the heat input to the substrate is directly related to HAZ depth. In the laser and CMT comparison test claddings, the maximum HAZ depth values at the last bead were 1.6 mm in laser cladding, and 2.0 mm in CMT

claddings (Table 50, p. 143). In other words, the HAZ depth was slightly lower for laser cladding than for CMT cladding, but the substrate plate heated to a higher temperature in laser cladding. This is reasonable, since the TS in the laser process was clearly higher, 1500 mm/min. So, although the single pass heated a smaller volume of the base material, the total accumulation of heat was higher in the laser cladding since the cladding took longer and the total energy input was larger, as explained in the previous paragraph.

4.3.4. Laser vs. CMT – microstructure

Both laser cladding and CMT cladding had quite similar microstructures in which the solidification was columnar dendritic. The microstructure of the laser cladding was slightly finer than that of CMT. The primary dendrite arm spacing in laser single bead cladding was around 5–9 μm (Fig. 117, p. 146) and in CMT single bead cladding it was around 10–12 μm (Fig. 122, p.149).

The laser cladding done with powder No. 12 contained a relatively large amount of inclusions in the microstructure, while hardly any inclusions were detected in the CMT cladding. These inclusions in the laser cladding appeared dark in both the OM (Fig. 118, p. 146) and SEM BE images (Fig. 119). When analysed with EDS, the inclusions consisted mainly of the elements O and Cr. Presumably, the main reasons for these inclusions in the laser cladding microstructure are:

1. The high TS of 1500 mm/min and the very fast solidification rate which do not leave time for the inclusions to rise and float on the melt pool surface. The dendrite arm spacing that indicates the solidification rate was in the order of 5–9 μm , which is clearly smaller than that of the CMT claddings.
2. According to the analyses certificate for powder No. 12, as presented in Table 12 on p. 70, powder No. 12 had very low contents of the elements Al and Ti, as well Si and Mn, and these can act as oxygen binders in the melt. So, due to the shortage of these elements, Cr oxide was formed instead, since there is plenty of Cr available.
3. The Gibbs free energies for the formation of some metal oxides together with oxide densities and melting temperatures are presented in Table 4 on page 33. Gibbs free energy for Cr_2O_3 is lower (-409 kJ/mol) than that of both Al_2O_3 (-800 kJ/mol) and TiO_2 (-650 kJ/mol). This means that Al and Ti oxides are formed first if these elements exist in the melt together with oxygen. So, in the absence of Al, Ti, Si and Mn, Cr was the only element that could react with the free oxygen in the melt. Normally, when there is some Al, Ti, Si and Mn, these oxides will form first, rather than Cr oxide.
4. The density of Cr_2O_3 (5.2 g/cm³) is higher than that of SiO_2 (2.7 g/cm³), Al_2O_3 (4.0 g/cm³) and TiO_2 (4.2 g/cm³) oxides. This may also have prevented the Cr_2O_3 inclusions from rising to the melt pool surface, so that they were left in the melt pool during solidification.
5. It is possible, and even likely, that these Cr and O-containing inclusions existed already in the alloy 625 powder No.12 and were not melted during the laser cladding process. However, the microstructure of the powder was not examined to confirm this.

However, it is unclear if these inclusions affected the formation of the hot cracks detected from the laser test claddings made with powder No. 12 (Fig. 118 and 119, p. 146). Neither is it clear whether these inclusions have a negative effect on the other properties examined in this study, i.e. corrosion and hardness. The laser cladding test samples exhibited similar pitting corrosion resistance as the alloy 625 plate and the CMT test cladding (Table 53, p. 152). In any case, inclusions do have an effect on the fatigue properties of the cladding. Inclusions act as an initiation site for fatigue cracks, but not as effectively as the hot cracks in the structure [204]. Nevertheless, the CMT claddings appeared to be nearly free of inclusions. A few dark spots that were detected from the microsections with an optical microscope appeared to be small pores (Fig. 124, p. 150). Some inclusions were also detected between the beads from the substrate-cladding interface (Fig. 123, p. 149).

4.3.5. Laser vs. CMT – cracks with powder No. 12

The laser cladding samples made with adjacent beads and powder No. 12 contained some small hot cracks. The characteristics of the laser cladding process where these cracks were formed are: 1. the substrate was inclined – the work angle was high (30°) in the process, and 2. the value of TD was small, 1.5 mm, so that the laser beam was focused mainly on the previous pass, not on the substrate surface. This causes the previous pass to heat up sharply, close to its melting temperature, and some low-melting point phases in the previous pass must have liquefied and tensile stresses must then have opened these liquid-containing areas between the dendrites. In other words, the specific type of cracks seem to be a liquation crack (section 1.6, p. 19). In a study by Mandziej [67], this type of hot crack has been termed microfissuring. According to Mandziej, microfissures are reheat-type fine cracks of about 1 mm or less in length when visible on the transverse sections of welds and up to a few millimeters long in the direction of the weld. They often form in the inter-bead and in the HAZ of multi-layer or multi-bead welds. Mandziej also presented an explanation, or a model, of how these microfissures are formed during welding [67].

4.3.6. Laser vs. CMT – corrosion resistance

According to the tests with the modified ASTM G150 test, the measured critical pitting corrosion temperature (CPT) for both laser and CMT cladding was around the same level, ~50 °C, with that of alloy 625 plate (Table 53, p. 152). This was very close to the temperature, 52.2 °C, that was measured with the same method in the study by Johansson et al. [202] on 3 mm thick alloy 625 sheet. This CPT of around 50 °C obtained with both laser and CMT cladding is good, if the fact that both tests claddings had only one cladding layer, is considered. Quite often the alloy 625 overlay welding with arc welding processes (cladding) is made with two layers to reach low iron content on the surface, and hence the the desired corrosion properties.

However, the laser cladding showed a slightly lower average CPT than the alloy 625 plate and the CMT cladding. Furthermore, the lowest test result for laser cladding (44 °C) was lower than that of alloy 625 plate and CMT cladding. There was some inherent deviation in the test results that may have originated from the fact that the method itself is not very accurate. However, it should be pointed out that the deviation of the test results for alloy 625 plate was

only ± 1 °C, and it probably originated from the fact that, as the material itself is very homogeneous, this is an inherent deviation or inaccuracy in the method itself.

Analysing the corrosion test surface with the SEM EDS method showed that even though the average Fe content of CMT claddings is low, around 5%, there were areas with a low Fe content of 2.5%, and higher of >7%, and these areas with higher content seem to be the same ones that were attacked by pitting corrosion during the corrosion tests (Fig. 130, p. 153). Also some areas with a slightly higher Fe content of 16% (Fig. 126, p 151) were found from the CMT cladding cross section. The CPT test surface of laser cladding seemed to be slightly more homogeneous with Fe content in the range of 6–8% (Fig. 131, p. 153), and no any higher Fe-containing areas were found from the the cross section of laser cladding.

5. Final conclusions and recommendations

5.1. Laser cladding

In laser cladding, some alloy 625 powder batches tested in this study showed some sensitivity to hot cracking and one powder batch, powder No. 3, was very prone to cracking. This sensitivity is related to the content of impurity elements, especially the boron content, but the most crack-sensitive powder, No. 3, was also free of aluminium (Al) and titanium (Ti) which also affected the hot crack sensitivity.

When most of the alloy 625 powders in this study were manufactured, around 2010–2011, the boron content of the powders was simply not mentioned in any of the analyses certificates. The boron content was mentioned in the analyses certificate of the most recent (2017) powder batch (No. 12), which was used to make the laser cladding vs. CMT comparison tests. However, this powder batch produced some small hot cracks and large number of inclusions containing Cr-O in the microstructure. This was apparently related to the shortage of other oxide forming elements, Al and Ti.

Variations in the composition of the alloy powder cause variations in dilution in laser cladding. This was proved to be related in the melt pool convection during the process. Surface active elements, mainly Al and Ti but presumably also silicon (Si) and manganese (Mn), have an effect on the melt pool surface tension and hence the direction of the melt pool convection. Al and Ti-free powder produces an inward flow in the melt pool that leads to deeper penetration, steeper thermal gradients and a columnar dendritic structure, so that the last-to-solidify melt is left at the weld centreline and hot cracks may form before the melt with the lower solidification temperature has totally solidified. Some Al and Ti content (~0.3%) in the powder decreases the melt pool surface tension and produces outward melt pool convection that supports a flat melt pool with low penetration. This outward melt flow in the melt pool leads to a lower temperature gradient and a more equiaxed dendritic structure, so that the last-to-solidify melt is not left at the weld centreline.

In order to ensure the reliability of the laser cladding process when using alloy 625 powder, the composition of the powder needs to be specified more strictly than is currently specified by the standards. In particular, the content of impurity elements, mainly boron, should be limited to low level, for example at the same level that it is for alloy 718, i.e. <0.006%. In addition, to ensure more stable penetration and dilution, the contents of Al and Ti should be controlled more strictly than they are at present, which is less than 0.4%. However, some Al and Ti seems to be beneficial, so there should be some lower limit for these elements, for example around 0.2%. In addition, if there are no other oxide-forming elements (Al, Ti, Mn, Si) except chromium (Cr) present in the alloy 625 powder, this may lead to Cr-oxide inclusions in the microstructure.

5.2. CMT process

In addition to CMT process, some tests were made with the conventional MIG and pulse MAG processes, especially to compare the actual process power in all three types of MIG/MAG

processes: conventional MIG, pulsed MIG and CMT. The results with single beads using oscilloscope to determine the average instantaneous power (AIP), showed that the actual arc power determined with AIP method is lower in the CMT process than it is in the conventional MIG and pulsed MIG processes. However, especially with CMT process, the actual arc power determined AIP method was higher (20–70%) than the power determined with the conventional method, in which the average current is multiplied with the average voltage ($I_{aver} \times U_{aver}$). With pulsed MIG process this difference was lower (15–30%) and with conventional MIG process, this difference did not exist.

The CMT process proved to be more stable than the conventional MIG and pulsed MIG processes in the sense that the CMT process produced sound and continuous weld beads with all the tested WFS rates of 5 –10 m/min with a minimum amount of spatter. Furthermore, there was less black soot by the bead with the CMT process than there was with the conventional MIG and pulsed MIG processes.

In the CMT process, the actual WFS is not the same as the set one. According to the results of this study, it seems that the actual WFS speed is usually around 10% higher than the set one when the values of the auxiliary parameters ALC and DC are both 0. This difference is even larger (~20%) with the auxiliary parameters combination ALC: 15, DC: -5.0, in which case the average actual WFS speed was around 10 m/min with a WFS set value of 8 m/min. This combination of auxiliary parameters, ALC: +15%, DC: -5.0 would be the optimum, since this combination yields the largest wire feed rate without increasing penetration and dilution too much. The reason for this is that with negative DC values, the current during the short circuit phase is higher and this melts more wire through resistive heating. In addition, this higher current during the short circuit phase did not seem to lead to spattering.

Unlike in laser cladding, the melt pool in the CMT process doesn't spread enough to enable lower bead heights. This is related to the high viscosity of the melt and the sluggish melt flow of alloy 625. In laser cladding process, it is easier to achieve lower beads by adjusting certain parameters, like powder feed rate (PFR) or travel speed (TS). This sluggish melt is particularly pronounced in the CMT process since the heat input and the melt pool temperature are lower than they are in the spray arc and pulsed MIG processes. However, according to the single bead tests that were done with the conventional MIG, pulsed MIG and CMT process (section 3.2.1, p. 106), the single bead height and width with the CMT process appeared to be at a comparable level to the other processes (Fig. 75, p. 111), but the penetration and dilution were lower. In this study, it was found that bead height/width ratios of 0.35 or less were achievable and beneficial in cladding with the CMT process and adjacent beads.

In cladding with the CMT process, the minimum cladding thickness with adjacent beads seems to be around 2 mm. Increasing the TS does not help to reduce the bead height, but instead the bead gets narrower and the variation in bead width and height starts to increase. This indicates the early stages of the humping type defect caused by erratic melt movements in the melt pool. So, if the TS is increased too much, it makes the melt pool very unstable and the melt occasionally gathers into ball-shaped 'hump' formations along the weld.

It was found that CMT cladding produces a wider bead and is more reliable if a helium (He)-containing shield gas is used. When cladding with single beads and 100% argon (Ar) shield gas, the melt is sluggish and produces high, narrow beads, with unstable width to height ratios. However, some successful cladding tests were done with a 100%Ar shield gas and adjacent beads with the lowest one tested, but still relatively high TS of 1000 mm/min. Cladding with a He-containing shield gas seems to be successful, at least up to a travel speed of 1200 mm/min. Beyond this speed, the beads did not get shallower, but were narrower and bead humping started to dominate the bead formation. With a moderate TS of 1000 mm/min, the danger of underfill-type defects, which are common in the CMT cladding process, was virtually eliminated.

According to the comparison of process productivity and the electrical efficiency of the CMT process was clearly much better than that of the laser cladding process (Table 52, p. 144). With a laser cladding process the measured deposition rate was 2.4 kg/h, whereas with the CMT process the deposition rate was doubled to 4.8 kg/h. This difference between processes is slightly lower 0.14 m²/h vs. 0.23 m²/h, if the comparison is based on cover rate, the area that can be covered in an hour, since with the CMT process the coating layer is thicker. According to the calculations, the laser cladding process needs 373 MJ (104 kWh) of electricity energy from the grid to produce one square meter of alloy 625 cladding. For the CMT process, the corresponding figure is only 66 MJ (18 kWh). Most of this saving can be attributed to the fact that a CMT welding power source is much more energy-efficient. However, this comparison does not take into account the energy needed to produce the feedstock material, alloy 625 in the form of powder or wire.

It was proved that the CMT process is able to produce claddings with low dilution and with relatively large productivity. The question mark in the CMT cladding process is the long-term durability of the components of the equipment. Some examples of problems that could be encountered in the long term are: wear of the contact tip, the accumulation of weld spatter in the shield gas nozzle, or wear of the wire liner inside the welding torch. Some of these problems were found with other feedstock wire materials that were tested with longer test runs during the Interreg North financed CMT project (2015–2017). However, these problems were not specifically studied with alloy 625 and are not presented in this study. Whereas it has been proved that the laser cladding process with blown powder can continue for several hours without interruptions, and the quality stays stable as long as the feedstock variables; grain size, composition etc. stay unchanged. Furthermore, it has to be acknowledged that the CMT cladding parameters used in this study, or even the process itself, have not yet been proven to operate so reliably without interruptions and with consistent quality.

References

1. YourDictionary. <http://www.yourdictionary.com/cladding> (09/2018).
2. Inconel – Trademark Details. <https://trademarks.justia.com/713/33/inconel-71333517.html> (11/2017).
3. Wikipedia: Inconel 625. https://en.wikipedia.org/wiki/Inconel_625 (11/2017).
4. Lai, G.Y. & Blogg, N. (2004). Unifuse® overlay cladding for surface protection against corrosion and erosion/corrosion in power boilers and waste heat recovery systems. OMMI (Vol.3, Issue) December 2004.
5. Näkki, J. unpublished results.
6. Inconel alloy 625 product specification. Special Metals Corporation (2013). <http://www.specialmetals.com/assets/smc/documents/alloys/inconel/inconel-alloy-625.pdf> (11/2017)
7. Eiselstein, H.L. & Tillack, D.J. (1991). The Invention and Definition of Alloy 625. Conference: Superalloys 718, 625 and Various Derivatives, ed. E.A. Loria, (TMS, Warrendale, PA, 1991), 1-14.
8. Smith, G.D., Tillack, D.J & Patel, S. J. (2001). Alloy 625 – Impressive Past/Significant Presence/Awesome Future. Conference: Superalloys 718, 625, 706 and Various Derivatives Edited by E.A. Loria. 2001.
9. Cladding Solutions for the Waste to Energy Industry – brochure. Voestalpine, UTP Maintenance. http://www.voestalpine.com/welding/content/download/7610/150591/file/025-2015-EN-GL_UTP_WasteToEnergy_WEB.pdf (05/2018).
10. Shoemaker, L.E. (2005). Alloys 625 and 725: Trends in properties and applications. Superalloys 718, 625, 706 and Derivatives 2005. Edited by E.A. Loria TMS (The Minerals, Metals & Materials Society), 2005.
11. EN ISO 18274 (2010). Welding consumables. Solid wire electrodes, solid strip electrodes, solid wires and solid rods for fusion welding of nickel and nickel alloys. Classification.
- 12 American Welding Society. A5.14/A5.14M:2018 Specification for nickel and nickel-alloy bare welding electrodes and rods. ISBN: 978-0-87171-931-7
13. ASTM F3056-14e1. Standard Specification for Additive Manufacturing Nickel Alloy (UNS N06625) with Powder Bed Fusion. ASTM International, 2014.
14. Dupont, J.N., Lippold, J.C. & Kiser, S.D. (2009). Welding metallurgy and weldability of nickel-base alloys. John Wiley & Sons. 2009. ISBN: 978-0-470-08714-5.
15. Reed, R.C. (2006). The Superalloys, Fundamentals and Applications. Cambridge University Press. 2006. ISBN-10 0-521-85904-2.
16. Amperprint – The powder to create, brochure (2017). H.C. Starck GmbH. https://www.hcstarck.com/hcs-admin/file/ae23e4b25ccebdc3015da241c6df5af9.de.0/AMPERPRINT_alle%20Tabellen.pdf (05/2018).
17. Material Specifications – TruForm™ 625 Metal Powder (2016). Praxair S.T. Technology, Inc. <http://www.praxairsurfacetechologies.com/-/media/us/documents/brochures/truform-625-metal-powder.pdf?la=en> (05/2018).
18. Previtali, B., Riva, G., Librera, E. Sbeti, M. Vanin, M. Biscaglia, G. Villarreal, F. Chann, B. & Lochman., B. (2015). Performance and efficiency of an industrial direct diode source with an extremely low BPP in laser cutting of Fe-based and reflective alloys. Lasers in Manufacturing Conference 2015.
19. Nickel, Cobalt, and Their alloys. ASM Specialty Handbook. ASM International. 2000.
20. Patel, S. J., & Smith, G. D. (2001). The role of niobium in wrought superalloys. In International Symposium on Niobium 2001 (pp. 1081–1108).
21. Floreen, S., Fuchs, G.E. & Yang, W.J. (1994). The Metallurgy of Alloy 625. Superalloys 718, 625, 706 and Various Derivatives. Edited by E.A. Loria. The Minerals, Metals&Materials Society, 1994.
22. Maguire, M. C., & Michael, J. R. (1994). Weldability of alloy 718, 625 and variants. In Proc. Conf. Superalloy (Vol. 718, pp. 881–892).

23. Silva, C.C., de Miranda, H.C., Motta, M.F., Farias, J.P., Afonso, C.R.M. & Ramirez., A.J. (2013). New insight on the solidification path of an alloy 625 weld overlay. *Journal of Materials Research and Technology*. Volume 2, Issue 3, July–September 2013, Pages 228–237. <http://dx.doi.org/10.1016/j.jmrt.2013.02.008>.
24. DuPont, J.N., Notis, M.R., Marder, A. R., Robino, C. V., & Michael, J. R. (1998). Solidification of Nb-bearing superalloys: Part I. Reaction sequences. *Metallurgical and Materials Transactions A*, 29(11), 2785-2796.
25. Guo, J.T., & Zhou, L.Z. (1996). The effect of phosphorus, sulphur and silicon on segregation, solidification and mechanical properties of cast Alloy 718. *Superalloys 1996*, 451–455.
26. Capitanescu, D. (1992). Alloy 625 weld overlays for offshore and onshore projects. *Pressure Vessel Technology*. 2, 1164–1177.
27. Voestalpine, UTP Maintenance. Strips and fluxes for electrosag and submerged arc welding – brochure (2017). http://www.voestalpine.com/welding/content/download/3589/58066/file/UTP_StripsFluxesForSAW_EN_2017.pdf (05/2018)
28. Discussion with a specialist of a powder manufacturer.
29. Moffat, W.G. (1984). *The Handbook of Binary Phase Diagram*, Vol. 1, General Electric Co., Schenectady, N.Y.
30. Portnoi, K.V., Romashov, V.M., Chubarov, V.M., Lavinskaya, M.Kh. & Salibekov, S.E. (1967). Phase diagram of the system nickel boron. *The methods and properties of materials*. Poroshkovaya Metallurgiya, No. 2 (50), pp. 15-21, Feb, 1967.
31. Kelly, T.J. (1989). Elemental Effects on Cast 718 Weldability. *Welding Journal*. Feb 1989. p44s – 51s.
32. Lingenfelter, A. (1989). *Welding of Inconel Alloy 718: a Historical Overview*. Superalloy 718 – Metallurgy and Applications. The Minerals & Materials Society 1989.
33. Chen, W., Chaturvedi, M.C., Richards, N.L. & McMahon, G. (1998). Grain Boundary Segregation of Boron in Inconel 718. *Metallurgical and Materials Transactions A* Volume 29A, July 1998. p. 1947–1954.
34. Chen, W., Chaturvedi, M.C. & Richards, N.L. (2001). Effect of Boron Segregation at Grain Boundaries on Heat-Affected Zone Cracking in Wrought INCONEL 718. *Metallurgical and Materials Transactions A*. Volume 32A, 2001.
35. Haynes 230® alloy brochure. <http://haynesintl.com/docs/default-source/pdfs/new-alloy-brochures/high-temperature-alloys/brochures/230-brochure.pdf> (01/2018).
36. Lippold, J.C. & Nissley, N.E. (2008). *Ductility-Dip Cracking in High Cr, Ni-Base Filler Metals. Hot Cracking Phenomena in Welds II*. Springer 2008.
37. Lippold, J.C. & Nissley, N.E. (2005). *Ductility-Dip Susceptibility of Filler Metal 52 and 52M Ni-base Filler Metals*. Proceedings of the 7th International Conference on Trends in Welding Research, May 2005. USA.
38. Kiser, S.D., Hinshaw, E.P., Crum, J.R. & Shoemaker, L.E. (2005). *Nickel alloy welding requirements for nuclear service. Focus on Nuclear Power Generation*.
39. Xiao, L., Chen, D.L., & Chaturvedi, M.C. (2004). Effect of Boron Concentration on Fatigue Crack Propagation Resistance and Low Cycle Fatigue Properties of Inconel 718. *Conference Superalloys 2004*, TMS, Warrendale, PA, 275-281.
40. Hackett, D. & Kopech, H. (2001). *Atomization advances in Thermal Spray Powder*. Advanced Materials & Processes. April 2001.
41. Tian, Y., Ouyang, B., Gontcharov, A., Gauvin, R., Lowden P. & Brochu, M. (2017). Microstructure evolution of Inconel 625 with 0.4 wt% boron modification during gas tungsten arc deposition. *Journal of Alloys and Compounds* 694 (2017). 429–438. <http://dx.doi.org/10.1016/j.jallcom.2016.10.019>.
42. Morscheiser, J., Thönnessen, L. & Friedrich, B. (2011). *Sulphur Control in Nickel-Based Superalloy Production*. Proceedings of EMC 2011.
43. Okamoto, H. J. *Phase Equilib. Diffus.* (2009) 30: 123. <https://doi.org/10.1007/s11669-008-9430-9>.

44. DeBarbadillo, J.J. (1983). Nickel-base Superalloys; Physical Metallurgy of Recycling. Metallurgical Transactions A, 1983, Vol. 14A, p. 329-341.
45. Cieslak, M.J., Headley, T.J., Kollie, T. & Romig Jr, A.D. (1988). A Melting and Solidification Study of Alloy 625. Metallurgical Transactions A. Vol 19A, Sept 1988.
46. Cieslak, M.J. (1991). The Welding and Solidification Metallurgy of Alloy 625. The Welding Journal, 1991, 70, pp 49s-56s.
47. Dupont, J.N., Robino, C.V. & Marder, A.R. (1998). Solidification and Weldability of Nb-Bearing Superalloys. Welding journal. 1998, vol. 77, no10, pp. 417s-431s (33 ref.).
48. Benhadad, S., Richards, N.L., & Chaturvedi, M.C. (2002). The influence of minor elements on the weldability of an Inconel 718-type superalloy. Metallurgical and Materials Transactions A, 33(7), 2005-2017.
49. Luer, K., Dupont, J., Marder, A. & Skelonis, C. (2001). Corrosion fatigue of alloy 625 weld claddings in combustion environments. Materials at high temperatures 18 (2001).
50. Seyhan, I. & Egry, I. (1999). The Surface Tension of Undercooled Binary Iron and Nickel Alloys and the Effect of Oxygen on the Surface Tension of Fe and Ni. International Journal of Thermophysics, Vol. 20, No. 4, 1999. Pages: 1017 – 1028.
51. Schirra, J.J., Caless, R.H., & Hatala, R.W. (1991). The effect of Laves phase on the mechanical properties of wrought and cast+ HIP Inconel 718. Confrence: Superalloys, 718(625), 375-388.
52. Radhakrishna, C.H., & Rao, K.P. (1997). The formation and control of Laves phase in superalloy 718 welds. Journal of Materials Science, 32(8), 1977-1984.
53. Ganesh, P., Kaul, R., Paul, C.P., Tiwari, P., Rai, S.K., Prasad, R.C. & Kukreja, L.M. (2010). Fatigue and fracture toughness characteristics of laser rapid manufactured Inconel 625 structures. Materials Science and Engineering A 527 (2010) 7490–7497.
54. Rombouts, M., Maes, G. & Persoons, R. (2011). Material study of laser clad Inconel 625. Innovative Developments in Virtual and Physical Prototyping. Proceedings of the 5th International Conference on Advanced Research in Virtual and Rapid Prototyping, Leiria, Portugal, 28 September – 1 October, 2011. 333-337.
55. Dinda, G.P., Dasgupta, A.K. & Mazumder, J. (2009). Laser aided direct metal deposition of Inconel 625 superalloy: Microstructural evolution and thermal stability. Mater. Sci. Eng. A 509, 98-104. <http://dx.doi.org/10.1016/j.msea.2009.01.009>
56. Rombouts, M., Maes, G., Mertens, M., & Hendrix, W. (2012). Laser metal deposition of Inconel 625: Microstructure and mechanical properties. Journal of Laser Applications, 24(5), 052007.
57. Guo, L., Zheng, H., Liu, S., Li, Y., Feng, C., & Xu, X. (2016). Effect of Heat Treatment Temperatures on Microstructure and Corrosion Properties of Inconel 625 Weld Overlay Deposited by PTIG. Int. J. Electrochem. Sci, 11, 5507-5519.
58. Antonsson, T. & Fredriksson, H. (2005). The Effect of Cooling Rate on the Solidification of Inconel 718. Metallurgical and Materials Transactions B. Volume 36B, Feb 2005.
59. SFS-EN ISO 17641-1. Destructive tests on welds in metallic materials. Hot cracking tests for weldments. Arc welding processes. Part 1: General. Mechanical Engineering and Metals Industry Standardization in Finland, 2004 (ISO 17641-1:2004).
60. Borland, J.C. (1960). Generalized theory of super-solidus cracking in welds and castings – an initial development. British Welding Journal. August 1960, pp. 508–512.
61. Lippold, J.C. (2005). Recent Developments in Weldability Testing. Hot Cracking Phenomena in Welds. Springer-Verlag Berlin Heidelberg.
62. SFS-EN ISO 5817. Welding. Fusion-welded joints in steel, nickel, titanium and their alloys (beam welding excluded). Quality levels for imperfections. Mechanical Engineering and Metals Industry Standardization in Finland, 2014 (ISO 5817:2014).
63. Cross, C.E. (2005). On the Origin of Weld Solidification Cracking. Hot Cracking Phenomena in Welds. Springer-Verlag Berlin Heidelberg 2005.
64. SFS-EN ISO 17641-2. Destructive tests on welds in metallic materials. Hot cracking tests for weldments. Arc welding processes. Part 2: Self-restraint tests. Mechanical Engineering and Metals Industry Standardization in Finland, 2015 (ISO 17641-2:2015).

65. Lippold, J.C., Sowards, J.W., Murray, G.M., Alexandrov, B.T. & Ramirez, A.J. (2008). Weld Solidification Cracking in Solid-Solution Strengthened Ni-Base Filler Metals. Hot Cracking Phenomena in Welds II. Springer.
66. Farrar, J.C.M. (2005). Hot Cracking Tests – The Route to International Standardization. Hot Cracking Phenomena in Welds. Springer-Verlag Berlin Heidelberg.
67. Mandziej, S.T. (2005). Testing for susceptibility to hot cracking on Gleeble™ physical simulator. In Hot cracking phenomena in welds (pp. 347-376). Springer, Berlin, Heidelberg.
68. Su, Y., Mills, K.C. & Dinsdale, A. (2005). A model to calculate surface tension of commercial alloys. Journal of Materials Science, Volume 40, 2185 – 2190.
69. Zacharia, T. (1994). Dynamic Stresses in Weld Metal Hot Cracking. Welding Journal. July 1994. Volume: 73:7. Pages 164–172.
70. Clyne, T.W., & Kurz, W. (1982). The effect of melt composition on solidification cracking of steel, with particular reference to continuous casting. Metall. Trans. B, Vol. 13A, pp. 259-266.
71. Matsuda, F., Nakagawa, H., Katayama, D. & Arata, Y. (1982). Weld metal cracking and improvement of 25% Cr-20% Ni (AISI 310S) fully austenitic stainless steel. Transactions of the Japan Welding Society, Vol. 13, pp. 41-58.
72. Pollard, B. (1988). The Effects of Minor Elements on the Welding Characteristics of Stainless Steel. The Effects of Minor Elements on the Welding Characteristics of Stainless Steel. Welding Research Supplement, Sept 1988, pp 202-213.
73. Holthaus, M. (2014). International Welding Engineer (IWE) training course material, HG2. GSI SLV mbH, Gesellschaft für Schweißtechnik international – Schweißtechnische Lehr- und Versuchsanstalten. SLV Duisburg.
74. Kou, S. (2003). Welding Metallurgy. Second edition. A John Wiley & Sons. ISBN: 0-471-43491-4.
75. Savage, W.F. & Dickinson, D.W. (1972). Welding Research Supplement. November 1972. 555-562.
76. Biradar, N.S. & Raman, R. (2012). Grain Refinement in Al-Mg-Si Alloy TIG Welds Using. Transverse Mechanical Arc Oscillation. Journal of Materials Engineering and Performance Volume 21(11) November 2012. pp 2495 – 2502.
77. Kou, S. & Le, Y. (1985). Grain structure and solidification cracking in oscillated arc welds of 5052 aluminum alloy. Metallurgical Transactions A. July 1985, Volume 16, Issue 7, pp 1345 – 1352
78. Kou, S. & Le, Y. (1985). Alternating grain orientation and weld solidification cracking. Metallurgical Transactions A. October 1985, Volume 16, Issue 10, pp 1887 – 1896.
79. Biradar, N.S. & Raman, R. (2012). Investigation of Hot Cracking Behavior in Transverse Mechanically Arc Oscillated Autogenous AA2014 T6 TIG Welds. Metallurgical and Materials Transactions A. Volume 43A, September 2012. pp. 3179 – 3191.
80. Kar, J., Roy, S.K. & Roy, G.G. (2017). Effect of Beam Oscillation on Microstructure and Mechanical Properties of AISI 316L Electron Beam Welds. Metallurgical and materials transactions A. Volume 48A, April 2017, pp 1759 – 1770.
81. Madhusudhana Reddy, G., Srinivasa Murthy, C.V., Srinivasa Rao, K. & Prasad Rao, K. (2009). Improvement of mechanical properties of Inconel 718 electron beam welds – influence of welding techniques and postweld heat treatment. International Journal of Advanced Manufacturing Technology (2009) 43. pp 671–680. <https://doi.org/10.1007/s00170-008-1751-7>
82. Sivaprasad, K., Ganesh, S., Sundara Raman. (2007). Influence of magnetic arc oscillation and current pulsing on fatigue behavior of alloy 718 TIG weldments. Materials Science and Engineering A 448 (2007) 120–127.
83. Lim, Y. C., Yu, X., Cho, J. H., Sosa, J., Farson, D. F., Babu, S. S. & Flesner, B. (2010). Effect of magnetic stirring on grain structure refinement: Part 1–Autogenous nickel alloy welds. Science and Technology of Welding and Joining, 15(7), 583-589.
84. Lim, Y. C., Yu, X., Cho, J. H., Sosa, J., Farson, D. F., Babu, S. S. & Flesner, B. (2010). Effect of magnetic stirring on grain structure refinement Part 2–Nickel alloy weld overlays. Science and Technology of Welding and Joining, 15(5), 400-406.
85. Feng, K., Chen, Y., Deng, B., Li, Y., Zhao, H., Lu, F., Li, R., Huang, J. & Li, Z. (2017). Improved high-temperature hardness and wear resistance of Inconel625 coatings fabricated by

- laser cladding. *Journal of Materials Processing Technology* 243 82–91.
<http://dx.doi.org/10.1016/j.jmatprotec.2016.12.001>
86. Näkki, J., Tuominen, J. & Vuoristo, P. (2017). Effect of minor elements on solidification cracking and dilution of alloy 625 powders in laser cladding. *Journal of Laser Applications*. 29, 012014 (2017); doi: 10.2351/1.4973673.
 87. Aidun, D.K. & Martin, S.A. (1997). Effect of sulphur and oxygen on weld penetration of high-purity austenitic stainless steels. *Journal of Materials Engineering and Performance*. Volume 6(4), 496-502.
 88. Mills, K.C. & Keene, B.K. (1990). Factors Affecting Variable Weld Penetration, *International Materials Reviews*, Vol:35, Pages:185-216
 89. Holt, M., Olson, D.L. & Cross, C.E. (1992). Interfacial tension driven fluid flow model for hot cracking. *Scripta Metallurgica et Materialia*. Volume 26, Issue 7, 1 April 1992, Pages 1119-1124.
 90. Wikipedia – Ellingham diagram. https://en.wikipedia.org/wiki/Ellingham_diagram (10/2018).
 91. Wikipedia – Oxides of metals. https://en.wikipedia.org/wiki/Oxide#Oxides_of_metals (01/2018).
 92. Heiple, C. & Roper, J. (1982). Mechanism for minor element effect on GTA fusion zone geometry. *Welding Journal*. Volume 61(4), 97-102.
 93. Zhao, C.X., Kwakernaak, C., Pan, Y., Richardson, I.M., Saldi, Z., Kenjeres, S. & Kleijn, C.R. (2010). The effect of oxygen on transitional marangoni flow in laser spot welding. *Acta Materialia* Volume 58, 6345–6357.
 94. Savage, W.F., Nippes, E.F. & Goodwin, G.M. (1977). Effect of Minor Elements on Fusion Zone Dimensions of Inconel 600. *Welding Journal*. April 1977. pp. 126 – 132.
 95. Savage, W.F., Nippes, E.F. & Goodwin, G.M. (1977). Effect of Minor Elements on Hot-Cracking Tendencies of Inconel 600. *Welding Journal*. August 1977. Vol. 56. pp. 245–253.
 96. Silva, C. C. (2013). Weld Overlay. In *Encyclopedia of Tribology* (pp. 4094-4101). Springer, Boston, MA. ISBN: 978-0-387-92897-5.
 97. Spicer, R.A., Baeslak, W.A. & Kelly, T.J. (1990). Elemental Effects on GTA Spot Weld Penetration in Cast Alloy 718. *Welding Journal*, August 1990. pp 285s-288s.
 98. Lee, Y., Nordin, M., Babu, S.S. & F. Farson., D.F. (2014). Effect of Fluid Convection on Dendrite Arm Spacing in Laser Deposition. *Metallurgical and Materials Transactions B*. Vol 45B, Aug 2014.
 99. Näkki, J., Pajukoski, H., Tuominen, J. & Vuoristo, P. (2013). The Effect of Minor Alloying Elements of Alloy 625 on the Laser Cladding Process. The International Congress on Applications of Lasers & Electro-Optics (ICALEO) paper ft. 2013.
 100. Gandy, D.W. & Findlan, S.J. (1993). Temperbead Welding Repair of Low Alloy Pressure Vessel Steels: Guidelines, tech. rep., EPRI Repair and Replacement Applications Center, Charlotte, NC, 1993.
 101. Avesta Welding manual – Practice and products for stainless steel welding. Avesta welding AB, 2004.
 102. Belinga, E.M.M. (2012). Applications and Benefits of Adaptive Pulsed GMAW. Master's Thesis. Lappeenranta University of Technology, 2012.
 103. Badisch, E. & Roy, M. (2013). Chapter 5, Hardfacing for Wear on book: *Erosion and Abrasion Surface Engineering for Enhanced Performance against Wear*. Springer-Verlag Wien 2013. ISBN 978-3-7091-0100-1.
 104. Kumar, V., Lee, C., Verhaeghe G. & Raghunathan, S. (2010). CRA Weld Overlay – Influence of welding process and parameters on dilution and corrosion resistance. *Stainless Steel World America 2010*, Houston, Texas, USA, 5-7 October 2010.
 105. Avery, R.E. & Tuthill, A.H. (1994). Guidelines for the welded fabrication of nickel alloys for corrosion-resistant service. A Nickel Development Institute Reference Book Series NO 11 012, 1994.
https://www.nickelinstitute.org/~media/Files/TechnicalLiterature/GuidelinesfortheWeldedFabricationofNickelAlloysforCorrosion_ResistantService_11012_.ashx (11/2017)
 106. Andersson, O. & Parker, K. (2013). Laser Cladding Offers Unique Advantages. *Fabricating and Metalworking magazine*.

<http://www.fabricatingandmetalworking.com/2013/12/laser-cladding-offers-unique-advantages/> (12/2017).

107. Metrode: Strip Cladding Applications brochure (2012). Metrode Products Ltd.
108. Sames, W.J., List, F.A., Pannala, S. Dehoff, R.R. & Babu, S.S. (2016). The metallurgy and processing science of metal additive manufacturing. *International Materials Reviews*. 07 March 2016. <http://dx.doi.org/10.1080/09506608.2015.1116649>
109. Brandl, E. Leyens, C. & Palm, F. (2009). Mechanical properties of additive manufactured Ti-6Al-4V using wire and powder based processes. *Trends in Aerospace Manufacturing 2009 International Conference*. doi:10.1088/1757-899X/26/1/012004
110. Wang, F., Mei, J. & Wu, X. (2006). Microstructure study of direct laser fabricated Ti alloys using powder and wire. *Applied Surface Science* 253. 1424–1430.
111. Syed, W.U.H., Pinkerton, A.J. & Li, L. (2005). A comparative study of wire feeding and powder feeding in direct diode laser deposition for rapid prototyping. *Applied Surface Science* 247, 268–276.
112. Heigel, J.C., Gouge, M.F., Michaleris, P. & Palmer, T.A. (2016). Selection of powder or wire feedstock material for the laser cladding of Inconel 625. *Journal of Materials Processing Technology* 231. 357–365. <http://dx.doi.org/10.1016/j.jmatprotec.2016.01.004>.
113. Borges, B., Quintino, L., Miranda, R.M. & Carr, P. (2010). Imperfections in laser cladding with powder and wire fillers. *International Journal of Advanced Manufacturing Technologies* 50:175–183. DOI 10.1007/s00170-009-2480-2.
114. Liu, S., Miller, E. & Doyle, B. (2016). Development of corrosion and wear resistance overlays by laser hot-wire cladding process. *ICALEO 2016, 35th International Congress on Applications of Lasers & Electro-Optics*. San Diego, USA.
115. Tuominen, J., Näkki, J., Pajukoski, H., Peltola, T., & Vuoristo, P. (2012). Recent developments in high power laser cladding techniques. *Proc. of 31st ICALEO*, 192-196.
116. Toyserkani, E., Khajepour, A. & Corbin, S. (2004). *Laser Cladding*. CRC Press, Boca Raton. 2004. ISBN: 9781420039177
117. Abioye, T.E., Farayibi, P.K. & Clare, A.T. (2017). A comparative study of Inconel 625 laser cladding by wire and powder feedstock, *Materials and Manufacturing Processes*, DOI: 10.1080/10426914.2017.1317787
118. Abioye, T.E., McCartney, D.G. & Clare, A.T. (2015). Laser cladding of Inconel 625 wire for corrosion protection. *Journal of Materials Processing Technology* 217. 232–240.
119. Xu, X., Mi, G., Chen, L., Xiong, L., Jiang, P., Shoa X. & Wang, C. (2017). Research on microstructures and properties of Inconel 625 coatings obtained by laser cladding with wire, *Journal of Alloys and Compounds* (2017), doi: 10.1016/j.jallcom.2017.04.252.
120. Nurminen, J. (2008). *Hot-wire Laser Cladding: Process, Materials and Their Properties*. PhD. Thesis. Tampere University of Technology. Vol. 765.
121. Ion, J. (2005). *Laser processing of engineering materials: principles, procedure and industrial application*. Elsevier.
122. Mendez, P.F., Barnes, N., Bell, K., Borle, S.D., Gajapathi, S.S., Guest, S.D. Izadi, H., Gol, A.K. & Wood, G. (2014). Welding processes for wear resistant overlays. *Journal of Manufacturing Processes* 16 (2014) 4–25.
123. Wang, S-H. & Dan., T. (2016). A market study on weld cladding in Canadian mining and mineral processing sectors. *National Research Council Canada, Report Number: NRC-EME-55753*. May 2016. <http://doi.org/10.4224/23001192>.
124. Wikipedia – Gas metal arc welding. https://en.wikipedia.org/wiki/Gas_metal_arc_welding (05/2018).
125. SFS-EN 14610. Welding and allied processes. Definitions of metal welding processes. *Mechanical Engineering and Metals Industry Standardization in Finland, 2005 (EN 14610:2004)*
126. SFS EN ISO 4063. Welding and allied processes. Nomenclature of processes and reference numbers. *Mechanical Engineering and Metals Industry Standardization in Finland, 2011 (EN ISO 4063:2010)*.
127. International Institute of Welding. (1976). *Classification of Metal Transfer*, IIW Doc. XII-636-76.

128. Norrish, J. (2003). A Review of Metal Transfer Classification in Arc Welding, IIW Doc. XII-1769-03.
129. Scotti, A., Ponomarev, V. & Lucas, W. (2012). Scientific application oriented classification for metal transfer modes in GMA welding. *Journal of Materials Processing Technology* 212 (2012). pp 1406 – 1413.
130. DSV 0973. Overview of process control variants for gas shielded metal-arc welding. Deutsches Institut für Schweißen und verwandte Verfahren e. V. 2015.
131. Kapustka, N. (2015). Achieving Higher Productivity Rates Using Reciprocating Wire Feed Gas Metal Arc Welding. *The Welding Journal*. April 2015.
132. ISO 15614-7:2016. Specification and qualification of welding procedures for metallic materials. Welding procedure test. Part 7: Overlay welding. ISO — International Organization for Standardization.
133. Hu, J., & Tsai, H.L. 2007. Heat and mass transfer in gas metal arc welding. Part I: The arc. *International Journal of Heat and Mass Transfer* 50 (2007) 833–846. doi:10.1016/j.ijheatmasstransfer.2006.08.025.
134. Lehtomaa, K. Pronius Oy / Fronius GmbH.
135. Sarrafi, R. & Kovacevic, R. (2010). Cathodic cleaning of oxides from aluminum surface by variable-polarity arc. *Welding journal*, 89(1), pp.1s-10s.
136. Scotti, A., Dutra, J. C., & Ferraresi, V. A. (2000). The influence of parameter settings on cathodic self-etching during aluminum welding. *Journal of Materials Processing Technology*, 100(1-3), 179-187.
137. Pépe, N., Egerland, S., Colegrove, P. A., Yapp, D., Leonhartsberger, A. & Scotti, A. (2011). Measuring the Process Efficiency of Controlled Gas Metal Arc Welding Processes. *Science and Technology of Welding & Joining*, Volume 16, Issue 5, Pages 412-417.
138. Joseph, A. P. (2001). Assessing the effect of GMAW-pulse parameters on arc power and welding heat input. Master's Thesis. Ohio State University.
139. ISO/TR 18491 (2015). Welding and allied processes — Guidelines for measurement of welding energies. ISO — International Organization for Standardization. 2015.
140. ISO/TR 17671-1 (2002). Welding – Recommendations for welding of metallic materials – Part 1: General guidance for arc welding. . ISO — International Organization for Standardization.
141. EN 1011-1 (2009). Welding. Recommendations for welding of metallic materials. Part 1: General guidance for arc welding. Finnish Standards association (SFS-EN 1011-1).
142. EN 1011-6 (2006). Welding. Recommendation for welding of metallic materials. Part 6: Laser beam welding. Finnish Standards association (SFS-EN 1011-6).
143. Blondeau, R. (Ed.). (2013). Metallurgy and mechanics of welding: processes and industrial applications. John Wiley & Sons.
144. Dutra, J. C., Silva, R. H. G., Marques, C. & Vivian, A. B. (2016). A new approach for MIG/MAG cladding with Inconel 625. *Welding in the World*. Nov 2016, Volume 60, Issue 6, pp 1201–1209.
145. Caron, J.L. & Sowards, J.W. (2014). Comprehensive materials processing, Chapter 6.09- Weldability of Nickel-Base Alloys. pp 152–179. 2014. Elsevier.
146. Chen, M., Zhang, D. & Wu, C. (2017). Current waveform effects on CMT welding of mild steel. *Journal of Materials Processing Technology* 243 (2017) 395–404.
147. Peak performance through innovation and expertise. (2006). Linde Gas Brochure. Linde AG.
148. Mison suojakaasuesite. (2015). Oy AGA Ab.
www.aga.fi/internet.lg.lg.fin/fi/images/AGA_MISON_Brochure_FI_A5634_257420.pdf?v=1.0
(02/2018)
149. Young, G. A. & Kikel, J. (2002). Factors affecting hydrogen embrittlement resistance of NiCrMnNb welds. 6th International Trends in Welding Research. Conference Proceedings, 15-19 April 2002, PineMountain, GA, ASM International, pp. 666-671.

150. Baixo, C. E. I. & Dutra, J. C. (2011). Effect of shielding gas and transfer mode on the application of 625 alloy in carbon steel. *Welding International* Vol. 25, No. 12, Dec 2011, 903–909.
151. Holthaus, M. International Welding Engineer training course material, HG1. GSI SLV mbH, Gesellschaft für Schweißtechnik international – Schweißtechnische Lehr- und Versuchsanstalten. 2014 SLV Duisburg.
152. SFS-EN ISO 6520-1 (2008). Welding and allied processes. Classification of geometrical imperfections in metallic materials. Part 1: Fusion welding. Finnish standards association.
153. SFS-EN ISO 5817 (2014). Welding. Fusion-welded joints in steel, nickel, titanium and their alloys (beam welding excluded). Quality levels for imperfections. Finnish standards association.
154. SFS-EN ISO 15614-7 (2016). Specification and qualification of welding procedures for metallic materials. Welding procedure test. Part 7: Overlay welding. Finnish standards association.
155. Nguyen, T.C., Weckman, D.C., Johnson, D.A. & Kerr, H.W. (2005). The humping phenomenon during high speed gas metal arc welding. *Science and Technology of Welding and Joining*, Vol. 10, No. 4 (2005), pp. 447-459.
156. Adebayo, A., Mehnen, J. & Tonnellier, X. (2012). Limiting Travel Speed in Additive Layer Manufacturing. *Trends in Welding Research 2012: Proceedings of the 9th International Conference*. June 4-8 2012, Chicago, Illinois.
157. Willinger, M. (2013). CMT PROCESS – Training Documentation. Fronius International GmbH Version 1/2013.
158. Singh, R. (2012). Chapter 8-Weld Defects and Inspection. *Applied Welding Engineering: Processes, Codes, and Standards*, 277-295.
159. Frostevarg, J. & Kaplan, A.F.H. (2014). Undercuts in Laser Arc Hybrid Welding. *Physics Procedia* 56 (2014), 663–672. doi: 10.1016/j.phpro.2014.08.071
160. Lukkari, J. (2002). Hitsaustekniikka: Perusteet ja kaarihitsaus. Opetushallitus.
161. Willinger, M. (2014). MIG/MAG, CMT & CMT Adv. Parameter Adjustments. Fronius International GmbH. March 2014.
162. Fronius TransPuls Synergic 5000 welding power source. Remote control unit RCU.
163. Pépe, N. (2010). Advances in Gas Metal Arc Welding and Application to Corrosion Resistant Alloy Pipes. PhD Thesis. Cranfield University, 2010.
164. Almeida, P.M.S. (2012). Process control and development on wire and arc additive manufacturing. Ph.D. Thesis. Cranfield University. 2012.
165. Egerland, S. & Helmholdt, R. (2008). Overlaying (Cladding) of high temperature affected components by using the cold metal transfer process. Safety and reliability of welded components in energy and processing industry. *Proceedings of the IIW international Conference*, July 2008, Graz, Austria.
166. Egerland, S. (2009). Status and Perspectives in Overlaying under Particular Consideration of Sophisticated Welding Processes. *Quarterly Journal of the Japan Welding Society*. Jan 2009. DOI: 10.2207/qjws.27.50s.
167. Daniels, T.W. (2015). Applicability of cold metal transfer for repair of dissimilar metal welds in stainless steel piping in nuclear power plants. Thesis, M.Sc. The Ohio State University 2015.
168. McVicker, N.P. (2015). Structural Weld Overlays for Mitigation of Primary Water Stress Corrosion in Nuclear Power Plants. Thesis, M.Sc. The Ohio State University 2015.
169. Frei, J., Alexandrov, B.T. & Rethmeier, M. (2016). Low heat input gas metal arc welding for dissimilar metal weld overlays part I: the heat-affected zone. *Welding in the World* (2016) 60. 459-473.
170. Rutzinger, B. (2012). Kierunki rozwoju w przemyśle energetycznym. Zastosowanie napawania metodą CMT w elektrowniach węglowych. *Biuletyn Instytutu Spawalnictwa*. No. 5/2012.
171. Rutzinger, B. (2014). Influence of the welding process to the dilution rate of weld overlays on unalloyed steel using the weld consumable ERNiCrMo-3 (Alloy 625). *Biuletyn Instytutu Spawalnictwa*. No. 4/2014

172. Rozmus-Górnikowska, M., Blicharski, M., Kusiński, J., Kusiński, L. & Marszycki, M. (2013). Influence of boiler pipe cladding techniques on their microstructure and properties. *Archives of Metallurgy and Materials*, Volume 58, Issue 4, 2013. DOI: 10.2478/amm-2013-0131.
173. Rozmus-Górnikowska, M., Cienik, L., Blicharski, M. & Kusiński, J. (2014). Microstructure and Microsegregation of an Inconel 625 Weld Overlay Produced on Steel Pipes by the Cold Metal Transfer Technique. *Archives of Metallurgy and Materials*, Volume 59, Issue 3, 2014. DOI: 10.2478/amm-2014-0185.
174. Rozmus-Górnikowska, M. & Blicharski, M. (2015). Microsegregation and precipitates in Inconel 625 arc weld overlay coatings on boiler pipes. *Archives of Metallurgy and Materials* Volume 60, 2015, Issue 4, DOI: 10.1515/amm-2015-0420.
175. Slania, J., Krawczyk, R. & Wójcik, S. (2015). Quality requirements put on the Inconel 625 austenite layer used on the sheet walls of the boiler's evaporator to utilize waste thermally. *Archives of Metallurgy and Materials*, Volume 60, 2015, Issue 2, DOI: 10.1515/amm-2015-0192.
176. Slania, J., Krawczyk, R. & Wójcik, S. (2015). Examination and detecting discontinuities in the austenite inconel 625 layer used in the sheet pile walls of the boiler's evaporator to utilize waste thermally. *Archives of Metallurgy and Materials*, Volume 60 2015, Issue 3, DOI: 10.1515/amm-2015-0294.
177. Solecka, M., Petrzak, P. & Radziszewska, A. (2015). The microstructure of weld overlay Ni-base alloy deposited on carbon steel by CMT method. *Solid State Phenomena* Vol. 231 (2015) pp 119-124. DOI: 10.4028/www.scientific.net/SSP.231.119.
178. Petrzak, P., Blicharski, M., Dymek, S. & Solecka, M. (2015). Electron microscopy investigation of Inconel 625 weld overlay on boiler steel. *Solid State Phenomena* Vol. 231 (2015) pp 113-118. DOI: 10.4028/www.scientific.net/SSP.231.113.
179. Ola, O.T. & Doern, F.E. (2014). A study of cold metal transfer clads in nickel-base INCONEL 718 superalloy. *Materials and Design* 57 (2014) 51–59.
180. Benoit, A., S. Jobez, S., Paillard, P., Klosek V & Baudin, T. (2011). Study of Inconel 718 weldability using MIG CMT process. *Science and Technology of Welding and Joining* 2011, Vol 16, No 6, pp 477-482.
181. Nutech mbH. Laser Cladding. <http://www.nutech.de/en/services/laser-centre/surface-engineering/laser-cladding> (05/2018)
182. Ding, D., Pan, Z., Cuiuri, D. & Li, H. (2015). A multi-bead overlapping model for robotic wire and arc additive manufacturing (WAAM). *Robotics and Computer-Integrated Manufacturing*, 31 101-110. <http://ro.uow.edu.au/eispapers/3307>.
183. Xiong, J., Zhang, G., Gao, h. & Wu, L. (2013). Modeling of bead section profile and overlapping beads with experimental validation for robotic GMAW-based rapid manufacturing. *Robotics and Computer-Integrated Manufacturing* 29(2013)417–423. <http://dx.doi.org/10.1016/j.rcim.2012.09.011>.
184. Nenadl, O., Ocelík, V., Palavra, A., & De Hosson, J. T. M. (2014). The prediction of coating geometry from main processing parameters in laser cladding. *Physics Procedia*, 56, 220-227.
185. Ocelík, V., Nenadl, O., Palavra, A., & De Hosson, J. T. M. (2014). On the geometry of coating layers formed by overlap. *Surface and Coatings Technology*, 242, 54-61.
186. Kim, J. S., Kim, I. J., & Kim, Y. G. (2014). Optimization of weld pitch on overlay welding using mathematical method. *International journal of precision engineering and manufacturing*, 15(6), 1117-1124. DOI: 10.1007/s12541-014-0445-3.
187. Chen, H. M., & Zeng, M. (2007). Waveform control high-speed welding system for arc welding robot. In *Robotic Welding, Intelligence and Automation* (pp. 235-242). Springer, Berlin, Heidelberg.
188. Adebayo, A., Mehnen, J. & Tonnellier, X. (2012). Limiting Travel Speed in Additive Layer Manufacturing. *Trends in Welding Research 2012: Proceedings of the 9th International Conference*. June 4-8 2012, Chicago, Illinois.
189. Pickin, C.G., Williams, S.W. & Lunt, M. (2011). Characterisation of the cold metal transfer (CMT) process and its application for low dilution cladding. *Journal of Materials Processing Technology* 211 (2011) 496–502.

190. Liang, Y., Hu, S., Shen, J., Zhang, H. & Wang, P. (2017). Geometrical and microstructural characteristic of the TIG-CMT hybrid welding in 6061 Al cladding. *Journal of Materials Processing Technology* 239 (2017) 18–30. <http://dx.doi.org/10.1016/j.jmatprotec.2016.08.005>.
191. Rajeev, G.P., Kamaraj, M. & Srinivasa R. Bakshi. (2014). Al-Si-Mn Alloy Coating on Aluminum Substrate Using Cold Metal Transfer (CMT) Welding Technique. *The journal of the Minerals, Metals & Materials Society* 66(6):1061-1067 C. June 2014.
192. Rajeev, G.P., Kamaraj, M. & Srinivasa R. Bakshi. (2014). Comparison of Stellite Coatings on Valve Steel Material Prepared by Plasma Transferred Arc and Cold Metal Transfer Techniques. TMS 2014, 143rd Annual Meeting & Exhibition. San Diego, 2014.
193. Rajeev, G.P., Kamaraj, M. & Srinivasa R. Bakshi. (2017). Hardfacing of AISI H13 tool steel with Stellite 21 alloy using cold metal transfer welding process. *Surface & Coatings Technology* 326 (2017) 63–71.
194. Zhang, H., Hu, S., Wang, Z. & Liang, Y. (2015). Development of Stellite Surface Coating on H13 Tool Steel Using Cold Metal Transfer (CMT) Welding Process. *Materials Science & Technology* 2015. Technical meeting and exhibition.
195. Tapiola, J. (2017). Cold metal transfer cladding of wear and corrosion resistant coatings in engine applications. Master of Science thesis. Tampere University of Technology.
196. Jiang, X., He, P., Feng, J. & Shi, C. (2007). Microstructure characteristics of CuSi3 cladding on 30CrMnSi steel with cold metal transfer technology. *Transactions of the China Welding Institution*. 2007-02.
197. Zhang, H., Hu, S., Wang, Z. & Liang, Y. (2015). The effect of welding speed on microstructures of cold metal transfer deposited AZ31 magnesium alloy clad. *Materials and Design* 86 (2015) 894–901. <http://dx.doi.org/10.1016/j.matdes.2015.07.143>.
198. Bradstreet, B. (1968). Effect of surface tension and metal flow on weld bead formation. *Welding journal*, 1968, Vol 47 (7). Page: 314–322.
199. Kujanpää, V.P. (1983). Weld Defects in Austenitic Stainless Steel Sheets – Effect of Welding Parameters. *The Welding Journal*, welding research supplement. Feb 1983.
200. Harris, I.D. (2009). High-Speed GMAW and Laser GMAW Hybrid Welding of Steel Sheet. PhD Thesis. Cranfield University.
201. Mendez, P.F. & Eagar, T.W. (2003). Penetration and Defect Formation in High-Current Arc Welding. *The Welding Journal*, 2003, Vol 82, (10), pp 296–306. DOI: 10.2172/835707
202. Johansson, E., Pettersson, R., Mameng, S. & Alfonsson, E. (2012). 654 SMO®: Moving the boundaries of stainless steel and challenging Ni-base alloys. ACOM 2-2012. A corrosion management and applications engineering magazine from Outokumpu.
203. Ahsan, M. R., Cheepu, M., Ashiri, R., Kim, T. H., Jeong, C., & Park, Y. D. (2017). Mechanisms of weld pool flow and slag formation location in cold metal transfer (CMT) gas metal arc welding (GMAW). *Welding in the World*, 61(6), 1275-1285.
204. Schijve, J. (2009). *Fatigue of Structures and Materials*. Springer. ISBN-13: 978-1-4020-6807-2
205. Discussion with a specialist at Fronius GmbH at Wels, Austria.

Tampereen teknillinen yliopisto
PL 527
33101 Tampere

Tampere University of Technology
P.O.B. 527
FI-33101 Tampere, Finland

ISBN 978-952-15-4252-7

ISSN 1459-2045